MONASH University

Selective Removal of Alkali and Alkaline Earth Metals from Low-Rank Xinjiang Coal

Song Zhou

A thesis submitted for the degree of

Doctor of Philosophy

Department of Chemical engineering

Monash University

2019

Copyright notice

Table of Contents

Abstract

Low-rank coals which account for larger than 50% of world coal reserves is widely used for local power generation. However, it is estimated that several billion dollars have to spent on the abating fouling-related issues in boilers, due to the high content of alkali and alkaline earth metals (AAEMs). Chemical leaching of AAEMs out of low-rank coal is the most efficient and straightforward way to reduce the ash fouling propensity of leached coal. However, the resultant waste leachate poses significant cost and environment challenges for the scale-up of low-rank coal leaching processes. In this PhD project, an efficient, cost-effective and environmentally benign leaching process has been developed for the selective removal of AAEMs from low-rank Xinjiang Coal, which integrates two core steps, leaching using recycled leachate and waste leachate treatment and recovery.

For coal leaching, attention was focused on the recyclability study of leaching reagents (water and hydrochloric acid (HCl acid)), via both the experimental investigation and kinetics modelling, which was rarely touched in literature. In terms of waste leachate treatment and recovery, which is crucial to turn the whole process into cost-effective and environmentally friendly, the core work was *1)* to determine the best wastewater treatment method which has a high water recovery rate, high impurities removal rate and low cost via integrating into the leaching process, and *2)* to develop an efficient method to dispose of the concentrated chloride wastes discharged from the wastewater treatment unit, so as to regenerate and recycle HCl acid and meanwhile obtain Cl-clean/free solid residues as by-products. All aims have been achieved in this thesis. It is found that the leachate recycling is crucial for the significant decrease of water and power consumptions, and reverse osmosis is proven to be the better waste leachate treatment method via being integrated into the leaching step. Additionally, the water-soluble Na removal decreases exponentially with the increase in cycle number, whereas the constant initial HCl acid concentration for each cycle results in a stable HCl-soluble element removal extent. Finally, the addition of $MgCl_2$ has been unveiled for the first time to have a double-side effect on the HCl regeneration from $CaCl_2$ via pyrohydrolysis at the presence of silica. From the atomic structure analysis, Ca-O-Mg_y-Cl_x is more likely to form at the co-pyrohydrolysis of $CaCl_2$ and $MgCl_2$, since Ca^{2+} is always preferentially bonded with O^{2-} at its first atomic shell.

The completion of this project is to address a global challenge facing the coal mining industry; how to upgrade low-rank coal to high-quality thermal fuel that can be burnt at high-efficiency and low-emission for power generation. It will give a good contribution to the understanding of recyclability of leaching reagents and chloride waste treatment in an environmentally-harmless manner.

Declaration

This thesis contains no material which has been accepted for the award of any other degree or diploma at any university or equivalent institution and that, to the best of my knowledge and belief, this thesis contains no material previously published or written by another person, except where due reference is made in the text of the thesis.

Signature: …… ……

Print Name: …….

Date: …….

Publications during Enrolment

Peer-reviewed journal papers

Zhou, S.; Hosseini, T.; Zhao, J.; Zhang, X.; Wu, H.; Zhang, L., Selective removal of sodium from low-rank Xinjiang coal upon a multi-stage counter-current water washing: experimental investigation and kinetic modelling. *Energy & Fuels* 2019, 33, 3, 2142-2152.

Zhou, S.; Qian B.; Hosseini, T.; Girolamo, A.D.; Zhang, L., Pyrohydrolysis of $CaCl_2$ waste for the recovery of HCl acid upon the synergistic effects from $MgCl_2$ and silica. *ACS Sustainable Chemistry & Engineering* 2019, 7, 3, 13-28.

Zhou, S.; Hosseini, T.; Zhang, X.; Haque, N.; Zhang, L., Selective removal of sodium and calcium from low-rank coal – Process integration, simulation and techno-economic evaluation. *Fuel Processing Technology* 2018, 172, 13-28.

Zhou, S.; Qian, B.; Liu, C.; Hosseini, T.; Zhang, L., Synchrotron X-Ray Absorption Spectroscopy (XAS) study on the atomic structures of chlorine and calcium derived from the co-pyrohydrolysis of alkaline earth metal chloride wastes. *Journal of Hazardous Materials* 2019 (**Under review**).

Conference papers

Zhou, S.; Hosseini. T.; Zhang, X.; Haque, N.; Zhang, L., Selective removal of sodium and calcium from low-rank coal – process integration, simulation and experimental investigation. *Chemeca Conference*, 2016, Adelaide, Australia.

Zhou, S.; Jin, J.; Hosseini, T.; Haque, N.; Zhang, L., Multistage counter-current water washing for the removal of sodium from Xinjiang coal. *2017 International Conference on Coal Science & Technology (ICCS&T)*, Sept, 2017, Beijing, China.

Thesis including published works declaration

I hereby declare that this thesis contains no material which has been accepted for the award of any other degree or diploma at any university or equivalent institution and that, to the best of my knowledge and belief, this thesis contains no material previously published or written by another person, except where due reference is made in the text of the thesis.

This thesis includes three original papers published in peer reviewed journals and one submitted journal paper. The core theme of the thesis is selective removal of alkali and alkaline earth metals from low-rank Xinjiang coal. The ideas, development and writing up of all the papers in the thesis were the principal responsibility of myself, the student, working within the Department of Chemical Engineering under the supervision of Lian Zhang.

The inclusion of co-authors reflects the fact that the work came from active collaboration between researchers and acknowledges input into team-based research.

In the case of chapters 3, 4 and 5, my contribution to the work involved the following:

Thesis chapter	Publication Title	Status	Nature and % of student contribution	Co-author name(s) Nature and % of Co-author's contribution	Co-author(s), Monash student
3	Selective removal of sodium and calcium from low-rank coal – Process integration, simulation and techno-economic evaluation	Published	88% Concept, experimental work and writing	1) Tahereh Hosseini, Experimental setup, 2% 2) Xiwang Zhang, Suggestions, 2% 3) Nawshad Haque, Suggestions, 3% 4) Lian Zhang, Suggestions 5%	No No No No
4	Selective removal of sodium from low-rank Xinjiang coal upon a multi-stage counter-current water washing: experimental investigation and kinetic modelling	Published	85% Concept, experimental work and writing	1) Jie Zhao, Experiment assistant 2% 2) Hongwei Wu, Suggestions 3% 3) Tahereh Hosseini, Suggestions 3% 4) Xiwang Zhang, Suggestions 2% 5) Lian Zhang, Suggestions 5%	Yes No No No No
5	Pyrohydrolysis of $CaCl_2$ waste for the recovery of HCl acid upon the synergistic effects from $MgCl_2$ and silica	Published	88% Concept, experimental work and writing	1) Binbin Qian, Data analysis 3% 2) Anthony De Girolamo, Experiment assistant 2% 3) Tahereh Hosseini, Suggestions 2% 4) Lian Zhang, Suggestions 5%	Yes No No No

I have renumbered sections of submitted or published papers in order to generate a consistent presentation within the thesis.

Student signature: **Date:**

The undersigned hereby certify that the above declaration correctly reflects the nature and extent of the student's and co-authors' contributions to this work.

Main Supervisor signature: **Date:**

Acknowledgements

PhD is a tough but amazing journey. At this moment that l am approaching the end of the journey; there are a lot of people to acknowledge.

Firstly, I would like to take this opportunity to thank my main supervisor A/Prof Lian Zhang for taking me on board as part of his research group. I am very grateful for his patience in revising my work and his continued support and encouragement throughout the length of my candidature. My PhD journey cannot be so successful without his continuous support. To my co-supervisor Dr Tahereh Hosseini, Dr Nawshad Haque and Prof Xiwang Zhang (first year) thank you for the valuable advice throughout this journey.

I acknowledge the China Scholarship Council (CSC) – Monash PhD Scholarship and Monash top-up scholarship for the financial supports. Without them, it is impossible to finish this project smoothly.

I want to thank my dear friends who have make my PhD journey a very pleasant and memorable one. Anthony, Baiqian, Binbin, Cheng, Miriam, Vincent, Qiaoqiao, Sasha, Ali, Tavir, Shenyong, Rabeeh, Jie, and Iman, it is my great honour to meet you guys to be in the same research group. You are not only the best friends for my PhD journey but also forever through the whole life no matter wherever we will be. I want to thank my colleagues from other groups, Yitian, Yang, Ruohui, Huadong, and others who have directly or indirectly given support or encouragement to me.

Thank you to all the Chemical Engineering department staff, particularly Tracy Groves, Lilyanne Price, Kim Phu, Harry Bouwmeester, Gus Austin, and Ross Ellingham.

Most importantly, thanks to my family for their continuous motivation and backing. My girlfriend (future wife) Yawei, thank you for your understanding and patience and staying by my side through these tough times.

List of Figures

Chapter 1

Chapter 3

Chapter 4

Chapter 5

Chapter 6

List of Tables

Chapter 2

Chapter 3

Chapter 4

Chapter 5

Chapter 6

Abbreviations and Nomenclature

Abbreviations

AAEMs	Alkali and alkaline earth metals
APEA	Aspen Process Economic Analyzer
AAS	Ammonium acetate soluble
AI	Acid insoluble
Ca	Calcium
Cl	Chlorine
EXAFS	Extended X-ray absorption fine structure spectroscopy
ED	Electrodialysis
H	Hydrogen
H^+	Proton
HCl	Hydrochloric
HAS	Hydrochloric acid soluble
ICP-OES	Inductively coupled plasma optical emission spectrometry
IER	Ion exchange resin
IRR	Internal rate of return
K	Potassium
LCF	Linear combination fitting
Mg	Magnesium
MSF	Multi-stage flash
n	Coordination number
Na	Sodium
NPV	Net present value
O	Oxygen
PVDF	Polyvinylidene fluoride
PSD	Particle size distribution
RO	Reverse osmosis

R	Bond length
SCM	Shrinking core model
Si	Silica
SEM	Scanning electron microscopy
UF	Ultrafiltration
WS	Water-soluble
XRD	X-ray diffraction
XRF	X-ray fluorescence
XAS	X-ray absorption spectroscopy
XANES	X-ray absorption near-edge spectroscopy

Nomenclature

C_I	Na^+ concentration in hypothetical centre point at any time *t* (mg/L)
C_{I0}	Maximum Na^+ concentration in the water contained in a coal particle (mg/L)
C_o	Na^+ concentration in bulk water at any time *t* (mg/L)
C_{o0}	Na^+ concentration in fresh/recycled water (mg/L)
C_{o0}^1	Na^+ concentration in the 1st used water (mg/L)
C_{o0}^2	Na^+ concentration in the 2nd used water (mg/L)
$C_{o1}\|_t$	Na^+ concentration in leachate at time *t* in reactor 1 (mg/L)
$C_{o2}\|_t$	Na^+ concentration in leachate at time *t* in reactor 2 (mg/L)
$C_{o3}\|_t$	Na^+ concentration in leachate at time *t* in reactor 3 (mg/L).
C'_{o1}	Amount of Na removed in stage 1 divided by the volume of bulk water (mg/L)
C'_{o2}	Amount of Na removed in stage 2 divided by the volume of bulk water (mg/L)
C'_{o3}	Amount of Na removed in stage 3 divided by the volume of bulk water (mg/L)
D_{eff}	Effective diffusion coefficient of Na^+ in coal particles (cm^2/s)
J	Flux of Na^+ through exterior surface of particle ($mg/(s\cdot cm^2)$)
k	Rate constant (min^{-1})
m_A	Mass of Na^+ in bulk water (mg)
M	Maximum water-soluble Na content of raw coal (mg/kg-coal)

M_1	Na content of 1st washed coal (mg/kg-coal)
M_2	Na content of 2nd washed coal (mg/kg-coal)
R	Radius of coal particle (cm)
t	Leaching time (s)
T	Total leaching time in one reactor (s)
V_l	Volume of bulk water corresponding to a single coal particle (L)
V_I	Volume of accessible pores of coal particles filled by water (L/kg-coal)
W_{ls}	Liquid-to-solid mass ratio
X	Element removal extent (%)
R^2	Correlation coefficient
ΔE_0	Energy shift
ΔR	Change in half-path length

Greek

σ^2	Debye-Waller factor
s_0^2	The scattering amplitude of photo-electron
ρ_c	Density of coal particle (kg/L)
ρ_l	Density of water (kg/L)

Superscripts

ad	Air-dried
d	Dried basis
daf	Dry ash free basis

Chapter 1 Introduction

1.1 Overview

Low-rank coal, more commonly referred to brown coal and sub-bituminous coal, contributes to more than 50% of the world's coal reserves [1]. It is abundant in many regions such as Australia, China, USA, and Germany and provides an economically attractive alternative to high-rank black coal (i.e. bituminous coal and anthracite) for electricity generation [2, 3]. The use of low-rank coal is becoming increasingly important with the ongoing depletion of high-rank bituminous coal. However, low-rank coal firing boilers have been afflicted by severe fouling caused by its higher content of alkali and alkaline earth metal (AAEMs, Na, K, Ca and Mg) [3, 4]. As a result, the boilers have to be shut down frequently and run at a low thermal load [4], resulting in a lower production rate, lower boiler efficiency and a higher emission rate of greenhouse gases. It is estimated that several billion dollars annually have to be spent on abate the fouling related issues [5].

A prior leaching to remove the troublesome AAEMs is a promising way to increase ash melting point and thus, reduce its propensity for fouling in the combustion boiler. Conventional coal cleaning techniques were exclusively targeted at high-rank coal with a large portion of its inorganic metals present as discrete grains and physically separate from the coal matrix [6]. As mineral matter has a larger density than the carbonaceous matrix, it can be removed physically and easily via the density difference [7]. Variations in surface properties can also allow for separation [8]. However, unlike that in black coal, AAEMs in low-rank coal are deeply and chemically embedded within the coal matrix [9]. Therefore, they cannot be removed using any physical approaches based on either density or surface property discrepancies between mineral matter and coal matrix. Instead, the chemical leaching or solvent extraction has been examined to remove AAEMs from low-rank coal. In particular, research has been focused on the removal

of all ash-forming metals to produce ultra-clean coals (UCC) or ash-free hyper-coal (HPC), from both high-rank and low-rank coals [9-12]. However, the corrosive acid/ alkali reagents and/or high pressure and temperature employed in the existing chemical leaching processes would raise severe environmental concerns, harsh requirement for equipment, and high capital/operating cost, limiting their advance in practical applications. The solvent extraction is also inappropriate for low-rank coal because of the low carbon yield (<30 wt%) resulting from its cross-linked carbonaceous structure [9]. For the conventional coal-fired boilers, the removal of all the ash-forming metals is also unnecessary, considering the fact that AAEMs are the main trigger for fouling and the removal of all ash forming metals will cause a significant increase on the operation cost. Most importantly, the research only focused on the once-through fresh leaching reagent, and the recyclability of leaching reagents has yet to be studied as shown in **Figure 1.1** of the research gap summary. In a practical application, to reduce water loss and enhance the removal extent of target elements, multi-step and leachate-recycling leaching process are normally employed. Additionally, the environmental impact arising from the resultant waste leachate impedes the deployment of low-rank coal leaching processes, and it is in urgent need of relevant studies on the environmentally-benign treatment of the concentrated wastes discharged from waste water treatment units, such as the retention of reverse osmosis which is widely used in the waste water cleaning industry.

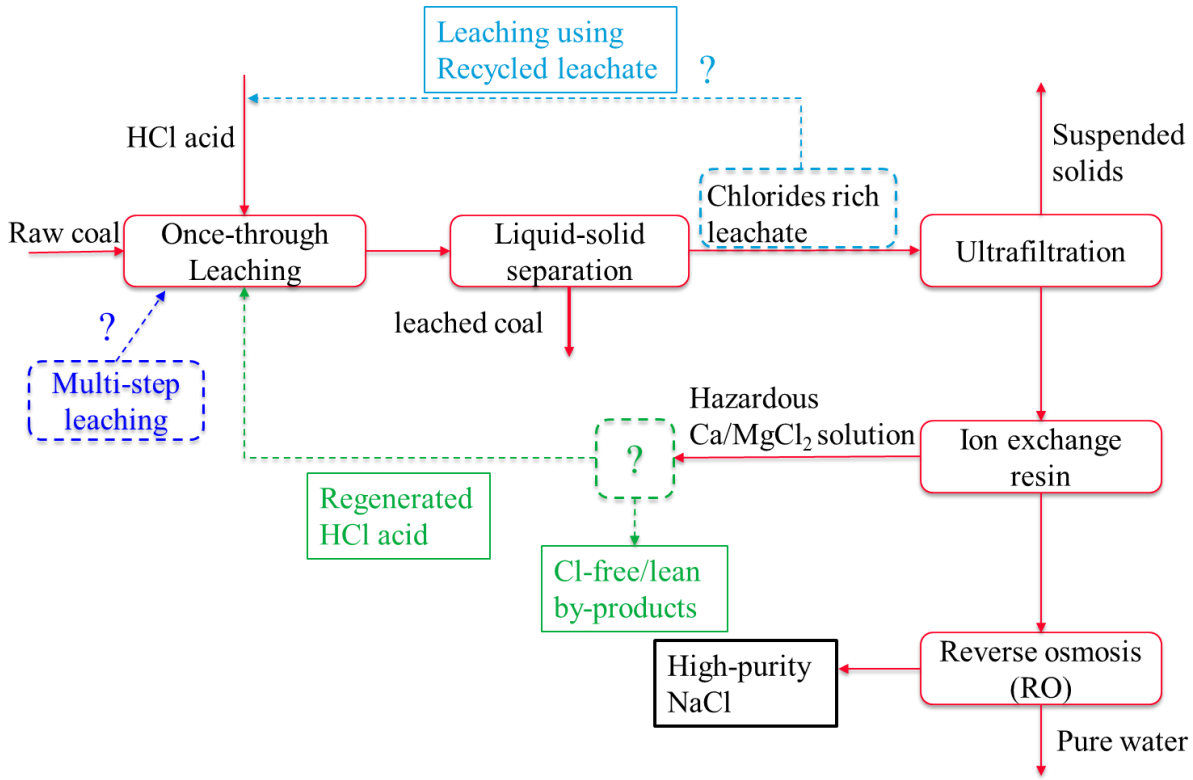

Figure 1.1 Research gap summary

In this PhD project, instead of removing all of the ash-forming metals, only AAEMs were selectively targeted, considering that these are the most critical triggers for ash fouling in a pulverized coal-fired boiler [3, 4, 13]. This project was motivated by the development of a low-rank coal leaching process that needs to be efficient, economically viable and most importantly environmentally benign. To achieve this, two core steps were focused on, including coal leaching, and waste leachate treatment and recovery. For coal leaching, attention was focused on the recyclability study of leaching reagents (water and hydrochloric acid (HCl acid)), via both the experimental investigation and kinetics modelling, which was rarely touched in literature. Regarding waste leachate treatment and recovery, which is crucial to turn the whole process into cost-effective and environmentally friendly, the core work was *1)* to determine the best wastewater treatment method which has a high water recovery rate, high impurities removal rate and low cost via integrating into the leaching process, and *2)* to develop an

efficient method to dispose of the concentrated chloride wastes discharged from the wastewater treatment unit, so as to regenerate and recycle HCl acid and meanwhile obtain Cl-clean/free solid residues as by-products. This PhD project has four innovation points as follows: *1)* the development of a leaching kinetics model, which can predict the recyclability of water in a multi-stage counter-current leaching process satisfactorily; *2)* the exploration and use of silica additive to eliminate the thermodynamic constraint of the pyrohydrolysis of $CaCl_2$; *3)* the discovery of the double-side effect of $MgCl_2$ addition on the pyrohydrolysis of $CaCl_2$ in the presence of silica; and 4) the discovery of Ca-O-Mg-Cl structure the co- pyrohydrolysis of $CaCl_2$ and $MgCl_2$, which helps to understand the interaction between Ca^{2+} and Mg^{2+} in terms of their affinity with Cl^- in the high-temperature reactions.

To achieve the project aims, a number of advanced experimental, analytical and modelling techniques have been used. First of all, Aspen Plus 8.4 was used for process simulation to establish flow sheets for integrated leaching and waste leachate treatment and recycling. Aspen Process Economic Analyzer (APEA) was afterwards integrated with Aspen Plus for the process economic analysis. Secondly, the shrinking core model (SCM) [14] was modified properly to predict the recyclability of leaching reagents. Subsequently, the pyrohydrolysis of chlorides for the HCl regeneration was conducted in an electrically heated horizontal furnace. Finally, the advanced synchrotron X-ray absorption spectroscopy (XAS) was applied for the fingerprints of both Ca^{2+} and Cl^- in the pyrohydrolysis residues. It can promote the understanding of the interaction between the two cations (Ca^{2+} and Mg^{2+}), in terms of their affinity with Cl^- in non-molten silicates, which helps explore the promotion mechanism of Mg^{2+} on the Cl release from the atomic perspective. Throughout this project, a large number of characterisation facilities were involved for quantitative/qualitative analysis. Inductively coupled plasma optical emission spectrometry (ICP-OES) and/or microwave digestion was used for AAEMs

quantification in raw coal and leachates. The SPECTRO IQ X-ray Fluorescence (XRF) was used for composition analysis of ash and pyrohydrolysis residues. The crystalized components in the pyrohydrolysis residues were identified by Rigaku MiniFlex600 XRD. Scanning electron microscopy (SEM) was used to distinguish the phase of the pyrohydrolysis residues. The thermodynamic calculation was conducted by Factsage 6.4 for the prediction of ash melting temperature and the composition of pyrohydrolysis residues.

The outcomes from this project include the development of a novel, cost-effective and environmentally-benign leaching process which can selectively remove AAEMs from low-rank coal, thereby reducing the fouling propensity of leached coal. Apart from the leaching experimental results, the leaching mechanism investigation and model development are pivotal to industry design. The completion of this project is to address a global challenge facing the coal mining industry; how to upgrade low-rank coal to high-quality thermal fuel that can be burnt at high-efficiency and low-emission for power generation. The low-rank coal is mainly used as a local fuel driving the power generation or industry boiler installed close to the mining site. This PhD project is therefore crucial for the power generation and industrial boilers burning low-rank coal that are suffering from severe fouling caused by AAEMs. Additionally, the research on the combination of coal washing and waste water treatment is essential for the development of new clean coal technologies which are viable in the carbon-constrained future. Last but not least, the novel HCl acid recovery method via the pyrohydrolysis of chloride waste is beneficial significantly for hydrometallurgy through the reduction of both the operating cost and environmental effect of waste leachate.

1.2 Research aims

This PhD project aims to develop an efficient, cost-effective and environmental friendly process which can selectively remove AAEMs in low-rank coal. In comparison to the past studies that either had only focused on the high-rank coal rich in discrete mineral grains, failed to test the recyclability of leachates, or did not touch the chloride waste treatment, this study conducted a detailed techno-economic analysis, explored the probability for the reusing of leachates, revealed the scientific mechanisms governing the leaching of AAEMs from low-rank coal, and developed an efficient HCl acid recovery method from chloride wastes, as summarised in **Figure 1.2**.

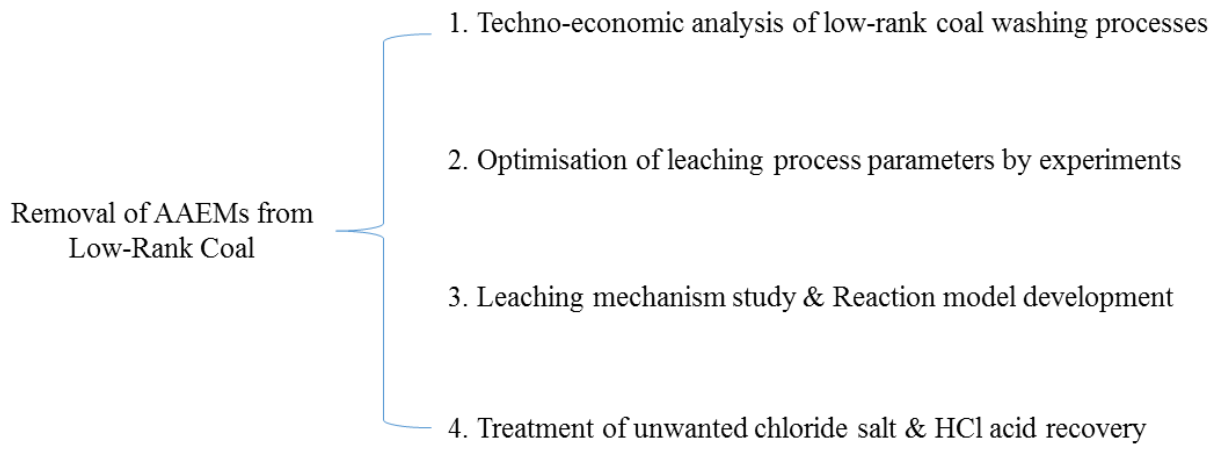

Figure 1.2 Research contents of the PhD project

The specific research targets for this PhD project are outlined as follows:

1. To establish a comprehensive process flowsheet and to conduct the techno-economic analysis to quantify the overall process efficiency, cost and their variation upon the use of different wastewater treatment techniques;

2. To wash out the AAEMs from low-rank coal to an extent that the ash fusion temperature of the resultant low-rank coal exceeds the general pulverised coal-fired boiler design temperature, 1200 °C;
3. To determine the optimum leaching conditions for two leaching reagents (H_2O, and HCl);
4. To develop a model to simulate the leaching kinetics of target elements and find the leaching mechanism;
5. To reveal the maximum allowable recycle times for each leaching reagent prior to it being treated;
6. To develop an HCl acid recovery method from the unwanted and environmentally devastating chloride salt discharged from the waste water treatment steps, and the exploitation of corresponding mechanism.

1.3 Thesis outline

Chapter 1 gives an overview of the research area and highlights the important research aims.

Chapter 2 is a review of the literature, specifically focusing on the modes of occurrence of AAEMs in low-rank coal, coal cleaning technologies, leaching reagent comparison, water recovery techniques, leaching kinetics models, and HCl acid regeneration methods from chlorides. This review ultimately led to the clarification of research gaps that established the fundament of this PhD project.

Chapter 3 gives a detailed study on the integrated low-rank leaching and waste water recovery process simulation using Aspen Plus and APEA. This chapter aimed to identify the most promising process configurations with respect to the AAEMs removal efficiency, water and energy consumption, and process costs. To achieve this, a comprehensive techno-economic analysis has been conducted for four proposed scenarios which consist of different coal leaching steps and waste water recovery techniques. The lab-scale experimental results were also carried out simultaneously to provide the necessary data for the simulation. In addition, the optimal low-rank coal leaching process was compared with a typical existing black coal beneficiation process, so as to prove its efficiency and feasibility.

This chapter has been published as a journal article: **Zhou, S.**; Hosseini, T.; Zhang, X.; Haque, N.; Zhang, L., Selective removal of sodium and calcium from low-rank coal–Process integration, simulation and techno-economic evaluation. *Fuel Processing Technology* 2018, 172, 13-28.

Chapter 4 explores the leaching mechanism of AAEMs from low-rank Xinjiang coal by both water and HCl acid, with special attention on the leaching using leachate. In a practical industrial application, a multi-step and multi-cycle leaching process is commonly employed in order to slash the water consumption and enhance the removal extent of target elements. Therefore, it is crucial to classify the leaching mechanism of using recycled leaching reagent, and then develop kinetics models to predict the recyclability of the leaching reagent.

Part of this chapter has been published as a journal article: **Zhou, S.**; Hosseini, T.; Zhao, J.; Zhang, X.; Wu, H.; Zhang, L., Selective removal of sodium from low-rank Xinjiang coal upon

a multi-stage counter-current water washing: experimental investigation and kinetic modelling. *Energy & Fuels* 2019, 33, 3, 2142-2152.

Chapter 5 studies an efficient HCl acid regeneration method from the mixture of alkaline earth metal chlorides waste via co-pyrohydrolysis with fixed additions of SiO_2 and steam. The motivation for this chapter was to examine if the chlorides waste ($Ca/MgCl_2$) discharged from the coal leaching process can be decomposed in an efficient and environmentally-benign manner, thus obtaining Cl-free solid residues and regenerating HCl acid. In this chapter, the effects of temperature, reaction time and $MgCl_2$ additions on the HCl recovery were studied. Additionally, the mechanism underpinning the HCl recovery from chlorides were extrapolated from the perspective of silicate structure.

This chapter has been published as a journal article: **Zhou, S.**; Qian B.; Hosseini, T.; Girolamo, A.D.; Zhang, L., Pyrohydrolysis of $CaCl_2$ waste for the recovery of HCl acid upon the synergistic effects from $MgCl_2$ and silica. *ACS Sustainable Chemistry & Engineering* 2019, 7, 3, 13-28.

Chapter 6 reveals the local atomic structure of chlorine (Cl) and its transformation upon the interaction between different cations during the co-pyrohydrolysis of $CaCl_2$ and $MgCl_2$ for the regeneration of HCl. An advanced analysis technique, synchrotron X-ray absorption spectroscopy (XAS) was used to fingerprint the Cl K-edge XANES spectra and Ca K-edge EXAFS spectra. In particular, the change on the local atomic environment of Ca^{2+} upon the intrusion of Mg^{2+} atom was interpreted. Consequently, an intermediate structure of Ca-O-Mg_y-

Cl_x was revealed to address the synergism between these two cations in the atomic coordination environment level.

This chapter has been submitted to *Journal of Hazardous Materials*: **Zhou, S.**; Qian, B.; Liu, C.; Hosseini, T.; Zhang, L., Synchrotron X-Ray Absorption Spectroscopy (XAS) study on the atomic structures of chlorine and calcium derived from the co-pyrohydrolysis of alkaline earth metal chloride wastes. *Journal of Hazardous Materials* 2019 (under review).

Chapter 7 gives the conclusions for this PhD project and recommendations for future work related to low-rank coal beneficiation and HCl acid recovery from chloride wastes.

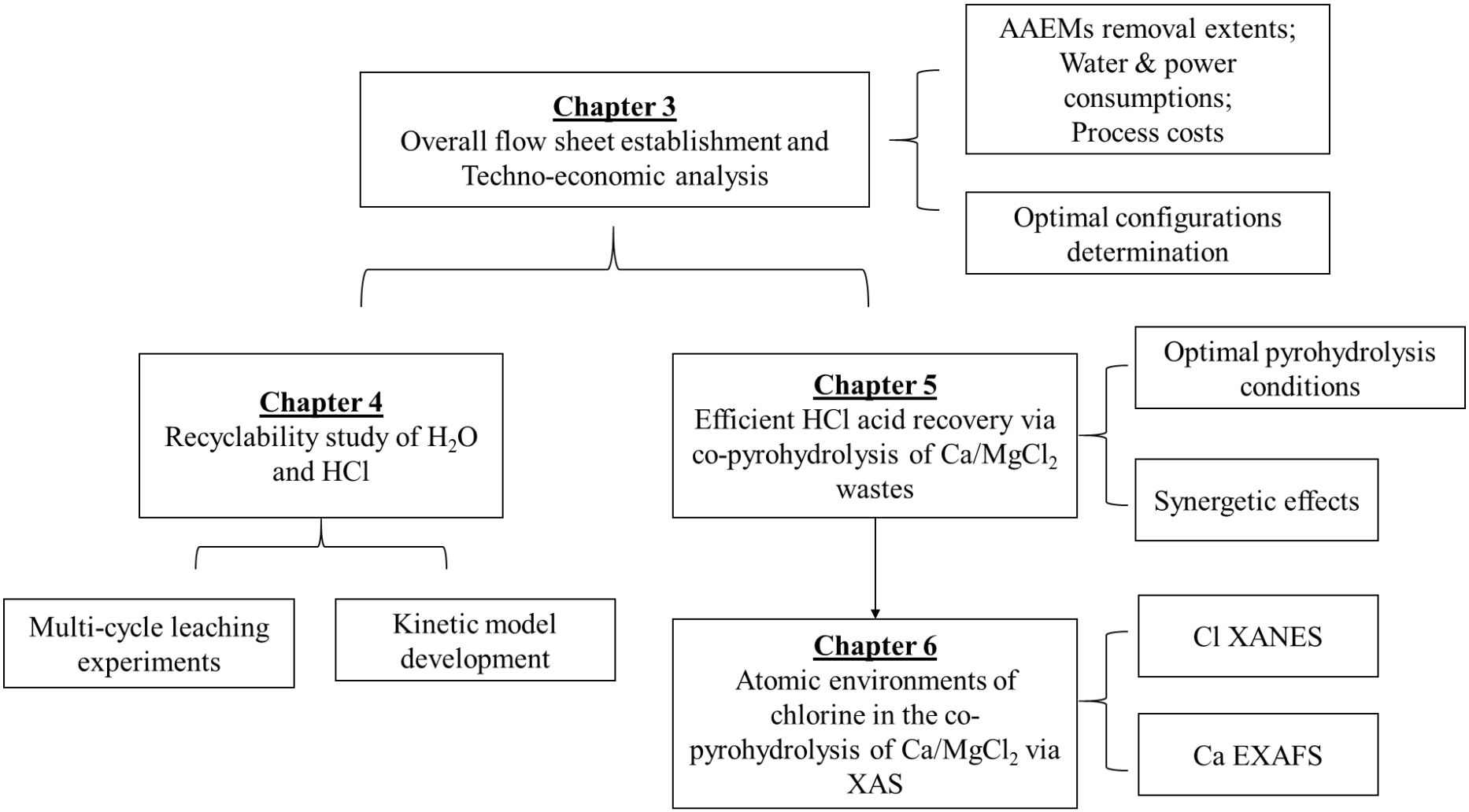

Figure 1.3 Thesis outline summary

Reference

1. Zhou, S.; Hosseini, T.; Zhang, X.; Haque, N.; Zhang, L., Selective removal of sodium and calcium from low-rank coal–Process integration, simulation and techno-economic evaluation. *Fuel Processing Technology* **2018**, *172*, 13-28.
2. Low, F.; De Girolamo, A.; Wu, X.; Dai, B.; Zhang, L., Inhibition of lignite ash slagging and fouling upon the use of a silica-based additive in an industrial pulverised coal-fired boiler: Part 3–Partitioning of trace elements. *Fuel* **2015**, *139*, 746-756.
3. Wu, X.; Zhang, X.; Yan, K.; Chen, N.; Zhang, J.; Xu, X.; Dai, B.; Zhang, J.; Zhang, L., Ash deposition and slagging behavior of Chinese Xinjiang high-alkali coal in 3 MWth pilot-scale combustion test. *Fuel* **2016**, *181*, 1191-1202.
4. Dai, B.-Q.; Low, F.; De Girolamo, A.; Wu, X.; Zhang, L., Characteristics of ash deposits in a pulverized lignite coal-fired boiler and the mass flow of major ash-forming inorganic elements. *Energy & Fuels* **2013**, *27*, (10), 6198-6211.
5. Barnes, I. *Slagging and Fouling in Coal-Fired Boilers*, *CCC/147*; IEA Clean Coal Research: 2009.
6. Gräbner, M., *Industrial coal gasification technologies covering baseline and high-ash coal*. John Wiley & Sons: 2014.
7. Planning, U. S. E. P. A. O. o. A. Q.; Standards, *Compilation of air pollutant emission factors*. US Environmental Protection Agency: 1979.
8. Speight, j. G., *The Chemistry and Technology of Coal*. CRC PR INC: 2016.
9. Wijaya, N.; Zhang, L., A Critical Review of Coal Demineralization and Its Implication on Understanding the Speciation of Organically Bound Metals and Submicrometer Mineral Grains in Coal. *Energy & Fuels* **2011**, *25*, (1), 1-16.
10. Steel, K. M.; Patrick, J. W., The production of ultra clean coal by chemical demineralisation. *Fuel* **2001**, *80*, (14), 2019-2023.
11. Jorjani, E.; Chapi, H. G.; Khorami, M. T., Ultra clean coal production by microwave irradiation pretreatment and sequential leaching with HF followed by HNO3. *Fuel Processing Technology* **2011**, *92*, (10), 1898-1904.
12. Okuyama, N.; Komatsu, N.; Shigehisa, T.; Kaneko, T.; Tsuruya, S., Hyper-coal process to produce the ash-free coal. *Fuel Processing Technology* **2004**, *85*, (8), 947-967.
13. Raask, E., *Mineral Impurities in Coal Combustion: Behavior, Problems, and Remedial Measures*. Hemisphere Publishing Corporation: New York, 1985.

14. Levenspiel, O., Chemical reaction engineering. *Industrial & engineering chemistry research* **1999**, *38*, (11), 4140-4143.

Chapter 2 Literature Review

Scope of literature review

This literature review covers the motivation for this work on the selective removal of AAEMs from low-rank Xinjiang coals. Specifically, the modes of occurrence of AAEMs in low-rank coal is presented at first. Subsequently, the current coal cleaning technologies and their limitations are evaluated. Afterwards, attentions are paid to leaching kinetics models and leaching reagent comparison. Additionally, the mature waste water recovery techniques is compared. Finally, the progress on the HCl acid regeneration from chlorides is discussed.

2.1 Modes of occurrence of AAEMs in low-rank coals

To remove AAEMs, the prerequisite is to understand their original modes of occurrence in low-rank coals. The most common way to determine this is by their solubility in different reagents. Four modes of occurrence can be inferred as **Table 2.1**.

Table 2.1 Mode of occurrence of AAEMs in low-rank coals.

Modes of occurrence	Characteristic
Water-soluble (WS)	Inorganic ions in the form of water-soluble salts, such as chloride, sulphate or hydrated ions; Soluble in water, ammonium acetate and hydrochloric acid
Ammonium acetate soluble (AAS)	Organic cations in carboxyl; Soluble in ammonium acetate but not in water
Hydrochloric acid soluble (HAS)	Inorganic ions in discrete minerals, such as carbonate; organic ions in coordination complexes; Soluble in hydrochloric but not in ammonium acetate and water
Acid insoluble (AI)	Aluminosilicate; Insoluble in water, ammonium acetate and hydrochloric

It has been widely reported that more than half of Na is water-soluble in a low-rank coal, with the rest being organically bound with carboxyl that can be leached away by ammonium acetate [1, 2]. For example, Wijaya, Choo et al. determined the modes of occurrence of the major elements found for two Victorian brown coal samples. It was found that more than half of the sodium in both coal samples can be removed when treated with water alone, and almost entirely removed when additionally leached with ammonium acetate. Similarly, in low-rank Xinjiang coal, Na is primarily partitioned between WS and AAS fractions, whereas the content of K is extremely low. In contrast, Ca, as the predominated metal within the Xinjiang coal showed no change upon the water washing, nevertheless decreased by almost half of its initial amount upon ammonia acetate leaching. The rest of Ca can be mobilized by hydrochloric acid. It suggests that Ca in the Xinjiang coal is mainly either bonded with organic functional groups, or discrete

minerals. Another alkaline earth metal, Mg witnessed a similar mode of occurrence to Ca, i.e., mainly AAS and HAS.

2.2 Coal cleaning technologies

2.2.1 Physical cleaning technologies

Coal cleaning exploiting the physical properties has been a well-developed, widely-used and economical approach in removing impurities from high-rank coal rich in mineral grains [3]. By applying distinctions of physical properties between impurities and high-rank coal matrix, such as variations in densities or surface properties, rocks and inorganically bound metals can be removed [3]. Based on the rational of physical cleaning technologies, the larger the fraction of organically bound minerals in the coal, the lower the fraction that can be removed out by physical ways [4]. Physical cleaning is limited in removing AAEMs from low-rank coal, in which a low proportion of these two elements present as isolated minerals [1]. As a result, it has led to the development of chemical cleaning technologies.

2.2.2 Chemical cleaning technologies

So far, few researches have been done upon the selective removal of AAEMs from low-rank coal. By contrast, the majority of studies were focused on the removal of all the ash-forming metals to produce ultra-clean coals (UCC) or ash-free hypercoal (HPC) [1]. Existing typical techniques of removing AAEMs from low-rank coal are summarised below.

Ultrasound was deployed to remove alkali metals from brown coals under ambient conditions, aiming to avoid the use of high temperature/pressure and to shorten the treatment time [5].

Ultrasonic water-leaching and ammonium acetate-leaching compared with agitation-incurred leaching was studied to explore the effect of ultrasound on the alkali metal (Na and K) removal from coal fines less than 210 μm in diameter. Two ultrasonic frequencies, 25 kHz and 430 kHz with 500 W power were used sequentially to generate cavitation and streaming effects of ultrasound. Experimental results showed that, for deionised water-washing experiment, after 30 min the sodium removal efficiency in ultrasonic washing was comparable with that of agitation, at ~25%; contrary to this, when ammonium acetate was used, the sodium removal was significantly enhanced by ultrasonic, increasing from 30% (stirring) to 85% (ultrasonic). This might be because the majority of water-soluble sodium was adhered to coal surface and easy to remove, so ultrasound did not show remarkable advantage over stirring. However, for ammonium acetate leaching, more ammonium acetate can penetrate into coals to react with ion-exchangeable sodium inside coal matrix due to the effects of ultrasound [6]. The mechanism of intensifying the sodium removal by ultrasonic chemical washing might consist of four stage, pitting of coal surfaces, formation of cracks, penetration of cracks into coal particles, and breakage of coal particles [7]. However, ultrasonic-chemical leaching did not apply to potassium, because in this studied coal, potassium existed in the manner of potassium silicate which can only react with strong acids [8]. The high power consumption is an obvious hurdle for the application of ultrasound to industrial coal washing.

Several studies have concluded that the effectiveness of removing sodium from coals with high sodium contents was a function of temperature, liquid/coal ratio and the particle size [9-11]. Higher temperatures, larger liquid-to-solid mass ratio and smaller coal particles can improve the removal rate for sodium. Meanwhile, Bing Z et al. presented that the hydrothermal treatment was much more effective, 90.5% of sodium removed and only 0.7% Na_2O in ash remained at 300 ℃ and 5.86 MPa after 30 min, than water washing which only removed 60%

at ambient environment [9]. This is because at high temperatures and high pressure, not only the covalent bonds between sodium and carboxyl are cleaved, but the diffusion of sodium ion can be enhanced. However, it has been reported that a considerable number of contaminants will be released at above 200 °C [12]. At higher temperatures, complicated decomposition and recombination reactions could happen, finally forming complicated and toxic substances, such as carcinogenic compounds. Waste water containing such toxic waste will be tricky to dispose and normally forbidden by regulations.

In 2009, in Montana, there was a project at the Center of Advanced Mineral and Metallurgical Processing (CAMP) whose target was to estimate and select the existing sodium-removal methods by carrying them out in pilot tests [13]. If no appropriate method was found, they would focus on an alternative approach. The criteria used to compare the different processes included, the sodium remove effectiveness, the removal rate, the property of produced wastes and the corresponding cost. Their preliminary researches indicated that for coals in which sodium existed in the form of adsorbed or organically bound sodium, the most suitable reagent might contain ion-exchangeable constituents, such as ammonium acetate/calcium chloride and HCl. Unfortunately, no further publication has been found to support their statement.

In 2004, to reduce the amount of AAEMs especially sodium and calcium, Dai et al. [14] compared three reagents, deionised water, ammonium acetate (1 m/l) and nitric acid (1 m/l), in the capacity of removing these metals under the ambient conditions. It was proved that ~30% Ca and 71% Na were removed by water, compared to 58% Ca and 95% Na by ammonium acetate as well as 91% Ca and 97% Na by nitric acid. This relies on the different existing mode of Na and Ca. For sodium, both original water-soluble Na and the reaction products between sodium

minerals and ammonium acetate, nitric acid ($NaNO_3$ and CH_3COONa) are readily soluble in water. However, because $CaCO_3$ and CaO were claimed to be the main mode of occurrence of Ca in raw coal, deionised water can only remove a small fraction of calcium owing to the poor solubility of $CaCO_3$ and $Ca(OH)_2$ (reaction 1). From reactions 2-5, ammonium acetate and nitric acid can remove calcium more significantly than water. Additionally, considering the difference in the solubility of $Ca(COOH)_2$ and $Ca(NO_3)_2$ as well as the nitric acid being a strong acid, nitric acid can achieve almost double removal yield than neutral ammonium acetate. Due to the remarkable decrease of especially Na in washed coals, the initial temperature for ash fusion increases from 700 °C (raw coals) to 900 °C after nitric acid washing and 1100 °C after the ammonium acetate washing. Similar results were also obtained by Domazetis, et al. [12], Finkelman, et al. [8], and Morgen, et al. [15].

$$CaO + H_2O \rightarrow Ca(OH)_2 \quad (1)$$

$$Ca(OH)_2 + 2HNO_3 \rightarrow Ca(NO_3)_2 + 2H_2O \quad (2)$$

$$CaO + 2HNO_3 \rightarrow Ca(NO_3)_2 + H_2O \quad (3)$$

$$CaO + 2CH_3COONH_4 \rightarrow Ca(CH_3COO)_2 + 2NH_3\uparrow + H_2O \quad (4)$$

$$Ca(OH)_2 + 2CH_3COONH_4 \rightarrow Ca(CH_3COO)_2 + 2NH_3\uparrow + 2H_2O \quad (5)$$

In 2003, Shi invented a new method of removing sodium by treating coals (particle size being 3-30 mm) under intermittently and greatly changing pressure (from 3-5.0 Mpa to 0.1-1 Mpa) and temperature (from 150-350 °C to 30-60 °C) [16]. The interval is approximately three minutes and the liquid-to-coal volume ratio is 3-5. In the process, substantially changing pressure and temperature can destroy the original internal structure of coal, so as to dissolve sodium in 8-15 wt% acetate acid or hydrochloric acid. The author claimed that the highest sodium removal

rate was 96%. However, the requirement for equipment resulting from the frequently changing temperature and pressure might cause the inability to be used on a large commercial scale.

In 2000, Quast proposed and tested a continuous counter-current sodium removal process in laboratory which aimed to reduce water consumption [17]. The experimental conditions were as follows: water-to-coal mass ratio of 2, washing time of 30 min, and sulfuric acid of PH 2 as leaching reagent. The sodium content of the tested Bowmans low-rank coal assaying 70% water-soluble and 30% organic bound sodium was reduced by 80% after two-stage leaching and by 88.5% after three-stage leaching. This method remarkably reduced the consumption of fresh water, as evident by that only 2 litres fresh water was consumed per kg of raw coal. However, the low water consumption was interrelated to the inter-stage dewatering of washed coal. After leaching, 9 ml flocculant was added; the slurry of washed coal settled for 30 min and then vacuum filtered. The author therefore pointed the significance of liquid and solid separation on sodium removal, since sodium was assumed to be in equilibrium in filtrate and water in coal. However, the treatment and recycling of waste water was not mentioned in this paper.

In 1991, in order to reduce Ca of low-rank coals, Hayashi et al. [11] treated three coal samples (pulverised to 0.105-0.210 mm), two subbituminous coals and one brown coal by carbonic acid (dissolving CO_2 in water under 600 kPa and 298 K) at a liquid-to-coal mass ratio of 30:(0.1-3.0). The results indicated that around 45% of Ca and 22% of Mg were removed from subbituminous coals in 12 h, compared with only 10% Ca and 3% Mg from the brown coal. It was claimed that it can be explained as follows. For the CO_2 treatment of coals, calcium existing as carbonate and sulphate minerals was removed more easily than that associated with

carboxyls. In other words, ion-exchangeable cations and non-ion exchangeable cations (such as sulphates, carbonates and clay minerals) were the dominated form of Ca and Mg in brown coal and subbituminous coal respectively. Additionally, Franklin et al. [18] reported that, carboxyl functional groups tend to decompose at a relatively lower temperature than other groups. Hayashi et al. therefore pre-heated coal samples at 573 K for 1.5 h and 1.0 h for the brown coal and subbituminous coal respectively before leaching by carbonic acid. As expected, 57% and 45% of calcium were removed from the pre-heated brown coal and subbituminous coal, experiencing a remarkable increase from 7% and 15% respectively.

In 1987, Blytas et al. [19] proposed a concept of removing sodium from low-rank coal which consisted two steps, leaching by deionized water, 0.01 m/l acetate acid or aqueous solution of CO_2 at ambient environment followed by contacting with weak acid (CO_2 injected into deionized water under 300 psi, or 0.03 m/l acetate acid). These two steps were to simulate coal leaching at a mine mouth and transportation of coal slurry in pipeline respectively. Liquid-to-solid mass ratio of 6 and 1.5 were adopted for two steps respectively. After treatment by 0.01m/l acetate acid for 1 hour and carbonic acid for 4 days, the highest sodium removal extent was achieved, at 40%, compared with ~16% when deionized water was used for both steps.

The above discussion about the typical AAEMs removal process targeted at low-rank coal has been summarized in **Table 2.2**.

Table 2.2 Summary of typical studies on the selective removal of AAEMs from low-rank coal.

Ref	Target elements & Coal samples	Treatment method & Leaching reagents	Operating conditions	Removal efficiencies	Recovery or recycling of leachate	Major findings
[5]	Sodium, Potassium; Brown coal	Ultrasonic; Deionized water, 1 M Ammonium acetate	Coal size: <212 μm; Liquid-solid mass ratio: 9; Time: 30 min; Agitation speed: 1500 rpm; Ultrasonic: 25 and 430 kHz, 500 W	Water washing: ~25% of total Na; Ammonium acetate: ~30% of total Na for agitation and ~85% for ultrasonic; ~5% K for all cases.	No	Ultrasonic can enhance sodium removal when ammonium acetate was used, owing to the cavitation and streaming phenomena caused by ultrasonic.
[9]	Sodium; Sub-bituminous coal	Hydrothermal treatment; Distilled water	Coal size: <0.2 mm; Liquid-solid mass ratio: 1-5; Time: 30 min; Temperature & Pressure: 120-300 °C & 0.34-5.86 MPa	At L-S mass ratio of 2, 90.5% of total Na was removed at 300 °C and 5.86 MPa, higher than 60% at ambient environment.	No	Hydrothermal treatment can enhance sodium removal due to the improved ion diffusion and breakage of covalent bonds at high temperature and pressure.

Ref	Target elements & Coal samples	Treatment method & Leaching reagents	Operating conditions	Removal efficiencies	Recovery or recycling of leachate	Major findings
[14]	Sodium & Calcium; Sub-bituminous coal	Comparison of leaching capacities of deionized water, ammonium acetate (1 m/l) and nitric acid (1 m/l)	Coal size: not mentioned; Liquid-solid mass ratio: 10; Time: 2 h; Temperature & Pressure: 20 °C and 1 barg	Na & Ca removal: 71.14% Na and 30% Ca (water); 95% Na and 58% Ca (ammonium acetate); 97% Na and 91% Ca (nitric acid)	No	1) The Na and Ca removal capacities of three reagents is in the following order: 1m/l HNO_3, 1m/l NH_4COOH, and deionised water; 2) A proper Ca removal extent was indicated, since the ash fusion temperature of washed coal by nitric acid is lower than that by ammonium acetate (900 °C vs 1100 °C).
[16]	Sodium; High-sodium coal, not specify the coal rank	Intermittently and greatly changing pressure and temperature; Acetate acid or hydrochloric acid (8-15 wt%)	Coal size: 3-30 mm; Liquid-solid mass volume ratio: 3-5; Time: 30-60 min; Temperature & Pressure: change between 150-350 °C & 3-5.0 MPa and 30-60 °C & 0.1-1 MPa	Na removal: highest at 96%	No	Largest pressure and temperature variation range (between 350 °C & 5 MPa and 30 °C & 0.1 MPa) achieved highest Na removal, at 96%.

Ref	Target elements & Coal samples	Treatment method & Leaching reagents	Operating conditions	Removal efficiencies	Recovery or recycling of leachate	Major findings
[17]	Sodium; Low-rank coal	A three-stage counter-current washing process; Sulfuric acid (PH:2)	Coal size: 91 wt% <4mm; Liquid-solid volume ratio: 2 liters/kg raw coal; Time: 30 min; Temperature & Pressure: ambient conditions	Na removal: 80% (two-stage leaching), 88.5% (three-stage leaching);	No	1) Less water consumed per kg of raw coal, at 2 litres/kg raw coal; 2) Inter-stage dewatering is crucial to the sodium removal, since sodium was regarded as be in equilibrium in filtrate and water in coal.
[11]	Calcium & Magnesium; Two subbituminous coals and one brown coal	CO_2 dissolved in water under 600 kPa and 298 K washing low-rank coals; Preheated coal followed by CO_2 solution with pressurization	Coal size: 0.105-0.210 mm; Liquid-solid mass ratio: 30: (0.1-3.0); Time: 12 h; Temperature & Pressure: 298 K & 600 kPa	In 12 h, 45% Ca and 22% Mg from subbituminous coals and 10% and 3% from brown coal; After preheating coal samples at 573 K for 1-1.5 h, 45% and 57% Ca removed from subbituminous and brown coal in only 2 h (15% and 7% before preheating)	No	1) In 12h, pressurized CO_2 in deionized water can remove 45% and 10% Ca from subbituminous coal and brown coal respectively, owing to in brown coal, more Ca bond with carboxyls, which are relatively hard to remove by carbonic acid; 2) Preheating low-rank coal can improve Ca removal yield by carbonic acid.

Ref	Target elements & Coal samples	Treatment method & Leaching reagents	Operating conditions	Removal efficiencies	Recovery or recycling of leachate	Major findings
[19]	Sodium; Low-rank coal	Two-step washing process for the simulation of coal washing at a mine mouth and following transportation in pipelines; Deionized water, 0.01 m/l acetate acid or aqueous solution of CO_2 at ambient environment, saturated CO_2 solution under 300 psi or 0.03 m/l acetate acid for step two.	Coal size: 150-1,400 μm for step one; <1400 μm for step two; Liquid-solid mass ratio: 6 (step one); 1.5 (step two); Time: 1 h (step one); 4 days (step two); Temperature & pressure: ambient environment (step one); ambient environment for all reagents except CO_2 solution under 300 psi (step two).	Highest Na removal: 40% for step one using 0.01 m/l acetate acid and high CO_2 solution for the second step.	No	0.01m/l acetate acid for step one and high CO_2 pressure for step two removed highest sodium, at 40%.

2.3 Leaching kinetics models

For an appropriate design and scale-up of the coal-leaching reactor, clarifying the kinetics governing the leaching of target elements is crucial. For the leaching of elements from a solid particle in the aqueous phase, the shrinking core model (SCM) developed by Levenspiel [20] is widely applied. SCM is used to model heterogeneous reactions where a single mechanism can control the overall leaching rate, including the diffusion of reaction products through liquid film on the surface of the solid particle or through the intra-particle inert ash layer, or the chemical reaction as described by the following equations respectively.

(1) liquid film diffusion control: $t/\tau_1 = X_B$ (6)

Where $\tau_1 = \frac{\rho_B R}{3bk_g C_{Ag}}$

(2) Intra-particle ash layer diffusion control: $t/\tau_2 = 1\text{-}3(1\text{-}X_B)^{2/3} + 2(1\text{-}X_B)$ (7)

Where $\tau_2 = \frac{\rho_B R^2}{6bD_e C_{Ag}}$

(3) Surface chemical reaction control: $t/\tau_3 = 1\text{-}(1\text{-}X_B)^{1/3}$ (8)

Where $\tau_3 = \frac{\rho_B R}{bk_s C_{Ag}}$

where t is reaction time (s); τ is time required for complete conversion (s); X_B is factional conversion; b is stoichiometric coefficient; ρ_B is molar concentration of mineral (kmol·m^{-3}); R is particle radius (m); k_g is mass transfer coefficient between liquid and particle; C_{Ag} is concentration of organometallic compound (kmol m^{-3}); D_e is diffusivity through porous coal (m^2·s^{-1}); k_s is first-order rate constant for the surface reaction.

In 2012, Zhu et al. [21] applied SCM to study the kinetics of sulfuric acid leaching of vanadium from stone coal. The predominated controlling step was proved to be chemical reaction when the acid concentration was below 4 M, whereas intra-particle ash layer diffusion dominates for the acid concentration above 4 M. Similar direct applications of SCM were also found elsewhere [22-24].

However, considering the possibility of the change in the mode of dissolution process, it might not be reasonable to consider only one limiting factor as the controlling step throughout the whole process. Therefore, a generic kinetic model based on SCM was proposed as shown in Equation 9 [25, 26]. It did not take into account the liquid film diffusion which can be eliminated with a stirring speed above 200 rpm [20].

$$t/\tau = 1-(1-X_B)^{1/3} + B[1-3(1-X_B)^{2/3} + 2(1-X_B)] \quad (9)$$

where $B = \tau_3/\tau_2$, $\tau = \rho r^2/2bMDC_{Ag}$ (all signals mean the same as before except that M is the molecular weight of washed mineral).

Bobeck et al. [25] studied the kinetic of dissolution of sphalerite (ZnS)/ by ferric chloride ($FeCl_3$) using SCM and the above model. It was found that the original SCM with only one controlling factor in equations 7 and 8 cannot describe the whole leaching process. It was inferred that the leaching might be dominated by the surface chemical reaction and internal diffusion at the early and later stage, respectively. Therefore, the generic model (equation 9) was further employed

to simulate the experimental data. Eventually, a satisfactory fitting was achieved at both temperatures, confirming the above postulation of two factors controlling the leaching process throughout the whole leaching step.

To accommodate the heterogeneity of a mineral, the "Variable Activation Energy SCM" has been further formulated by Brittan [27] and used by Beolchini et al. [28] and Veglio et al. [29] in Equation 10. This equation was solved by a non-linear regression analysis to estimate the adjustable parameters. Note that, when $b_1 = 0$, Equation 10 will represent a model with a constant activation energy. The general assumptions for this refined SCM model are as follows:

(1) The concentration of leaching reagent reduces with time;

(2) The mineral dissolution chemical reaction might not conform to linear kinetics with the leaching reagent and targeted metals;

(3) Due to the different accessibility and reactivity of mineralogical forms, reactants in the mineral varies with time, resulting in a variable activation energy during the leaching.

$$\frac{dX}{dt} = C' \exp\left[-\left(\frac{E_A}{R}\left(\frac{1}{T}-\frac{1}{T'}\right)+\frac{b_1 X^{b_2}}{RT}\right)\right](C_{A0}-C_{As}X)^{na}(C_{S0}-C_{Ss})^{ns}(1-X)^{2/3} \quad (10)$$

where b_1 and b_2 are the parameters about the conversion to the activation energy (b_1: kJ/mole; b_2: dimensionless); X is the target metal conversion; C' is a constant; E_A is the reaction activation energy (kJ/mole); T' is a reference temperature (K); C_{A0} and C_{S0} are the initial leaching reagent 1 and 2 concentration (M) respectively; na and ns are the reaction order with

respect to leaching reagent 1 and 2 respectively; C_{As} and C_{Ss} are the stoichiometric requirement for leaching reagent 1 and 2 (M).

Beolchini et al. [28] used this variable activation energy SCM to model the manganese extraction over the leaching time successfully. In this case, the leaching reagent 1 and 2 were sulfuric acid and sucrose as reducing agent. The comparison between experimental data and the values calculated by the variable activation energy model (Equation 10) showed a much better fitting, compared to that by the constant activation energy model. It suggested that the leaching process was controlled by chemical reaction with a variable activation energy.

Based on the above discussion, the mineral leaching kinetics mechanism is complex and case-dependent. The kinetics mathematical model is related to various factors, including the leaching reaction, the properties of leaching reagent, the mineral particle size, the liquid-solid mass ratio, the mineral particle shape, etc.

2.4 Leaching reagent comparison

In order to develop a variable industrial process of removing AAEMs from low-rank coals by chemical leaching, the selection of leaching reagents is essential. In selecting leaching reagents, the following factors should be considered:

1) The effectiveness of removing AAEMs
2) Possibility of recovery and reusing
3) Availability and cost

4) The change in calorific value of leached coal

5) Effect of the leaching reagent residue on the washed coal on the coal-fired boiler

6) Environmental impacts of leaching reagents

7) Operation safety

The environmentally benign water unfortunately can only remove a part of sodium and trivial calcium for a single stage leaching under the ambient conditions. The ammonium acetate should be ruled out due to its high price [30], marginal effects on the removal of Ca and Mg, and the difficulty in the regeneration of ammonia. Sulfuric acid is also unsuitable in this study, since low-rank coals have very high Ca contents, resulting in the quick formation of numerous $CaSO_4$ upon the attack of sulfuric acid. As a result, the stubborn $CaSO_4$ precipitation within the coal particles will clog the diffusion paths, ceasing thus the leaching process.

Nitric acid was also confirmed to mobilize high fractions of AAEMs from low-rank coals. However, the drawback of using nitric acid leaching is notable. Firstly, the reaction between coal compositions and nitric acid is sensitive to the operation conditions, generating various products according to reactions 11-14 [1]. The release of toxic H_2S and NO might pose a restriction on the application of nitric acid on coal leaching. Secondly, nitrating agent, NO_2^+ might form according to reaction 9 (H_2SO_4 produced from reaction 13). Consequently, coal might be oxidized and a new nitrogen-containing species in coal might be formed, resulting in the reduction in calorific value of coal and increase in nitrogen content [1].

$$FeS_2 + 2HNO_3 \rightarrow Fe(NO_3)_2 + H_2S + S \quad (11)$$

$$2FeS_2 + 6HNO_3 \rightarrow 2Fe(NO_3)_2 + 3H_2S + S \quad (12)$$

$$6FeS_2 + 30HNO_3 \rightarrow 3Fe_2(SO_4)_3 + 3H_2SO_4 + 30NO + 12H_2O \quad (13)$$

$$HNO_3 + 2H_2SO_4 \leftrightarrow NO_2^+ + H_3O^+ + 2HSO_4^- \quad (14)$$

In terms of hydrochloric acid which is widely used in hydrometallurgy, it possesses a number of advantages, compared to other acids, such as sulfuric acid and nitric acid [31]. Firstly, it has a strong capacity of removing targeted AAEMs as summarized in **Table 2.1**. Secondly, it can ease the leaching process without the precipitation trouble, such as $CaSO_4$. Thirdly, a higher leaching kinetics can be expected. Finally, metal complex has a higher solubility in HCl acid. On the other hand, the difficulty of disposing of the wastewater rich in chlorides has always been the big hurdle for the application of HCl acid [12]. This problem is one of the core topics in this study and will be explored in depth in chapters 5-6. Regarding the disadvantages, the acid residual on the leached coal might incur corrosion to the alloy in boilers, but this can be mitigated significantly via using a bunch of physical solid and liquid separation units, such as separation screen and centrifuge. Also, this effect can be slashed through using low-concentration HCl acid. The comparison is summarized in **Table 2.3**.

Table 2.3 Comparison of leaching reagents.

Leaching reagents	Advantages	Disadvantages
Pure H_2O	Environmentally-benign	Weak ability to remove AAEMs for single stage under ambient environment
H_2SO_4	1. Strong ability to remove AAEMs, except Ca 2. No volatilization	1. The leaching process will cease quickly due to the precipitation of $CaSO_4$ on coal particles 2. Corrosion to boiler steel brought from sulfur
HNO_3	Strong capacity of removing AAEMs	1. Oxidation of coal causes the reduction on the calorific value 2. Increase in nitrogen within coal 3. Sensitive to operation conditions, might resulting in release of H_2S and NO during the leaching stage
HCl	1. Strong capacity of removing AAEMs 2. Free of precipitation trouble, such as $CaSO_4$ 3. Higher leaching kinetics 4. Higher solubility for metal complex 5. HCl acid can be recovered from the chloride waste	1. Acid concentration should be low, to minimize its volatilization

2.5 Water recovery techniques

To minimise the costs associated with the continuous consumption of leaching reagents and make a coal leaching process economically viable, integrating the recycling and treatment of the used water into the demineralisation of coal is critical. For salt water specifically, three mature water recovery technologies exist to date: evaporation, electrodialysis and reverse osmosis.

2.5.1 Evaporation

Multi-stage flash (MSF) vaporisation is the most widely used of the evaporation methods in the desalination industry. It is a well-established, simple technique that involves multiple flash vaporising drums in series in order to separate out the water based on different boiling conditions [32, 33]. The solution is pressurised, heated and then fed into a series of flash drums where the sudden drop in pressure below its saturated vapour pressure causes the water to rapidly vaporise and separate from the unwanted contaminants. This process is mostly applied for feed streams with salt concentration of greater than 50,000ppm and for large-scale water treatment.

Although MSF vaporisation produces high quality recovered water that has low levels of contaminants, it requires considerable amounts of energy to heat and pressurise the water before it can be flashed – translating into high operating cost as shown in **Table 2.4** [34]. MSF vaporisation requires between 19.5 and 27.3 kWh/m^3 which is far more energy than other water recovery techniques [35]. MSF systems are quite large requiring large land areas and involve an extensive amount of equipment and piping. This gives them a large capital investment and moderate maintenance costs [36].

2.5.2 Reverse osmosis

Reverse osmosis (RO) is a mature separation process that has continued to improve over time. It relies on a pressure differential to force water molecules across semi-permeable membranes, leaving the unwanted contaminants that are not allowed to pass behind [37-40]. Operating conditions are maintained at a pH of 2-11 and temperature of 5-55°C to maximize diffusion and limit damage to the membrane. Any contaminant that has a molecular weight of more than 200 is likely to be removed by an RO unit. This is due to particles smaller than 0.1nm being able to pass through the membrane with the water.

The United States Environmental Protection Agency (USEPA) selected RO as the best technology for removing inorganic contaminants, where numerous full-scale facilities exist in industry [41]. **Table 2.4** shows that RO systems are also cheap and simple to build; requiring only 1.5-3 kWh/m^3 [35] and can remove both inorganic and organic material with a satisfactory water recovery rate especially for relatively lower salt concentration feed streams. However, they require a clean in place (CIP) system, where regular maintenance and replacement of membranes and pumps result in significant operating costs [42].

2.5.3 Electrodialysis

Electrodialysis (ED) is an emerging separation process that is able to reduce the ionic content of water [43]. ED runs in an equipment called electrodialysis cell in which several dilute compartments and concentrate compartments are formed by anion exchange membranes and cation membranes placed between the anode and cathode. Due to the selective permeability of ion-exchangeable membranes, cations and anions will transport and concentrate in concentrate

compartments under the effect of electric potential difference. As a result, diluted water can be obtained in dilute compartments. With a relatively low energy requirement of 2.64 - 5.5 kWh/m^3 [35] and little production of waste, ED presents as a more environmentally and economically friendly alternative. **Table 2.4** summarises the technical specifications and costs.

As ED is only effective for desalination, it is inappropriate for removing organic matter and other non-ionic contaminants. Suspended solids with a diameter larger than 10μm (which would be present in the black water) must also be removed to prevent blockage of membrane pores [44]. Membranes are also subject to fouling, although less frequently than for RO, with an average seven-year lifespan [45].

ED is only economically efficient for brackish waters that have a total dissolved-solids (TDS) content of less than 4,000 mg/L. This is a result of power consumption being directly proportional to the salinity of the water [46]. Additionally, more attention needs to be paid to electrode corrosion and fouling, which might shorten the lifespan of electrode and increase the maintenance cost. Compared to RO, the desalinization rate of ED is lower.

Table 2.4 Comparison of water recovery methods.

Water Recovery Method	Technical Specification	Capital Cost	Operating Cost	Energy consumption	Advantages	Disadvantages
Evaporation	**pH range:** N/A **Temp range:** 90-115°C [47] **Concentration:** >50000ppm [48] **Particle size:** N/A	US$1200-$2300/m^3 [49]	$1.10-$1.50/m^3 [49]	19.5-27.3 kWh/m^3 [35]	1. Long established 2. High quality water product 3. Moderate maintenance and cleaning requirements	1. High energy consumption 2. High capital investment
Reverse Osmosis	**pH range:** 2-11 [40] **Temp range:** 5-55°C [40] **Concentration:** <50000 ppm [50] **Particle size:** >0.1nm [50]	US$380-$562/m^3 [51]	$0.45-$0.92/m^3 [49]	1.5-3 kWh/m^3 [35]	1. Widely used 2. High water recovery ratio for lower salt concentration feeds 3. Low energy consumption 4. High ion removal extent	1. Membrane fouling (2-5 year lifespan) 2. Regular maintenance and cleaning
Electrodialysis	**pH range:** 2-11 [52] **Temp range:** 4.5-43 °C [52] **Concentration:** 3000-12000 ppm [48] **Particle size:** <10μm [43]	$600-$700/m^3 [52]	$0.25-$0.35/m^3 [53]	2.64-5.5 kWh/m^3 [35]	1. High water recovery ratio 2. Little waste produced 3. Lower energy consumption	1. Membrane fouling (~7 year lifespan) 2. Cannot remove organic matter 3. Electrode corrosion and fouling 4. Lower desalination rate than RO

2.6 Hydrochloric acid regeneration from chloride wastes

HCl acid regeneration from the lixiviant which is rich in chlorides, is vital to the commercialisation of the low-rank coal leaching process, via slashing the cost through reducing the amount of male-up HCl acid, and eliminating the environmental impact through producing Cl-free/lean waste [54]. This part will summarise the widely studied HCl acid regeneration methods, including electrowinning, metal sulphate salt crystallisation and pyrohydrolysis.

2.6.1 Electrowinning

Electrowinning was firstly used for HCl regeneration from a nickel chloride solution, as illustrated in **Figure 2.3**. A cell with three compartments was created to separate catholyte, ampholyte and anolyte by two exchange membranes, so as to avoid the generation of chlorine on the anode. It was claimed that 1 M HCl can be recovered when using a current density of 200 A m^{-2}, 1 and 0.2 M $NiCl_2$ as catholyte and ampholyte, respectively at 50 °C. However, this technique is largely hindered by membrane selectivity for chloride, durability and operating cost. Since 1990s, related work has been published.

2.6.2 Metal sulphate salt crystallisation

Based on the chemical reaction between added sulphuric acid and chlorides, metal ions can be precipitated out, during which Cl is released as HCl acid. This method is mainly used for calcium chloride, attributing to the low solubility of calcium sulphate. It was reported that the crystallisation process can be affected by various factors, including the addition rate of sulphuric acid, temperature, the using of seed material, sulphuric acid concentration and the initial concentration of chlorides [54]. A slow sulphuric acid addition rate can promote well-crystallised gypsum, whereas a gel-like substance will form under a fast addition of sulphuric

acid. The morphology of gypsum will exert a notable effect on the following solid-liquid separation step. Higher operation temperature, the addition of seed and dilution of sulphuric acid to around 50% help the crystal growth. Additionally, an initial calcium chloride concentration of 3-4 M is necessary for the production of azeotropic strength acid, followed by an evaporation step. It was claimed that 5.5 M HCl can be regenerated from calcium chloride through this method.

The most significant advantage of sulphate salt precipitation is the low operation temperature, < 100 °C. However, it is susceptible to a bundle of operation parameters. Apart from the effect factors discussed above, the solid-liquid separation is also tricky. Poor filtration rate can be caused by the formation of fibrous calcium sulphate anhydrite, while calcium sulphate dehydrate and alpha-hemihydrate enable effective solid-liquid separation [55, 56].

2.6.3 Pyrohydrolysis

Theoretically, pyrohydrolysis can be applied for all metal chlorides, ending up with HCl acid and metal oxides; however, it has been commercialised for only three metal chlorides, $MgCl_2$, $NiCl_2$ and $FeCl_2$ [54]. The pyrohydrolysis of $MgCl_2$ was patented firstly as Aman process using reaction temperature up to 800 °C [57]. The $MgCl_2$ solution and combustion gases are fed into a 3-10 m tall reactor from the top and bottom, respectively. Consequently, 20% HCl acid can be produced. However, the intensive energy requirement from Aman process prohibits its application in larger scale. Similar issues affiliate the pyrohydrolysis of $NiCl_2$ [58]. Aiming to reduce the energy requirement, an extra exothermic reaction was added, the oxidation of $FeCl_2$ into the pyrohydrolysis of $FeCl_2$ [59]. Despite the favourable thermodynamics which enhances its economic feasibility, the pyrohydrolysis of $FeCl_2$ is hindered by the lack of $FeCl_2$ solution in

most cases. In light of this, the study of pyrohydrolysis is far from completion to promote it to more metal chlorides, such as widely spread $CaCl_2$ and even rare earth metal chlorides.

2.7 literature review summary and research gaps

According to the above literature review, low-rank Xinjiang coal has abundant Na, Ca and Mg, which results in the troublesome fouling of its ash in combustion. As a result of the unsuitability of physical beneficiation methods for low-rank coal, chemical leaching has to be employed to extract AAEMs out of coal matrix. This chapter has given an in-depth literature review of the current state of knowledge regarding the low-rank Xinjiang coal property, coal leaching techniques, leaching kinetics models, waste water treatment methods, properties of leaching reagents and HCl acid regeneration approaches from chloride wastes. Accordingly, the main research gaps have been identified as follows:

1. Previous leaching studies have particularly focused on once-through leaching using fresh reagents. Few was about the leaching using recycled leachate especially in multi-step processes if it is still capable to remove reasonable extents of target elements, although this method can reduce water consumption significantly. Meanwhile, the corresponding study of kinetics models which can predict the recyclability of leaching reagent is absent.

2. There is a lack of comprehensive techno-economic analysis for the flowsheet which integrate leaching and waste water treatment steps. This restricts the scale-up of low-rank coal leaching processes.

3. With regard to the HCl regeneration from the lixiviant which is rich in chlorides, few study was about the pyrohydrolysis of $CaCl_2$, not to mention the co-pyhydrolysis of $CaCl_2$ and $MgCl_2$, which co-exist in the waste leachate discharged from the low-rank coal leaching process. There is no study on the mechanism exploitation of pyrohydrolysis from atomic level, which helps us to manipulate the HCl recovery effectively.

Reference

1. Wijaya, N.; Zhang, L., A Critical Review of Coal Demineralization and Its Implication on Understanding the Speciation of Organically Bound Metals and Submicrometer Mineral Grains in Coal. *Energy & Fuels* **2011**, *25*, (1), 1-16.
2. Prationo, W.; Zhang, J.; Abbas, H. A. A.; Wu, X.; Chen, X.; Zhang, L., Influence of External Clay and Inherent Minerals on Lignite Optical Ignition and Volatile Flame Propagation in Air-Firing and Oxy-Firing. *Industrial & Engineering Chemistry Research* **2014**, *53*, (7), 2594-2604.
3. Speight, J. G., *The chemistry and technology of coal*. CRC press: 2012.
4. Wang, L. K.; Pereira, N. C.; Hung, Y.-T.; Wang, L. K., *Advanced air and noise pollution control*. Springer: 2005.
5. Balakrishnan, S.; Reddy, V. M.; Nagarajan, R., Ultrasonic coal washing to leach alkali elements from coals. *Ultrason. Sonochem.* **2015**, *27*, 235-240.
6. Ambedkar, B.; Nagarajan, R.; Jayanti, S., Ultrasonic coal-wash for de-sulfurization. *Ultrason. Sonochem.* **2011**, *18*, (3), 718-726.
7. Ambedkar, B., *Ultrasonic coal-wash for de-ashing and de-sulfurization: experimental investigation and mechanistic modeling*. Springer Science & Business Media: 2012.
8. Finkelman, R.; Palmer, C.; Krasnow, M.; Aruscavage, P.; Sellers, G.; Dulong, F., Combustion and leaching behavior of elements in the Argonne premium coal samples. *Energy & fuels* **1990**, *4*, (6), 755-766.
9. Bing, Z.; Jiarui, W.; Fanmin, C., Hydrothermal treatment to remove sodium from high sodium coal and its influence on combustion characteristics. *Journal of Fuel Chemistry and Technology* **2014**, *42*, (12), 1416-1422.
10. Aho, M.; Ferrer, E., Importance of coal ash composition in protecting the boiler against chlorine deposition during combustion of chlorine-rich biomass. *Fuel* **2005**, *84*, (2-3), 201-212.
11. Hayashi, J.-i.; Takeuchi, K.; Kusakabe, K.; Morooka, S., Removal of calcium from low rank coals by treatment with CO2 dissolved in water. *Fuel* **1991**, *70*, (10), 1181-1186.
12. Domazetis, G.; Barilla, P.; James, B., Lower emission plant using processed low-rank coals. *Fuel Processing Technology* **2010**, *91*, (3), 255-265.
13. McCloskey, J.; Twidwell, L.; Miranda, P.; Young, C.; Cameron, D.; Dudley, S.; Pascoe, B. In *Enhancement of Montana coal, sodium removal technology evaluation and*

development, XVI International Coal Preparation Congress, Lexington, Kentucky, April, 2010; 2010; pp 26-29.

14. Dai, B., Wu, X., Zhang, Z., Influence of coal washing on mtal migration and ash fusion characteristics of coal with a high alkali content. Journal of Engineering for thermal energy & power **2014**, *29*, (1), 76-80.
15. Morgan, M. E.; Jenkins, R. G.; Walker Jr, P. L., Inorganic constituents in American lignites. *Fuel* **1981**, *60*, (3), 189-193.
16. Shi, D. A method to remove sodium in an intermittent manner. CN201310095748.XA, 2013.
17. Quast, K., Counter-current ion exchange for the removal of organically bound sodium from low-rank coals. *Minerals engineering* **2000**, *13*, (13), 1423-1428.
18. Franklin, H. D.; Cosway, R. G.; Peters, W. A.; Howard, J. B., Effects of cations on the rapid pyrolysis of a Wyodak subbituminous coal. *Industrial & Engineering Chemistry Process Design and Development* **1983**, *22*, (1), 39-42.
19. Blytas, G. C.; Trogus, F. J., Reduction of sodium in coal by water wash and ion exchange with a weak electrolyte. In Google Patents: 1987.
20. Levenspiel, O., Chemical reaction engineering. *Industrial & engineering chemistry research* **1999**, *38*, (11), 4140-4143.
21. Zhu, X.; Zhang, Y.; Huang, J.; Liu, T.; Wang, Y., A kinetics study of multi-stage counter-current circulation acid leaching of vanadium from stone coal. *International Journal of Mineral Processing* **2012**, *114*, 1-6.
22. Cheng, W.-P.; Fu, C.-H.; Chen, P.-H.; Yu, R.-F., Dynamics of aluminum leaching from water purification sludge. *Journal of hazardous materials* **2012**, *217*, 149-155.
23. Qiu, H.; Zhang, H.; Zhao, B.; Zhu, J.; Liu, D., Dynamics study on vanadium extraction technology from chloride leaching steel slag. *Rare Metal Materials and Engineering* **2013**, *42*, (4), 696-699.
24. Gharabaghi, M.; Irannajad, M.; Azadmehr, A. R., Leaching behavior of cadmium from hazardous waste. *Sep. Purif. Technol.* **2012**, *86*, 9-18.
25. Bobeck, G. E.; Su, H., The kinetics of dissolution of sphalerite in ferric chloride solution. *Metall. Trans. B* **1985**, *16*, (3), 413-424.
26. Sahu, S.; Sahu, K.; Pandey, B., Leaching of zinc sulfide concentrate from the ganesh-himal deposit of nepal. *Metallurgical and Materials Transactions B* **2006**, *37*, (4), 541-549.

27. Brittan, M., Variable activation energy model for leaching kinetics. *International journal of mineral processing* **1975**, *2*, (4), 321-331.
28. Beolchini, F.; Papini, M. P.; Toro, L.; Trifoni, M.; Veglio, F., Acid leaching of manganiferous ores by sucrose: kinetic modelling and related statistical analysis. *Minerals Engineering* **2001**, *2*, (14), 175-184.
29. Veglio, F.; Trifoni, M.; Pagnanelli, F.; Toro, L., Shrinking core model with variable activation energy: a kinetic model of manganiferous ore leaching with sulphuric acid and lactose. *Hydrometallurgy* **2001**, *60*, (2), 167-179.
30. Wijaya, N.; Choo, T. K.; Zhang, L., Generation of ultra-clean coal from Victorian brown coal: Effect of hydrothermal treatment and particle size on coal demineralization and the extraction kinetic of individual metals. *Energy & Fuels* **2012**, *26*, (8), 5028-5035.
31. McKinley, C.; Ghahreman, A., Hydrochloric acid regeneration in hydrometallurgical processes: a review. *Mineral Processing and Extractive Metallurgy* **2017**, 1-12.
32. Banat, F. In *Economic and technical assessment of desalination technologies*, IWA Conference-New Technologies for Water and Wastewater Treatment in the 21st Century, Geneva, Switzerland, June, 2007; 2007; pp 6-8.
33. Wankat, P. C., *Separation process engineering*. Pearson Education: 2006.
34. Van der Bruggen, B.; Vandecasteele, C., Distillation vs. membrane filtration: overview of process evolutions in seawater desalination. *Desalination* **2002**, *143*, (3), 207-218.
35. Malek, P.; Ortiz, J.; Schulte-Herbrüggen, H., Decentralized desalination of brackish water using an electrodialysis system directly powered by wind energy. *Desalination* **2016**, *377*, 54-64.
36. Bernat, X.; Gibert, O.; Guiu, R.; Tobella, J.; Campos, C., The economics of desalination for various uses. In *Re-thinking water and food security*, ROUTLEDGE in association with GSE Research: 2010; Vol. 329, pp 329-346.
37. Malaeb, L.; Ayoub, G. M., Reverse osmosis technology for water treatment: state of the art review. *Desalination* **2011**, *267*, (1), 1-8.
38. Water, D.; Reclamation, C. W. W.; Waters, R.; Water, B., Reverse osmosis. *Internet: http://www. aquatruewater. com/whychoose-reverse-osmosis-water [Sep. 3, 2011]* **2012**.
39. Fane, A.; Tang, C.; Wang, R., Membrane technology for water: microfiltration, ultrafiltration, nanofiltration, and reverse osmosis. *Treatise on water science* **2011**.

40. Reverse Osmosis Water Treatment. http://www1.agric.gov.ab.ca/$department/deptdocs.nsf/all/agdex5432
41. Adham, S.; Gillogly, T.; Hansen, E.; Lehman, G.; Rosenblum, E., Desalination And Water Purification Research and Development Program Report No. 97: Comparison of advanced treatment methods for partial desalting of tertiary effluents. *US Department of the Interior, Denver, Colorado* **2009**.
42. Australia, U., Economic and technical assessment of desalination technologies in australia: With particular reference to national action plan priority regions. *Detailed Report* **2002**.
43. Strathmann, H., Electrodialysis, a mature technology with a multitude of new applications. *Desalination* **2010**, *264*, (3), 268-288.
44. Electrodialysis membrane technology. https://www.lenntech.com/electrodialysis.htm
45. Valero, F.; Barceló, A.; Arbós, R., Electrodialysis technology–theory and applications, desalination, trends and technologies. *Michael Schorr (Ed.)* **2011**.
46. Younos, T.; Tulou, K. E., Energy needs, consumption and sources. *Journal of Contemporary Water Research & Education* **2005**, *132*, (1), 27-38.
47. Hawaidi, E. A.; Mujtaba, I. M., Simulation and optimization of MSF desalination process for fixed freshwater demand: Impact of brine heater fouling. *Chem. Eng. J.* **2010**, *165*, (2), 545-553.
48. Australia. Department of Agriculture, F. a. F. N. D. S. P. A. U. A. Introduction to desalination technologies in Australia : summary report.
49. Commission, A. N. W. *Emerging trends in desalination : a review*; 2008.
50. Guide, W. T. Feed water quality for reverse osmosis systems: problems and solutions. http://www.watertreatmentguide.com/feed_water_quality.htm
51. Dos Anjos, N. D. F. R., Source book of alternative technologies for freshwater augmentation in Latin America and the Caribbean. *International Journal of Water Resources Development* **1998**, *14*, (3), 365-398.
52. Bungay, J. K., *Synthetic Membranes:: Science, Engineering and Applications*. Springer Science & Business Media: 2012; Vol. 181.
53. Stephenson, D. J., *Water and Wastewater Systems Analysis*. Elsevier Science: 1988.
54. McKinley, C.; Ghahreman, A., Hydrochloric acid regeneration in hydrometallurgical processes: a review. *Mineral Processing and Extractive Metallurgy* **2018**, *127*, (3), 157-168.

55. Feldmann, T.; Demopoulos, G. P., The crystal growth kinetics of alpha calcium sulfate hemihydrate in concentrated CaCl2–HCl solutions. *Journal of crystal growth* **2012**, *351*, (1), 9-18.

56. Feldmann, T.; Demopoulos, G. P., Phase transformation kinetics of calcium sulfate phases in strong CaCl2HCl solutions. *Hydrometallurgy* **2012**, *129*, 126-134.

57. De Bakker, J. The recovery of magnesium oxide and hydrogen chloride from magnesium chloride brines and molten salt hydrates. 2011.

58. Thornhill, P.; Wigstol, E.; Van Weert, G., The Falconbridge matte leach process. *JOM* **1971**, *23*, (7), 13-18.

59. Brown, C.; Olsen, D. In *Regeneration of hydrochloric acid pickle liquors by crystallization*, Third International Symposium in Iron Control in Hydrometallurgy, Montreal, Canada, October, 2006; 2006; pp 1-4.

Chapter 3

Flow-sheet Establishment, Simulation and Techno-Economic Analysis

The literature review in chapter 2 has shown that there is a lack of techno-economic viable leaching process which is suitable for the selective removal of AAEMs from low-rank coals, especially the integration of the treatment and recycling of waste leachate. To examine the feasibility of low-rank coal washing processes integrating leachate recycling and to promote to large-scale application, it is essential to conduct a comprehensive techno-economic analysis first to obtain the most promising process configuration. Four integrated leaching and waste leachate treatment and recycling processes have been proposed and compared comprehensively using Aspen Plus and Aspen Process Economic Analyser in this chapter. The most appropriate process configuration was determined in terms of the AAEMs removal extents, energy consumption and process costs. The overall efficiency of the process was also compared to a typical black coal beneficiation process, proving its feasibility. This chapter has been reformatted from a manuscript published in ***Fuel Processing Technology***: **Zhou, S.**; Hosseini, T.; Zhang, X.; Haque, N.; Zhang, L. *Selective Removal of Sodium and Calcium from Low-Rank Coal – Process Integration, Simulation and Techno-Economic Evaluation*. ***Fuel Processing Technology***, 2018, 172, 13-28.

Abstract

This paper has addressed the techno-economic feasibility regarding the selective removal of sodium (Na) and calcium (Ca) from low-rank sub-bituminous coal, aiming to reduce the ash fouling propensity in the pulverized coal-fired boilers. Four novel process integrations were proposed and simulated in Aspen Plus. Both a three-stage counter-current water leaching process and one-stage acid leaching process have been proven to improve the ash fusion temperature satisfactorily, reducing the mass fraction of Na_2O in ash from 4.32 *wt%* to 0.85 and 0.21 *wt%*, respectively. In addition, the use of acid removes around 13% Ca and 19 *wt%* total ash. For the recycling and treatment of wastewater, the water gain is desirable for the use of an evaporator, owing to the dewatering of the initially high-moisture coal (25 *wt%*) in the centrifugal and the high water recovery rate from the evaporator. However, the good performance of evaporator is counteracted by the considerable capital cost caused by the huge heat transfer area requirement. Instead, the use of reverse osmosis (RO) results in a water loss up to 251.2 kg/t coal. Additionally, prior to the RO treatment unit, the recycling and reusing of the unsaturated water is critical in reducing both the water and power consumption. The water consumption drops to 41.9 kg/t coal and 51.8 kg/t coal for the three-stage water leaching and acid leaching process, respectively. Both are remarkably lower than 85 kg-water/t black coal. In terms of the power consumption, it decreases to ~10.3 kWh/t coal for the three-stage water leaching process and further down to 6.0 kWh/t for the acid case, which is even lower than 6.3 kWh/t for the black coal process. Furthermore, the integration of acid leaching and RO is also demonstrated to be economically viable by its high NPV, IRR and short payback period. Sensitivity analyses indicate that, the original Na content in raw coal is the most influential variable on the water and power consumption of the overall process, followed by the initial moisture content in the raw coal. For a low-rank coal containing >2150-2520 ppm Na and/or <19 *wt%* moisture, the leaching process proposed would turn economically unviable compared

to the existing black coal leaching process. A minimum selling price of 136 RMB/t (-32% deviation) is also necessary to keep both NPV and IRR positive as well as the payback period shorter than the project lifetime.

Keywords: Low-rank coal; Sodium and calcium removal; Process simulation; Techno-economic evaluation

3.1 Introduction

Low-rank coal, commonly referred to as brown coal and sub-bituminous coal, contributes to more than 50% of the world's coal reserves [1]. It is abundant in regions such as Australia and China and provides an economically attractive alternative to high-rank black coal (i.e. bituminous coal and anthracite) for electricity generation [2, 3]. The use of low-rank coal is becoming increasingly important with the ongoing depletion of high-rank bituminous coal. However, low-rank coal boilers are afflicted by severe fouling inside the boiler caused by the high content of alkali and alkaline earth metal (AAEMs, Na, Ca, K and Mg) [3, 4] of low-ran coal.

Conventional coal cleaning techniques are exclusively targeted at high-rank coal with a large portion of its inorganic metals present as discrete grains and separate from the coal matrix [5]. As the mineral matter has a larger density than the carbonaceous matrix, it can be removed physically [6]. Variations in surface properties can also allow for separation [7]. However, unlike black coal, AAEMs in low-rank coal are deeply and chemically embedded within the coal matrix. Therefore, they cannot be removed using any physical approaches based on either density or surface property discrepancy between mineral matter and coal matrix [8]. Instead, chemical leaching or solvent extraction has been examined to remove these two elements from low-rank coal. In particular, research has been focused on the removal of all ash-forming metals to produce ultra-clean coals (UCC) or ash-free hyper-coal (HPC), from both high-rank and low-rank coals [8-11]. However, the corrosive acid/ alkali reagents and/or high pressure and temperature employed in existing chemical leaching processes raise severe environmental concerns, the harsh requirement for equipment, and high capital/operating cost, limiting their advance in practical applications. Solvent extraction is also inappropriate for low-rank coal because of the low carbon yield (<30 *wt%*) resulting from its cross-linked carbonaceous

structure [8]. For conventional coal-fired boilers, the removal of all ash-forming metals is also unnecessary.

In this study, instead of removing all of the ash-forming metals, only Na and Ca were selectively targeted, considering that these two metals have higher contents and critical triggers for ash fouling in a pulverized coal-fired boiler [3, 4, 12]. Moreover, based on the high-water solubility of Na in low-rank coals, the existing water-leaching process for black coal was adapted for the low-rank coal. That is, multiple-stage water leaching, either with or without acid dosing was employed to leach the low-rank coal, whereas the resultant leachate was repeatedly used before it is saturated and then sent to the wastewater treatment unit to remove the inorganic impurities. The innovative characteristics of the new water-leaching process are hypothesized from the following three perspectives, *1)* the water consumption can be reduced significantly by the recycling of leachate; *2)* the mature existing waste water treatment and recovery techniques, once integrated efficiently with the coal leaching process, can further help recover the water cost-effectively; and *3)* the introduction of acid can significantly increase the extraction yields of both Na and Ca out of coal matrix [8, 13].

In this paper, we have conducted process simulations to assess four scenarios so as to optimize the integration of individual units to produce a leached low-rank coal that has comparable contents of Na and Ca with these in black coal. Furthermore, the ash of resultant leached coal is expected to have an ash fusion temperature above the boiler operating temperature, at 1200 °C. Aspen Plus has been employed for the process flow-sheeting. Aspen Process Economic Analyzer (APEA) was further used to perform the economic evaluation based in the context of China. Finally, sensitivity analysis was undertaken to examine the robustness of the overall

process including the water and power consumption, and economic feasibility. As far as the authors are aware, such a study has yet to be examined in the literature. The results achieved are expected to promote the deployment of low-rank coal leaching in a large industrial and commercial scale in the future.

3.2 Methodology

3.2.1 Coal properties

A low-rank sub-bituminous coal, termed Xinjiang Zhundong coal was used for this study. The low-rank coal leaching plant was assumed to be located beside a coal mine in Xinjiang, China, which is rich in low-rank coal [14]. Additionally, a reference black coal was tested for comparison. Their properties are tabulated in **Table 3.1**. The volatile content (30.2 *wt%*) in Xinjiang coal indicates that it belongs to sub-bituminous coal [15]. It is much higher than the value of black coal, at 7.8 *wt%*. The sub-bituminous coal is also characterized by the high moisture of 24.5% and low ash content of 7.8%, compared with black coal reference. The gross heat value of 24.9 MJ/kg shows that this sub-bituminous belongs to the intermediate-heating-value coal [15]. With respect to the particle size distribution of the as-mined Xinjiang coal shown in **Table 3.2**, one can see that this coal is very fine with a mass percentage of 49% less than 4 mm. One major reason is due to its low-ash content.

Table 3.1 Compositions of as-received Xinjiang low-rank coal and black coal.

Components	Low-rank coal (*wt%*)	Black coal (*wt%*)
Moisture [ad]	24.5	9.68
Ash [d]	7.78	22.49
Volatile [d]	30.2	7.78
FC [d]	62.02	69.73
Chlorine [d]	0.09	-
Gross heat value [daf]	24.89 MJ/kg	26.93 MJ/kg

[ad] air-dried, [d] dried basis, [daf] dry ash free basis

Table 3.2 PSD of as-received Xinjiang low-rank coal and black coal.

Low-rank coal		Black coal	
PSD/mm	*wt%*	PSD/mm	*wt%*
<0.2	8	0-5	30
0.2-0.6	12	5-40	60
0.6-1.0	8	>40	10
1.0-4.0	21		
4.0-8.0	15		
>8.0	36		

Table 3.3 compares the ash compositions of the two coals, which are expressed as the most stable oxide of each element. It is observed that the contents of both Na_2O and CaO in low-rank coal are significantly higher than in black coal, which is in agreement with the past studies [3, 4, 12]. In terms of the modes of occurrence of Na and Ca in Xinjiang coal, it has been widely

reported that more than half of Na was water-soluble, with the rest being organically bound with carboxylic acid that can be entirely leached away by ammonium acetate [8, 16]. Conversely, Ca mainly present as discrete minerals, which can be mobilized by hydrochloric acid [16].

Table 3.3 Typical ash compositions of Xinjiang low-rank coal and black coal.

Sample	Ash [d]	Na_2O	MgO	Al_2O_3	SiO_2	P_2O_5	SO_3	K_2O	CaO	Fe_2O_3
Low-rank coal	7.8	4.32	22.65	3.27	5.67	0.52	15.06	0.21	46.96	1.34
Black coal	22.5	1.48	1.05	28.14	52.14	0.21	2.97	1.91	1.48	10.62

[d] on the dried coal basis (*wt%*)

3.2.2 Low-rank coal leaching process

The whole process consists of two major components, coal leaching, and waste water treatment and recycling. The raw coal first undergoes sieving and crushing to obtain the particles less than 4 mm in diameter, before being sent to the leaching reactor by a belt conveyer. With respect to the coal leaching unit, three options were proposed hereafter: the use of a single stage water leaching shown in **Figure 3.1**(a), the use of three-stage counter-current flow of water in **Figure 3.1**(b), and the single stage of acid in **Figure 3.1**(c) and (d). With respect to the waste water treatment and recycling, the mixture of leached coal and water from the leaching step is firstly separated by a dewatering screen. Subsequently, the wet leached coal is transferred to a centrifuge to squeeze out the remaining water and make the final product that contains around 11% moisture. The resultant water from the centrifuge is mixed with coal fine-water slurry received from the dewatering screen, and then passes through a thickener and pressure filter to yield the final by-products, wet tailings containing 22% moisture and wastewater with a low

solid content. All the water streams are finally mixed together. It is either reused and sent back to the leaching unit, or treated downstream by an evaporator or reverse osmosis (RO). Note that, except the coal leaching tank, all the other units proposed are the same as these being used in the existing black coal leaching process which will be detailed later.

Back to **Figure 1**, the four scenarios were designed and compared hereafter to address the discrepancy, between single-stage and multi-stage water leaching unit via Scenarios 1 versus 2; between evaporator and RO on water recovery via Scenarios 2 and 3; and between water-leaching and acid-doped leaching via Scenarios 3 and 4.

Scenario 1 is the simplest process to mimic the black coal leaching process, using a single-stage water leaching in combination with an evaporator for water recovery. Based on the optimum condition from experimental examination, a liquid-solid ratio of 1.5 is applied, resulting in around 34% Na and 0.5% Ca removed in 30 min, under ambient conditions. After a bundle of solid-liquid separation units, the dirty water containing fine coal particles, Na and Ca is transported into an evaporator. Free flue gas at 150 °C produced by the adjacent power generation plant is used as the heating source of the evaporator. Evaporated water coming from the top of the evaporator is condensed inside a cooler, which uses cooling water as the coolant. The bundle of evaporator-condenser allows unwanted salts to be separated and exit the process as waste.

Scenario 2 adopts a counter-current three-stage water leaching process, thereby removing more than twice the amount of Na than Scenario 1. However, due to the low water-solubility of organic Ca and $CaO/CaCO_3/CaSO_4$, Ca removal extent increased marginally, at 0.7% totally.

The leaching conditions in each reactor remains the same as in Scenario 1. The counter-current leaching process is introduced to rinse off any possible ions and the other unwanted species deposited on the coal particle surface in the last reactor.

Scenario 3 was further proposed to evaluate the use of RO for the wastewater recovery. Upstream of the RO, an ultrafiltration system (UF) to remove the suspended particles and a strong-acid cation ion exchange resin (IER) to trap calcium ions were installed [17-19].

Scenario 4 provides the integration of an acid leaching unit and the use of RO for water recovery, aiming to reduce the amount of leaching tanks and meanwhile to improve the process efficiency. The wastewater recycle process remains the same as that in Scenario 3.

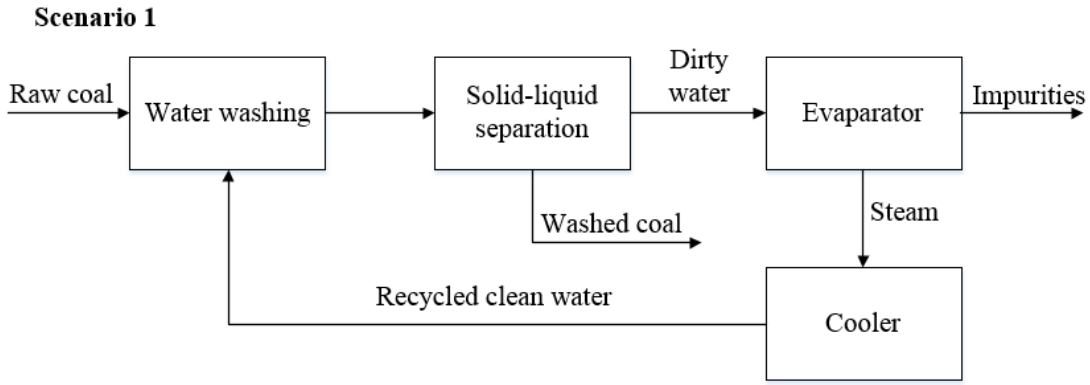

(a)

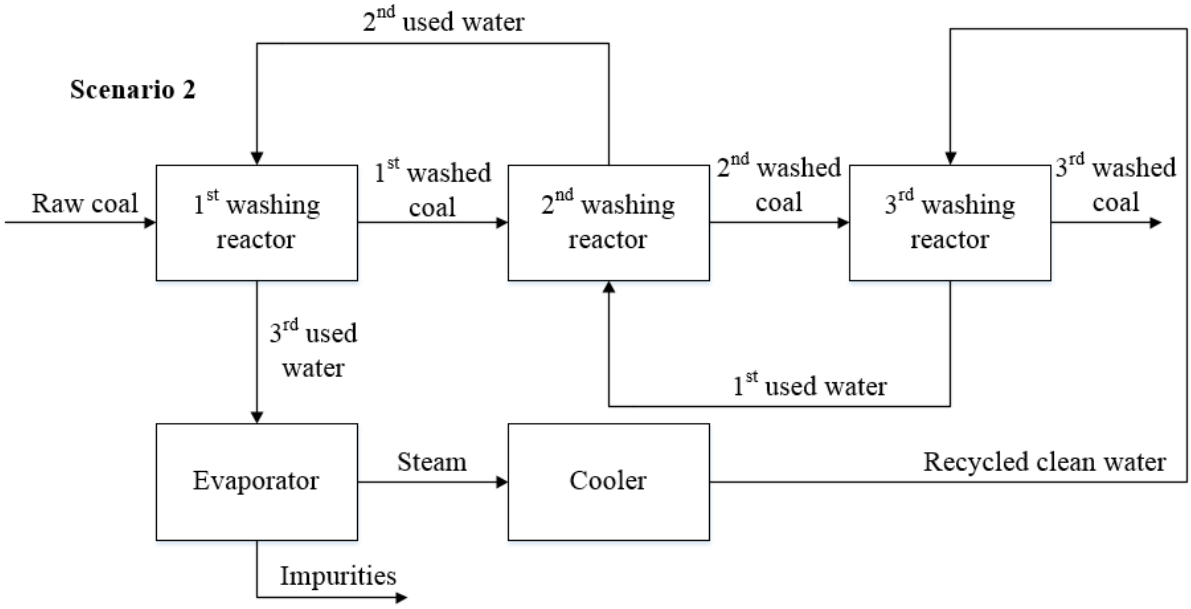
Scenario 2
2nd used water
Raw coal
1st washing reactor
1st washed coal
2nd washing reactor
2nd washed coal
3rd washing reactor
3rd washed coal
3rd used water
1st used water
Evaporator
Steam
Cooler
Recycled clean water
Impurities

(b)

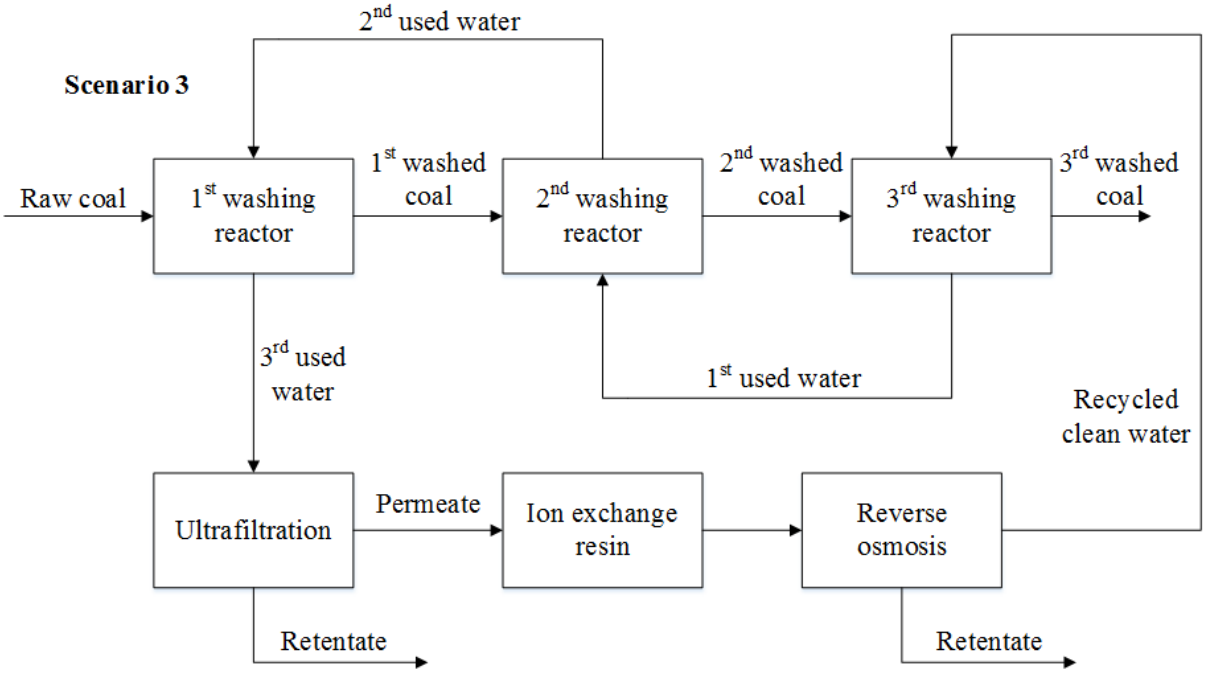
Scenario 3
2nd used water
Raw coal
1st washing reactor
1st washed coal
2nd washing reactor
2nd washed coal
3rd washing reactor
3rd washed coal
3rd used water
1st used water
Recycled clean water
Ultrafiltration
Permeate
Ion exchange resin
Reverse osmosis
Retentate
Retentate

(c)

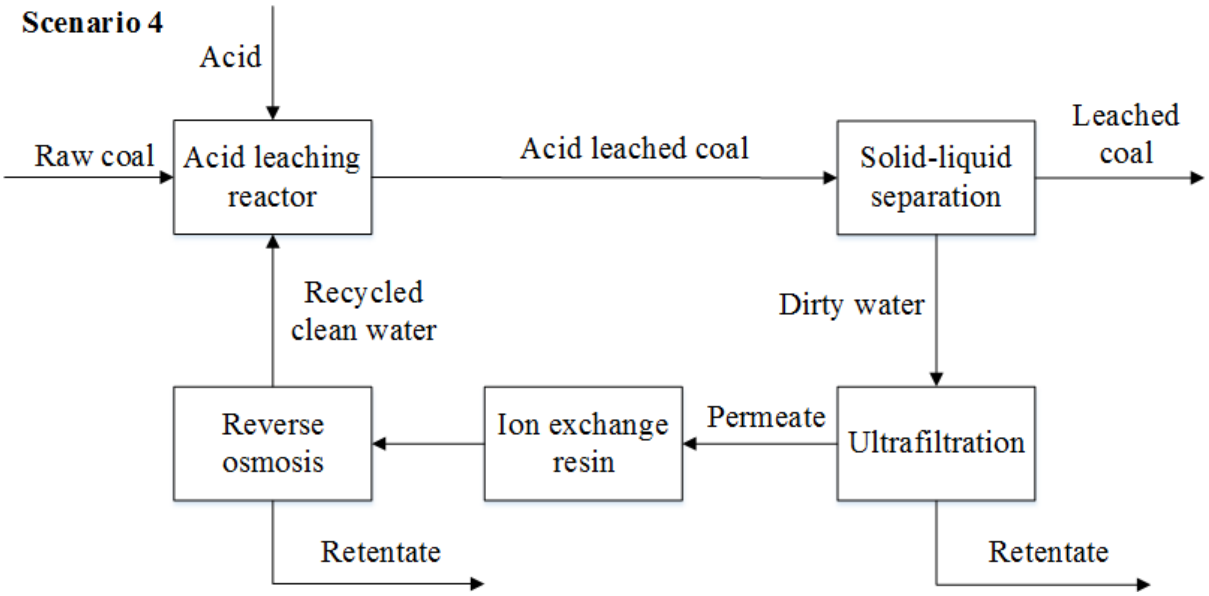

(d)

Figure 3.1 Simplified low-rank coal leaching diagram for Scenario 1 (one stage water leaching with evaporator), Scenario 2 (counter-current water leaching with evaporator), Scenario 3 (counter-current water leaching with RO) and Scenario 4 (acid leaching with RO).

3.2.3 Model development and validation

Aspen Plus is claimed as a commercially reliable field-tested software for more than 30 years and widely used by engineering design companies [20]. Aspen Plus V8.4 was employed to simulate the above-mentioned four low-rank coal leaching scenarios, for a plant capacity of 400,000 tonnes coal per annum. In addition, the lab-scale coal leaching experiments were conducted to produce the extraction yields that are essential for the Aspen Plus simulation. Furthermore, to validate the accuracy of the Aspen plus model, an existing black coal leaching process was simulated and compared with the plant data. A jig machine which can reduce the ash content of black coal by ~50% (reported value from a black coal leaching plant from the industry partner) was employed and simulated in the black coal leaching process.

3.2.3.1 Aspen Plus simulation

Based on the composition of Xinjiang low-rank coal as in **Tables 3.1** and **3.3**, it was assumed that Na exists as a mixture of NaCl and Na_2O which represents the water-soluble and organic sodium that is bonded with carboxylic acid, respectively. Similarly, Ca was postulated to be made up of $CaSO_4$ and CaO. Carbon was assumed to make up the remainder of the coal, on the dried and ash-free basis. Furthermore, to accommodate the default electrolyte module in Aspen Plus, the oxides (Na_2O and CaO) were further converted into the respective hydroxides (NaOH and $Ca(OH)_2$). **Table 3.4** outlines the simplified composition of the two target elements in the raw low-rank coal tested here.

Table 3.4 The simplified composition of Xinjiang low-rank coal for simulation.

Components	*wt%*
Moisture [ad]	24.5
NaCl	0.15
NaOH	0.19
$Ca(OH)_2$	3.57
$CaSO_4$	0.87
C	70.72

[ad] air-dried

The leaching reactor for low-rank coal was modelled by a stoichiometric reactor block (RStoic) [20]. For each reaction in RStoic, the reaction stoichiometry, fractional conversion of each reactant and the reaction condition were specified, based on the experimental results that are

summarised in **Tables 3.5** and **3.6**. The experimental procedure will be outlined in the next section. Except the leaching reactor and waste water treatment units, the same type equipment as in an existing black coal leaching plant has been used, as summarised in **Table 3.7**. The pressure increase in each pump was assumed to be approximately 1 bar, which was deemed to be sufficient in overcoming the pressure drop within the equipment (e.g. 0.5 atm in a vertical flash separator [20]), and the pressure drop caused by piping in the plant. The outlet temperature of the cold side of the evaporator was set to be 101 °C because the saline water had a bubble point higher than 100 °C but lower than 101 °C in this study (Based on Aspen Plus simulation result between the bubble point of saline water and the concentration of salt).

Table 3.5 Na and Ca removal yields.

Process	Element	Reactor	Removal yield / %
Three-stage water leaching	Na	First	34
	Na	Second	14
	Na	Third	10
	Ca	First	0.5
	Ca	Second	0.2
	Ca	Third	0
One stage acid leaching	Na	Acid	67
	Ca	Acid	13

Table 3.6 Optimum operational conditions.

Process	Variable	Value
Water leaching	Residence time	30 min
	Liquid-solid mass ratio	1.5
	Particle size	1-4 mm
HCl leaching	Residence time	30 min
	Liquid-solid mass ratio	1.5
	Particle size	1-4 mm
	HCl concentration	0.7 M

Table 3.7 Summary of assumed input data in Aspen Plus.

Equipment item	Variable	Value
Pump	Efficiency	0.75 [20]
	Pressure increase	1 bar
Reactor	Operating condition	1 bar, 25°C
Dewatering screen	Cut-off size	0.5 mm
Centrifuge	Water in solid outlet	0.08 [21]
	Solid in solid outlet	0.97 [21]
Pressure filter	Water in solid outlet	0.22 [21]
	Solid in solid outlet	0.98 [21]
Evaporator	Outlet temperature of cold side	101 °C
Ultrafiltration	Water recovery rate	96% [22]
	Suspended fine solid removal	100%
	Feeding pressure	310 kPa [22]

IER	Ca^{2+} removal yield	100%
RO (three-stage)	Water recovery rate	75.3% [22]
	Na^{+} removal yield	100%
	Type of RO membrane	TFC 2832 HF-560 magnum
	Feeding pressure	5,520 kPa [22]
	Maximum allowable salinity	32,800 mg/L [22]

In terms of RO simulation, the component separators were employed to simulate both the RO membrane and the ultrafiltration membrane installed upstream of the RO to pre-treat the water feed. In addition, the anion ion exchange resin (IER), a pre-treatment unit to RO to remove Ca^{2+}, was simulated by a combination of RStoic and component separator, with the former one in which a reaction between SO_4^{2-} and Ca^{2+} occurs to precipitate Ca^{2+} and the latter to remove the $CaSO_4$ precipitate. In this study, TFC 2832 HF-560 magnum RO membrane was chosen, due to its high maximum allowable salinity of feeding stream, at 32,800 mg/L, when the feeding stream pressure is 5,520 kPa, at 25°C [22]. To achieve a high water recovery rate, a three-stage RO system was employed hereafter, ending up with a 75.3% water recovery rate shown in **Table 3.7**, where each stage of the RO was simulated as a pressure vessel containing four membranes in series (11% water recovery rate for single membrane). In addition, the feeding stream pressure and water recovery rate were set to be constant at 5,520 kPa and 75.3% respectively, although a lower salinity of feeding stream can increase the water recovery rate slightly and requires a lower feeding pressure. This assumption can simplify the simulation and cause a lowest water recovery rate and a highest power consumption, enhancing the credibility of simulation. The UF system was assumed to recover 96% of water and remove all the suspended fine solids [22].

3.2.3.2 Lab-scale experimental procedure

Lab-scale experiments were conducted to clarify the extraction yields of the two target ions, Na and Ca as a function of residence time, coal particle size, liquid-to-solid mass ratio, the use of fresh and used water, as well as acid, to yield the necessary data as the input in Aspen Plus. The single-stage leaching was firstly conducted in a glass beaker to examine its optimum operating condition. To conduct the three-stage counter-current water leaching experiment in the laboratory, the pure water was first used to leach raw coal for 30 min rather than the 2nd leached coal shown in the leaching part of **Figure 3.1**(b), yielding a leached coal, termed as Coal A and used water. This is because the 2nd leached coal is unavailable at the start-up. Subsequently, the used water was applied to leach Coal A for another 30 min to attain a two-times-leached coal, as Coal B, which was finally leached with pure water to obtain the 3rd leached coal and 1st used water as shown in **Figure 3.1**(b). Afterwards, 1st used water was employed to leach Coal A for 30 min, obtaining 2nd used water and 2nd leached coal. Finally, raw coal was leached by the 2nd used water to get 1st leached coal and 3rd used water. All the leaching experiments were conducted at a batch-scale. The acid leaching experimental procedure is the same as the single-stage water leaching process, except the utilization of acid.

Inductively coupled plasma optical emission spectrometry (ICP-OES) was employed to quantify the contents of Na and Ca in both raw coal and leachates, following a previously established standard procedure [23]. Additionally, the ash fusion temperature of raw coal and leached coal was calculated by a commercial thermodynamic equilibrium software, FactSage$^{6.1}$. The ash compositions in a coal sample, such as the results for raw coal ash listed in **Table 3.3** were used as input for the calculation, plus a weak gas environment (1 vol% CO, 5% O_2, 10% H_2O and N_2 in balance) at 1 atm as an input too [24]. This is to mimic the local gas environment near a coal-fired burner in the boiler. A temperature span of 800 °C to 1600 °C

was simulated, and the built-in FToxide_?Slag database in FactSage was selected to quantify the ash melting percentage versus temperature [4].

3.2.3.3 Black coal leaching validation

An existing black coal leaching plant with a coal feeding rate of 50 t/h of raw coal for a plant capacity of 400,000 tonne coal per annum was simulated. The black coal leaching process mainly consists of a jig machine to remove the coarse minerals by the difference in the specific density of coal and coarse minerals in the pulsating water, and a variety of downstream liquid-solid separation units that are the same as these for the proposed low-rank coal leaching process. As shown in **Figure 3.2**, the coal is firstly screened by a vibrating screen with a cut-off size of 40 mm. The resultant oversize is then sent to a crusher to reduce its size down to 40 mm. Subsequently, coal is leached in a jig machine which employs an air stream of 64.5 m^3/min and a water to solid mass ratio of 2.8 to remove the ash content by ~50%, same as that reported by the plant operation. A component separator was chosen to simulate the jig machine. Subsequently, the outlet stream from the jig machine is transferred to a dual deck vibrating dewatering screen with two cut-off sizes of 25 mm and 0.7 mm, separating out the lump coal larger than 25 mm with a moisture content of 8%, and those between 0.7 and 25 mm seeing a moisture content of 28%, respectively. Afterwards, the slurry of coal fine-water is sent to a peat screen with a 0.5 mm cut-off size to remove the fine coal particles. Simultaneously, the overflow of the peat screen and the coal with a size of 0.7-25 mm is transferred to a centrifuge to reduce the moisture down to 11%, as well as to recover water. The water coming from both centrifuge and peat screen is then mixed and sent to a thickener where the coal fines is agglomerated by using a coagulant namely polyacrylamide (PAM), with a mass concentration of 1 g/m^3-slurry. The agglomerates passes through a pressure filter to squeeze out the water. The thickener, which is not a built-in block in Aspen Plus was simulated by a component

separator. Finally, the water is recycled back into the jig machine to reuse and the by-product wet tailings of 22 *wt%* moisture is obtained.

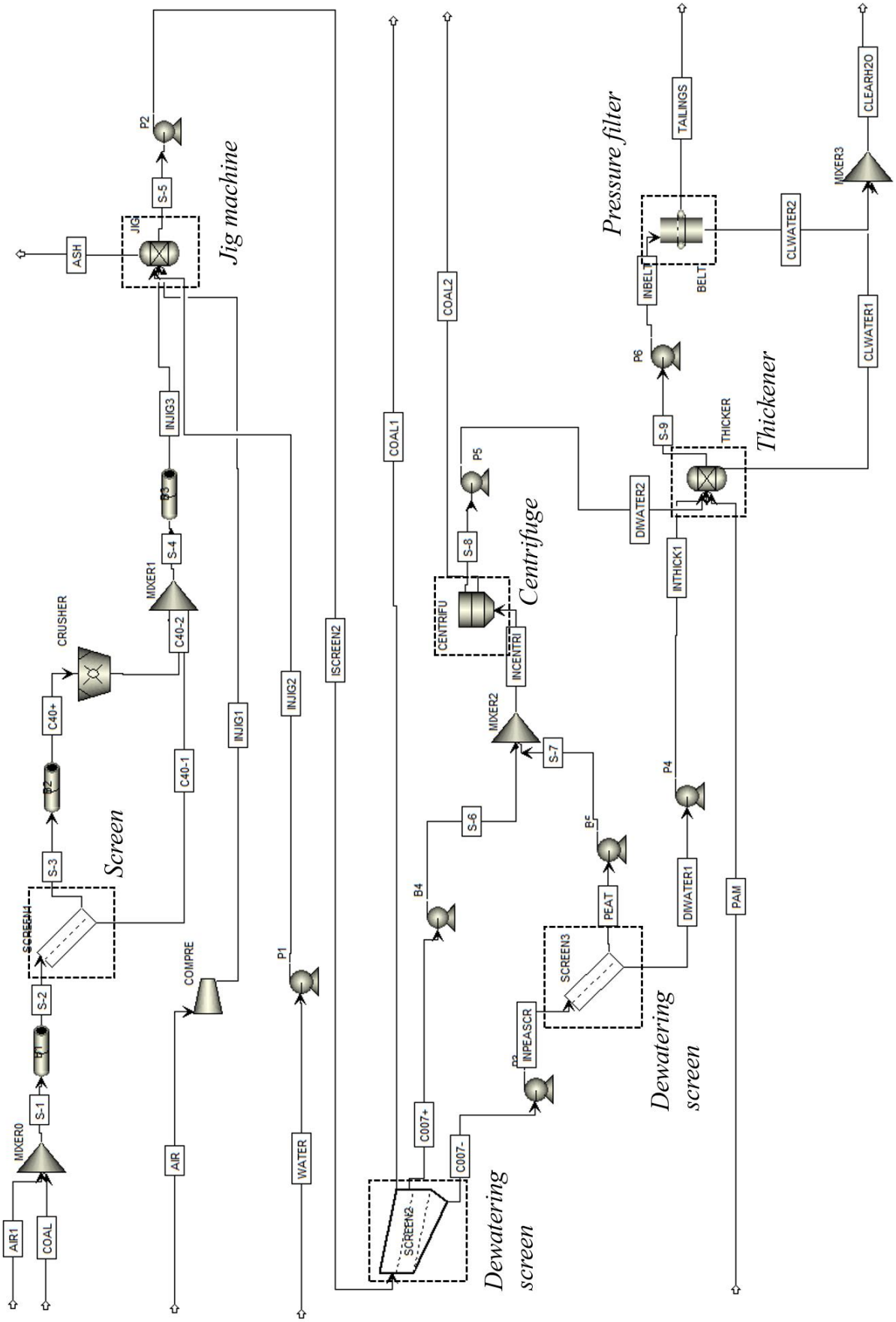

Figure 3.2 Aspen Plus flowsheet for the black coal beneficiation process.

3.2.3.4 Cost estimation methodology

Aspen Process Economic Analyzer (APEA) [20] was finally integrated with Aspen Plus to estimate the cost for each scenario proposed above.

Since the plant is located in Xinjiang, China, all the cost figures were expressed as Renminbi (RMB) by a USD/RMB currency conversion rate of 6.60, based on 2017 data. Subsequently, necessary parameters were specified, including the project type, project starting date, annual operating time, project fluids, utilities, labor cost, raw materials and product streams, as outlined in **Table 3.8**. For the flue gas used as a hot stream in Scenarios 1 and 2, it was assumed as free of charge since the adjacent power plant is able to provide it. So was the hydrochloric acid that can be provided by an adjacent electrolyzer for the production of sodium hydroxide, according to the report of the industrial partner, Hubei Yihua Chemical Co Ltd. However, effort was still made to vary the price of HCl acid to assess its effect on the process feasibility. The prices of raw coal, electricity, water, coagulant polyacrylamide and labor were obtained based on the existing black coal-leaching plant. The net present value (NPV), internal rate of return (IRR) and payback period were calculated by cash flow analysis [25] and the corresponding parameters were also outlined in **Table 8**.

Table 3.8 Input economic parameters to Aspen process economic analyser.

General economic parameters		**Cash flow analysis parameters**	
Plant location	Xinjiang, China	Depreciation	5% per year
Currency conversion rate	RMB/USD 6.60	Tax rate	30%
Project type	Clear field	Interest rate	10%
Source of utilities	Across the fence	Project lifecycle	20 years
Project fluids	Liquids and solids	Discount rate	10%
Operating hours per year	8000	Depreciation method	Straight line
Start date for engineering	1-Jan-17	Working capital	6.7% of the fixed capital cost
Raw material process		**Utilities**	
Raw Xinjiang coal	46 RMB/t[a]	Electricity	0.255 RMB/kWh[a]
Polyacrylamide	6500 RMB/t[a]	Flue gas	Free
Hydrochloric acid (31%)	Free[a]		
Water	3.7 RMB/m^3 [a]		
Products		**Labour**	
Leached low-rank coal	200 RMB/t[a]	Operator	9.17 RMB/Operator/H[a]
Wet tailings	10 RMB/t[a]		

[a] Reported values from a black coal leaching plant in China

Based on the equipment cost library in APEA, each unit in Aspen Plus needs to be mapped to size and further estimate the cost referring to the vendor quotes in the specified plant location. Centrifugal pumps and rotary lobe pumps were applied for pumping pure water and water-coal

slurry, respectively [26]. Due to the volatility and corrosion of 31 *wt%* HCl, an enclosed agitated tank reactor of carbon steel shell lined by PVDF (polyvinylidene fluoride) was employed. Additionally, the pump in contact with HCl was mapped by the plastic centrifugal pump. Carbon steel was used for all other agitated open-up water leaching reactors as the shell material. In light of the residence time of 30 min, reactors was sized as an internal diameter of 2.59 m and height of 9.14 m. Rotary crusher was used for sizing of the coal crusher. The conveyor length and belt width of all belt conveyors were assumed to be 10 m and 500 mm, respectively, which was capable of conveying coal of any flow rates in the process [27]. Long tube vertical evaporator and field assembly cooling tower were selected for evaporator and cooling tower, respectively. However, due to the lack of built-in model for RO in APEA, the cost of RO units were calculated based on an existing water treatment plant using RO in USA [28], which was further corrected by taking into account the plant capacity, location factor, inflation index, and currency exchange rate [29]. The assumptions for RO cost estimation are summarized in **Table 3.9**.

Table 3.9 The assumption for RO cost estimation.

Variable	Value
Plant capacity (Million gallon per day) [28]	150
Currency conversion rate	RMB/USD 6.38
Location factor for China [30]	0.95
Cost index 2001 [27]	406
Cost index 2017 [27]	1125

3.3 Results and discussion

3.3.1 Simulation validation using the existing black coal leaching process

Table 3.10 illustrates the simulation results including the water and power consumption per tonne raw black coal, and the total equipment cost, with the actual plan operating data for comparison.

Table 3.10 Comparison of the actual and simulation values for black coal beneficiation process.

Variable	Simulation result	Actual value [a]	Unit
Water consumption	71	51-85	kg/t of raw coal
Power consumption	3.9	3.5-6.3	kWh/t of raw coal
Total equipment cost	5.1	4.2 (5.5)	million RMB

[a] Reported values from a black coal leaching plant in China which was built in 2013. The number in the bracket is the present value by converting 4.2 in 2013 to 2017 when this simulation is being conducted.

It is clear that the Aspen Plus simulation results are credible, particularly for the high accuracy for the total equipment cost by comparing the simulation result (5.1) with the present value of actual data (5.5). It is worth emphasizing that the actual value (4.2) in the year 2013 needs to be converted to the present value (5.5) based on 2017 firstly by taking into account the cost inflation indexes of 852 and 1125 for the year 2013 and 2017 respectively [27]. For the other two variables, the simulation results are also reasonable and right in the range of the plant data. It should be noted that the plant operation generally has a fairly large fluctuations on coal compositions and operational conditions, leading to a large variation on the water and power consumptions. Even so, given the fact that the major liquid-solid separation units including

dewatering screen, thickeners, pressure filter and centrifuges in the black coal leaching process have been considered and included in the modelling and the same units will be used for low-rank coal leaching, the results in **Table 3.10** provide a reasonable credibility to the simulation results obtained for the low-rank coal leaching results to be discussed later. In addition, it is noteworthy that, the water loss for the black coal leaching mainly takes place in the centrifugal stage where the final product reaches an equilibrated moisture content of 11 *wt%*. With respect to the power consumption, it is mainly attributed to the jig machine that consumes a power of 2.3 kWh/t coal.

3.3.2 Comparison of low-rank coal leaching stages via Scenarios 1 and 2

3.3.2.1 Lab-scale coal leaching results

Table 3.11 compares the ash composition change of leached coal produced by the Scenarios 1 and 2, where coal was leached by a single-stage and three-stages, respectively. The total ash rarely reduces in Scenario 1, although the mass fraction of Na_2O in ash decreases noticeably from original 4.32 *wt%* down to 1.01 *wt%*. Scenario 2 is clearly more pronounced, achieving a reduction of 1.4 *wt%* for the total ash, and a lower value of 0.85 *wt%* for Na_2O in the ash. **Figure 3.3** demonstrates that the majority of the ash produced by Scenario 2 does not melt until the temperature reaches 1200 °C, which is the design temperature for the combustion chamber in a pulverized coal-fired boiler.

Table 3.11 Ash composition changes after different leaching processes.

Sample	Ash/%	Na_2O	MgO	Al_2O_3	SiO_2	P_2O_5	SO_3	K_2O	CaO	Fe_2O_3
Raw coal	7.8	4.32	22.65	3.27	5.67	0.52	15.06	0.21	46.96	1.34
Scenario 1	7.6	1.01	24.32	3.04	4.03	0.52	16.94	0.25	47.77	2.12
Scenario 2	6.4	0.85	21.23	4.38	6.59	0.45	19.86	0.21	45.95	0.48
Scenario 4	6.3	0.21	19.16	4.85	7.86	0.40	37.30	0.19	29.50	0.53

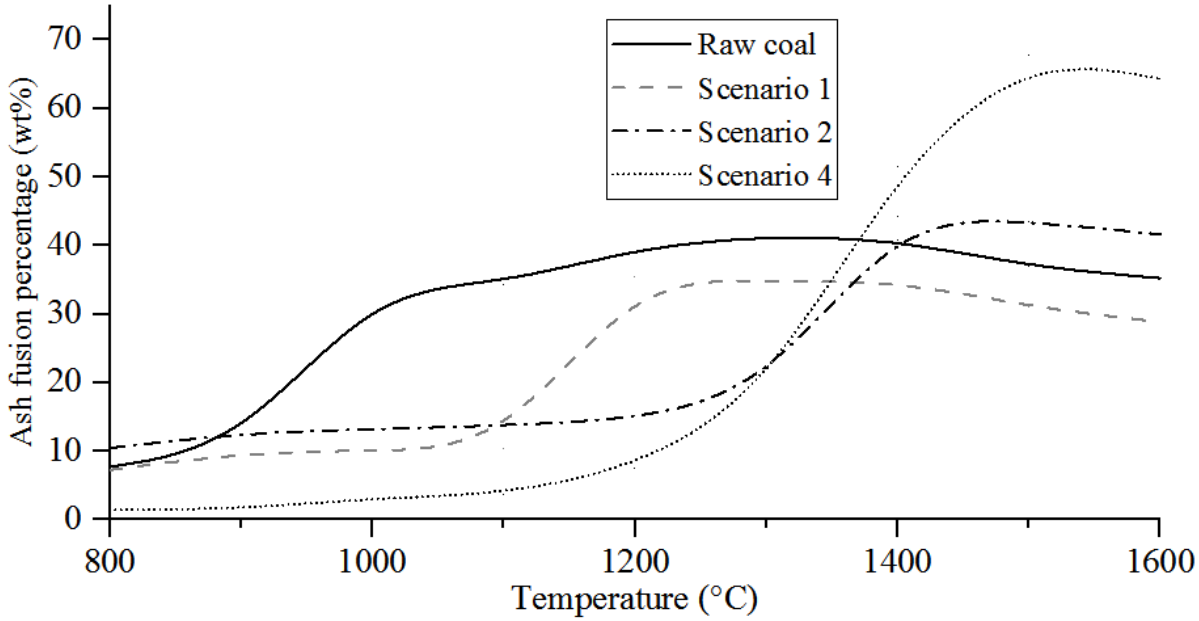

Figure 3.3 Ash melting point comparison for Scenarios 1, 2 and 4.

3.3.2.2 Aspen Plus simulation results

The Aspen Plus flow-sheets for Scenarios 1 and 2 share same process units, except the leaching stages. The water recovery rate, water and power consumption of both scenarios are presented in **Table 3.12**. Interestingly, both new processes can produce, rather than lose about 140 kg water per tonne raw coal. This is a result of the 24.5 *wt%* moisture content in raw coal that is down to 11 *wt%* after centrifugal dewatering, resulting in more water recovered than what is

lost in the tailing and other units. In terms of the external fresh water added into the process, the proposed two scenarios can recycle almost same fraction that is close to 93%, which is also close to the black coal leaching process. However, the total power consumption for Scenario 2 is more than twice that for Scenario 1, 10.3 versus 5.1 kWh/t raw coal. This is mainly due to the use of extra pumps and agitation tanks for the three-stage leaching that consumed 7.4 kWh/t coal in Scenario 2, triple of the power caused by only one tank in Scenario 1.

Table 3.12 Comparison of water and power consumption for single and three-stage water leaching.

Variable	Single stage	Three stages	Unit
Water consumption	144.1 (gain)	137.0 (gain)	kg/t of raw coal
Water recovery rate	93.3	92.8	%
Total power consumption	5.1	10.3	kWh/t of raw coal
Agitated tank power consumption	2.4	7.4	kWh/t of raw coal

3.3.3 Comparison of waste water treatment methods via Scenarios 2 and 3

Since the waste water treatment unit is crucial for the feasibility of the overall process, efforts were made to assess Scenario 3 where the three-stage leaching unit plus a downstream RO-based wastewater treatment unit are adopted. **Table 3.13** demonstrates the simulation results for its water and power consumption as well as water recovery rate, with the results of Scenario 2 included for comparison. Unsurprisingly, Scenario 3 consumed much more water, due to the low water recovery rate of the RO system, 75.3% (**Table 3.7**). Accordingly, the application of RO system caused a lower water recovery rate for Scenario 3. A total of 251 kg/t coal water was thus lost in Scenario 3, compared with 137 kg/t coal water gain for Scenario 2. The water

loss ratio in Scenario 3 is also far more than the 85 kg-water/t coal consumed for the black coal leaching process. In this regard, the RO system seems to be overshadowed by the evaporator. However, the better performance of Scenario 2 about water recycling rate might be counteracted by the considerable capital cost was caused by the huge heat transfer area of the evaporator and cooling tower (further discussed later).

Table 3.13 Comparison of water and power consumption for three-stage leaching using evaporator and RO.

Variable	Using evaporator	Using RO	Unit
Water consumption	137.0 (gain)	251.2 (loss)	kg/t of raw coal
Water recovery rate	92.8	68.3	%
Power consumption	10.3	13.4	kWh/t of raw coal

With respect to the large discrepancy in the power consumption between these two scenarios, the feeding stream pump in the RO system is crucial. Two feeding pumps had to be added in to satisfy the specific feeding stream pressure into ultrafiltration system and reverse osmosis system, at 310 kPa and 5,520 kPa, respectively. As a result, the total power consumption of Scenario 3 is 13.4 kWh/t of raw coal, which is larger than 10.3 kWh/t raw coal of Scenario 2, as evaporator consumes hot flue gas rather than electricity. In addition, compared to black coal which requires approximately 6.3 kWh/t coal for leaching, the energy consumption for low-rank coal leaching, as predicted here, is much higher especially for Scenario 3, indicating that a further optimization is necessary.

The discrepancy in the capital and operating costs between Scenarios 2 and 3 is also noteworthy. Although both scenarios require further optimization, clarifying the costs of different waste water treatments and their percentages in the total capital cost is important for the following process optimization. **Figure 3.4** (a) presents the breakdown of capital costs for these two scenarios. The total capital cost of Scenario 3 using RO was estimated to be around half of the figure of Scenario 2 incorporating evaporator and cooling tower, due to the smaller equipment and piping costs for Scenario 3. By breaking down the equipment cost, it is found that for Scenario 2, the cost of evaporator and cooling tower is the largest contributor to the purchased equipment cost, might due to the requirement of large heat transfer area. It is made up of 69.5% and is more than four times the cost of RO system in Scenario 3. Additionally, the annual operating costs for the two scenarios are demonstrated in **Figure 3.4** (b). Two scenarios have similar operating costs, of which the total raw material cost makes up the largest proportion. Due to the higher power consumption for Scenario 3, it is reasonable that the expenditure of utilities is higher than that of Scenario 2. Similarly, the marginal higher total raw material cost is also observed for Scenario 3 due to a slightly larger water consumption. However, Scenario 3 required much lower maintenance cost than Scenario 2, based on an assumption of allocating around 2% of the fixed capital cost to the maintenance fee [20], causing its even smaller total operating cost.

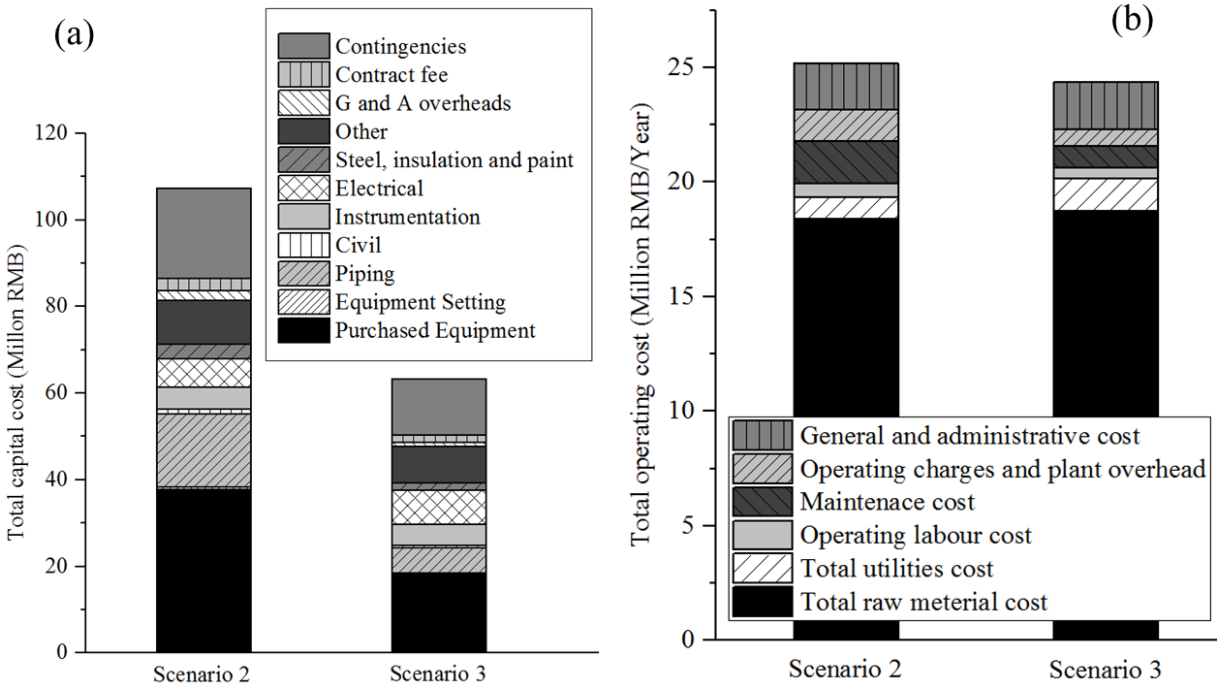

Figure 3.4 Break-downs of capital and operating cost per year for Scenarios 2 and 3.

3.3.4 Optimization of Scenarios 3 for the integration of multi-stage leaching units and RO technique

3.3.4.1 Increasing the cycle numbers of waste water

The first optimization option chosen is to reuse the semi-clean water obtained after the bundle of the solid-liquid separation units. Such a waste water, if unsaturated with salts, could be still sent back to and reused in the 3rd leaching tank. The hypothesis is that the unsaturated used water still has the capability to extract sodium out of the coal matrix, since the water solubility of Na-bearing species is usually large, e.g. 359 g/L for NaCl under the ambient conditions.

To find the possible maximum allowable cycle number of the semi-clean water, experiments were first conducted to leach the raw coal with pure NaCl solutions of 0.2 *wt%* and 1 *wt%*, under the optimum condition as mentioned in the subsection 2.3.1. These two NaCl solutions

were made to mimic the water that has been reused once and six times, respectively. Due to the reusing of the water, the concentration of Na^+ should increase steadily upon a continuous dissolution of NaCl out of coal. **Figure 3.5** shows time-resolved concentration profiles of Na^+ in the two NaCl solutions. Clearly, the use of 0.2 *wt%* is still able to extract Na out of coal. However, the content of Na^+ in the 1 *wt%* NaCl solution remains relatively constant, indicating that the Na^+ concentration in the bulk solution might be equal or close to 1 *wt%* NaCl and thus has no momentum to diffuse out. In other words, the 1 *wt%* Na^+ referring to the reusing of water for six times is the possible maximum allowable concentration of Na^+ in the used water. In addition, such a maximum allowable concentration of Na^+ is far lower than the highest salinity of the feed stream, 32,800 mg/L with an equivalence of approximately 3 *wt%* NaCl that can be tolerated by the TFC 2832 HF-560 magnum RO membrane chosen here. However, the concentrate of a RO membrane is the feed to the next RO membrane. Therefore, the salinity of the feeding stream to the third-stage RO membrane is the highest, which was calculated to be 4,307 mg/L based on the simulation result after the first cycle of leaching. The maximum possible cycle number by RO membrane is thus seven times (4,307 divided by 32,800), which is close to the six cycles determined by NaCl leaching experiments.

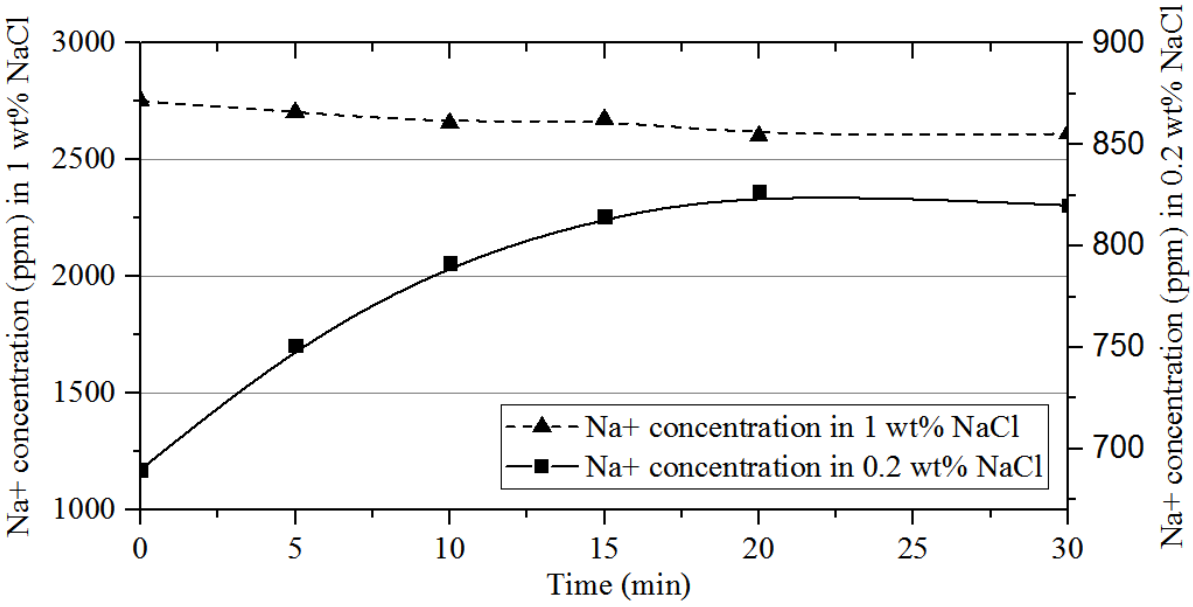

Figure 3.5 Na^+ concentration change in 0.2 *wt%* and 1*wt%* NaCl versus time.

Table 3.14 compares the change in the water and power consumptions upon implementing the maximum six cycles for the reusing of the wastewater prior to it being treated by the RO system. Interestingly, the water loss rate declines significantly from around 251 to 42 kg/t coal, which is even less than the half of the value for black coal leaching process. The power consumption also decreases by 3 kWt/t coal, resulting from less use of the feeding pump prior to the RO system. However, it is still larger than that of black coal leaching process, since the three agitation tanks are still the major component which consume huge energy.

Table 3.14 Comparison of water and power consumption before and after the recycling.

Variable	Before	After	Black coal process	Unit
Water consumption	251.2 (loss)	41.9 (loss)	85	kg/t of raw coal
Power consumption	13.4	10.3	6.3	kWh/t of raw coal

3.3.4.2 Acid dosing

Further effort was made to reduce the coal leaching steps by introducing acid-controlled leaching. The hypothesis is that the acid dosing would achieve a close or even higher Na/Ca removal extents than the three-stage water leaching using less leaching steps, considering that the acid will mobilize the part of Na/Ca which cannot be removed by water. In light of this, the coal leaching process was further optimized as Scenario 4, in which only one coal leaching tank is used.

Back to **Tables 3.5**, it is obvious that the removal of both sodium and calcium has been improved remarkably. Back to **Table 3.11**, the percentages of Na_2O and CaO in ash decline significantly to 0.21 and 29.50 *wt%*, respectively, resulting in a decrease of 19% in total ash content. Consequently, the ash fusion temperature of leached coal by Scenario 4 exceeds 1200 °C, as presented in **Figure 3.3**.

Table 3.15 compares all the simulation results for the Scenarios 3 and 4. With regard to the possible maximum allowable cycle times, the number for Scenario 4 is smaller than Scenario 3 (4 versus 6), due to the higher Na and Ca removal extents in a single cycle. Therefore, the Scenario 4 consumes more water, at around 52 kg/t coal, which is however still far lower than 85 kg/t coal required for the black coal leaching process. In addition, the power consumption declines greatly, by 40% from 10.3 kWh/t coal for Scenario 3 to 6.0 kWh/t coal that is slightly below the black coal case, 6.3 kWh/t coal. Clearly, the use of less agitation energy is much more influential than the increased energy consumption for the RO system. The use of less tank also reduced the capital cost.

Table 3.15 Comparison of Scenarios 3 and 4 after recycling

Variable	Three-stage with RO	Acid with RO	Unit
Na removal yield	58	67	%
Ca removal yield	0.7	13	%
Water consumption	41.9 (loss)	51.8 (loss)	kg/t of raw coal
Power consumption	10.3	6.0	kWh/t of raw coal
Capital cost	64	50	million RMB
Operating cost	24	23	million RMB/Year

3.3.5 Sensitivity analysis for Scenario 4

3.3.5.1 Effects of the principal variables on the number of water recycle, water and power consumptions

Considering the heterogeneity of raw coal, and uncertainty related to the dewatering performance of centrifuge caused by the hydrophilicity difference between the differently ranked coals, sensitivity analyses were further carried out to assess the changes of water and power consumption in Scenario 4, upon the variation of raw coal properties outlined in **Table 3.16**. In brief, the moisture content in raw coal varies from 10 *wt%* for the equilibrated content to the maximum possible value of 30 *wt%* as that was reported for Xinjiang coal [12], with an interval of 5 *wt%*. The mass percentage of coal size less than 0.5 mm (cut-off size of the screen after the coal leaching unit) varies from nil to 90 *wt%* at an interval of 20 *wt%*, considering that the low-rank coal is generally soft and fine compared to black coal. In addition, the contents of chlorine (Cl) and Na in the raw coal are crucial, affecting the recycle number of waste water. The contents of Cl and Na varies from 200 to 2000 ppm and 700 to 5200 ppm in raw coal, respectively, which is considered to include all possible contents [31]. Finally, the moisture of

coal out of centrifuge is also varied. This is based on the concern that the commercial plant for low-rank coal leaching and dewatering does not exist yet. Lab-scale experiments have been conducted in a batch-scale centrifuge (Allegra X-22 Centrifuge). It confirms that the lowest moisture in the dewatered Xinjiang coal is around 22 *wt%*. The discrepancy between the industry-reported value (8 *wt%*) and lab-based value (22 *wt%*) might be a result of the different configuration of centrifuges as well as the strong hydrophilicity of low-rank coal. Therefore, the moisture of centrifuge-dewatered coal is set as a sensitivity variable with a variation range of 8 to 22 *wt%*.

Table 3.16 Sensitivity variables and variation ranges.

Variable	Variation range	Variation pace
Initial moisture of raw coal	10 ~ 30 *wt%*	5 *wt%*
Mass fraction of coal fines < 0.5 mm	0 ~ 90 *wt%*	20 *wt%*
Total Cl content in raw coal	200 ~ 2000 ppm	200 ppm
Total Na content in raw coal	700 ~ 5200 ppm	500 ppm
Moisture in dewatered coal	8 ~ 22 *wt%*	2 *wt%*

As shown in **Figure 3.6** (a), the Na content in raw coal is the most sensitive variable, varying the wastewater recycle number from fourteen to only one upon the rise of its original content in coal from 700 to 5200 ppm. Accordingly, the water and power consumptions are also highly sensitive to the variation of the original Na content, as evident in the panels (b) and (c). The highest cycle number for a minimum Na content of 700 ppm leads to the lowest water and power consumption, around 14 kg/t coal and 5.1 kWh/t coal, respectively. However, once the Na content in raw coal reaches around 2150-2520 ppm (the base case is 1670 ppm), the water

consumption and power consumption of Scenario 4 will reach the same values, 85 kg/t coal and 6.3 kWh/t coal for the black coal, respectively. With respect to another element of interest, Cl in the raw coal, its influence is marginal on the three dependent variables.

The initial moisture in the raw coal is the second most influential variable, which directly determines the amount of total water entering the process. The cycle number is therefore proportional to the initial moisture in the raw coal, ranging from three to five upon the change in the initial moisture from 10 to 30 *wt%*. Consequently, the water consumption declines from 103 to 30 kg/t coal, reaching the same water consumption figure for black coal in the case that initial moisture is around 19 *wt%* in the raw Xinjiang coal. Compared to the black coal with 10 *wt%* moisture, such a threshold value in the Xinjiang coal is clearly high. This is because the Xinjiang coal is fine in size, resulting in a percentage of 13 *wt%* for the waste tailing. More interestingly, although the entry of high-moisture coal into the system results in the rise on the amount of the waste water to be processed in the RO unit, such a side effect is counteracted by the increase in maximum cycle number. Therefore, the rise of coal moisture content from 10 to 30 *wt%* indeed results in a slight decline in the power consumption from 5.9 to 5.6 kWh/ t coal, as evident in panel (c).

With respect to the mass fraction of coal fines, its decrease results in more coal to be sent to the centrifuge that produces a much lower moisture content (11 *wt%*) in the resultant dewatered coal, compared with the moisture of the wet tailings that is generally 22 *wt%*. As a result, the water consumption decreases slightly from 58 to 46 kg/t coal when the particles smaller than 0.5 mm reduces from 90 to 0 *wt%*. Nonetheless, such a change is quite marginal and affects little on the water cycle number and power consumption, as evident in panels (a) and (c).

Finally, the increase in the moisture of coal out of centrifuge causes larger water consumption and smaller power consumption due to the decline in the water transferred to RO feeding pump, the main power consumption unit. However, it affects little on the cycle number.

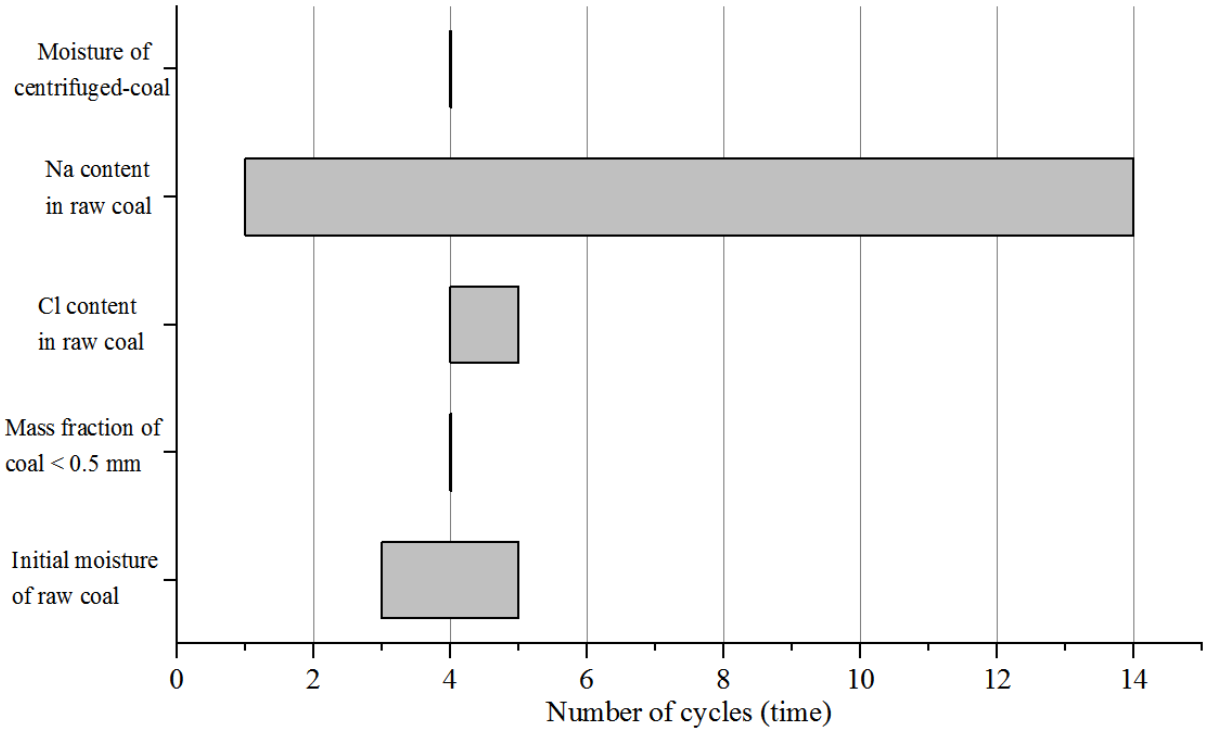

(a)

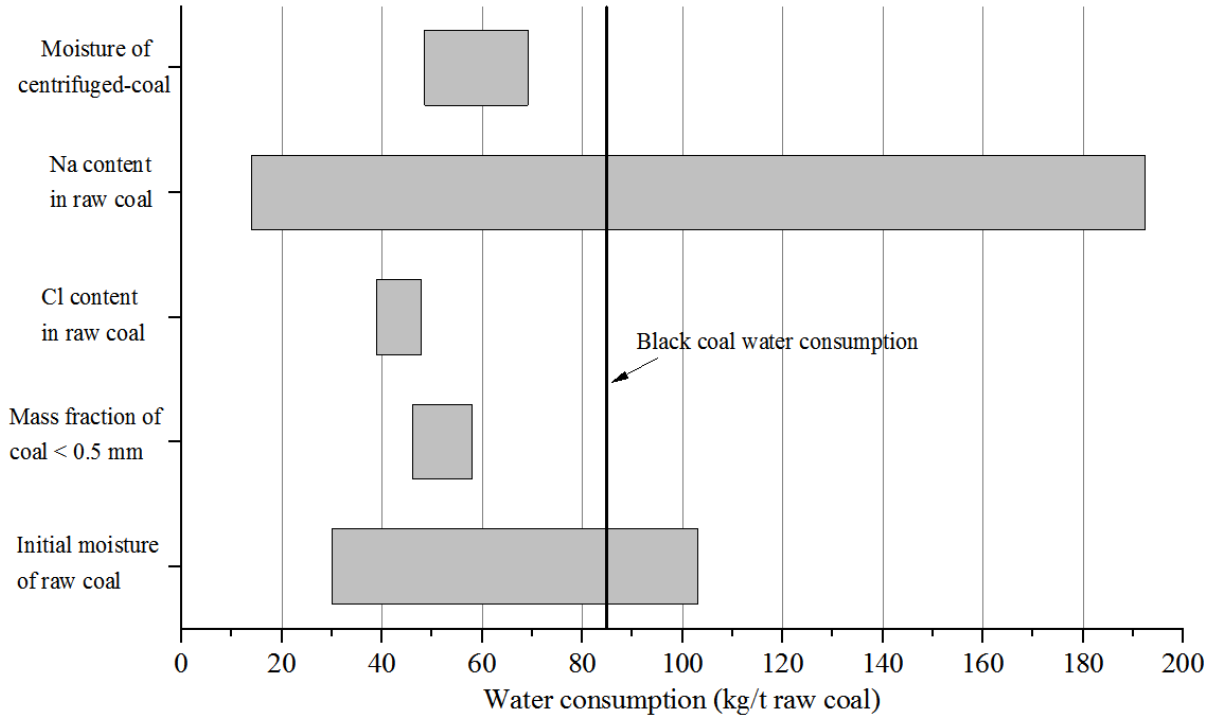

(b)

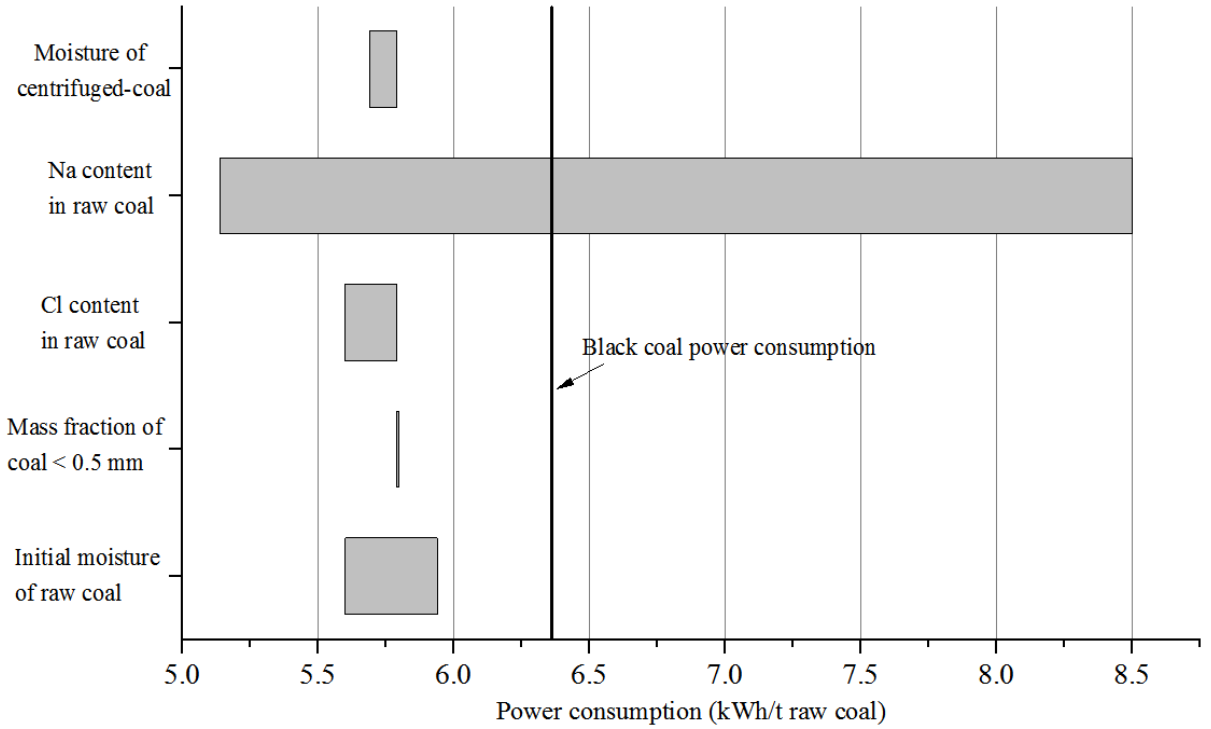

(c)

Figure 3.6 Sensitivity analyses of the variables on the number of cycles (a), water consumption (b) and power consumption (c) for Scenario 4.

3.3.5.2 Effects of the principal variables on NPV, IRR and Payback Period

Cash flow analysis was implemented to determine the variation of NPV, IRR and payback period for Scenario 4. To reiterate, the income of this project is from the sale of the main product, leached coal with a price of 200 RMB/t in the local market, and by-product tailings at 10 RMB/t. With an economic lifecycle of 20 years for the base case Scenario 4, NPV, IRR and payback period are 87 million RMB, 28% and 4.7 years, respectively, indicative of a strong investment temptation. IRR is almost fivefold larger than the highest inflation rate in China in recent ten years, at 5.9% [27], showing a strong risk tolerance. In particular, considering the high NPV of 87 Million RMB and a short payback period of 4.7 years, a satisfactory profitability is envisaged.

Figure 3.7 demonstrates the sensitivity of the economic analysis results upon a ±50% variation of the principal variables except the HCl price changing from 0 to 260 RMB/t that is the market price in China. Based on the panel (a), it is obvious that the NPV is mostly susceptible to the variation of the selling price of the final product, leached coal. A 50% increase in the selling price can make NPV soar to 220 million RMB approximately. By contrast, NPV turns negative when the selling price decreases by 32% (136 RMB/t). With respect to the annual operating cost, its 50% increase causes NPV to drop to 20 million RMB, compared to the 154 million RMB when the operating cost decreases by 50% from the base case. The capital cost is a relatively insensitive parameter for NPV, as suggested by a much less steep slope. The HCl price also exerts a marginal effect on the NPV. Its 260% increase only results in NPV to decline from 87 to 50 million RMB.

In regard to the IRR in panel (b), the selling price of the final product is still the most influential parameter. A decrease to 45% for the final product price results in the IRR plummeting from ~52% to nil, and then negative upon a further decline in the selling price of the main product. The variation of capital cost can also change the IRR greatly from 53% to 19% upon its change by -50% and +50% respectively. A similar trend is observed for the impact of the annual operating cost on IRR. A 50% increase in the operating cost makes IRR decline to 14% or so from 28% (the base case value). HCl price is the least sensitive variable to IRR, indicated by its rather flat slope. The IRR still remains above 20% even with a 260% increase in the HCl price.

Regarding the payback period, the selling price of the product also presents the highest sensitivity. Here again, a minimum selling price of 136 RMB/t (-32% deviation from base-case value) is essential to ensure that the payback period smaller than the lifespan of the project (20 years). A 50% rise in the selling prices, however, will shorten the payback period from 4.7 to 2.4 years. The sensitivities of payback period towards the annual operating cost and capital cost are close, increasing from approximately 2.5 years at -50% deviations of each of the variables to 10.8 and 7.7 years upon +50% deviations of the operating cost and capital cost respectively. With the increase in HCl price from 0 to 260 RMB/t, the payback period increases gradually from 4.7 to 6.8 years, indicating the least sensitivity of the variation of HCl price to payback period.

Finally, it is noteworthy that, the simulation and cost estimation results here are merely for a preliminary estimation and comparison with black coal purpose. The cost calculation results of this stage could have ±30% error [20]. Detailed and more accurate pilot plant testing is underway

to further adjust the results predicted here. Even so, one still can envisage that the proposed low-rank coal leaching process is a promising technology solving the alkali element – related problems during the combustion of low-rank coals.

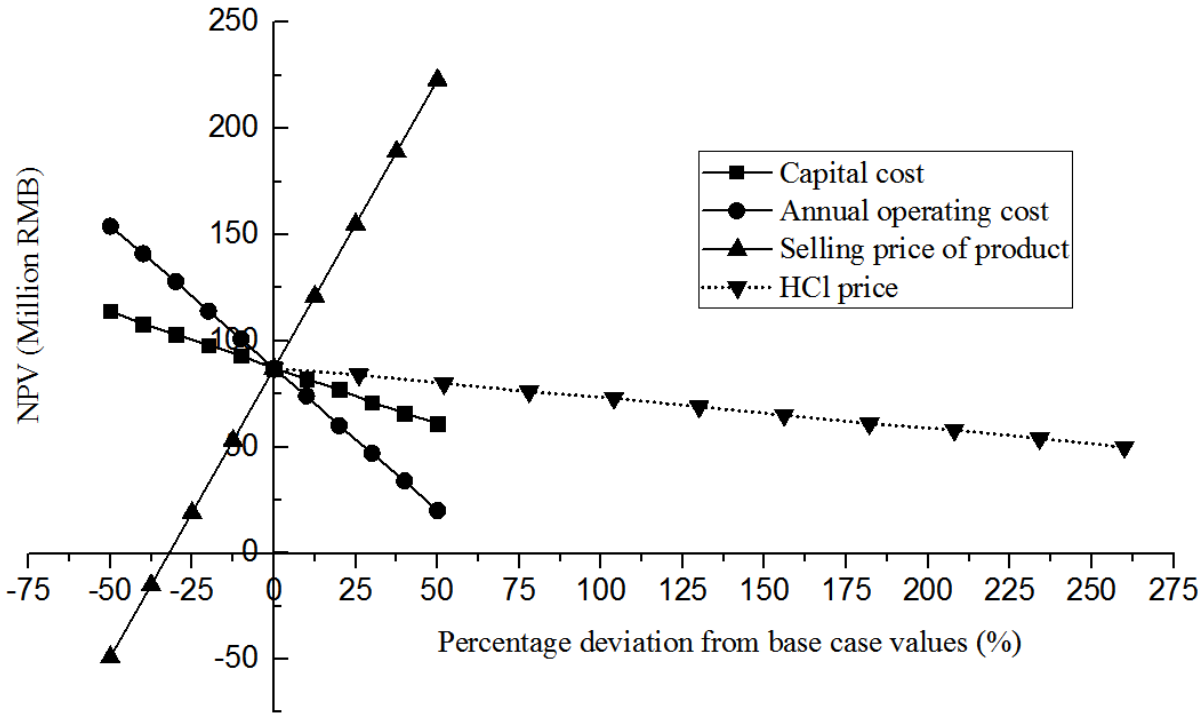

(a)

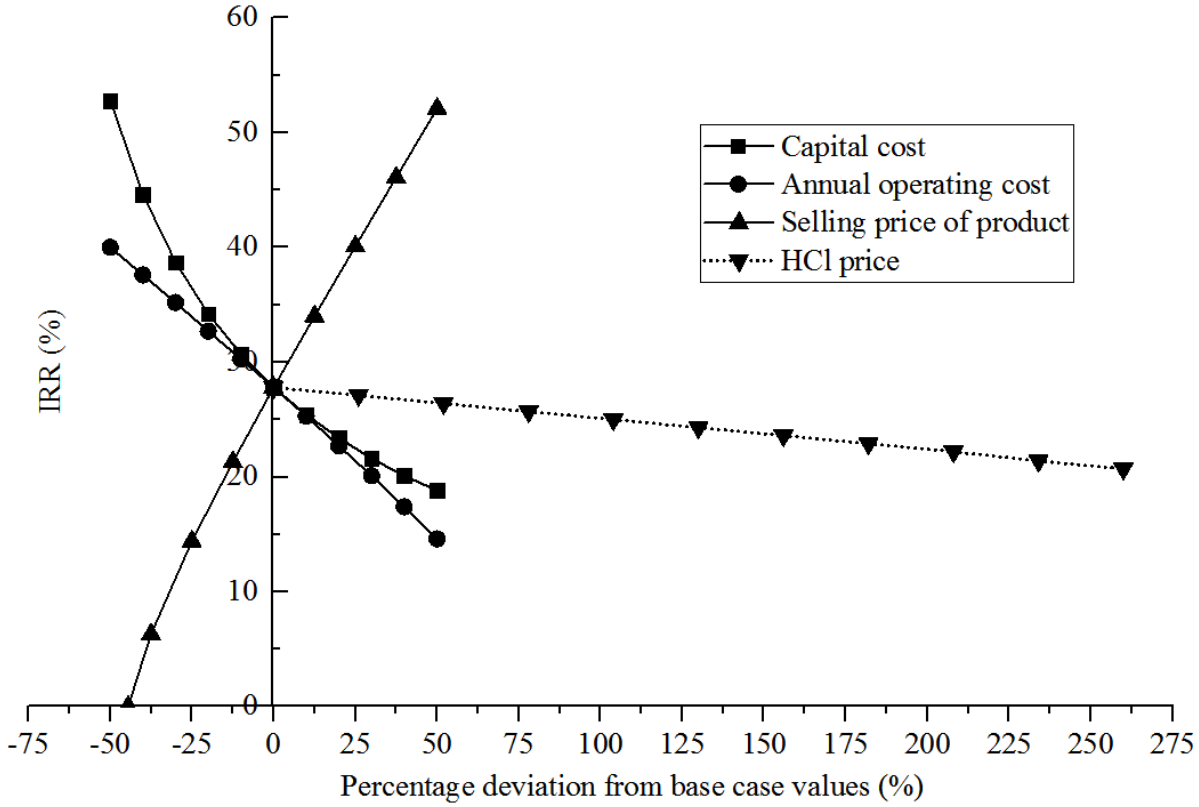
IRR (%)
Percentage deviation from base case values (%)
Capital cost
Annual operating cost
Selling price of product
HCl price

(b)

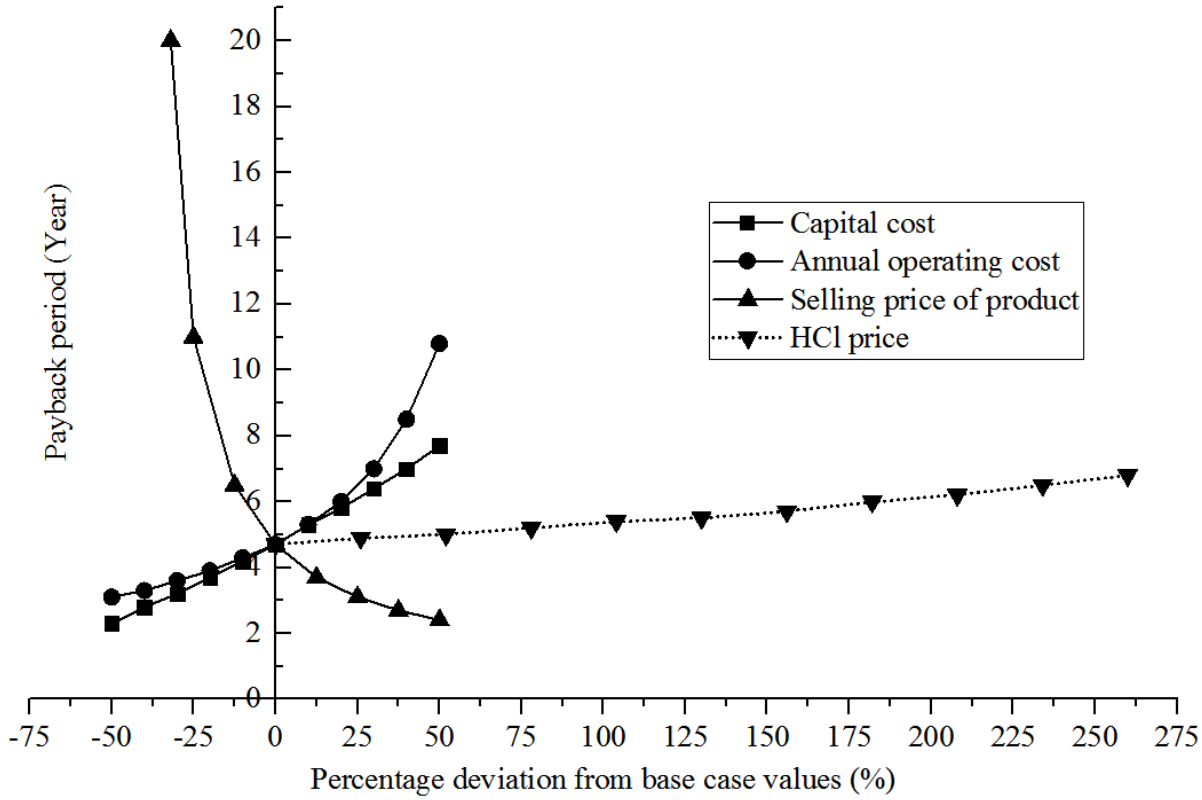
Payback period (Year)
Percentage deviation from base case values (%)
Capital cost
Annual operating cost
Selling price of product
HCl price

(c)

Figure 3.7 Sensitivity analyses of effects of capital cost, annual operating cost, the selling price of product and HCl price on NPV (a), IRR (b) and Payback Period (c) for Scenario 4.

3.4 Conclusions

This paper has performed the techno-economic analysis of four different scenarios for the selective removal of Na and Ca from a low-rank sub-bituminous coal, targeting to improve the ash fusion temperature of the leached coal to reduce its fouling propensity in the pulverized coal-fired boilers. The major conclusions achieved are as follows:

1) From the technical perspective, the use of a three-stage counter-current water leaching or a single-stage acid leaching is essential for the improvement of the ash fusion temperature above the operating temperature of the boilers. These two scenarios can reduce the mass fraction of Na_2O in ash from original 4.32 *wt%* down to 0.85 and 0.21 *wt%*, respectively. The acid leaching is also able to remove 13% calcium and 19% total ash.

2) For the recycling and treatment of wastewater, the water gain is desirable for the use of evaporator for a base case low-rank coal containing 25 *wt%* water. This is because the water in coal can be mostly squeezed out in the centrifuge. Instead, the use of RO results in a water loss accounting for maximum 251.2 kg/t coal. However, prior to the RO treatment unit, the reusing of the unsaturated water is beneficial in reducing both the water and power consumption. The water consumption drops to 41.9 and 51.8 kg/t coal for the three-stage water leaching and acid leaching process, respectively. Both are remarkably less than 85 kg-water/t coal for the black coal case. The power consumption drops to around 10.3 kWh/t coal for the three-stage water leaching process and further

down to 6.0 kWh/t in the case that acid-control leaching is adopted, which is lower than 6.3 kWh/t for the black coal.

3) For the best scenario integrating acid leaching and RO unit, its base case is economically viable. Based on a local selling price of 200 RMB for the leached coal, an NPV of 87 million RMB and IRR of 28% as well as short payback period of 4.7 years have been confirmed.

4) Sensitivity analysis indicates that the original Na content in raw coal is the most influential variable on the water and power consumption of the overall process, followed by the initial moisture content in the raw coal. For a low-rank coal containing >2150-2520 ppm Na and/or <19 *wt%* moisture, the leaching process proposed would turn economically unviable compared to the existing black coal leaching process. The influence of other three variables is rather marginal.

5) The selling price of leached coal influences the economic indexes mostly. Its 50% increase can improve the NPV and IRR from 87 million RMB and 28% (base case values) to 223 million RMB and 52%, respectively. A minimum selling price of 136 RMB/t (-32% deviation) is essential to keep both NPV and IRR positive as well as the payback period shorter than the project lifespan.

Reference

1. De Girolamo, A.; Dai, B. Q.; Wu, X.; Zhang, L., *A study of slagging and fouling: Current theory and experimental characterisation of deposits*. 2013; Vol. 4, p 2767-2773.
2. Low, F.; De Girolamo, A.; Wu, X.; Dai, B.; Zhang, L., Inhibition of lignite ash slagging and fouling upon the use of a silica-based additive in an industrial pulverised coal-fired boiler: Part 3–Partitioning of trace elements. *Fuel* **2015,** *139*, 746-756.
3. Wu, X.; Zhang, X.; Yan, K.; Chen, N.; Zhang, J.; Xu, X.; Dai, B.; Zhang, J.; Zhang, L., Ash deposition and slagging behavior of Chinese Xinjiang high-alkali coal in 3 MWth pilot-scale combustion test. *Fuel* **2016,** *181*, 1191-1202.
4. Dai, B.-Q.; Low, F.; De Girolamo, A.; Wu, X.; Zhang, L., Characteristics of ash deposits in a pulverized lignite coal-fired boiler and the mass flow of major ash-forming inorganic elements. *Energy & Fuels* **2013,** *27*, (10), 6198-6211.
5. Gräbner, M., *Industrial coal gasification technologies covering baseline and high-ash coal*. John Wiley & Sons: 2014.
6. Planning, U. S. E. P. A. O. o. A. Q.; Standards, *Compilation of air pollutant emission factors*. US Environmental Protection Agency: 1979.
7. Speight, J. G., *The chemistry and technology of coal*. CRC press: 2012.
8. Wijaya, N.; Zhang, L., A Critical Review of Coal Demineralization and Its Implication on Understanding the Speciation of Organically Bound Metals and Submicrometer Mineral Grains in Coal. *Energy & Fuels* **2011,** *25*, (1), 1-16.
9. Steel, K. M.; Patrick, J. W., The production of ultra clean coal by chemical demineralisation. *Fuel* **2001,** *80*, (14), 2019-2023.
10. Jorjani, E.; Chapi, H. G.; Khorami, M. T., Ultra clean coal production by microwave irradiation pretreatment and sequential leaching with HF followed by HNO3. *Fuel Processing Technology* **2011,** *92*, (10), 1898-1904.
11. Okuyama, N.; Komatsu, N.; Shigehisa, T.; Kaneko, T.; Tsuruya, S., Hyper-coal process to produce the ash-free coal. *Fuel Processing Technology* **2004,** *85*, (8), 947-967.
12. Wu, X.; Zhang, X.; Dai, B.; Xu, X.; Zhang, J.; Zhang, L., Ash deposition behaviours upon the combustion of low-rank coal blends in a 3 MWth pilot-scale pulverised coal-fired furnace. *Fuel Processing Technology* **2016,** *152*, 176-182.
13. Hayashi, J.-i.; Takeuchi, K.; Kusakabe, K.; Morooka, S., Removal of calcium from low rank coals by treatment with CO2 dissolved in water. *Fuel* **1991,** *70*, (10), 1181-1186.

14. Li, J.; Querol, X.; Zhuang, X.; Font, O., *Comparative Study of Coal Qualities from Three Large Coal Basins in Xinjiang, Northwest China*. 2011; p 121-122.
15. China, S. A. o. t. P. s. R. o., Division of variety and grading for coal products (GB/T 17608-2006). In Standards Press of China: 2007.
16. Prationo, W.; Zhang, J.; Abbas, H. A. A.; Wu, X.; Chen, X.; Zhang, L., Influence of External Clay and Inherent Minerals on Lignite Optical Ignition and Volatile Flame Propagation in Air-Firing and Oxy-Firing. *Industrial & Engineering Chemistry Research* **2014,** *53*, (7), 2594-2604.
17. Osada, Y.; Nakagawa, T., *Membrane science and technology*. CRC Press: 1992.
18. Wilf, M.; Schierach, M. K., Improved performance and cost reduction of RO seawater systems using UF pretreatment. *Desalination* **2001,** *135*, (1-3), 61-68.
19. Pearce, G., UF/MF pre-treatment to RO in seawater and wastewater reuse applications: a comparison of energy costs. *Desalination* **2008,** *222*, (1-3), 66-73.
20. Hosseini, T.; Haque, N.; Selomulya, C.; Zhang, L., Mineral carbonation of Victorian brown coal fly ash using regenerative ammonium chloride–Process simulation and techno-economic analysis. *Applied energy* **2016,** *175*, 54-68.
21. Shuangquan, Z., *Meihuaxue*. China University of Mining and Technology Press: 2009.
22. Yuelian, P.; Zhenping, Q.; Hong, M.; Futai, C., *Mojishu qianyan ji gongcheng yingyong*. China Textile & Apparel Press: 2009.
23. Low, F.; Zhang, L., Microwave digestion for the quantification of inorganic elements in coal and coal ash using ICP-OES. *Talanta* **2012,** *101*, 346-352.
24. Zhang, J.; Wang, Q.; Wei, Y.; Zhang, L., Numerical modeling and experimental investigation on the use of brown coal and its beneficiated semicoke for coal blending combustion in a 600 MWe utility furnace. *Energy & Fuels* **2015,** *29*, (2), 1196-1209.
25. Haque, N.; Bruckard, W.; Cuevas, J. In *A techno-economic comparison of pyrometallurgical and hydrometallurgical options for treating high-arsenic copper concentrates*, XXVI International Mineral Processing Congress, New Delhi, India, 2012; 2012.
26. Vogelsang Maschinenbau, H., Injection housing–optimising rotary lobe pumps for liquids with high solids content. *World Pumps* **2007,** *2007*, (489), 36-38.
27. http://mini.eastday.com/a/160709100113671.html?btype=index&subtype=caijing&idx=6&ishot=0

28. Gabelich, C. J., *Nonthermal technologies for salinity removal*. American Water Works Association: 2001.
29. Peters, M. S.; Timmerhaus, K. D.; West, R. E.; Timmerhaus, K.; West, R., *Plant design and economics for chemical engineers*. McGraw-Hill New York: 1968; Vol. 4.
30. Richardson, *Richardson international construction factors manual*. COST DATA ON LINE, INC: 2007.
31. Zhang, X.; Wu, X.; Xu, X.; Zhang, J.; Yan, K.; Dai, B.; Zhang, J.; Zhang, L. In *Experimental Study on Ash Melting Behavior of Xinjiang High-Alkali Coal Blended with Low-Alkali Coal During Coal Combustion*, International Symposium on Coal Combustion, 2015; Springer: 2015; pp 53-58.

Chapter 4

Multiple Cycle Leaching Using Water and Hydrochloric Acid: Experimental Investigation and Kinetic Modelling

In chapter 3, closed-loop single/multi-stage leaching flowsheets have been developed and compared comprehensively. It demonstrated that both the three-stage counter-current water leaching process and single-stage HCl acid leaching process are feasible. For both processes, the recycling of unsaturated leachate can help reduce the water and power consumption significantly. However, so far, few study was about the leaching performance using recycled leachate, not to mention the respective kinetics model, which is essential for the scale-up of the coal leaching process. In this chapter, leaching using recycled leachates (water/HCl acid) via both multi-cycle three-stage counter-current water leaching and single-stage acid leaching process were studied in detail to reveal the recyclability of leachates. To achieve this, apart from experimental investigations, a kinetic model was developed and validated for water leaching case, and an existing model can fit HCl leaching scenario well. This chapter has been reformatted from a manuscript published in ***Energy & Fuels***: **Zhou, S.**; Hosseini, T.; Zhao, J.; Zhang, X.; Wu, H.; Zhang, L. *Selective Removal of Sodium from Low-Rank Xinjiang Coal upon a Multi-Stage Counter-Current Water Leaching: Experimental Investigation and Kinetic Modelling*. ***Energy & Fuels***, 2019, 33, 3, 2142-2152.

Abstract

Coal prior leaching is an essential step for the minimisation of ash-related fouling inside a coal-fired boiler. With regard to the coal leaching process, the recyclability of the leaching reagent is critical from both cost-effectiveness and efficiency perspectives. This paper addresses the leaching kinetics of AAEMs from three low-rank Xinjiang coals using both fresh and recycled water and HCl acid, to alleviate the ash-related fouling in low-rank coal-fired boilers. Apart from once-through fresh reagent leaching, leaching using recycled leachate via three-stage counter-current water leaching processes and multi-cycle single-stage HCl acid leaching process were studied in detail to investigate their recyclabilities. Additionally, a modified shrinking core model (SCM) was developed to reveal the water-soluble Na^+ removal mechanism. Experimental results shows that, the water-soluble Na^+ removal decreases with the recycling of water, due to an increase in the Na^+ concentration in the recycled water and/or a decrease in the Na^+ content in the leached coal. The modelling approached further confirms that the removal of water-soluble Na^+ is dominated by the intra-particle diffusion of Na^+ within coal matrix. The effective diffusion coefficient of Na^+ is within the range of $0.28\text{-}3.75\times10^{-6}$ cm^2/s, which agrees with reported values in the literature. Additionally, a novel iterative calculation method integrating the modified SCM into the three-stage counter-current leaching process has been proposed to predict the Na^+ removal at each stage for each cycle. The results show that the Na^+ removal decreases exponentially with the water cycle number, with the maximum of 15 times in the counter-current process. By contrast, acid-soluble element removals can only be fitted well by a H^+ intra-particle diffusion model which considers a decreasing proton concentration in bulk acid. Consequently, a constant removal extent is obtained upon the recycling of HCl acid providing the initial H^+ concentration being same.

Keywords: Kinetic model; alkali and alkaline earth metal removal; Low-rank coal; recycling of water and HCl acid

4.1 Introduction

Electricity generation from coal-fired power stations is projected to continue to increase ~1 trillion kWh by 2040 although its share is foreseen to decline from the current 38% in the global energy matrix [1]. Use of low-rank coals for power generation becomes more attractive because of its abundant reserves and much lower price compared with black coals. For instance, 90% of the power in Victoria, Australia is generated in power stations firing the local hugely-reserved brown coal [2]. The situation is similar in Xinjiang Uyghur Autonomous Region, China [3]. However, boilers firing low-rank coals are known to suffer from severe fouling, among which the abundance of alkali and alkaline earth metals (AAEMs, sodium (Na), potassium (K), calcium (Ca) and magnesium (Mg)) is the main reason [4, 5]. It is estimated that billions dollars have to be spent annually on abating the fouling-related issues [6].

A prior leaching to remove AAEMs out of coal is the most straightforward and efficient approach to increase the fusion temperature of ash, and hence, reduce its fouling propensity [3]. To date, nearly all the coal beneficiation technologies were developed and/or tested for the high-rank coals which are rich in discrete mineral grains. None of these technologies are suitable for low-rank coal that is rich in organically bound species coal [3]. With regard to the researches on low-rank coal leaching, most of them were conducted based on the use of different fresh leaching reagents without considering their recyclability at all. The recycling is critical for a cost-effective operation of the process and in particular important for the plant location where the water is scarce, such as the Xinjiang region in China [3, 7].

For leaching kinetic modelling, Neavel et al. [8] claimed that the water-soluble Na^+ removal from Illinois coal by fresh water can be fitted by a graphical solution of a diffusion model proposed

by Crank [9]. The diffusion coefficient of Na^+ was found sensible to the leachng time even for a fixed particle size range. However, no explanation has yet been given. This model was later applied by Readett et al. [10] to the removal of water-soluble Na^+ from a different lignite. It was found that the model for smaller particle size ranges failed to correlate satisfactorily with the experimental observations. Therefore, a semi-empirical model was proposed and claimed to match the experimental results. The empirical nature of this model caused a failure of calculation on the diffusion coefficients. Moreover, these existing models always assumed that the amount of water was significantly in excess of that of coal, which is, however, instinctively different from the reality where the liquid-to-solid ratio usually remains as small as possible to minimise the water usage and loss [3]. In addition, the leaching mechanism underpinning a multi-cycle leaching processes where the spent reagent is reused has yet to be explored.

This study for the first time aims to investigate the leaching kinetics of both water-soluble Na^+ from low-rank Xinjiang coals in a multi-cycle three-stage counter-current leaching process, and acid-soluble AAEMs removal in a multi-cycle single-stage HCl leaching process. A low liquid-to-solid ratio close to industrial application is employed. Results are firstly reported from intensive experiments to assess the effect of various process parameters including coal particle size, liquid-to-solid ratio, and in particular the number of cycles for reusing the used water/HCl acid. Specific efforts are made to explore the saturation point, and hence the maximum cycle numbers of water/HCl acid, via the use of NaCl solutions/its mixture with HCl acid mimicking the recycled water/HCl acid with a high Na^+ concentration. Subsequently, effort was made to derive a modified shrinking core model (SCM) to accommodate the use of both fresh and used water. For HCl acid leaching, it can be fitted by an H^+ diffusion based model which considered a decreasing H^+ concentration in bulk leachate.

4.2 Methodology

4.2.1 Coal properties

Three Xinjiang sub-bituminous coal samples (namely Coals A, B and C hereafter) were used. Coal A and B were used for water leaching process, and Coal C for HCl acid leaching case. **Tables 4.1-4.3** list their properties with a variety of particle sizes**.** Note that, these sizes are abundant and make up the majority of the two coals here. The moisture contents of these coal samples range from 10 to 22 wt% (as-received). The ash contents of these coal samples exhibit a similar dependence on particle size, broadly the ash content deceasing with increasing coal size. However, the ash content of coal B is twice higher than that of Coal A, approximately 12 wt% in Coal B versus 6 wt% on average for Coal A. Coal C has the lowest ash content, at around 4 wt%.

The contents of AAEMs in coal samples (on the as-received coal mass basis) were quantified by inductively coupled plasma optical emission spectrometry (ICP-OES), following a previously-established standard procedure [11]. Since the water leaching process is only able to remove AAEMs that are water soluble, effort was thus first made to determine the content of water-soluble, i.e., maximum water leachable AAEMs in each coal. The raw coal was firstly crushed to a sample less than 100 mesh [12] which was then leached using fresh water (deionised water) at a liquid-to-solid ratio (on a mass basis) of 2.5 for 90 minutes. After solid and liquid separation, the residue was rinsed with fresh water to remove any possibly-remaining ions. Finally, the content of water-soluble AAEMs in the raw coal was determined via analysing the leachate by ICP-OES. For three coals, around 50-60% of the total Na are water-soluble. The Na content of Coal B is the lowest, about half of these of the other two. By contrast, the proportions of water-soluble Ca and Mg are tiny, despite the total content of Ca is very high,

reaching 10,000 ppm approximately. The K content is negligible, which agrees with the literature study [13]. A distinct correlation between AAEMs content and particle size seems to be absent.

Table 4.1 Properties of raw Xinjiang Coal A.

Particle size (mm)	0.2-0.6	0.6-1	1-4	4-8
Proximate analysis	(wt %)			
Moisture [ad]	20.24	21.05	21.35	21.94
Volatile [d]	35.33	34.56	37.12	35.07
Fixed Carbon [d]	58.41	59.48	56.65	60.71
Ash [d]	6.26	5.96	6.23	4.22
Ultimate analysis	(wt %, db)			
Carbon	70.24	71.87	71.40	73.07
Hydrogen	3.77	3.92	4.02	4.04
Oxygen	24.73	22.94	22.71	21.72
Nitrogen	0.69	0.67	0.66	0.77
Sulphur	0.57	0.60	1.21	0.40
Element content	(ppm, as-received raw coal)			
Total Na	2930	2753	3036	2919
Maximum water-soluble Na	1604	1905	1400	1562

[ad] air-dried, [d] dried basis

Table 4.2 Properties of raw Xinjiang Coal B.

Particle size (mm)	0.2-0.6	0.6-1	1-4	4-8
Proximate analysis	(wt %)			
Moisture	16.1	16.1	16.7	16.7
Volatile	27.5	29.2	28.3	29.0
Fixed Carbon	61.9	62.3	63.2	65.4
Ash	12.5	12	10.2	8.6
Ultimate analysis	(wt %, db)			
Carbon	70.3	70.9	71.1	73.6
Hydrogen	3.3	3.3	3.4	3.2
Oxygen	25.54	24.58	24.56	22.04
Nitrogen	0.61	0.72	0.69	0.76
Sulphur	0.35	0.4	0.35	0.3
Element content	(ppm, as received-raw coal)			
Total Na	1138	1324	1234	1365
Maximum water-soluble Na	602	720	727	751

Table 4.3 Properties of raw Xinjiang Coal C.

Particle size (mm)	0.2-0.6	0.6-1	1-4	4-8
Proximate analysis	(wt %)			
Moisture	11.85	12.77	10.92	12.10
Volatile	34.57	33.48	35.94	33.29
Fixed Carbon	60.54	63.06	59.90	62.96
Ash	4.89	3.46	4.16	3.75
Ultimate analysis	(wt %, db)			
Carbon	70.04	71.75	71.27	72.72
Hydrogen	3.80	3.91	4.03	4.04
Oxygen	24.98	23.12	22.89	22.06
Nitrogen	0.68	0.67	0.65	0.73
Sulphur	0.50	0.55	1.16	0.45
Element content	(ppm, as-received raw coal)	The number in parentheses means the water-soluble contents		
Na	2522 (1457)	2390 (1308)	2355 (1156)	2450 (1501)
Ca	9711 (137)	9609 (58)	11513 (192)	9695 (90)
Mg	1189 (45)	1253 (22)	1351 (50)	1296 (46)
K	62	51	46	45

4.2.2 Experimental procedure

Three sets of water leaching experiments were conducted at room temperature and atmospheric pressure, as illustrated in **Figure 4.1**. These three sets are named as, *fresh water – raw coal*, *used water – raw coal*, and *used water – leached coal*, respectively. The first set refers to the

simplest once-through single-stage fresh water leaching experiment in *panel (a)*. Briefly, 30 g of raw coal and 45 g fresh water were mixed and magnetically stirred in a glass beaker at a liquid-to-solid ratio of 1.5 (close to the practical value used in the industry [3]). For different liquid-to-solid ratios, the mass of water was adjusted proportionally while the coal mass remained unchanged. During the leaching, the leachate was sampled at intervals of 1-15 minutes. The leachate samples were then analysed using ICP-OES for quantifying the concentration of Na^+ in leachates according to a standard procedure [11]. After leaching, the resultant leachate and solid residue were separated via vacuum filtration using a filter paper with a cut-off size of 2 μm. This set of experiments were conducted to determine the optimal leaching conditions. The second set for the *used water – raw coal* is shown in *panel (b)*, aiming to determine the maximum allowable Na^+ concentration in the used water. It is expected that upon recycling the used water, the Na^+ is accumulated in the solution and Na^+ may also possibly redeposit on coal surface. Therefore, the Na^+ saturation point has to be determined to guarantee the leaching effectiveness of the used water. To start the single-stage multicycle water leaching experiment, fresh water was used in the first cycle. After filtration, the used water was used instead of fresh water for leaching in the next cycle, until the used water was inactive to remove Na^+. The last *used water – leached coal* set is designed in a batch scale to mimic the practical three-stage counter-current water leaching process shown in *panel (c)*. In this case, fresh water is firstly used to wash the raw coal for 30 minutes, yielding a leached coal, termed as Coal 1 and used water. Subsequently, the used water was applied to wash Coal 1 for another 30 minutes to attain a two-time-leached coal, as Coal 2, which was finally leached by fresh water to obtain the 3rd leached coal and 1st used water as shown in *panel (c)*. Afterwards, the 1st used water was used to wash Coal 1 for 30 minutes, obtaining 2nd used water and 2nd leached coal. Finally, the raw coal was leached by the 2nd used water to get 1st leached coal and 3rd used water.

Three sets of HCl acid leaching experiments were carried out at ambient environment, as shown in **Figure 4.2**. Apart from *panel (a)* for fresh HCl acid leaching raw coal which used as the same procedure as **Figure 4.1**(a) expect the application of acid, other two sets of experiments were carried out subsequently. Since HCl can remove both the water-soluble and HCl-soluble elements, it is firstly necessary to remove the former. As show in *panel (b)*, firstly, raw coal was leached by fresh water for approximately 5 times until no target elements can be detected in leachate. Proceeding is a fresh HCl leaching stage, where the water-leached coal was leached by fresh HCl by applying the optimal leaching conditions (fresh HCl leaching raw coal) decided beforehand. In terms of *panel (c)* for used HCl – raw coal, it is totally as same as **Figure 4.1**(b), except the using of HCl. To note, to guarantee a constant H^+ concentration in the spent HCl for each cycle, extra HCl was added after each cycle after quantifying the consumed H^+ via NaOH titration method.

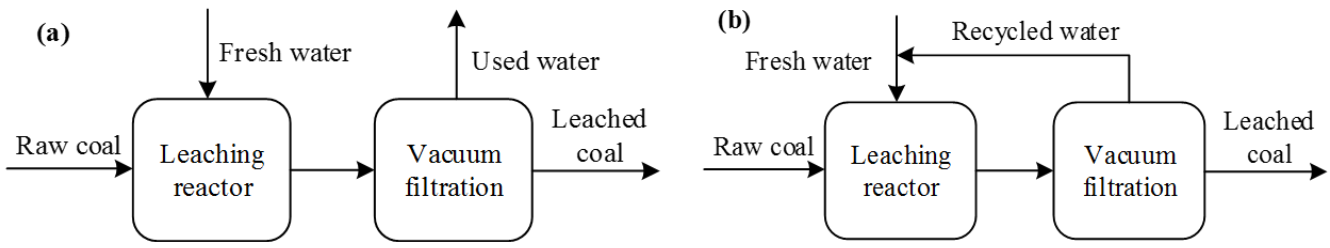

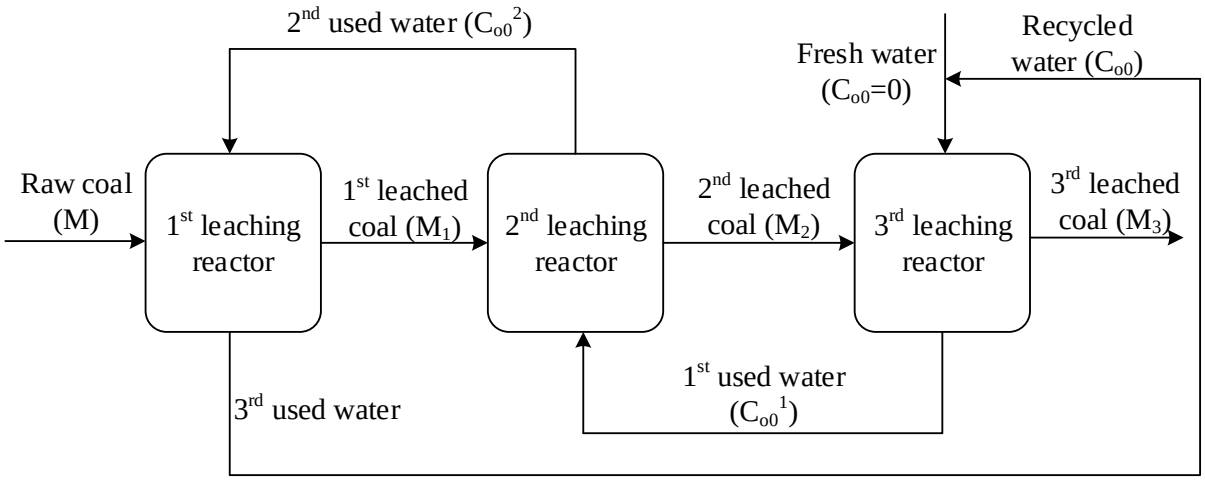

Figure 4.1 Water leaching experimental diagrams ((a): Fresh water versus raw coal, (b): Single-stage multicycle water leaching, (c): Three-stage counter-current water leaching).

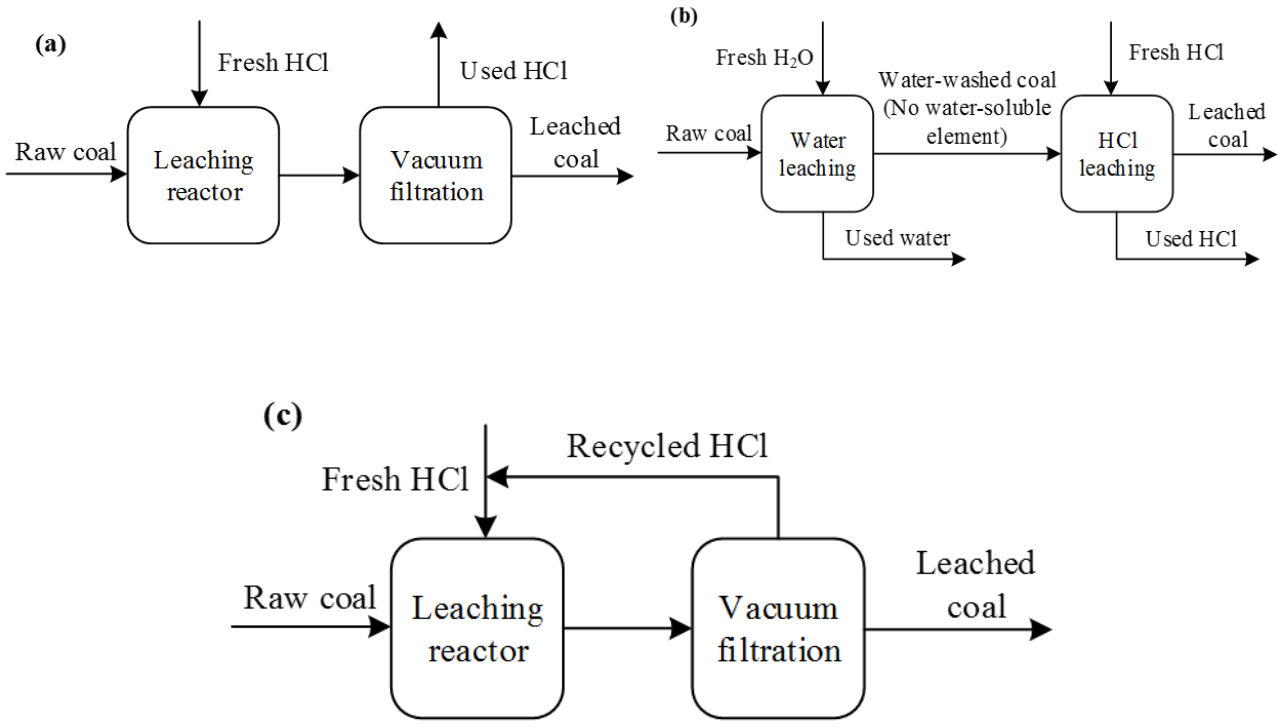

Figure 4.2 HCl acid leaching experimental diagrams ((a): Fresh HCl versus raw coal, (b): Fresh HCl versus water-leached coal (no water-soluble elements), (c): Single-stage multicycle HCl leaching).

4.2.3 Modified shrinking core model

Considering that the proposed coal leaching process is a dissolution of water-soluble Na^+ of coal, the overall rate for Na^+ removal is very likely intra-particle diffusion controlled. In light of this, the widely applied leaching model, shrinking unreacted-core model (SCM) [14] is firstly considered here. However, there are two substantial differences between the classic SCM and the required model in this study. Firstly, in the classic SCM, ash-diffusion-controlled formula is derived based on the liquid reactant diffusing inward to the unreacted shrinking core. However, the water-soluble Na removal is an opposite process which might be governed and driven by the concentration gradient of Na^+ between internal pore and the bulk water outside the coal particles. Therefore, the intra-particle resistance against the outward diffusion of Na^+ out of coal particles might be rate-limiting. Secondly, the classical SCM assumes a sharp reaction interface and an unreacted shrinking core with a constant molar density of solid reactant, so as to achieve a relationship between solid reactant conversion and the decreasing radius of the shrinking, unreacted core. However, in this study, the water-soluble Na^+ concentration remaining in the shrinking core keeps decreasing, because the water-soluble Na^+ dispersed in a whole coal particle gradually diffuses outwards during the process. This does not agree with the fundamental assumption of a constant element concentration inside the shrinking core in the classical SCM model.

In this study, the following assumptions are made to modify SCM depicted in **Figure 4.3**.

1) In the original coal particle, the water-soluble Na^+ is present in the capillary water entrapped inside the pores [10, 15, 16];

2) The overall removal of Na^+ is controlled by its outward diffusion towards the bulk water, whereas the diffusion resistance in bulk water and liquid film out of particle can be eliminated at a certain stirring speed [14];

3) All coal particles are spherical and homogenous [14];

4) The radius of particle remains constant during the leaching process. It is valid since the coal particle size distribution remains unchanged;

5) All the water-soluble Na^+ is assumed to exist in a hypothetical centre point of a single particle, and hence, its distribution is irrelevant to particle radius;

6) The flux of Na^+ is constant throughout particle radius [14].

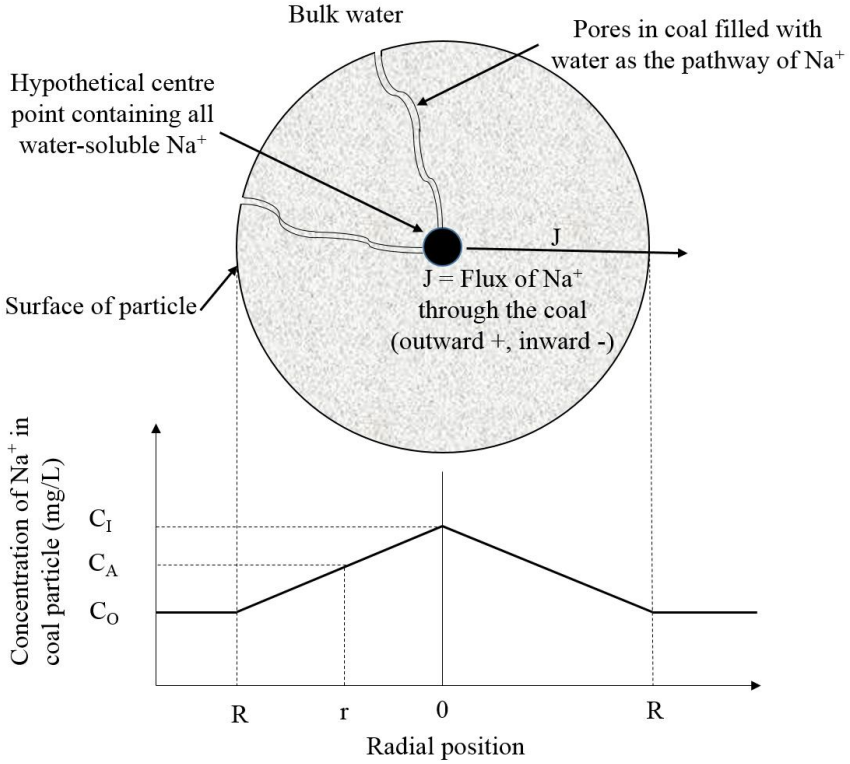

Figure 4.3 Diagram of a reacting particle when intra-particle diffusion of Na^+ is the controlling resistance.

The modified SCM derivation block diagram is shown in **Figure 4.4**. In brief, based on the above assumptions and specific to one single coal particle, the Na^+ mass change in bulk water can be expressed by the classic formula of flux and Fick's first diffusion law. Upon a unit conversion and integration in terms of time, a virgin model formula including an unknown parameter C_I can be derived. Afterwards, C_I is expressed via Na^+ mass conservation, so as to obtain the final model equation. Aside from the single-stage fresh-water leaching, this model is further combined with the Na^+ mass balance in each stage and overall process and applied into the three-stage counter-current process, in order to predict the Na^+ removal in each cycle and the recyclability of water. **Figure 4.5** illustrates the derivation diagram for the three-stage process. According to **Figure 4.1** (c) and **Figure 4.5**, two Na^+ mass balance equations including only two unknown variables, the Na^+ removal extents in 2^{nd} and 3^{rd} stage respectively, can be finally derived and solved. Furthermore, by plugging these two values into the model, the Na^+ removal in the 1^{st} stage can be acquired easily. Finally, the Na^+ removal in each cycle can be calculated via an iterative calculation. The detailed derivation is shown below.

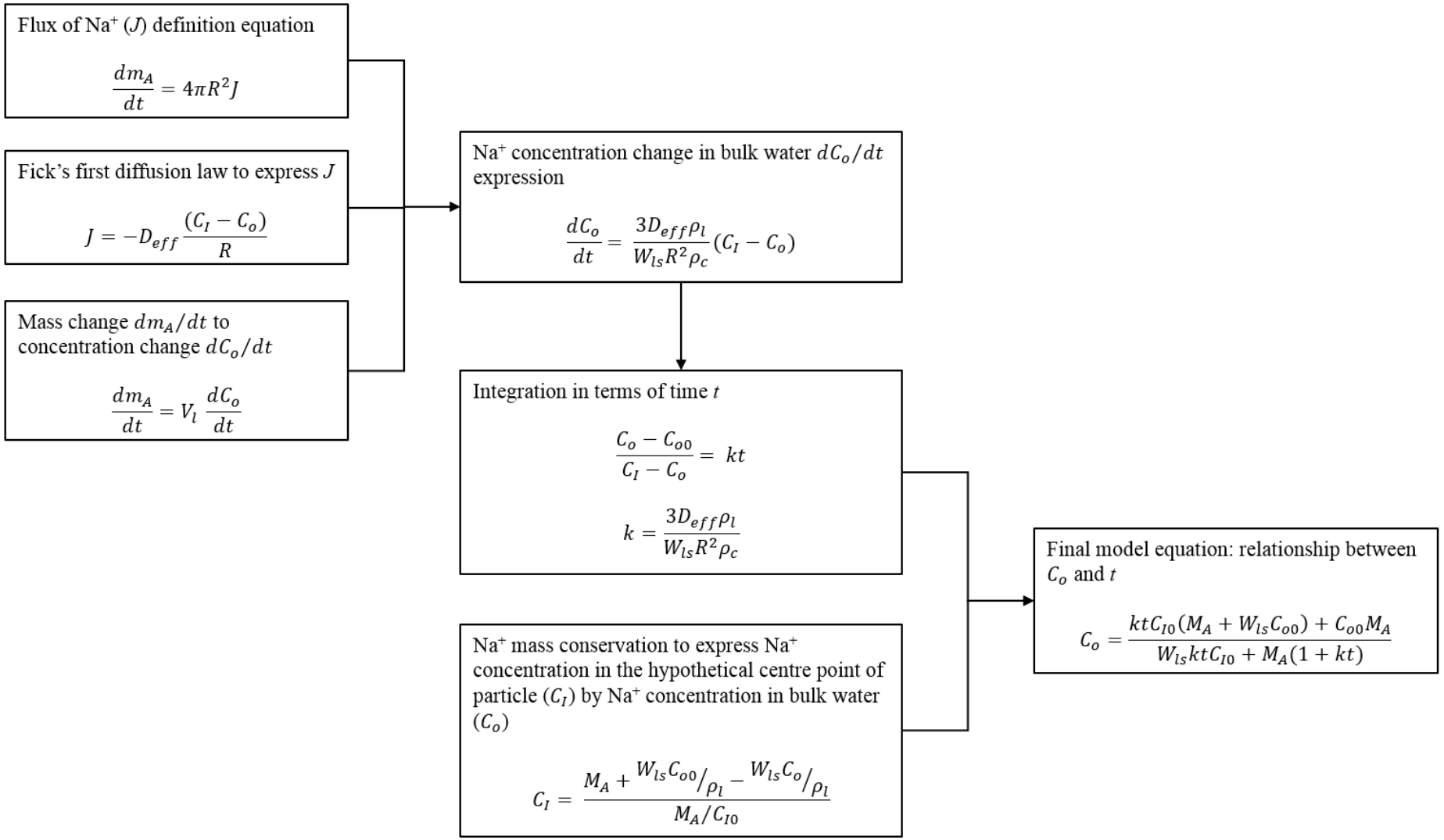

Figure 4.4 Modified SCM derivation block diagram.

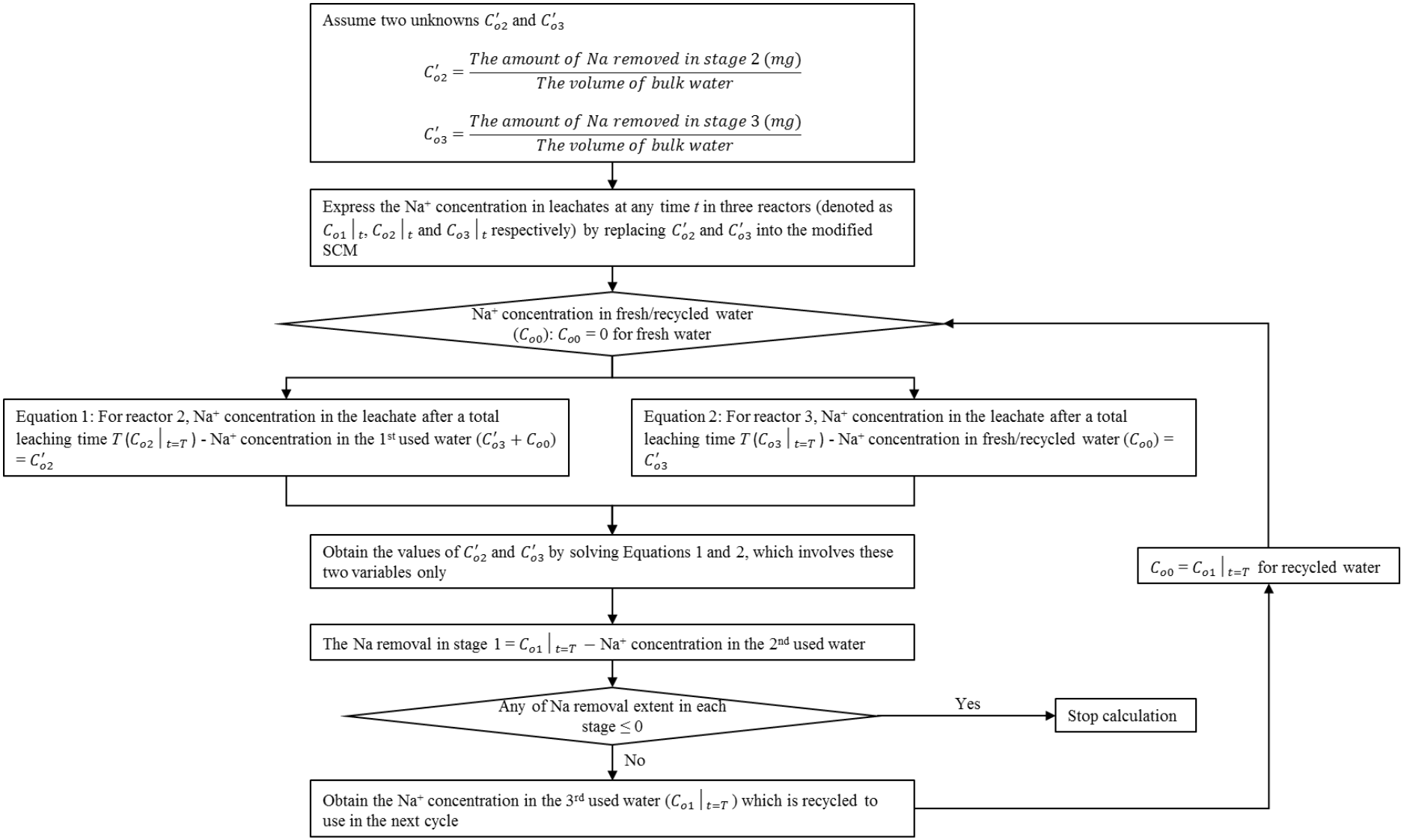

Figure 4.5 Three-stage counter-current process model derivation block diagram.

Assume that m_A is the mass of Na^+ in bulk water, the mass change of Na^+ in bulk water can be expressed by **Equation (1)** based on a single coal particle, where *J* is the flux of Na^+ through the exterior surface of each particle (mg/(s· cm^2)) [14].

$$\frac{dm_A}{dt} = 4\pi R^2 J \quad (1)$$

where *t* is the leaching time (s), and *R* is the radius of coal particle (cm).

As per the assumptions No 5 and No 6, *J* can be expressed by **Equation (2)** according to Fick's first diffusion law [14].

$$J = -D_{eff}\frac{(C_I - C_o)}{R} \times 1000 \quad (2)$$

where D_{eff} is the effective diffusion coefficient of Na^+ in coal particles (cm^2/s), C_I and C_o are the Na^+ concentration in the hypothetical centre point (mg/L) and in bulk water (mg/L) at any time *t*, respectively. Same as the derivation of the original SCM, the diffusion distance is simplified as *R* without the consideration of the tortuosity of coal particles. Combining **Equations (1-2)**, **Equation (3)** is obtained.

$$\frac{dm_A}{dt} = -4\pi R^2 D_{eff}\frac{(C_I - C_o)}{R} \times 1000 \quad (3)$$

The mass change dm_A/dt is converted to concentration change of Na^+ in bulk water as shown by **Equations (4-5)**.

$$\frac{dm_A}{dt} = V_l \frac{dC_o}{dt} \tag{4}$$

$$V_l = W_{ls} \frac{\frac{4}{3}\pi R^3 \rho_c}{\rho_l} \times 1000 \tag{5}$$

where V_l is the volume of bulk water corresponding to a single coal particle (L), W_{ls} is liquid-to-solid mass ratio, and ρ_c and ρ_l are the density of coal particle and water (kg/L), respectively. Substituting **Equations (4-5)** into **(3)**, we have

$$\frac{dC_o}{dt} = \frac{3D_{eff}\rho_l}{W_{ls}R^2\rho_c}(C_I\text{-}C_o) \tag{6}$$

Through the integration of **Equation (6)** with respect to *t*, and based on the boundary conditions of C_o=C_{o0} at *t*=0 and C_o=C_o at *t*, we can yield

$$\frac{C_o\text{-}C_{o0}}{C_I\text{-}C_o} = \frac{3D_{eff}\rho_l}{W_{ls}R^2\rho_c} t \tag{7}$$

where C_{o0} is the initial Na^+ concentration in bulk water (mg/L), which is zero for a fresh water whilst not zero for a recycled/used water. Upon the combination of all the constants in the right-

hand side of **Equation (7)** as a rate constant *k* (**Equation (8)**), **Equation (9)** is further established.

$$k = \frac{3D_{eff}\rho_l}{W_{ls}R^2\rho_c} \quad (8)$$

$$\frac{C_o\text{-}C_{o0}}{C_I\text{-}C_o} = kt \quad (9)$$

According to the conservation of Na^+ mass, C_I can be expressed as **Equation (10)**.

$$C_I = \frac{M + {W_{ls}C_{o0}}/{\rho_l} - {W_{ls}C_o}/{\rho_l}}{V_I} \quad (10)$$

$$V_I = \frac{M}{C_{I0}} \quad (11)$$

where M is the maximum water-soluble Na^+ content in the raw coal (mg/kg-coal), V_I is the volume of accessible pores of coal particles filled by water (L/kg-coal), which is assumed constant during water leaching, and C_{I0} is the maximum Na^+ concentration in the water contained in a coal particle (mg/L),

Substituting **Equations (10-11)** and ρ_l =1 kg/L for water into **Equation (9)**,

$$\frac{C_o\text{-}C_{o0}}{\frac{M + W_{ls}C_{o0}\text{-}W_{ls}C_o}{M/C_{I0}}\text{-}C_o} = kt \quad (12)$$

Finally, the Na^+ concentration in bulk water (C_o) can be expressed as **Equation (13)** by rearranging **Equation (12)**.

$$C_o = \frac{ktC_{I0}(M + W_{ls}C_{oo}) + C_{oo}M}{W_{ls}ktC_{I0} + M(1 + kt)} \quad (13)$$

The Na^+ removal extent *X* is defined as

$$X = \frac{Na^+ \text{ concentration in leachate* } W_{ls}}{\text{Maximum water-soluble Na content of coal}} \times 100\%$$

$$X = \frac{(C_o\text{-}C_{oo})W_{ls}}{M} \times 100\% \quad (14)$$

For the three-stage counter-current water leaching process shown in **Figure 4.1**(c), the values of M and C_{oo} in **Equation (13)** vary from one stage to another. The value of M for maximum water-soluble Na^+ decreases gradually from the initial value of Na^+ content for raw coal at stage 1 to the lowest value for the 2nd leached coal at stage 3. In contrast, the value of C_{oo} for the concentration of Na^+ in water increases gradually from zero in fresh water (1st cycle) at stage 3 to the highest value in the 2nd used water at stage 1. It is impossible to use **Equation (13)** directly to predict the Na^+ concentration in the leachate of stage 1, due to the lack of Na^+ conversion in the other two stages and thus an unknown C_{oo} in this equation. Similarly, if **Equation (13)** is used for a back calculation from stage 3 first, an unknown M exists and it does not allow for a completion of the calculation either.

To address these concerns, the following derivations are further conducted in regard to the three-stage counter-current water leaching, as illustrated in **Figure 4.5**.

According to **Figure 4.1**(c), at stage 1 (1st leaching reactor), the Na^+ concentration in the 2nd used water, denoted as C_{o0}^2, can be expressed by **Equation (15)**.

$$C_{o0}^2 = C_{o2}^{'} + C_{o3}^{'} + C_{o0} \quad (15)$$

where $C_{o2}^{'}$ and $C_{o3}^{'}$ are the amounts of Na^+ removed in stage 2 and 3 divided by the volume of bulk water, respectively (mg/L), and C_{o0} is the original Na^+ concentration in recycled water ($C_{o0} = 0$ for fresh water).

Replacing C_{o0} in **Equation (13)** with C_{o0}^2, **Equation (16)** is obtained, which involves two variables, $C_{o2}^{'}$ and $C_{o3}^{'}$ (C_{o0}=0 for first cycle using fresh water).

$$C_{o1}\big|_t = \frac{ktC_{I0}(M + W_{ls}C_{o0}^2) + C_{o0}^2 M}{W_{ls}ktC_{I0} + M(1 + kt)} \quad (16)$$

where $C_{o1}\big|_t$ is the Na^+ concentration in leachate at time *t* in reactor 1 (mg/L) and *k* can be determined in single stage. Assigning symbol *T* for the total leaching time in one reactor, the Na content of 1st leached coal, denoted as M_1 (mg/kg-coal), is then equal to the difference

between the Na^+ content in raw coal (M) and removed Na^+ in reactor 1 after leaching time *T*, shown in **Equation (17)**.

$$M_1 = M\text{-}W_{ls}\left(C_{o1}\big|_{t=T}\text{-}C_{oo}^{2}\right) \tag{17}$$

For stage 2, the Na^+ concentration in the 1st used water is defined as C_{oo}^{1}.

$$C_{oo}^{1} = C_{o3}^{'} + C_{oo} \tag{18}$$

Similar to stage 1, after substituting C_{oo} in **Equation (13)** by C_{oo}^{1}, we obtain **Equation (19)**.

$$C_{o2}\big|_{t} = \frac{ktC_{I0}(M_1 + W_{ls}C_{oo}^{1}) + C_{oo}^{1}M}{W_{ls}ktC_{I0} + M(1+kt)} \tag{19}$$

where $C_{o2}\big|_{t}$ is the Na^+ concentration in leachate at time *t* in reactor 2 (mg/L). Meanwhile the Na^+ content in the 2nd leached coal, M_2 (mg/kg-coal), can be expressed by **Equation (20)**.

$$M_2 = M\text{-}W_{ls}\left(C_{o1}\big|_{t=T}\text{-}C_{oo}^{2}\right)\text{-}W_{ls}\left(C_{o2}\big|_{t=T}\text{-}C_{oo}^{1}\right) \tag{20}$$

After leaching for a total time of *T* in reactor 2, the value of C'_{o2} in **Equation (15)** is equal to the difference between the Na^+ concentration in the leachate ($C_{o2}\big|_{t=T}$) and the value in the 1st used water (C^1_{o0}), shown in **Equation (21)**.

$$C_{o2}\big|_{t=T} - C^1_{o0} = C'_{o2} \tag{21}$$

Similar to stages 1 and 2, we obtain the equations for stage 3 as follows.

$$C_{o3}\big|_{t} = \frac{ktC_{I0}(M_2 + W_{ls}C_{o0}) + C_{o0}M}{W_{ls}ktC_{I0} + M(1+kt)} \tag{22}$$

where $C_{o3}\big|_{t}$ is the Na^+ concentration in leachate at time *t* in reactor 3 (mg/L).

Similar to **Equation (21)**, **Equation (23)** can be obtained.

$$C_{o3}\big|_{t=T} - C_{o0} = C'_{o3} \tag{23}$$

At the first cycle when the fresh water is used in stage 3, the value of C_{o0} is zero. There are thus only two variables C'_{o2} and C'_{o3} involved in **Equations (21)** and **(23)**. After obtaining the values of C'_{o2} and C'_{o3} by solving **Equations (21)** and **(23)**, the Na^+ removed in stage 1, C'_{o1} can be calculated by **Equation (24)**.

$$C'_{o1} = C_{o1}\big|_{t=T} - C^2_{o0} \quad (24)$$

Based on **Equation (13)**, the Na^+ removal percentage at each stage at any time can be finally attained.

The Na^+ removal extent in the following cycles can be obtained by an iterative calculation. As shown in **Figure 4.1**(c), in the second cycle, the Na^+ concentration of the recycled water back to stage 3 (C_{o0}) is exactly the same as the value of the 3rd used water after a total leaching time T ($C_{o1}\big|_{t=T}$) in the first cycle. Thus, the Na^+ removal extent in the second cycle can be obtained by repeating the above calculation and substituting the value of C_{o0} (C_{o0} =0 in first cycle) with $C_{o1}\big|_{t=T}$. Finally, the relationship between the Na^+ removal extent and cycle number can be obtained by an iterative calculation.

4.3 Experimental results and discussion

Experiments were repeated for at least three times per run. A satisfactory accuracy has been confirmed, as evident in **Figure 4.6** which bears a standard deviation of around 0.5% only.

4.3.1 Fresh water leaching raw coal

4.3.1.1 Effect of stirring speed

Figure 4.6 demonstrates the effect of stirring speed on the water-soluble Na^+ removal extent after a leaching duration of 90 minutes, for the coarsest coal particle size of 4-8 mm and a liquid-to-solid ratio of 2.5. Note that, coal A was used hereafter, otherwise specified. Clearly,

the Na removal extent increases marginally with the initial increase in the stirring speed and reaches a plateau in excess of 300 rpm. This can be contributed to the elimination of liquid film layer outside of particles and external diffusion resistance [17, 18]. However, a further rise on the stirring rate to 350 rpm results in a decrease in the Na removal down to the same level as that achieved at 100 rpm. It is believed that the coal particles may rotate with the liquid water synchronously, which in turn lead to the regeneration of the negative influence of external diffusion and liquid film outside the coal particles [19]. Therefore, a stirring speed of 300 rpm was employed for the remaining experiments in this study.

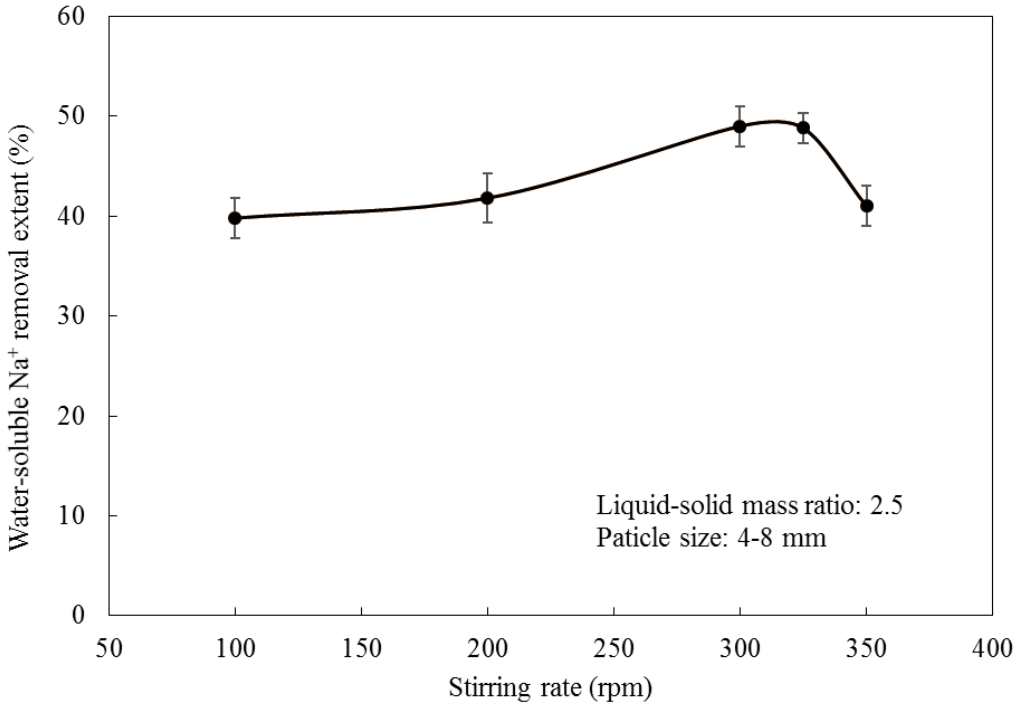

Figure 4.6 Effect of stirring rate on the water-soluble Na^+ removal extent.

4.3.1.2 Effect of liquid-to-solid ratio

Figure 4.7 illustrates the effect of liquid-to-solid ratio on the removal extent of Na^+ from two extreme particle size ranges, the smallest size bin of 0.2-0.6 mm and the coarsest one of 4-8 mm in *panels (a)* and *(b)*, respectively. For the smallest size of 0.2-0.6 mm (*panel (a)*), the Na^+

removal extent remains constant across the three different ratios and levels off rapidly in around 5 min. It suggests that there is a negligible external diffusion resistance whereas the intra-particle diffusion resistance may exist [17, 20]. In contrast, the Na^+ removal extent for the coarsest size of 4-8 mm experiences a remarkable rise when the liquid-to-solid ratio increases from 1.25 to 1.5. Upon a further increase in the liquid-to-solid ratio to 2.5, there is however no change on the removal of Na^+. This is a clear indicator of the existence of an external diffusion at the lowest liquid-to-solid ratio in the case of the coarsest coal size, which cannot be eliminated unless the liquid-to-solid ratio reaches 1.5 or above. This is different from the smallest coal size and shall be attributed to the smaller contact area from the coarse coal particles. Since the coal leached in reality is a mixture of various sizes, a liquid-to-solid ratio of 1.5 has been chosen hereafter, which is noted to be considerably lower than that (reported to be 2.8 [3]) for black coal leaching process.

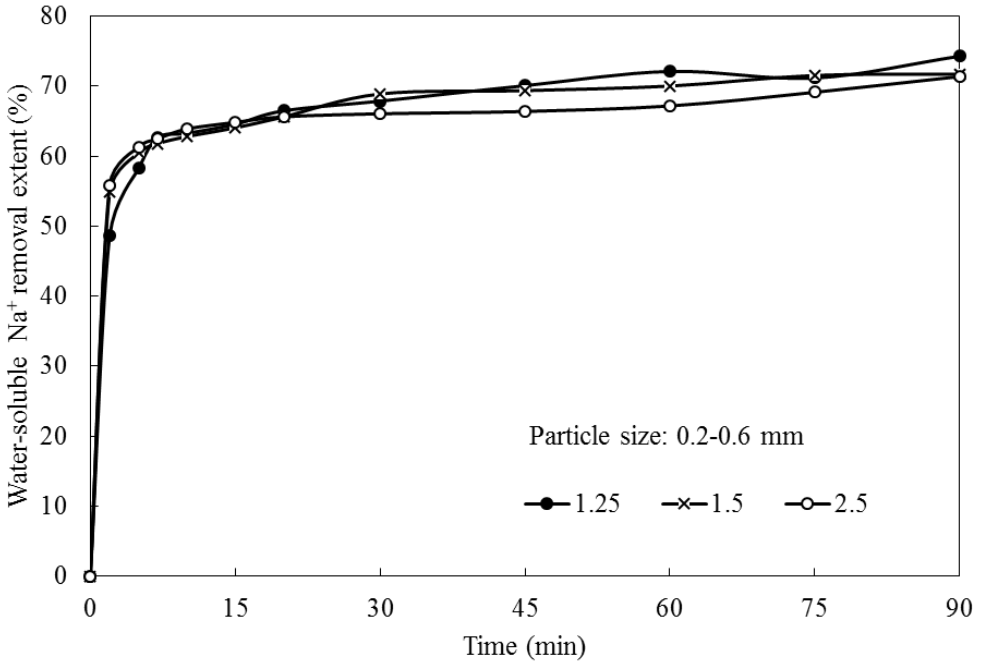

(a)

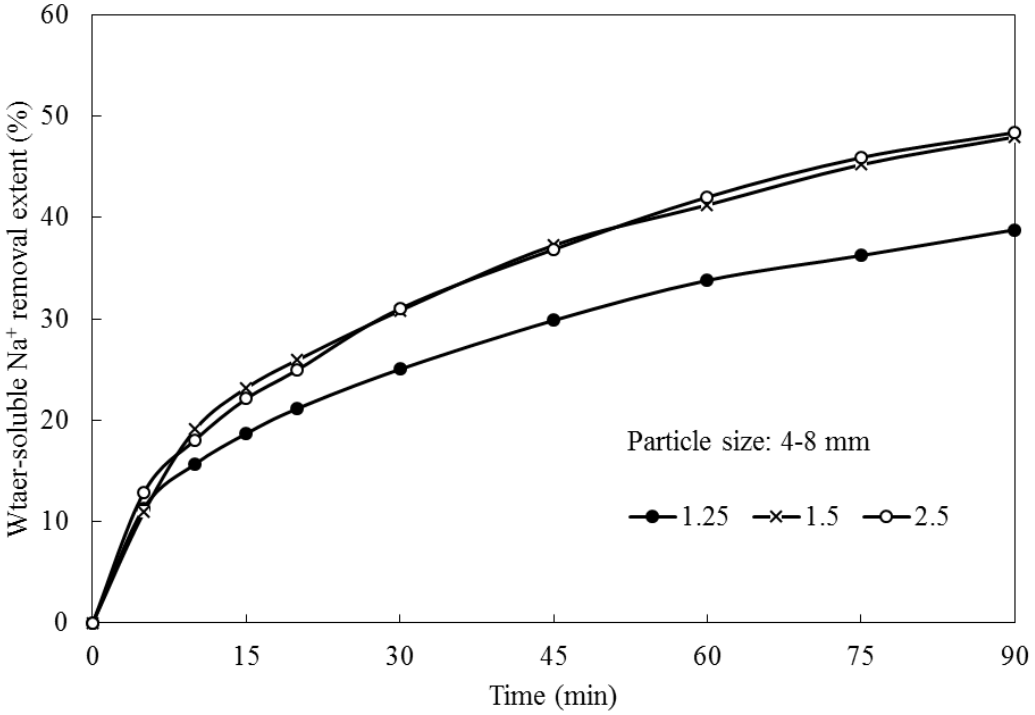

(b)

Figure 4.7 Effect of liquid-to-solid mass ratio on water-soluble Na^+ removal extent for coal particles of 0.2-0.6 mm (a) and 4-8 mm (b).

4.3.1.3 Effect of coal particle size

Figure 4.8 shows the removal extent of Na^+ as a function of coal particle size at optimised conditions (liquid-to-solid ratio: 1.5, stirring speed: 300 rpm). Clearly, the Na^+ removal extent decreases quickly with increasing coal particle size. For the smallest coal particles (0.2-0.6 mm), the Na^+ removal soars up to 60% in the first five minutes and then only increases slowly to 70% within the subsequent 25 minutes. For the two medium-sized coal samples, the Na^+ removal extent increases much slower, approaching the final Na removal extent of 70% in a considerably longer duration of ~90 minutes. For the largest coal particles, leaching is the slowest and time-consuming, resulting in a Na^+ removal extent of only 45% after 90 min

leaching. Clearly, intra-particle diffusion plays an increasingly important role in Na^+ removal from coal particles as coal particle size increases.

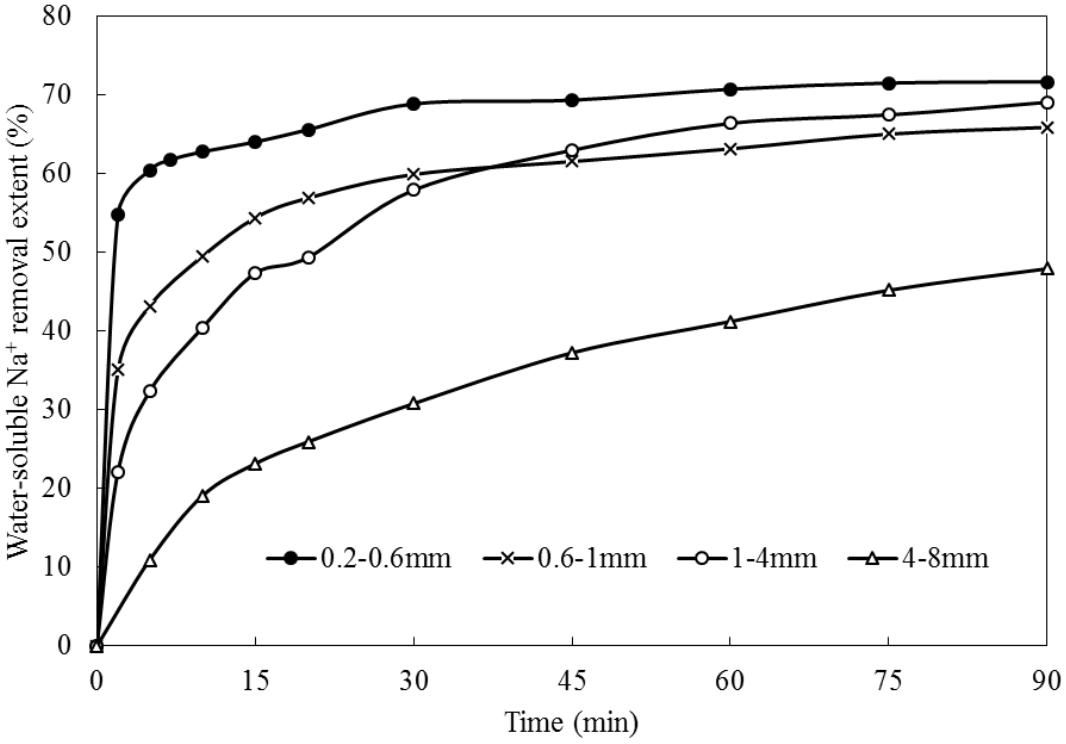

Figure 4.8 Effect of coal particle size on water-soluble Na^+ removal.

4.3.2 Used/Recycled water leaching raw coal

Following the experiments on the leaching of raw coal by fresh water, Coal B was selected for experiments in the second scenario shown in **Figure 4.1**(b) to assess the Na^+ removal extent from raw coal upon the reuse of spent water.

The change of Na^+ removal efficiency upon using the repeatedly-recycled water is presented in **Figure 4.9**. It is clear that the Na^+ removal extent declines steadily with the increasing cycle number of water. This shall be due to a continuous increase in the Na^+ concentration dissolved in the recycled water, as evident for the concentrations of the major ions for the 4^{th} recycled

water in **Table 4.4**. It results in a gradual decrease on the diffusion driving force. More interestingly, for the 2nd to 4th cycle where recycled water was used, the first five minutes always witnesses a rapid rise in the Na^+ removal extent, which then slows down and levels off gradually from five minutes onwards. This indicates that the dissolved Na^+ in the leachate can quickly reach an equilibrium with those remaining in the coal particles, thereby hindering the further outward diffusion of Na^+.

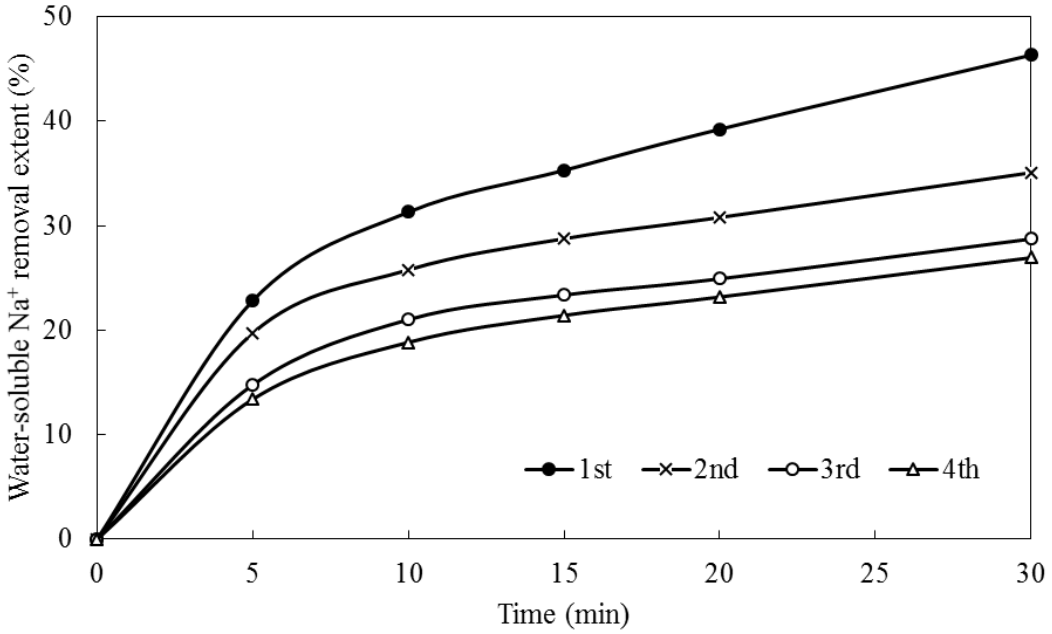

Figure 4.9 Water-soluble Na^+ removal extent change upon the recycling of used water leaching of raw coal.

Table 4.4 Concentration of main ions in the used water after four cycles.

Ions (ppm)	Cl^-	Na^+	SO_4^{2-}	Ca^{2+}	Mg^{2+}	K^+
Value	0.0448	0.0450	0.0126	0.0073	0.0044	0.0002

Based on **Table 4.4**, it is obvious that the content of Na^+ is almost equivalent to that of Cl^- (the most abundant anion) on a molar basis. It is thus inferable that almost all of the dissolved Na^+

shall be associated with Cl^-, which is in line with previous reports [8, 10]. In light of this, the pure NaCl solutions with different concentrations were used to reveal the saturation or the turning point by which the recycled water losses its leaching capability of Na^+. The use of pure NaCl solution rather than the recycled water is due to the fact that the concentration of Na^+ within it increases very slowly. As shown in **Table 4.4**, the Na^+ content only increases to 0.045 mol/L after four times recycle, which is far below the theoretical solubility for NaCl in water, 6.14 mol/L [21]. It was also assumed that the other elements including Ca^{2+} and SO_4^{2-} found in the recycled water in **Table 4.4** played little role on the removal of Na^+. These ions were speculated to dissolve in parallel with Na^+ into water. The raw coal sizing of 1-4 mm was used for the test here, and the results achieved are depicted in **Figure 4.10**.

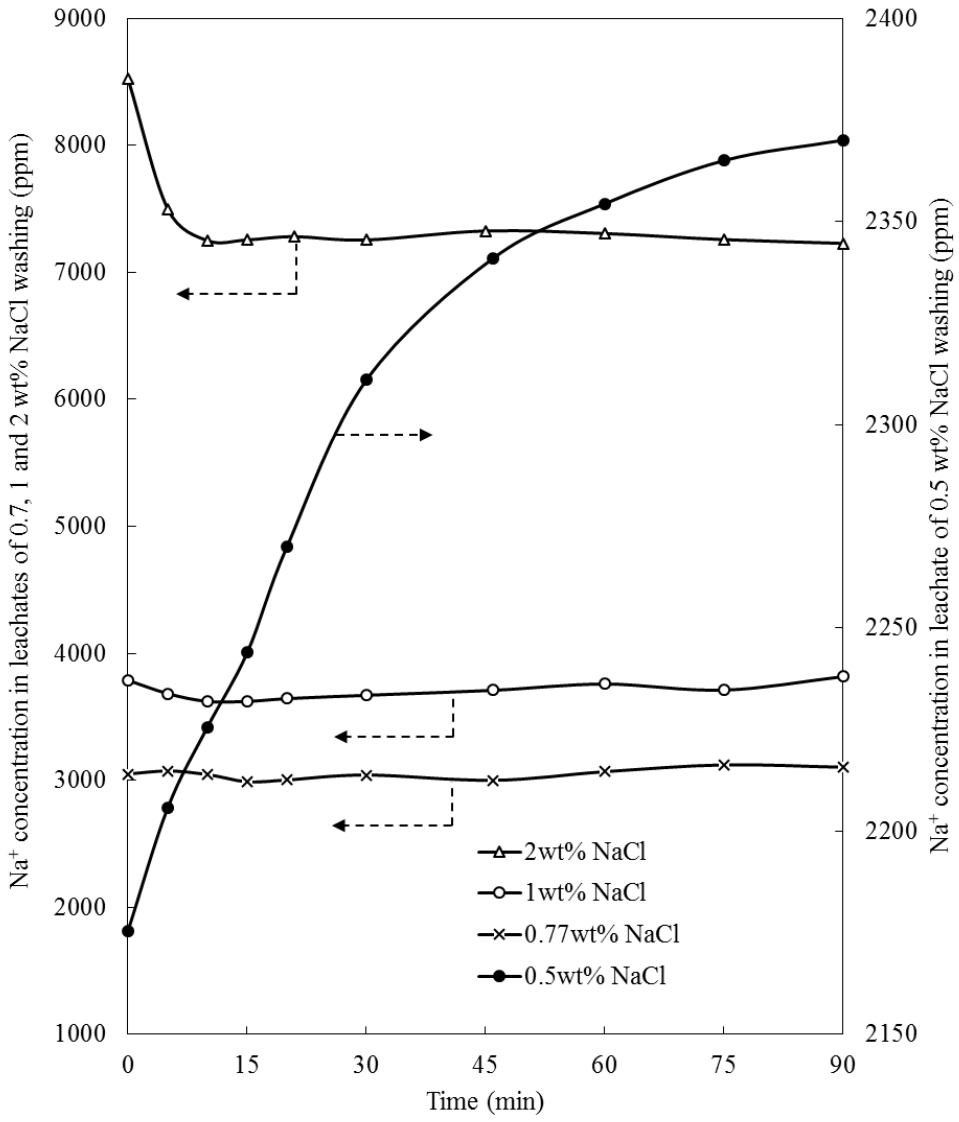

Figure 4.10 Na^+ concentration in leachates change upon leaching time in different NaCl solutions.

As shown in **Figure 4.10**, the Na^+ in the leachate keeps increasing over time when the coal is leached by the 0.5 wt% NaCl solution, suggestive of an unsaturation state for this solution. Instead, the concentration of Na^+ in the leachate remains unchanged when the coal is leached by 0.77 wt% NaCl. However, when the coal is leached by the two higher concentrations, the original Na^+ in the leachate is quickly absorbed on the coal surface in less than 10 minutes. After it, a Na^+ concentration equilibrium inside and outside coal particles is achieved, leading

to an unchanged concentration of Na^+ in the leachate. Clearly, the maximum allowable Na^+ concentration in the recycled water shall be around the value of 0.77 wt% NaCl solution (~3,000 ppm), beyond which the leaching capability of the leachate will be lost, due to the reverse deposition of Na^+ on the coal surface. Such a saturation point is far below the solubility of NaCl in water, 359 g/L (~36 wt%) at room temperature [21].

4.3.3 Three-stage counter-current leaching

Effort was further made to explore the ultimate three-stage, counter-current water leaching process in which the used water encounters the leached coal. The results are plotted in **Figure 4.11**. In agreement with the results shown in above section, the used water still has the capability to remove Na^+ even from the leached coal. In terms of the Na^+ removal extent, it reaches around 51% in stage 1 where the raw coal encountered the 'dirtiest' used water, 22% in stage 2 where the less leached coal encountered the 'dirtier' used water, and finally 15% in stage 3 where the intensively leached coal further encountered fresh water. Such a decrease reflects a continuously reducing driving force which is the Na^+ concentration difference between the inside and outside of coal particles.

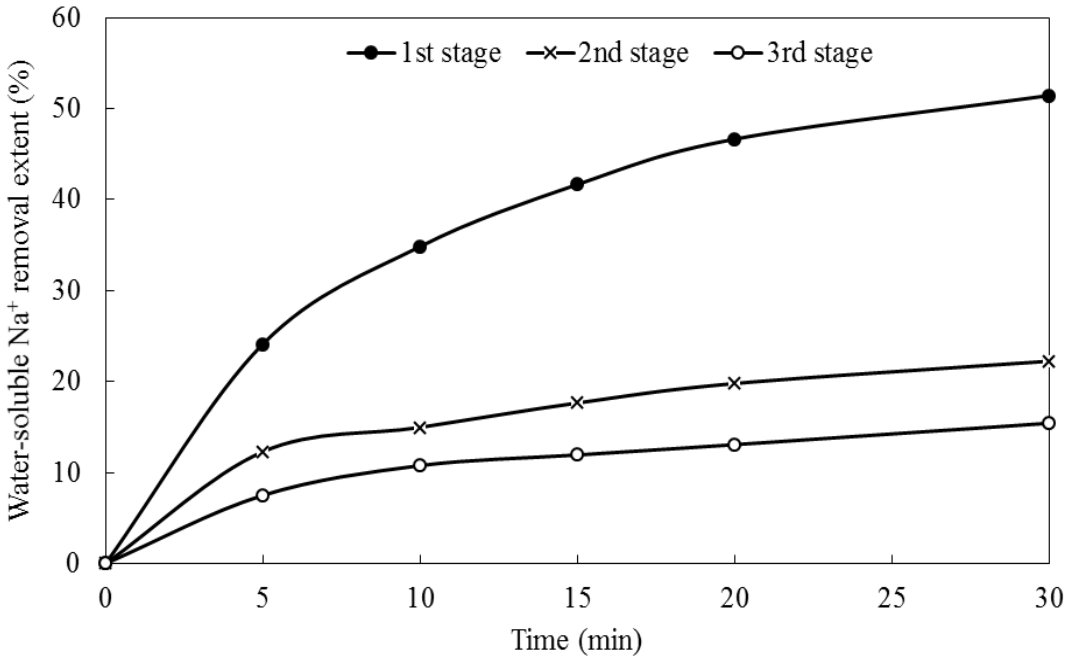

Figure 4.11 Experimental water-soluble Na^+ removal extent in each stage.

4.3.4 Fresh HCl acid leaching raw coal

4.3.4.1 Effect of leaching time

Figure 4.12 illustrates the leaching kinetics of the three elements (Na, Ca & Mg) from a raw coal particle of 1-4 mm under a liquid-to-solid ratio of 1.5 via 0.7 M fresh HCl acid. Coal C was used throughout the HCl leaching. The three elements show an almost same leaching performance, with nearly 80% removed out of coal in 90 min in a gradual increase rate. It is similar to the leaching of water-soluble Na^+ from the same particle size (**Figure 4.8**) and the application of HCl acid fails to shorten the leaching time. This suggests an intra-particle diffusion control for the three elements.

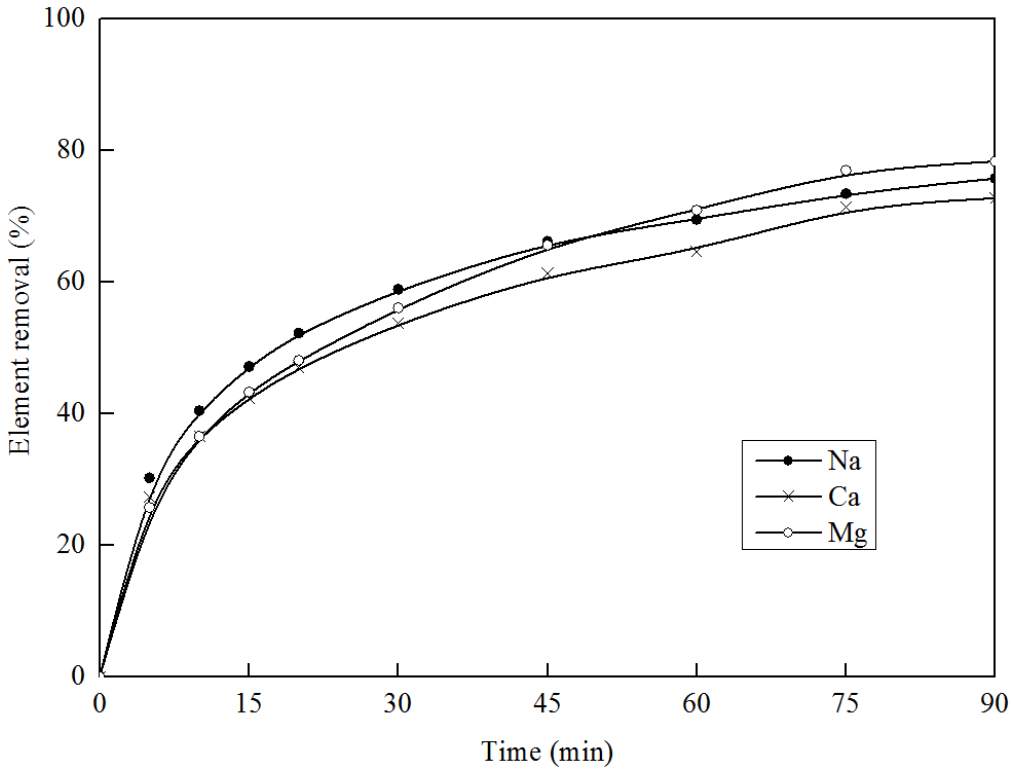

Figure 4.12 Leaching kinetics of Na, Ca & Mg by fresh HCl from raw coal.

4.3.4.2 Effect of HCl acid concentration

Figure 4.13 demonstrates the effect of HCl concentration on the removal extents of Na, Ca and Mg after a leaching duration of 30 min, for coal particle size of 1-4 mm and a liquid-to-solid ratio of 1.5. An around 15% growth of Na removal is observed with an increase in the HCl concentration from 0.1 to 0.4 M. Afterwards, no further Na can be removed even at a higher HCl concentration. A similar relationship can be found for Ca and Mg, despite the stable point being 0.7 M especially for Ca whose removal experiences a relatively large increase from 0.4 to 0.7 M. It is likely to suggest that the acid-soluble element removal might be dominated by intra-particle diffusion of proton or chemical reaction which can be boosted by the rise of acid concentration. And the higher HCl concentration for Ca and Mg could be attributed to their higher contents in raw coal as shown in **Table 4.3**. 0.7 M was hence employed for the remaining experiments to attain the highest element removals.

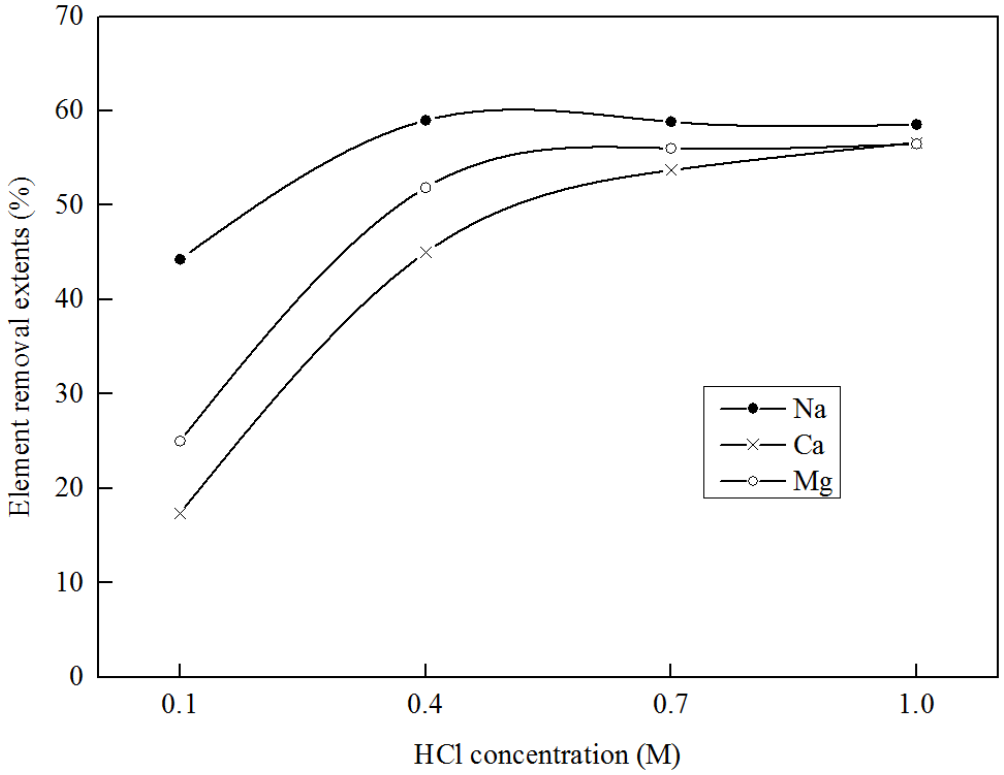

Figure 4.13 Effect of HCl concentration.

4.3.5 Fresh HCl leaching water-leached coal

The HCl-soluble element removal efficiency by fresh 0.7 M HCl (**Figure 2**(b)) is plotted in **Figure 4.14**. To note, the removal extent was calculated based on the content of HCl-soluble elements. Interesting, the removal rate of Na is almost double than these of Ca and Mg which are almost same. This might be attributed to their different modes of occurrence in coal [22]. The HCl-soluble Na mainly exists as ion-exchangeable cations associated with oxygen-containing sites, such as carboxylic acid, which can be accessed easily. By contrast, Ca and Mg occur in fine minerals primarily which are dispersed deeply in coal matrix, resulting in them being harder to be reached by acid compared to Na. Slower removal rates of Ca and Mg can thus be expected.

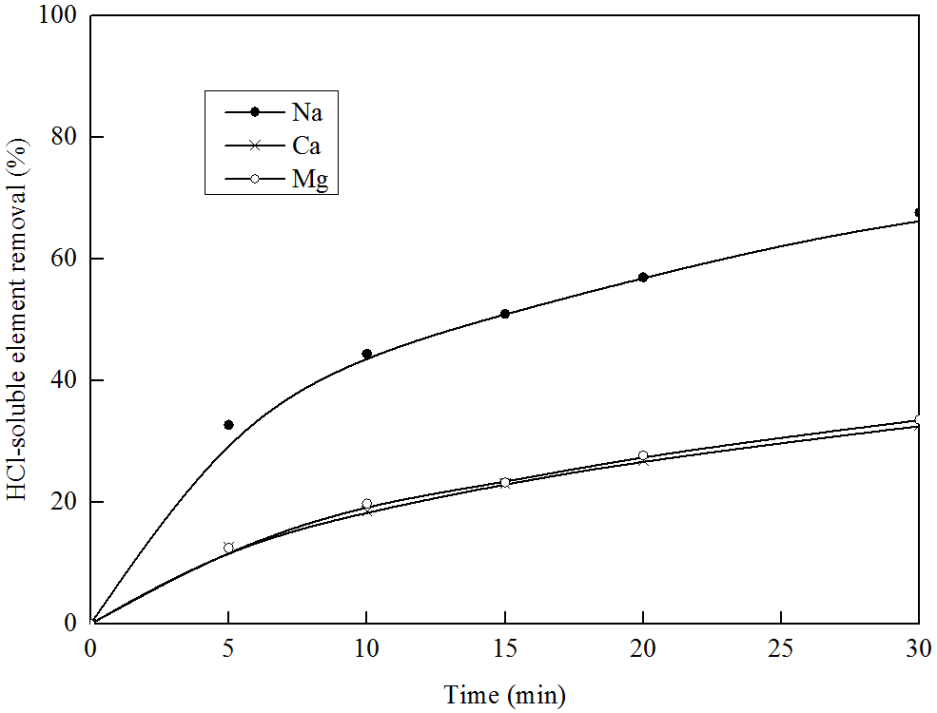

Figure 4.14 HCl-soluble element removal vs leaching time by fresh HCl (0.7 M).

4.3.6 Used/Recycled HCl leaching raw coal

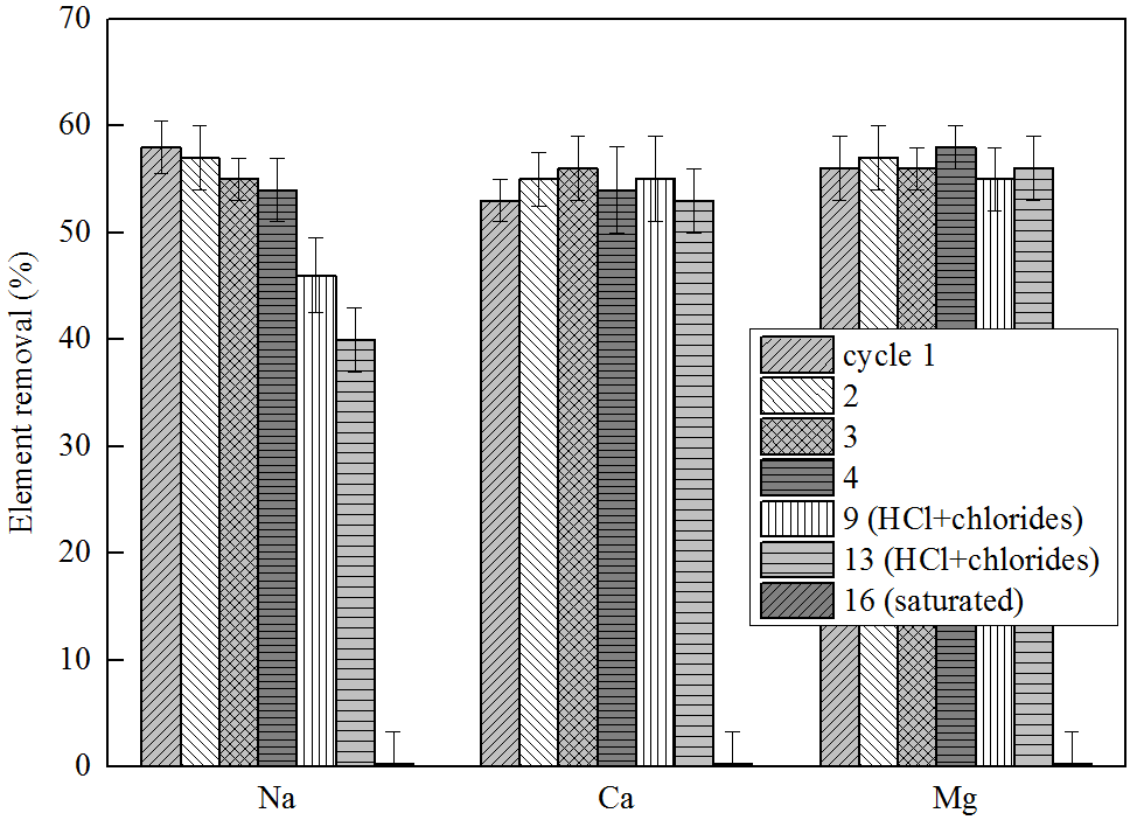

Figure 4.15 Element removal extents vs cycle number of HCl acid.

Last effort was made to explore the element removal efficiencies from raw coal upon the recycling of HCl acid with a constant initial proton concentration for each cycle (0.7 M H^+). The result is compared in **Figure 4.15**. To note, the first four cycle used recycled HCl, whereas the other results (cycle 9, 12 and 16) used the mixture of fresh HCl and pure chlorides (Na/Ca/$MgCl_2$) with various concentrations. For cycle 16, the initial chloride concentration reached its saturation point in 0.7 M HCl acid, which was determined by trial and error method. Because it is impossible to conduct the recycling experiments for so many times in a lab-scale. The three chlorides were mixed in a ratio which is as same as that of the leachate after 1st cycle. It can be observed that the Na removal extent is almost constant for the first four cycles, then drops to 40% approximately in the 13th cycle, and finally plummets to nil upon the using of

leaching reagent which is saturated to NaCl, $CaCl_2$ and $MgCl_2$. Regarding the removal of Ca and Mg, they are almost invariant for each cycle until the using of saturated leachate which results in zero removal extent. This leaching behaviour differs from that observed for water recycling leaching which displays an exponential decrease in water-soluble Na removal upon the recycling of water. This might imply that the HCl-soluble element removal is dominated by the intra-particle diffusion of proton, considering that the initial acid concentration for each cycle is persistent. The decrease in the Na removal should be attributed to the decrease on the water-soluble Na^+ removal upon the recycling of leachate which has been discussed before. It is reasonable to conclude that providing a constant initial acid concentration for each cycle, a constant element removal extent can be achieved until reaching the saturated point where nil element can be removed any more.

4.4 Kinetic modelling

For the case of water leaching, the modified SCM was first validated by fitting the result of the first set experiments, *fresh water versus raw coal*. This aims to verify that the water-soluble Na^+ removal is mainly controlled by the intra-particle diffusion of Na^+. Afterwards, the second set experiments, *used water versus raw coal*, was modelled to validate the application of the modified SCM to used water leaching and to predict the recyclability of water. Finally, the ultimate three-stage counter-current water leaching experiment was simulated, to predict the Na^+ removal extent of each stage at each cycle and the maximum allowable recycle number of water. On the other hand, the removal of acid-soluble elements was modelled by a proton intra-particle diffusion control model which took a decreasing proton concentration in the bulk leachate into account, namely Zhuravlev, Lesokhin and Templeman model [23].

4.4.1 Modelling of fresh water leaching raw coal with various particle sizes

For comparison, the removal of Na^+ from raw coal by fresh water was firstly modelled against both the chemical reaction control and intra-particle water diffusion control defined by SCM [14]. The respective correlation coefficients (R^2) for the modelling accuracy are listed in **Table 4.5**. Clearly, the original SCM failed to fit the experimental data accurately, with the exception of the coarsest particle of 4-8 mm with a R^2 of 0.9959 for the diffusion control.

Table 4.5 R^2 using the reaction-controlled model and diffusion controlled model defined by the original SCM.

Particle size (mm)	Reaction controlled model	Diffusion controlled model
	$1 - (1 - X)^{1/3}$	$1 – 3 (1-X)^{2/3} + 2 (1-X)$
0.2-0.6	0.4435	0.6195
0.6-1	0.6252	0.7963
1-4	0.8060	0.9461
4-8	0.9091	0.9959

Instead, the Na^+ intra-particle diffusion control defined by the modified SCM presented in **Equation (12)** was proven to fit all the experimental results satisfactorily. As evident in **Figure 4.16**, the correlation coefficients achieved are beyond 0.98 for all the four sizes. Additionally, based on **Equation (8)**, the effective diffusion coefficient D_{eff} of Na^+ through the water phase contained in coal particles can be calculated, as listed in **Table 4.6**. These values fall in the reported range of the order of 10^{-7}-10^{-5} cm^2/s [8, 24]. On the other hand, D_{eff} increases with the increasing coal particle size, which is consistent with previous studies [8, 25, 26]. It can be

explained as follows. As shown in **Equation (25)** [26], in which *D* is molecular bulk diffusion coefficient of Na^+ that is an invariant at a fixed pressure and temperature, D_{eff} is only proportional to the porosity φ of coal particles if the tortuosity τ is assumed to be same for all particle size ranges. Therefore, the larger coal particles tend to possess a larger D_{eff}, since it has higher porosity values as evident by elsewhere [27]. Both the reasonable value of D_{eff} and right relationship between D_{eff} and coal particle size verified the physical meaning of this modified SCM. This further confirmed that the water-soluble Na^+ removal out of raw coal by fresh water is dominated by its intra-particle diffusion.

$$\frac{D_{eff}}{D} = \frac{\varphi}{\tau} \tag{25}$$

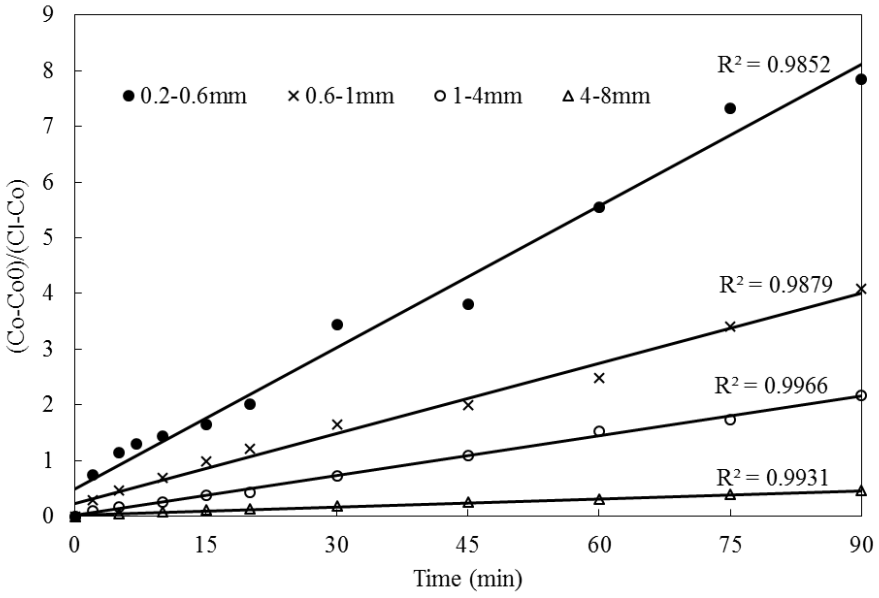

Figure 4.16 Plots for Na^+ diffusion out of coal particle defined by the modified SCM.

Table 4.6 Effective diffusion coefficient (D_{eff}) of each particle size range.

Particle diameter (mm)	Average particle diameter (mm)	D_{eff} ($\times 10^{-6}$ cm^2/s)
0.2-0.6	0.4	0.28
0.6-1	0.8	0.56
1-4	2.5	3.13
4-8	6.0	3.75

4.4.2 Modelling of single-stage multicycle used water leaching of raw coal

For the single-stage multicycle used water leaching fitting result, **Table 4.7** summarises the R^2, overall rate constant k (the slope of **Equation (12)**) and the initial Na^+ concentration in water for the first three cycles. The value of k is only a function of D_{eff} (**Equation (8)**) for a fixed particle size, which should be independent of Na^+ concentration. Therefore, aside from the high R^2, the relatively constant value of k for each cycle verifies the good fitting of the modified SCM. In addition, the applicability of this modified SCM has also been proven by the satisfactory fitting to Coal B to some extent.

Table 4.7 R^2 and k using the intra-particle Na^+ diffusion-controlled model defined by the modified SCM.

Recycle number	R^2	k (min^{-1})	Initial Na^+ concentration in water (ppm)
1st	0.9892	0.0197	0
2nd	0.9810	0.0208	262
3rd	0.9833	0.0196	565
0.5 wt% NaCl	0.9814	0.0232	2175

To examine if the modified SCM can be extended to the leaching by used water whose Na^+ concentration is accumulated to a very high value, the experimental result of 0.5 wt% NaCl leaching raw coal shown in **Figure 4.10** was further simulated. It can be observed from **Table 4.7** that R^2 is above 0.98 for such a high initial Na^+ concentration. This satisfactory fitting allows us to use this model to predict the Na^+ removal change upon the recycling of the used water. Based on the results in **Table 4.7**, the average of *k* values of the first three cycles and the Na^+ concentration in the leachate after three cycles were calculated and substituted into **Equations (13-14)**. Subsequently, the Na^+ removal in the fourth cycle was predicted and compared with the experimental result. As demonstrated in **Figure 4.17**, one can see a close match between the model prediction and the experimental observation. By an iterative calculation, the relationship between Na^+ removal extent and the cycle number of water can be further predicted, which is illustrated in **Figure 4.18**. This indicates that the Na^+ removal extent decreases exponentially upon the increase in the water recycling number. Once the recycling number approaches 20, the water nearly losses its leaching capability for the raw coal, and hence, has to be desalinated.

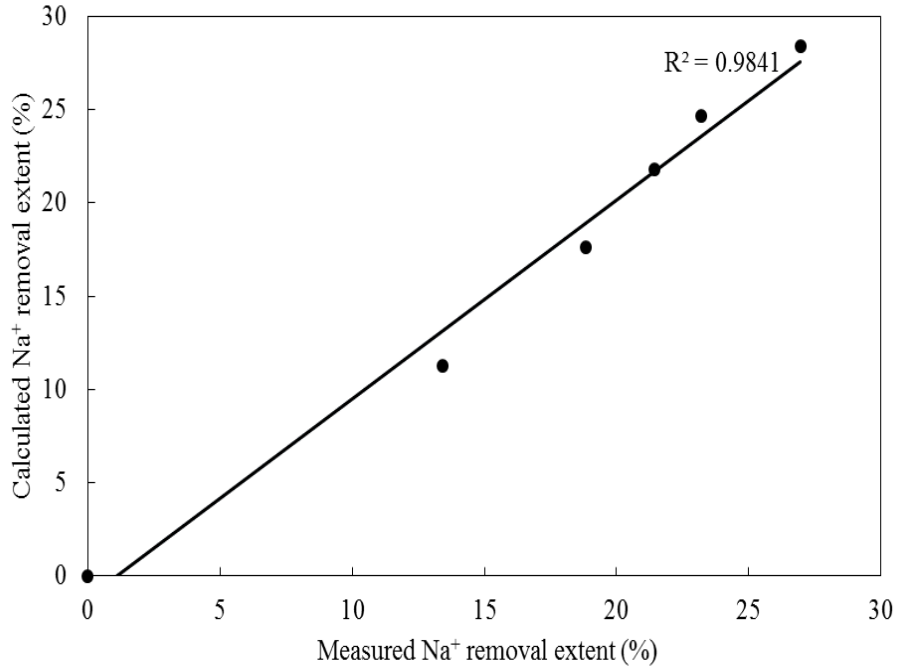

Figure 4.17 Comparison between calculated and measured Na^+ removal extent at the fourth cycle.

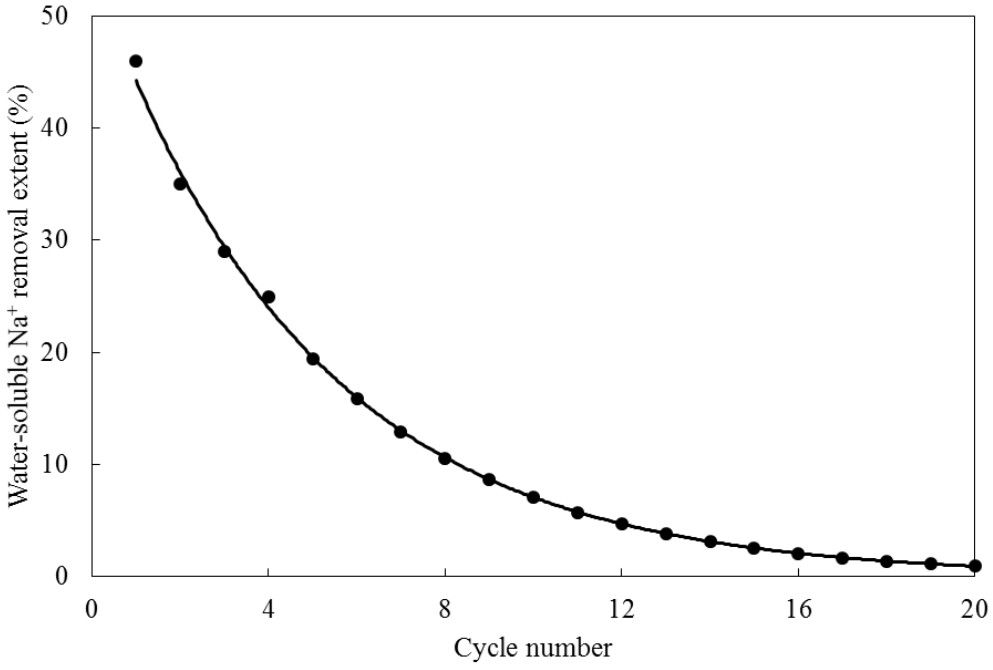

Figure 4.18 Na^+ removal extent change upon the recycling of used water.

4.4.3 Modelling of three-stage counter-current water leaching process

The fitting result of three-stage counter-current water leaching is tabulated in **Table 4.8**. The high R^2 of each stage indicates that all leaching conditions included in the counter-current leaching can be modelled very well by the modified SCM, irrespective of fresh or used water, and raw or leached coal. In addition, the validation of the modified SCM is substantiated by the close value of k for each stage, which is independent on the Na^+ concentration in bulk water and Na^+ content in coal.

Table 4.8 R^2 and k for three-stage counter-current leaching fitted by the modified SCM.

Stage number	R^2	k (min^{-1})
1st	0.9984	0.0239
2nd	0.9942	0.0235
3rd	0.9842	0.0238

Plugging the value of k into the calculation of **Equations (15-24)**, the water-soluble Na^+ removal at each stage was further predicted, to examine the proposed calculation approach specific to the counter-current leaching process. **Figure 4.19** compares the calculated and experimental Na removal extent of each stage. The excellent linear relationship with high R^2 proves that this calculation method can accurately predict the Na^+ removal extent at every stage at any time.

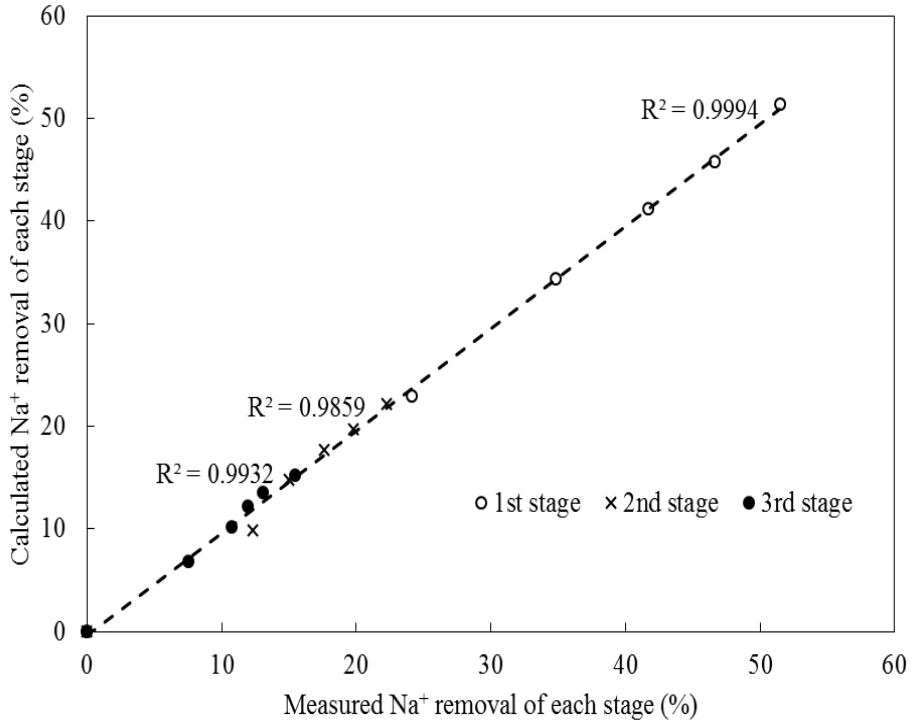

Figure 4.19 Comparison between calculated and experimental Na^+ removal extent of each stage.

Similar to **Figure 4.14**, the relationship between the total Na^+ removal of three-stage counter-current water leaching process and the recycling of water was predicted and presented in **Figure 4.20**(a). Again, the total Na^+ removal extent (sum of Na removal extents of three stages) decreases exponentially upon the increase in the recycling number. However, the water loses its Na removal ability after 15 times recycles, which is less than 20 times confirmed for the single-stage multicycle leaching in **Figure 4.18**. This is mainly a result of the higher Na removal extent in each cycle that can be achieved by the three-stage leaching process. Moreover, the relationship between Na^+ removal and the initial Na^+ concentration in water can also be obtained, as shown in **Figure 4.20**(b). This confirms a linear decrease in the Na^+ removal extent upon the rise of Na^+ concentration in the leachate, *i.e.* the recycling of the water.

It can be expected from **Equations (13-14)**. Once the original Na^+ reaches around 3000 ppm, the recycled water losses its washability.

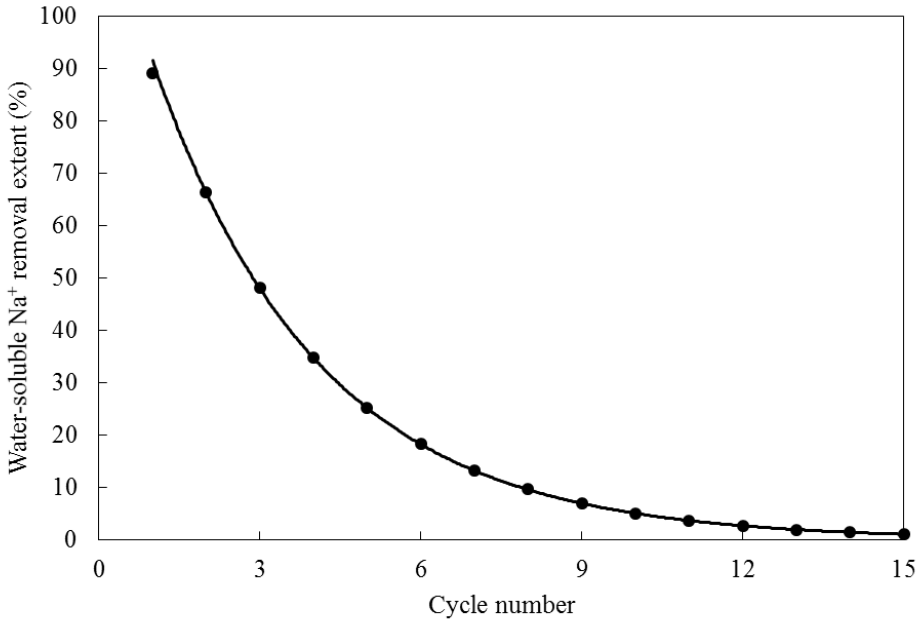

(a)

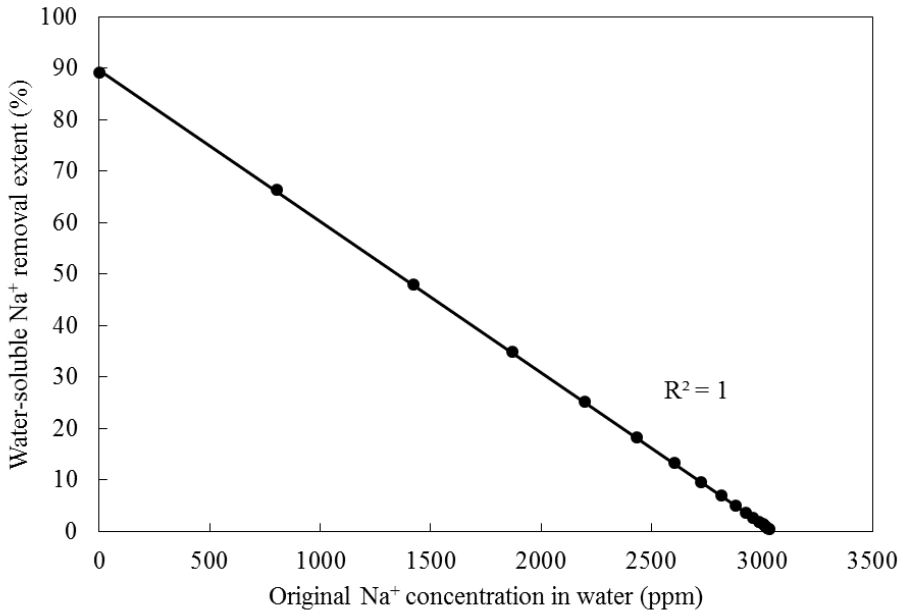

(b)

Figure 4.20 Total Na^+ removal extent of three-stage counter-current leaching versus the recycling of used water (a); original Na^+ concentration in water (b).

4.4.4 Modelling of fresh HCl leaching

In the simulation of HCl-soluble element removal, both the original and modified SCM were firstly proven to be unsuitable. Afterwards, attention was paid to the concentration profile of proton in the bulk leachate with the extension of leaching time. The proton concentration as illustrated in **Figure 4.21** was calculated according to the stoichiometric relations between proton and the three elements (Na^+, Ca^{2+} and Mg^{2+}). A notable decrease tendency can be observed, especially in the first five minutes, and an around 40% of decline is achieved in 30 min. This explains the failure of the fitting by SCM which assumes a constant H^+ concentration in leachate with leaching time. In light of this, it was found that a proton intra-particle diffusion model with a decreasing H^+ concentration profile (**Equation (26)**) [23] can simulate our case well as shown in **Figure 4.22**. The detailed derivation can be found elsewhere [23]. This satisfactory fitting confirms that the HCl-soluble element removal is predominated by the intra-particle diffusion of H^+ but with a decreasing concentration in leachate. It explains why an invariant element removal extent is achieved upon the recycling of HCl acid which keeps a constant initial H+ concentration for each cycle (**Figure 4.15**).

$$((1\text{-}X)^{-\frac{1}{3}}\text{-}1)^2 = kt \qquad (26)$$

where *X* and *t* are the element removal extent and leaching time, respectively, and *k* is fitting constant.

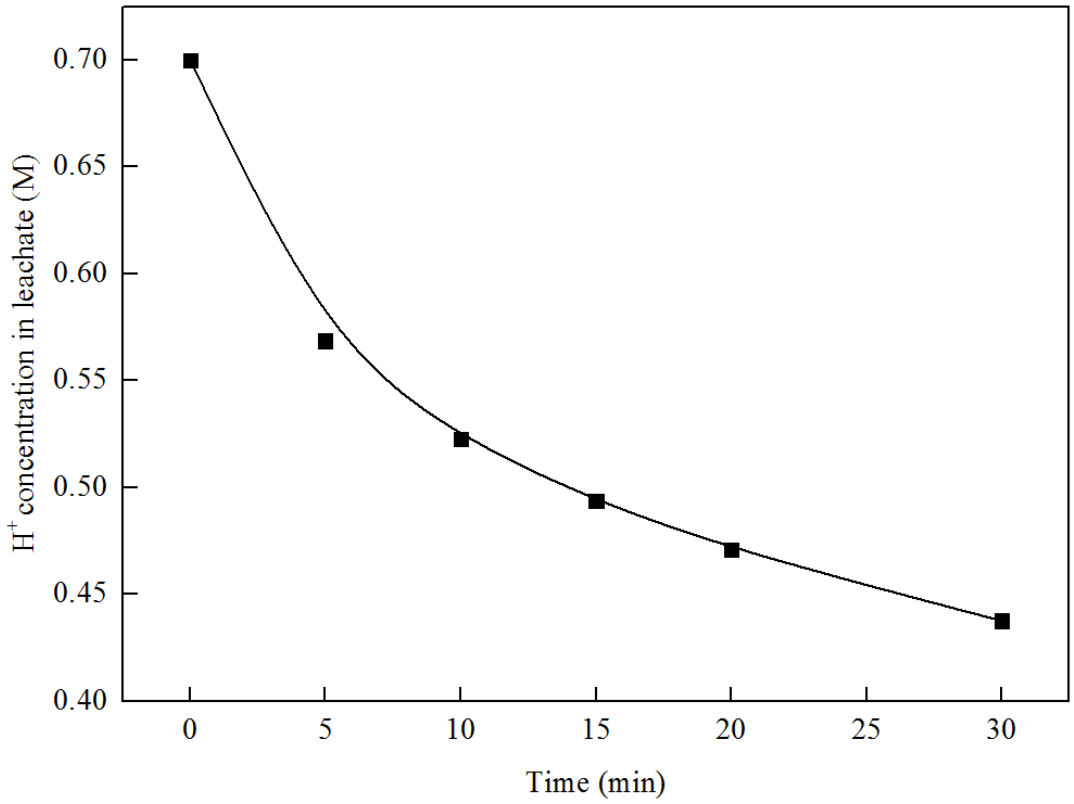

Figure 4.21 The concentration profile of proton in bulk leachate versus leaching time.

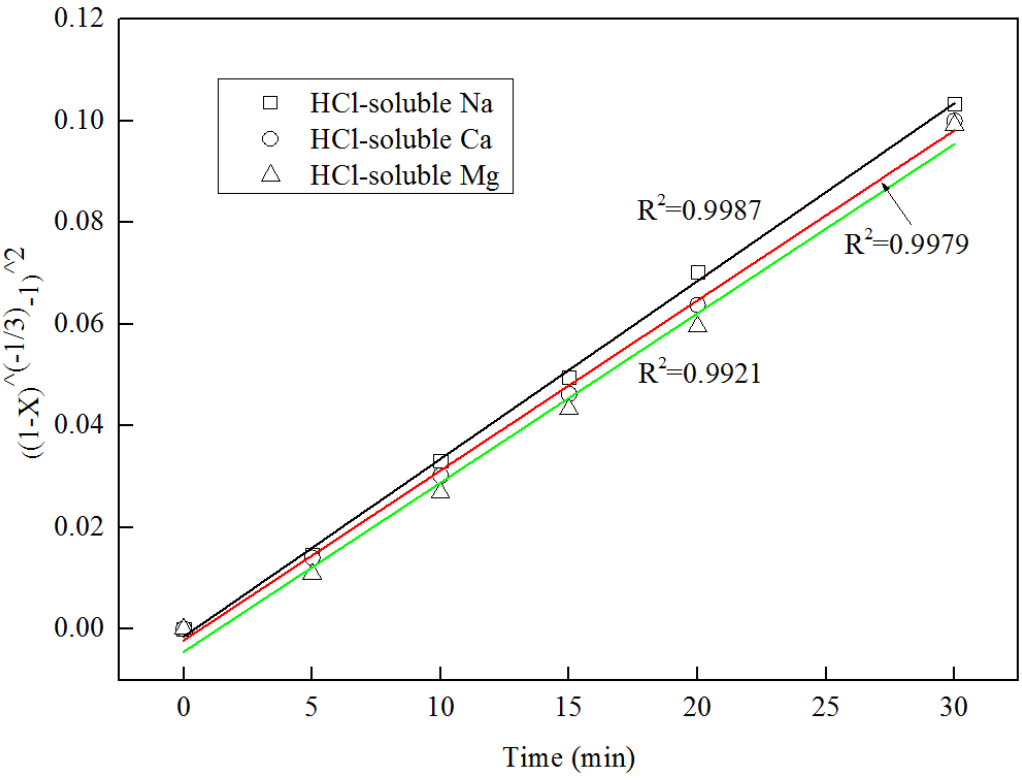

Figure 4.22 Plots for H^+ intra-particle diffusion with a decreasing H^+ concentration defined by Zhuravlev, Lesokhin and Templeman model.

4.5 Conclusions

A comprehensive investigation on the leaching propensity of Na, Ca and Mg from three types of low-rank Xinjiang coals using both fresh and used water/HCl acid has been performed, from both experimental and modelling perspectives. Apart from the parametric study on the once-through fresh reagents leaching raw coal, other two multi-cycle leaching scenarios including three-stage counter-current water leaching and single-stage multicycle HCl leaching have also been conducted. This aims to reveal the element removal extents upon the recycling of lachates and the recyclability of leaching reagents. The major conclusions achieved are as follows:

1) A modified SCM integrated with iterative calculation is developed for the multi-stage counter-current water leaching processes, which is successfully validated by high correlation coefficients between experimental and model results, and reasonable D_{eff} ranging from 0.28-3.75×10^{-6} cm^2/s which is in line with the reported values. The model indicates that the water-soluble Na^+ removal rate is controlled by the intra-particle diffusion of Na^+.

2) Specific to the threes-stage counter-current process, it is found that the water loses its capability to remove Na^+ after recycling 15 times. Upon the increase in the cycle number, the overall Na^+ removal extent decreases exponentially from around 90% in the first cycle quickly down to negligible in the 15^{th} cycle. The overall Na^+ removal extent bears a reverse proportion to the concentration of Na^+ accumulated in the used water.

3) The removal of acid-soluble elements can be fitted satisfactorily by a H^+ intra-particle diffusion model which takes account in a decreasing proton concentration in bulk acid. This explains the reason why an stable element removal extent for each cycle is achieved provided that the initial acid concentration for each cycle is constant. No element can be removed after recycling for 15 times when the concentration of NaCl, $CaCl_2$ and $MgCl_2$ in the recycled acid reach the saturation point, at 15900, 67400 and 10600 ppm, respectively.

Reference

1. https://www.bp.com/en/global/corporate/energy-economics/statistical-review-of-world-energy/electricity.html
2. Li, C.-Z., *Advances in the science of Victorian brown coal*. Elsevier: 2004.
3. Zhou, S.; Hosseini, T.; Zhang, X.; Haque, N.; Zhang, L., Selective removal of sodium and calcium from low-rank coal–Process integration, simulation and techno-economic evaluation. *Fuel Processing Technology* **2018**, *172*, 13-28.
4. Wu, X.; Zhang, X.; Yan, K.; Chen, N.; Zhang, J.; Xu, X.; Dai, B.; Zhang, J.; Zhang, L., Ash deposition and slagging behavior of Chinese Xinjiang high-alkali coal in 3 MWth pilot-scale combustion test. *Fuel* **2016**, *181*, 1191-1202.
5. Dai, B.-Q.; Low, F.; De Girolamo, A.; Wu, X.; Zhang, L., Characteristics of ash deposits in a pulverized lignite coal-fired boiler and the mass flow of major ash-forming inorganic elements. *Energy & Fuels* **2013**, *27*, (10), 6198-6211.
6. Barnes, I. *Slagging and Fouling in Coal-Fired Boilers, CCC/147*; IEA Clean Coal Research: 2009.
7. Gao, Y.; Ding, L.; Li, X.; Wang, W.; Xue, Y.; Zhu, X.; Hu, H.; Luo, G.; Naruse, I.; Bai, Z., Na&Ca removal from Zhundong coal by a novel CO2-water leaching method and the ashing behavior of the leached coal. *Fuel* **2017**, *210*, 8-14.
8. Neavel, R.; Nahas, N.; Koh, K., Removal of sodium from Illinois coal by water extraction. *Trans. Soc. Min. Eng. AIME;(United States)* **1977**, *262*, (3).
9. Crank, J., *The mathematics of diffusion*. Oxford university press: 1979.
10. Readett, D.; Quast, K.; Mulcahy, D.; Ketteridge, I. In *Modelling the leaching of NaCl from Bowmans lignite*, Symposium on'Extractive Metallurgy', The Aus. IMM Melbourne Branch, 1984; 1984; pp 103-109.
11. Low, F.; Zhang, L., Microwave digestion for the quantification of inorganic elements in coal and coal ash using ICP-OES. *Talanta* **2012**, *101*, 346-352.
12. Finkelman, R.; Palmer, C.; Krasnow, M.; Aruscavage, P.; Sellers, G.; Dulong, F., Combustion and leaching behavior of elements in the Argonne premium coal samples. *Energy & fuels* **1990**, *4*, (6), 755-766.
13. Prationo, W.; Zhang, J.; Abbas, H. A. A.; Wu, X.; Chen, X.; Zhang, L., Influence of External Clay and Inherent Minerals on Lignite Optical Ignition and Volatile Flame Propagation in Air-Firing and Oxy-Firing. *Industrial & Engineering Chemistry Research* **2014**, *53*, (7), 2594-2604.

14. Levenspiel, O., Chemical reaction engineering. *Industrial & engineering chemistry research* **1999**, *38*, (11), 4140-4143.
15. Zhang, J.; Han, C.-L.; Yan, Z.; Liu, K.; Xu, Y.; Sheng, C.-D.; Pan, W.-P., The varying characterization of alkali metals (Na, K) from coal during the initial stage of coal combustion. *Energy & fuels* **2001**, *15*, (4), 786-793.
16. Matsuoka, K.; Yamashita, T.; Kuramoto, K.; Suzuki, Y.; Takaya, A.; Tomita, A., Transformation of alkali and alkaline earth metals in low rank coal during gasification. *Fuel* **2008**, *87*, (6), 885-893.
17. Wijaya, N.; Choo, T. K.; Zhang, L., Generation of ultra-clean coal from Victorian brown coal: Effect of hydrothermal treatment and particle size on coal demineralization and the extraction kinetic of individual metals. *Energy & Fuels* **2012**, *26*, (8), 5028-5035.
18. Lee, I.-H.; Wang, Y.-J.; Chern, J.-M., Extraction kinetics of heavy metal-containing sludge. *Journal of Hazardous Materials* **2005**, *123*, (1-3), 112-119.
19. Fan, X.; Xing, W.; Dong, H.; Zhao, J.; Wu, Y.; Li, B.; Tong, W.; Wu, X., Factors research on the influence of leaching rate of nickel and cobalt from waste superalloys with sulfuric acid. *International Journal of Nonferrous Metallurgy* **2013**, *2*, (02), 63.
20. Prasassarakich, P.; Thaweesri, T., Kinetics of coal desulfurization with sodium benzoxide. *Fuel* **1996**, *75*, (7), 816-820.
21. Sodium chloride solubility. https://en.wikipedia.org/wiki/Sodium_chloride
22. Wijaya, N.; Zhang, L., A Critical Review of Coal Demineralization and Its Implication on Understanding the Speciation of Organically Bound Metals and Submicrometer Mineral Grains in Coal. *Energy & Fuels* **2011**, *25*, (1), 1-16.
23. Dickinson, C.; Heal, G., Solid–liquid diffusion controlled rate equations. *Thermochim. Acta* **1999**, *340*, 89-103.
24. Piret, E. L.; Ebel, R.; Kiang, C.; Armstrong, W., DIFFUSION RATES IN EXTRACTION OF POROUS SOLIDS. 1. SINGLE PHASE EXTRACTIONS. *CHEMICAL ENGINEERING PROGRESS* **1951**, *47*, (8), 405-414.
25. Grathwohl, P., *Diffusion in natural porous media: contaminant transport, sorption/desorption and dissolution kinetics*. Springer Science & Business Media: 2012; Vol. 1.
26. Ingham, D. B.; Pop, I., *Transport phenomena in porous media*. Elsevier: 1998.
27. Xin, W.; Changwu, L., Analysis of moulded coal porosity base on surface characteristics. *Procedia Engineering* **2011**, *26*, 1058-1064.

Chapter 5

Pyrohydrolysis of $CaCl_2$ Waste for the Recovery of HCl Acid upon the Synergistic Effects from $MgCl_2$ and Silica

It has been hypothesised and validated that HCl acid can remove AAEMs from low-rank Xinjiang coal in a more efficient way than water in both Chapters 3 and 4. However, it will result in enormous waste leachate which is rich in $CaCl_2$ and $MgCl_2$ (as demonstrated in **Figure 1.1**) and is forbidden from discharging directly due to its obnoxious environmental effects. This chapter has explored a novel and efficient HCl acid recovery method from the mixture of $CaCl_2$ and $MgCl_2$ at the presence of silica and steam, and Cl-lean/free solid by-products can be obtained simultaneously. The synergistic effect from $MgCl_2$ and silica has been investigated intensively. This chapter has been reformatted from a manuscript published in ***ACS Sustainable Chemistry & Engineering***: **Zhou, S.**; Qian B.; Hosseini, T.; Girolamo, A.D.; Zhang, L. *Pyrohydrolysis of $CaCl_2$ waste for the recovery of HCl acid upon the synergistic effects from $MgCl_2$ and silica*. ***ACS Sustainable Chemistry & Engineering***, 2019, 7, 3, 13-28.

Abstract

In this paper, an efficient HCl acid recovery method from the mixture of alkaline earth metal chlorides waste was demonstrated via co-pyrohydrolysis in a lab-scale horizontal furnace at a temperature range of 700–1000 °C, and fixed additions of SiO_2 and steam. The synergistic effect of $MgCl_2$ on the HCl recovery from $CaCl_2$ was explored intensively. A double-sided effect is revealed. For the reaction temperatures below 1000 °C, the $MgCl_2$ addition delays the HCl release through competing with $CaCl_2$ for the inclusion into silica matrix. In contrast, once the chloride mixtures are subjected to 1000 °C with a noticeable residence time (e.g. 2 h) and at a minimum molar ratio of 0.5 of $MgCl_2$ to $CaCl_2$, the $MgCl_2$ addition promotes the HCl release remarkably, via promoting the conversion of $Ca_3(SiO_4)Cl_2$ into $Ca_8Mg(SiO_4)_4Cl_2$. A portion of Mg^{2+} derived from the early decomposition of $MgCl_2$ substitutes the Ca(I) site in $Ca_3(SiO_4)Cl_2$, thereby resulting in the formation of weak Mg-Cl bond that is in favour of the HCl release. Additionally, the remaining Mg^{2+} consumes the excessive SiO_2 so as to cause the skeleton of $[SiO_4]^{4-}$ to be fully affiliated and balanced by cations to form $Ca_8Mg(SiO_4)_4Cl_2$, in which the weaker ionic polarisation between Ca^{2+} and adjacent anions further enhances the breakage of the Ca-Cl bonds.

Keywords: Pyrohydrolysis; Alkaline earth metal chlorides; HCl regeneration; Cl release; Silica

5.1 Introduction

In the field of hydrometallurgical processing industry, hydrochloric acid possesses notable merits compared with other acids for the extractive leaching of metals, offering higher extraction kinetics, simpler leaching condition, larger solubilities of metal complexes, and simplicity of the pre-treatment requirement [1, 2]. However, one major barrier to hydrochloric acid leaching is the difficulty of disposing of the waste lixiviant that is rich in chlorides. The chlorine-bearing lixiviant is prohibited for a direct landfilling, since it is corrosive and detrimental to the aquatic environment [3, 4]. On the other hand, as an important chemical in most chemical industries [1], hydrochloric acid is primarily produced by the electrolysis of NaCl solution that is energy intensive, cost ineffective and prone to electrode corrosion and fouling [5-8]. Due to these considerations, a successful regeneration of HCl acid from chloride-based lixiviant is crucial for the sustainability of the HCl-based industries across the world.

To date, extensive research has been conducted to regenerate HCl gas from chloride solutions, including electrowinning, sulfation precipitation and pyrohydrolysis [1]. Compared to the other two methods, pyrohydrolysis has only been proven and commercialised for three metal chlorides, $MgCl_2$, $FeCl_2$ and $NiCl_2$ [1]. To further advance the pyrohydrolysis technology on a large scale, it is critical to investigate the other metal chlorides such as $CaCl_2$, which is an abundant by-product produced from a broad variety of hydrometallurgy processes [9-14]. Moreover, since they have similar properties and co-exist in a large number of natural minerals and man-made wastes, $CaCl_2$ and $MgCl_2$ are often produced simultaneously, such as from the leaching of low-rank coal and its ash by HCl acid [9-11], the production of magnesia from dolomite by HCl acid leaching [12, 13], and the production of high-purity magnesia from brine via the addition of slaked lime that generates 1.38–2.75 tonne $CaCl_2$/tonne MgO [14].

The pyrohydrolysis of $MgCl_2$ involves dehydration, hydrolysis, and thermal decomposition in sequence [15]. An intermediate product, MgOHCl is formed at 235 °C that subsequently converts to MgO and HCl gas at 415 °C via the reaction with steam. By contrast, the pyrohydrolysis of $CaCl_2$ is refractory due to the larger ionic bond energy of Ca-Cl than Mg-Cl, 409 vs 327 kJ mol^{-1} [16]. To resolve the breakage of Ca-Cl bond, the co-addition of silica and steam has been examined at 770–870 °C, for different molar ratio of silica to $CaCl_2$, various acidic solids and partial pressure of steam [17]. The overall reaction route has been proposed as reaction **Equation (1)** below. At the temperatures below its melting point (772 °C), $CaCl_2$ tends to dissolve into the cage of solid acid to form the $CaCl_2 \cdot SiO_2$ solid solution, from which HCl gas is then released. However, the detailed crystal structures of $CaCl_2 \cdot SiO_2$ and any of its intermediate compounds have yet to be clarified, and hence, the mechanisms underpinning this reaction still remain vague. More importantly, the effect of $MgCl_2$ on the pyrohydrolysis of $CaCl_2$ has not been explored at all. Upon the co-existence of these two alkaline earth metal chlorides, a quick decomposition of $MgCl_2$ at low temperatures presumably results in the formation of free MgO that may compete with $CaCl_2$ for the inclusion into silica matrix, thereby delaying the decomposition of $CaCl_2$. However, in the later stage when $CaCl_2 \cdot SiO_2$ solid solution is formed, the invasion of Mg^{2+} cation into the matrix and its substitution to Ca^{2+} could weaken the Ca-Cl affinity, and hence, promote the decomposition of $CaCl_2$.

$$CaCl_2 \cdot SiO_2\,(s) + H_2O\,(g) \rightarrow CaO \cdot SiO_2\,(s) + 2HCl\,(g) \quad (1)$$

In this study, a series of experiments were designed to prove the above-mentioned hypothesis, and to explore the synergism between $MgCl_2$ and $CaCl_2$ during the co-pyrohydrolysis. The

pyrohydrolysis experiment was conducted in a lab-scale fixed bed reactor, under the conditions of 700–1000 °C, a fixed steam partial pressure of 0.7 bar and varying retention time at the terminal temperature. A non-isothermal heating procedure was first employed, so that the residues produced at intermediate temperatures were quenched and subjected to X-ray fluorescence (XRF) and X-ray diffraction (XRD) to quantify the remaining Cl content and its crystalline species, respectively. Scanning electron microscopy (SEM) analysis was also conducted to distinguish the phase of the residues. The changes on the atomic structure of the residues were further determined by CrystalMaker software [18]. In addition, thermodynamic calculations were conducted in FactSage 6.4 [19]. All these efforts were made to attain the mechanistic insights governing the co-pyrohydrolysis of $CaCl_2$ and $MgCl_2$, and hence, to promote the HCl regeneration rate from this abundant, mixed waste.

5.2 Experimental methodology

5.2.1 Experimental rig and conditions

An electrically heated horizontal furnace was employed, the schematic of which is illustrated in **Figure 5.1**. The thermal decomposition took place inside a quartz tube with an inner diameter of 51 mm and a total length of 1200 mm. A sample-laden corundum plane (Al_2O_3 >99.7%) was placed into the middle of the furnace. Argon was blended with steam and used to purge the reactor continuously, which also swept away the HCl gas once generated.

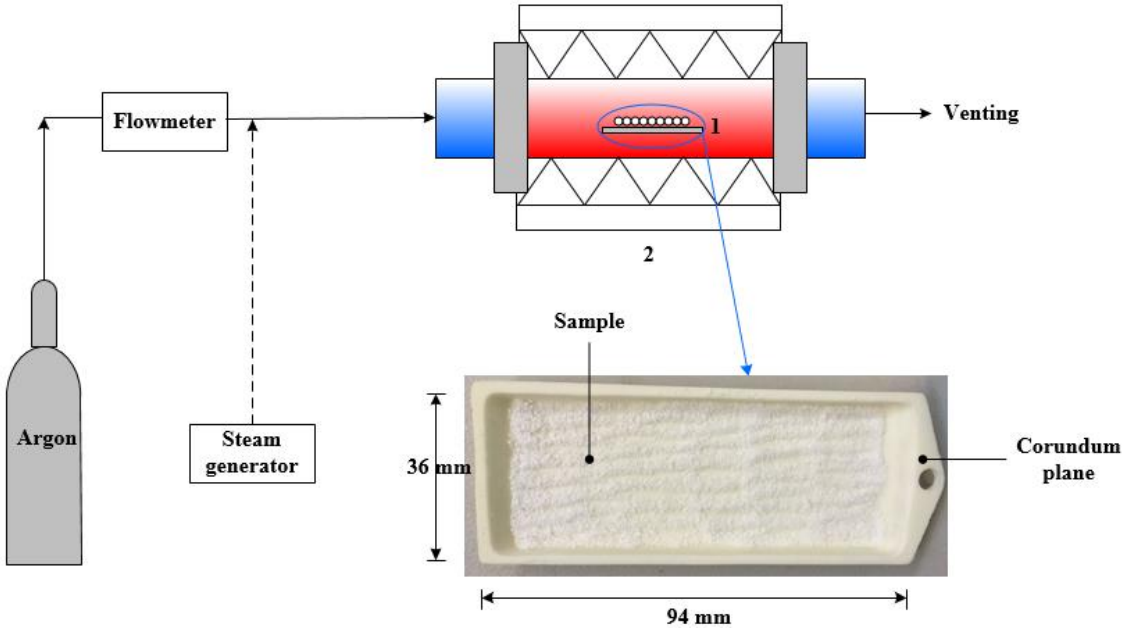

Figure 5.1 Horizontal thermal decomposition rig schematic and sample loading pan. (1. Sample loading pan; 2. Heating furnace).

For each run, approximately 1 g of $CaCl_2 \cdot 4H_2O$ was blended thoroughly with $MgCl_2 \cdot 6H_2O$ by roll mill, with varying molar ratios. The amount of $MgCl_2 \cdot 6H_2O$ varied from 0 to 4 mole/mole of $CaCl_2 \cdot 4H_2O$. Additionally, SiO_2 was further mixed with each chloride mixture on an equi-molar ratio. All the reagents used are analytical reagent grade with a purity > 99% and purchased from Merck. Ltd (chlorides) and Sigma-Aldrich Co (silica). The reaction temperature ranged from 700 to 1000 °C with an interval of 100 °C. The temperature was ramped from room temperature at a heating rate of 10 °C/min and then maintained at the target temperature for various durations, ranging from 0 to 6 h. Once the experiment was finished, the sample pan was quickly pulled out and moved to the cold end of the quartz tube, whereas the steam was stopped immediately while pure argon of around 10 L/min was turned on to quench the hot decomposition residue. The volumetric percentage of steam in the feeding gas was fixed at 70 v/v%, to guarantee a complete conversion of Cl radicals released to HCl gas.

The overall Cl-bearing gas is simply HCl, and its release extent for the pyrohydrolysis of $CaCl_2$ or $MgCl_2$ alone or their mixtures was determined by the mass difference of Cl between the original chloride sample and its decomposition residue, as shown in **Equation (2)** below.

$$\textit{Overall Cl Release extent (\%)} = \frac{M_1 \times P_1 - M_2 \times P_2}{M_1 \times P_1} \times 100 \qquad (2)$$

Where M_1 and M_2 are the mass of the original chloride and its residue respectively, and P_1 and P_2 denote the Cl mass percentage of the original chloride and its residue tested by XRF (SPECTRO IQ II), respectively. The XRF was prior calibrated by the Cl-bearing mixtures ($MgCl_2$ and SiO_2) with different Cl contents.

5.2.2 XRD and crystal structure analysis

Each reaction residue was ground to less than 45 μm to minimise the preferred orientation and improve the statistical distribution of the lattice plains in the reflection. The XRD patterns were recorded on a Rigaku, Miniflex 600 with CuKα radiation (λ = 0.15406 nm) under 40 kV and 15 mA. The powdered samples were scanned between 10° and 80° with a D/teX Ultra detector, with a scanning speed of 5°/min and a scanning step of 0.02°. The optical configuration was a fixed divergence slit (1.25°) and a fixed incident antiscatter slit (2.5°). The standards used for the XRD fitting are listed in **Table 5.1**. Note that, a portion of these standards highly overlap with one another at their most intense peak of approximately 33°. However, their 2nd and 3rd most intense peaks are highly distinctive and sufficient for differentiation. All the Cl-bearing standards bear a very large discrepancy of peak positions, and hence, can be identified easily.

The crystal structure for each identified species was further extracted from the software CrystalMaker through simply importing the respective CIF files shown in **Table 5.1**. In order to extract the local atomic environment of individual atom, the function of 'Define Cluster' was applied via defining the cluster range centering on the target atom [18].

Table 5.1 The species used for XRD peak fitting.

Chemical formula	ICSD	Most intense peak		2nd most intense		3rd most intense	
		2 theta	(h k l)	2 theta	(h k l)	2 theta	(h k l)
$Ca_3(SiO_3)_3$	26553	45.9023	330	27.6113	132	27.5093	13-2
MgO	248386	43.0028	002	62.4423	022	78.8159	222
$CaCl_2 \cdot 6H_2O$	59142	41.7919	121	22.5589	110	32.0495	111
Mg_2SiO_4	34816	36.4822	112	32.2305	130	52.1829	222
$CaMgSiO_4$	31106	33.6938	131	34.7296	112	50.2850	222
$Ca_8Mg(SiO_4)_4Cl_2$	68243	33.5774	044	60.0384	448	30.7718	115
$Ca_3Mg(SiO_4)_2$	26002	33.4072	013	33.5656	411	33.8410	020
$Ca_3SiO_4Cl_2$	38359	32.6570	10-4	31.3331	310	26.3451	020
Ca_2SiO_4	81096	32.0365	10-3	32.5935	200	32.1746	12-1
$CaCl_2 \cdot 2H_2O$	960	31.9865	122	20.5417	111	42.8606	204
$CaMg(SiO_3)_2$	10222	29.7909	22-1	35.8265	002	30.5935	310
$CaCl_2$	26686	29.1249	111	19.8091	110	8.5430	211
$Ca_{10}(Si_2O_7)_3Cl_2$	1226542(SD)	28.9587	131	30.3333	132	30.9522	006

$CaSiO_3$	20571	27.7992	12-1	36.1734	402	41.2801	521
SiO_2	174	26.6294	011	20.8468	010	50.1214	112

5.2.3 Thermodynamic equilibrium calculation

FactSage 6.4 was employed to conduct thermodynamic equilibrium calculations. The equilibrium mode was chosen as OPEN that is specifically designed to simulate a continuous flow system as used in this study. The total step number of injecting gases in the OPEN mode was set as the largest allowable number of 25 to be as close to the practical condition as possible. To reiterate, the inlet gas was defined as 70 v/v% of steam and 30 v/v% argon, which are exactly the same as the experimental condition mentioned above. The thermodynamic databases applied included FactPS and FToxid. The output products include ideal gas, liquid and solids phases [19].

5.3 Results and discussion

Table 5.2 provides a summary of all the HCl release extents from the experiments conducted throughout this study. Note that, the reliability of these experimental data has been assessed by repeating some of the pyrohydrolysis experiments three times. A high accuracy has been confirmed. For instance, for the condition of $CaCl_2$ only at 1000 °C for 2 h, its HCl recovery extents were found to be 89%, 89% and 90%, bearing a standard deviation of 0.6% only. Additionally, the gaseous Cl-bearing species has also been sampled by impinge trains containing sulphuric acid. The collected Cl^- ion was quantified by a chlorine ion selective electrode detector. The mass balance of Cl reached 95-98% in most of the cased.

Table 5.2 Summary of HCl release extents obtained at each experimental condition.

Sample	Molar ratio of $CaCl_2$:$MgCl_2$	Steam?	SiO_2?	Reaction T (°C)	Holding time at target T (h)	Overall HCl release from mixture (%)	HCl release extent from $CaCl_2$ (%)
$MgCl_2$	-	No	No	600	2	46	-
$MgCl_2$	-	Yes	No	600	2	99	-
$CaCl_2$	-	Yes	No	1000	2	-	0
$CaCl_2$	-	Yes	Yes	1000	2	-	90
$CaCl_2$	-	Yes	Yes	700	0	-	0
$CaCl_2$	-	Yes	Yes	800	0	-	25
$CaCl_2$	-	Yes	Yes	900	0	-	60
$CaCl_2$	-	Yes	Yes	1000	0	-	89
$CaCl_2$	-	Yes	Yes	1000	2	-	90
$CaCl_2$	-	Yes	Yes	1000	4	-	91
$CaCl_2$	-	Yes	Yes	1000	6	-	92
$CaCl_2$ & $MgCl_2$	1:4	Yes	Yes	700	0	80	0
$CaCl_2$ & $MgCl_2$	1:4	Yes	Yes	800	0	90	20
$CaCl_2$ & $MgCl_2$	1:4	Yes	Yes	900	0	93	43
$CaCl_2$ & $MgCl_2$	1:4	Yes	Yes	1000	0	98	84
$CaCl_2$ & $MgCl_2$	1:4	Yes	Yes	1000	2	99	94
$CaCl_2$ & $MgCl_2$	1:4	Yes	Yes	1000	4	99	98
$CaCl_2$ & $MgCl_2$	1:4	Yes	Yes	1000	6	99	99
$CaCl_2$ & $MgCl_2$	1:0	Yes	Yes	1000	2	90	90

$CaCl_2$ & $MgCl_2$	1:0.25	Yes	Yes	1000	2	93	90
$CaCl_2$ & $MgCl_2$	1:0.5	Yes	Yes	1000	2	96	93
$CaCl_2$ & $MgCl_2$	1:1	Yes	Yes	1000	2	98	94
$CaCl_2$ & $MgCl_2$	1:2	Yes	Yes	1000	2	98	94
$CaCl_2$ & $MgCl_2$	1:4	Yes	Yes	1000	2	99	94

5.3.1 Pyrohydrolysis of $MgCl_2$ and $CaCl_2$ alone

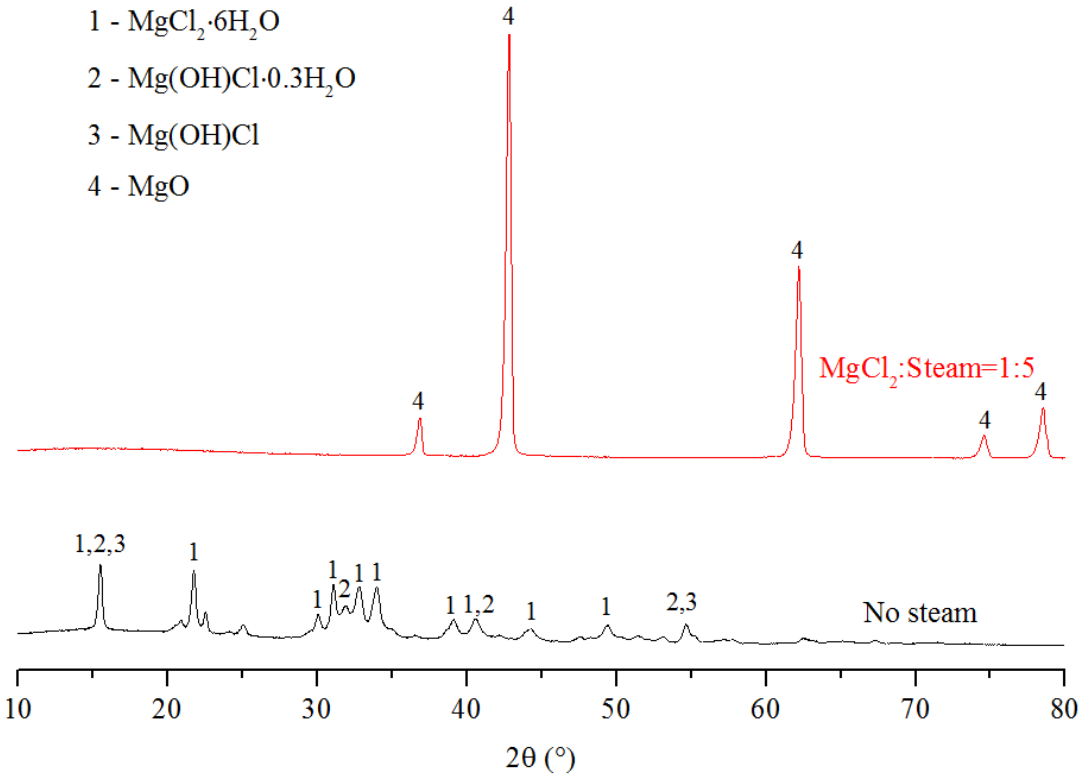

Figure 5.2 Effect of steam on the decomposition of $MgCl_2$ at 600 °C.

The decomposition of $MgCl_2$ alone was first conducted as a reference. As shown in **Table 5.2** and **Figure 5.2**, the addition of steam is essential, promoting the decomposition extent of $MgCl_2$ to 99% at 600 °C for 2 h, relative to 46% only in the absence of steam. In contrast, for the pyrohydrolysis of $CaCl_2$ alone, a higher temperature up to 1000 °C is critical, so is the co-

addition of steam and SiO_2, as evident in **Table 5.2**. Upon the addition of SiO_2 at an equi-molar ratio to $CaCl_2$, the HCl release extent reaches 90% at 1000 °C for 2 h, relative to a non-detectable extent in the presence of steam only. The XRD patterns for the respective residues in **Figure 5.3** demonstrate that the $CaCl_2 \cdot 4H_2O$ feedstock is only partially dehydrated in the absence of silica. The inset SEM picture indicates a dense surface for the residue due to the melting of $CaCl_2$ which has a low melting point of 772 °C [20]. In this case, instead of gaseous HCl, the gaseous $CaCl_2$ should be formed due to its liquid-gas equilibrium partitioning. Moreover, the molten cluster could hinder the outward diffusion of Cl radicals and the inward diffusion of steam water molecules. By contrast, the addition of SiO_2 leads to the conversion of $CaCl_2$ into the form of $Ca_{10}(Si_2O_7)_3Cl_2$ which has a melting point of 1065 °C. The residue thus remains as fine solid particles with large porosity evident by the inset SEM picture. Such a large surface area and the inter-atomic clearance in the solid crystal clearly facilitates an easy dissociation of Cl, and an inward diffusion of steam to react with Cl radicals to form HCl. This finding is in line with the previous study [17].

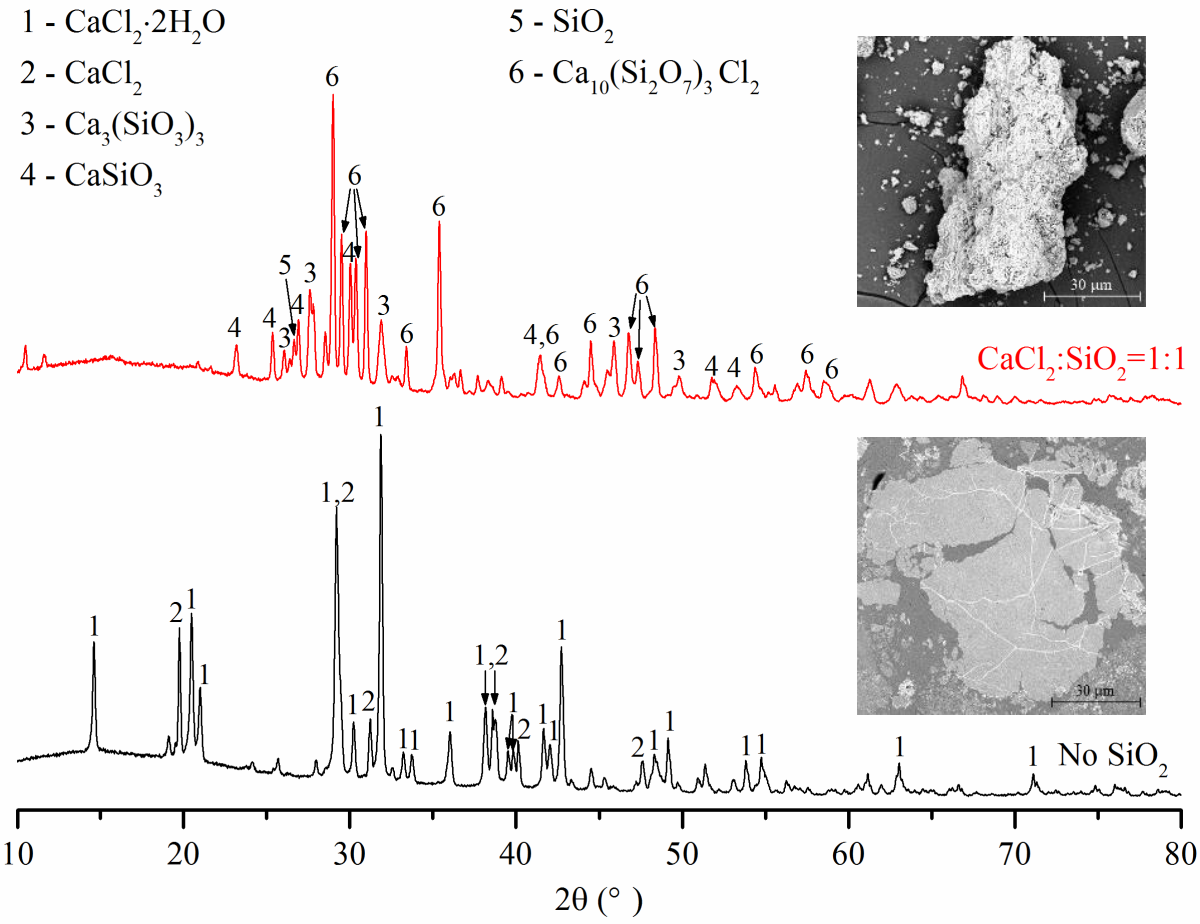

Figure 5.3 Effect of SiO_2 addition on the pyrohydrolysis of $CaCl_2$ at 1000 °C for 2 h. (The SEM of decomposition residue is included).

5.3.2 Co-pyrohydrolysis of $CaCl_2$ and $MgCl_2$ in the presence of silica

5.3.2.1 HCl release from $CaCl_2$ as a function of temperature

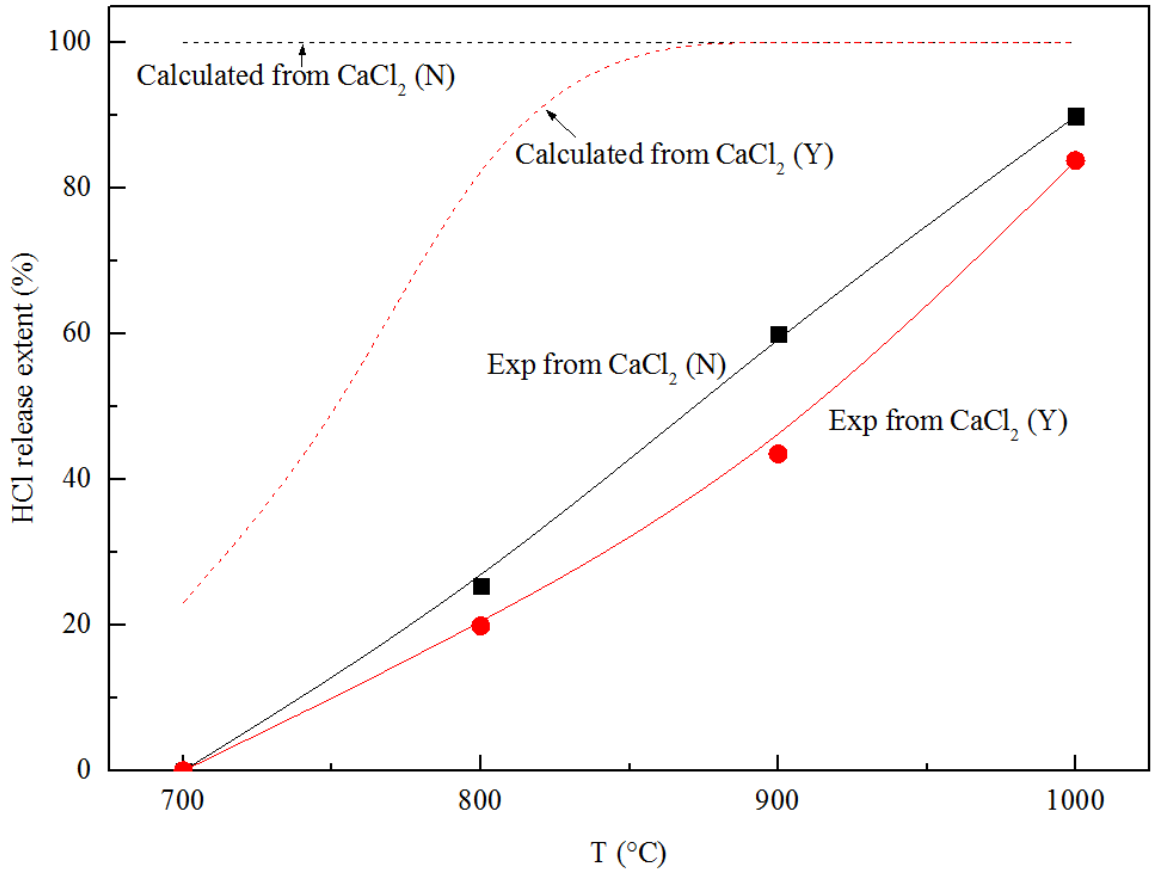

Figure 5.4 Experimental and Factsage calculated HCl release extent with and without $MgCl_2$ addition versus reaction temperature. (Y and N in parenthesis refer to the cases with and without $MgCl_2$ addition, respectively; solid and dash lines are for the experimental and calculated results, respectively; molar ratio of $CaCl_2$:$MgCl_2$ = 1:4).

Figure 5.4 shows both the experimental and thermodynamic equilibrium prediction results for the co-pyrohydrolysis of $CaCl_2$ and $MgCl_2$ at a fixed molar ratio of 1:4 and different reaction temperatures. Note that, for the experimental works conducted at different temperatures, the X-axis refers to the terminal temperature to which the samples have reached upon a non-isothermal heating. Once the terminal temperature was reached, the solid residues were quickly quenched. Moreover, considering the full decomposition of $MgCl_2$ before 700 °C, the Y-axis was calculated for the HCl release extent from $CaCl_2$ alone, by assigning the remaining Cl in

the residue to $CaCl_2$. For all the conditions examined here, the molar ratio of silica was fixed as 1 mole/mole to $CaCl_2$.

In principle, upon the absence of $MgCl_2$, $CaCl_2$ alone can decompose entirely into HCl from 700 °C. The addition of $MgCl_2$ would however postpone the full decomposition of $CaCl_2$ until 900 °C, due to their competition on the inclusion into silica matrix. However, the experimental investigation reveals a very slow release of HCl from $CaCl_2$, irrespective of the addition of $MgCl_2$. This is an indicator of the kinetic control for the overall reaction before 1000 °C. At 1000 °C, the HCl release extent is much closer to the thermodynamic prediction, demonstrating a diminutive effect of the kinetic control. Moreover, the inhibitory effect of $MgCl_2$ is experimentally confirmed, which commences at 800 °C, maximises at 900 °C, but slightly reduces at 1000 °C. Apparently, this links with the change on the crystalline structures of the Cl-bearing residue and its intermediates.

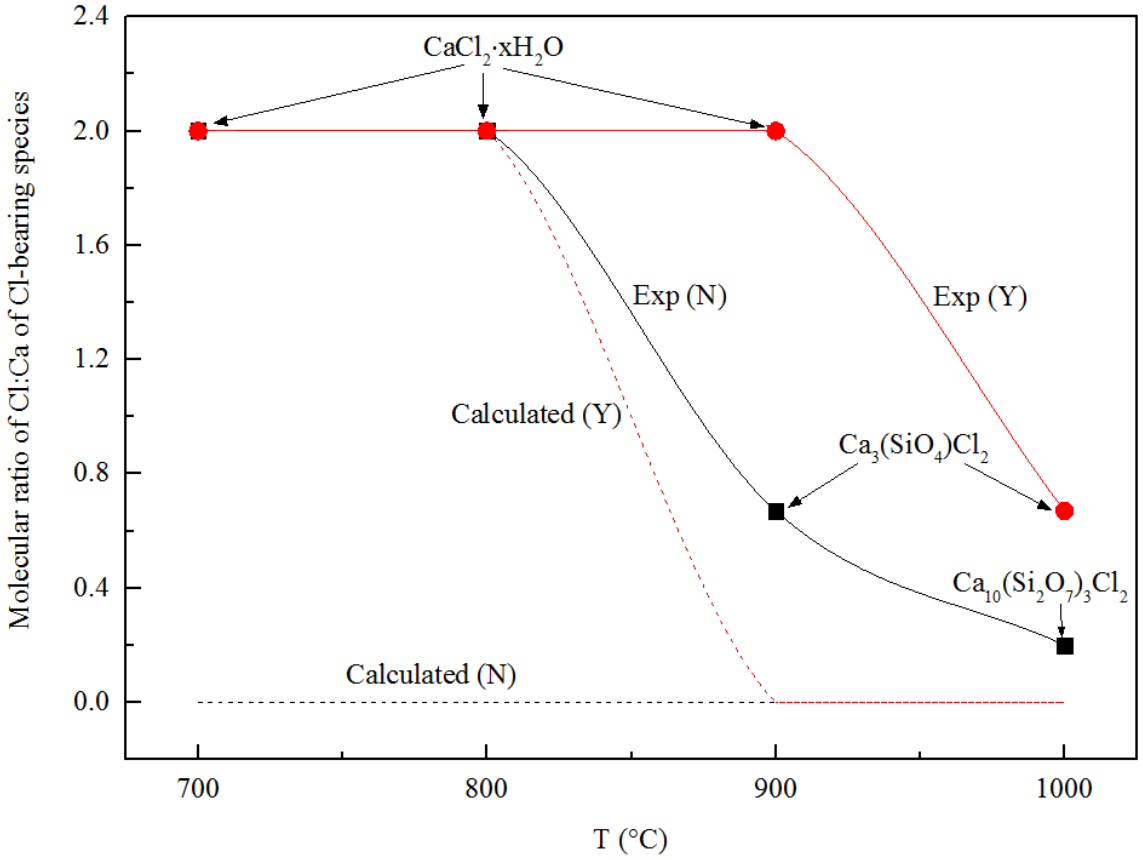

Figure 5.5 Molecular ratio of Cl/Ca of the Cl-bearing species in the decomposition residues obtained from experiments and Factsage calculations versus reaction temperature. (Y and N Y and N in parenthesis refer to the cases with and without $MgCl_2$ addition, respectively; Experimental results were determined by XRD).

Considering that each residue only contained one Cl-bearing species which also consists of Ca (due to the strong affinity of these two elements), the molecular ratio of Cl/Ca of the Cl-bearing species in the resultant residue is plotted versus reaction temperature as solid lines in **Figure 5.5**. For comparison, the thermodynamic equilibrium calculation results are included as dash lines. According to the thermodynamic equilibrium prediction, no Cl-bearing species is present (thus Cl/Ca = 0) for the case of $CaCl_2$ alone across the whole temperature range. In contrast, $CaCl_2$ remains stable until 900 °C for the case of the addition of $MgCl_2$. This proves the

thermodynamic preference for the inclusion of MgO (derived from $MgCl_2$) into the silica matrix before 900 °C. With regard to the experimental observation, $CaCl_2$ disappears at 900 °C when no $MgCl_2$ is added, converting into $Ca_3(SiO_4)Cl_2$ as the sole Cl-bearing component with a molar Cl/Ca ratio of 0.67, relative to 2.0 for $CaCl_2$. Upon a further rise of the temperature to 1000 °C, the Cl-bearing species converts into $Ca_{10}(Si_2O_7)_3Cl_2$ with a Cl/Ca ratio of 0.2, demonstrating the continuous release of the remaining Cl out of the Ca-Cl affinity. The remaining Cl should be tightly embedded within the matrix, and hence, not able to be released easily. Regarding the case with $MgCl_2$ addition, $CaCl_2$ does not disappear until the temperature reaches 1000 °C where $Ca_3(SiO_4)Cl_2$ with a Cl/Ca molar ratio of 0.67 is formed. Clearly, the addition of $MgCl_2$ delays the formation of the above two intermediate products that are not predicted by the thermodynamic equilibrium model at all. The stronger ability of MgO to react with SiO_2 agrees with the calculation results.

5.3.2.2 HCl release from $CaCl_2$ as a function of reaction time at 1000 °C

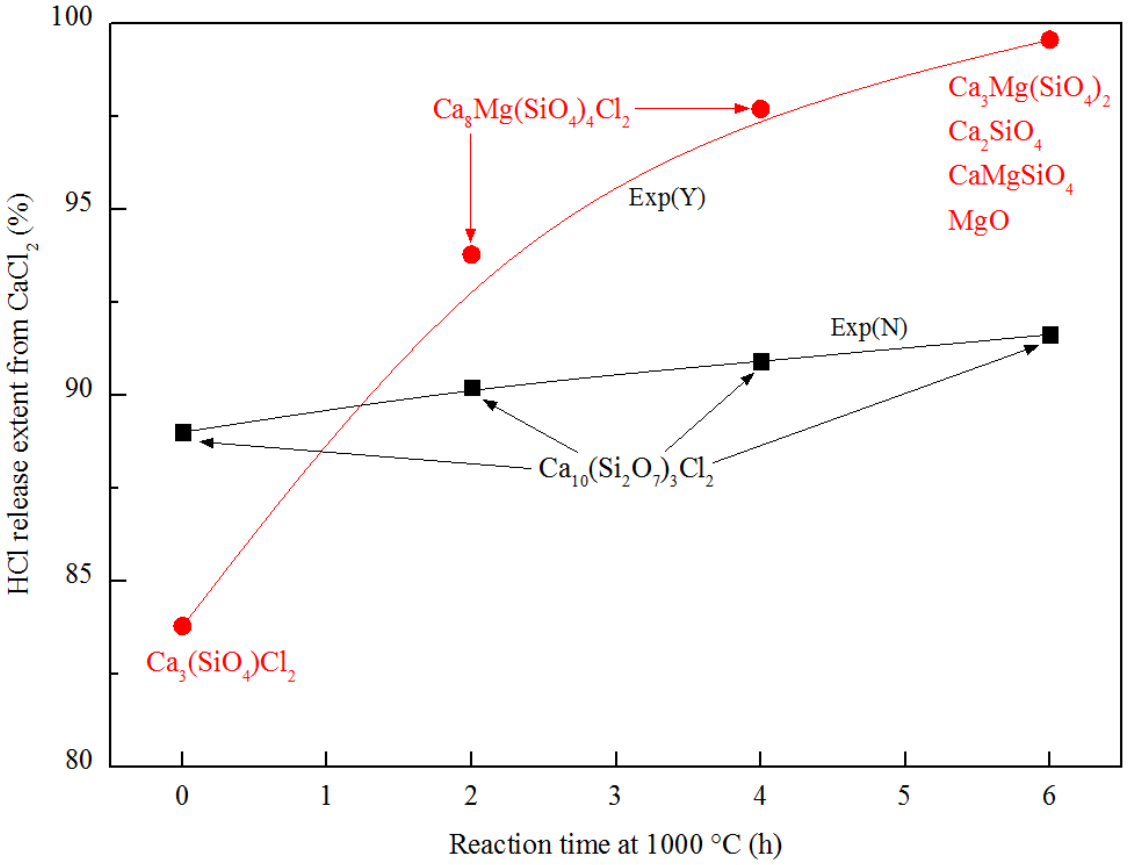

Figure 5.6 Experimental HCl release extents from $CaCl_2$ with and without $MgCl_2$ after different reaction time at 1000 °C. (The Cl-bearing species determined by XRD is included).

To further narrow down and even eliminate the inhibitory effort of $MgCl_2$, different retention time at 1000 °C was experimentally explored. The resultant residues were characterised by XRD. **Figure 5.6** compares the HCl release extent with and without the addition of $MgCl_2$ as a function of retention time, where the principal Cl-bearing species and other major compounds in the residues are also listed. As expected, the HCl release extent with the addition of $MgCl_2$ is slightly lower than that without $MgCl_2$ at the beginning, 84% versus 89%. Interestingly, the HCl release extent upon the addition of $MgCl_2$ increases quickly to 94% after a retention period of 2 h, overtaking the value achieved in the absence of $MgCl_2$ that is almost unchanged. It

further increases exponentially, reaching almost 100% in 6 h. Clearly, the effect of $MgCl_2$ addition turns positive upon the increase in the reaction time at 1000 °C.

For the absence of $MgCl_2$, $Ca_{10}(Si_2O_7)_3Cl_2$ is the only Cl-bearing species in the residue, regardless of the retention time. It is transformed from $Ca_3(SiO_4)Cl_2$, which is also the only Cl-bearing species at 900 °C (**Figure 5.5**). Upon the addition of $MgCl_2$, the Cl-bearing species changes its structure from $Ca_3(SiO_4)Cl_2$ (Cl/Ca = 0.67) to $Ca_8Mg(SiO_4)_4Cl_2$ (Cl/Ca =0.25), and then to the mixture of $Ca_3Mg(SiO_4)_2$, Ca_2SiO_4 and $CaMgSiO_4$ with none of them containing Cl at all.

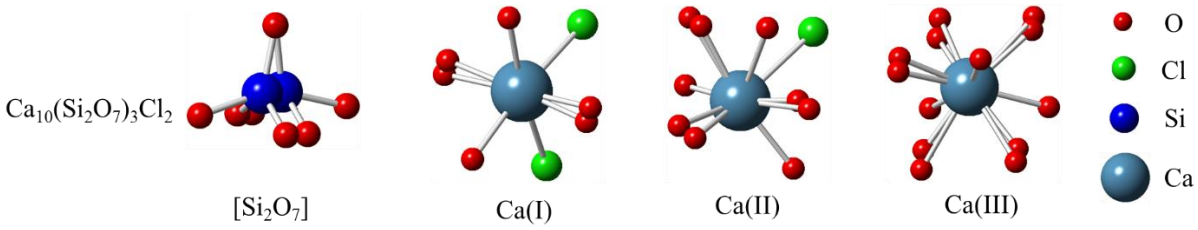

Figure 5.7 Crystal structure of $Ca_{10}(Si_2O_7)_3Cl_2$ obtained by CrystalMaker software (clusters size defined as 3 Å).

The crystal structure of $Ca_{10}(Si_2O_7)_3Cl_2$ is displayed in **Figure 5.7**. It holds a monoclinic structure with a pace group $P2_1/a$ [21-23]. Its basic skeleton is made of isolated groups of $[Si_2O_7]^{6-}$, which are 'face-sharing', as shown in **Figure 5.7**. Each $[Si_2O_7]^{6-}$ is transformed from two units of $[SiO_4]^{4-}$ (the basic skeleton of $Ca_3(SiO_4)Cl_2$) via sharing one oxygen apex. The isolated $[SiO_4]^{4-}$ only exists in the case of sufficient cations to reach a charge balance [23]. In other words, when the molar ratio of $CaCl_2/SiO_2$ is only one in this study, the molar amount of Ca^{2+} is far from enough to establish a $[SiO_4]^{4-}$-based structure requiring a molar ratio of Ca/Si≥2.

Consequently, $[SiO_4]^{4-}$ sites may have to combine on its own to transform into a $[Si_2O_7]^{6-}$-based structure, $Ca_{10}(Si_2O_7)_3Cl_2$ with a smaller Ca/Si of 1.67. This is accompanied by the combination of a portion of silica (SiO_2) with free Ca^{2+} to form another state species, $CaSiO_3$ and unreacted SiO_2 due to the insufficiency of Ca^{2+}. Back to the sole Cl-bearing species $Ca_{10}(Si_2O_7)_3Cl_2$, $[Si_2O_7]^{6-}$ is 'face-sharing' in its atomic structure, in which calcium ions of three types are coordinated with oxygens and/or chlorines. Ca(I) is coordinated with two chlorine and six oxygen, Ca(II) with one chlorine and nine oxygen, and Ca(III) with thirteen oxygen [23]. The remarkable ionic polarisation between Ca^{2+} and its adjacent anions (O^{2-} and Cl^-) might induce the deviation of their electron clouds to each other, thus leading to varying degrees of overlap of their outer orbitals. Consequently, the bond length and polarity of Ca-Cl decrease, resulting in a transformation of the Ca-Cl bond from purely ionic to 'intermediate bond' with the properties of covalent bond.[23] This is beneficial for the release of Cl out of the solid matrix.

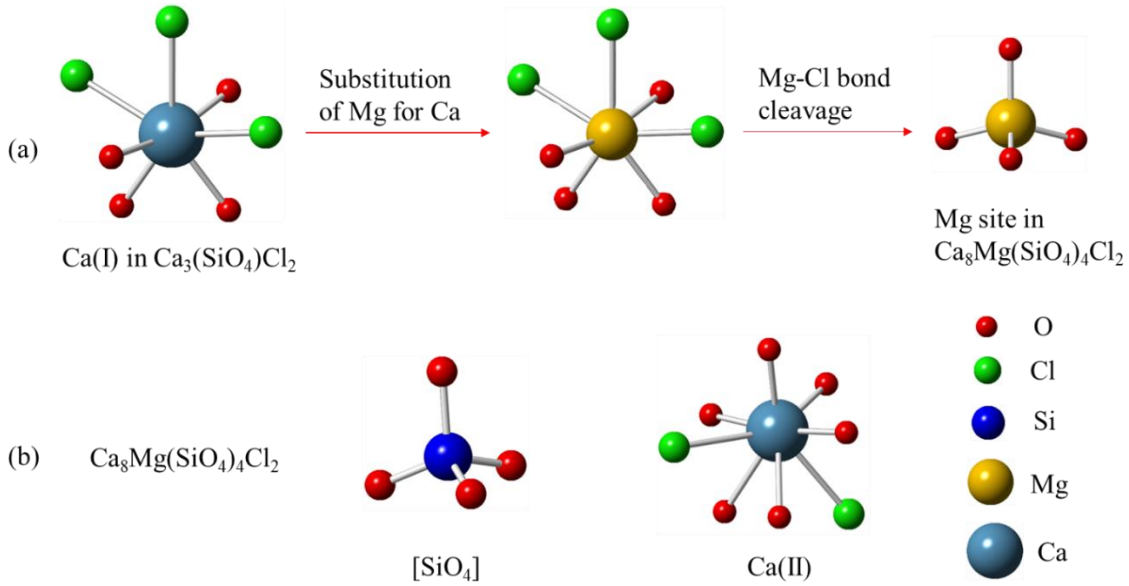

Figure 5.8 Role of Mg in the formation process of $Ca_8Mg(SiO_4)_4Cl_2$ from $Ca_3(SiO_4)Cl_2$ *(a)* and the local atomic environments of Si and Ca(II) in $Ca_8Mg(SiO_4)_4Cl_2$ *(b)*.

Regarding the addition of $MgCl_2$, $Ca_3(SiO_4)Cl_2$ forms at the reaction time of 0 h is of a monoclinic structure, with space group $P2_1/c$ and $[SiO_4]^{4-}$ tetrahedrons as the basic skeleton.[24] It was studied that a portion of Ca^{2+} in this species is present as Ca(I) that stays in between the lamellar layers of $[SiO_4]^{4-}$ tetrahedrons, being the mostly weakly bonded and thus the most favourably substituted by any other divalent cations such as Mg^{2+}. Instead, the remaining Ca^{2+} as Ca(II) and Ca(III) sitting in the plane of $[SiO_4]^{4-}$ tetrahedrons are too tough to be substituted [24]. A portion of Ca(I) in $Ca_3(SiO_4)Cl_2$ is gradually substituted by Mg^{2+} and transferred into $Ca_8Mg(SiO_4)_4Cl_2$, as shown in **Figure 5.8**(a). The resultant Mg-Cl bonds easily breaks down and releases the Cl. Such a solid-solid substitution reaction is obviously slow, and hence, its effect is only observed when the reaction time is extended to 2 h at 1000 °C. In addition, a portion of the original silica is consumed by Mg^{2+} to form magnesium silicates, leading to sufficient cations to balance the negative charges of the $[SiO_4]^{4-}$ skeleton. In other words, the addition of Mg^{2+} inhibits the self-combination of $[SiO_4]^{4-}$. In terms of the Ca^{2+} coordination environment, Ca(II) as the only site bonded with chlorine is coordinated with six oxygen and two chlorines, as illustrated in **Figure 5.8**(b). It is affiliated with less anions (O^{2-} and Cl^-) than in $Ca_{10}(Si_2O_7)_3Cl_2$. This may result in weaker ionic polarisation between the Ca^{2+} and adjacent anions and the longer bonds of Ca-Cl in $Ca_8Mg(SiO_4)_4Cl_2$ [21, 22, 25, 26]. Consequently, the Cl release is easier from $Ca_8Mg(SiO_4)_4Cl_2$ than $Ca_{10}(Si_2O_7)_3Cl_2$. Upon the release of Cl, the skeleton of $Ca_8Mg(SiO_4)_4Cl_2$ collapses gradually, leading to the formation of various nesosilicates including Ca_2SiO_4, $Ca_3Mg(SiO_4)$ and $CaMgSiO_4$.

5.3.2.3 Effect of $MgCl_2$ amount on the HCl release from $CaCl_2$

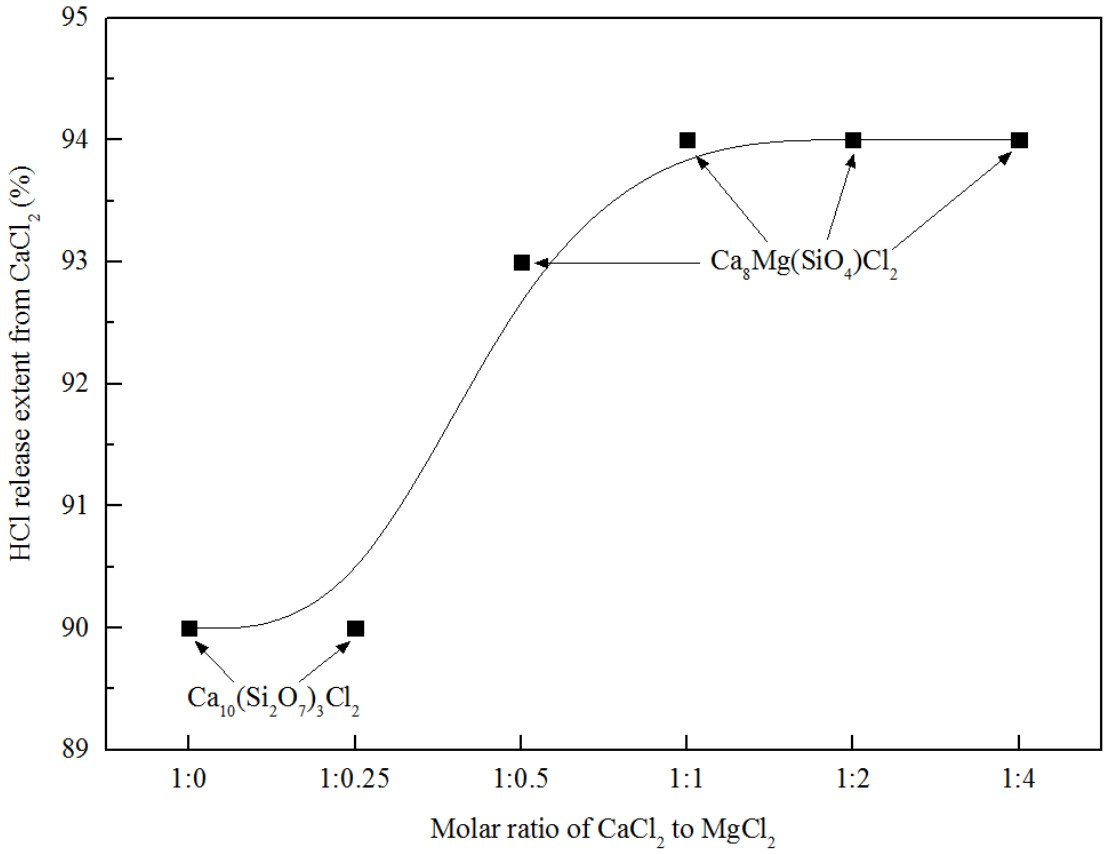

Figure 5.9 Effect of the $MgCl_2$ addition amount on the HCl release from $CaCl_2$ at 1000 °C for 2 h obtained by experiments. (The Cl-bearing species determined by XRD is also included here).

Last effort was made to further confirm and optimise the promotion effect of $MgCl_2$ addition at 1000 °C. The decomposition experiments were conducted by mixing various amounts of $MgCl_2$ into the mixture of $CaCl_2$ and SiO_2 at equi-molar ratio at 1000 °C for 2 h. As demonstrated in **Figure 5.9** for both HCl release extent from $CaCl_2$ and the major Cl-bearing species in the residues, the HCl release extent is almost stabilised at 90% at the $MgCl_2$ addition ratio less than 0.25, and then experiences a notable increase to approximately 94% at the equi-molar ratio between these two chlorides. Again, this is due to the transferring of Cl-bearing

species from $Ca_{10}(Si_2O_7)_3Cl_2$ to $Ca_8Mg(SiO_4)_4Cl_2$ that is formed at the Mg/Ca molar ratio of 0.5 and above. Clearly, the $Ca_8Mg(SiO_4)_4Cl_2$ is fully saturated and stabilised at this ratio. The excessive $MgCl_2$ added simply converts into free MgO. The reason for optimum dosage of 0.5 mole $MgCl_2$/mole $CaCl_2$ should be attributed to the atomic coordination structure of $Ca_8Mg(SiO_4)_4Cl_2$. A robust explanation from atomic perspective will be necessary.

5.4 Conclusions

Upon the assistance of silica and steam, HCl has been successfully recovered from the co-pyrohydrolysis of alkaline earth metal chlorides ($CaCl_2$ and $MgCl_2$). The effects of a variety of variables have been examined, including reaction temperature and time, and molar ratio between two alkaline earth chlorides. In particular, the synergistic effect of $MgCl_2$ on the pyrohydrolysis of $CaCl_2$ has been discussed extensively. As far as the authors are aware, a double-sided effect of the $MgCl_2$ addition has been revealed for the first time in this study: *1)* impediment of HCl release in the temperature-rise period (700−1000 °C) via competing with $CaCl_2$ for inclusion into the solid silica matirx; *2)* promotion of HCl release in the retention period at 1000 °C through the formation of an intermediate Cl-bearing compound, $Ca_8Mg(SiO_4)_4Cl_2$, in which the weaker ionic polarisation between the Ca^{2+} and adjacent anions facilitates the release of Cl as HCl. Additionally, the addition of 0.5 mole $MgCl_2$/mole of $CaCl_2$ is found as the optimal dosage, which increases the HCl release notably due to the formation of $Ca_8Mg(SiO_4)_4Cl_2$.

This study is primarily significant for the environmental management of the chloride wastes which has not yet found a viable manner for the disposal. Additionally, this study and the results achieved are critical to a variety of hydrometallurgy processing industry, in which the

HCl acid recovery from the alkaline earth metal chloride is a critical step to improve both the environmental friendliness and cost-effectiveness. Upon a successful regeneration from the solid chlorides, the resultant HCl gas can be further reused in the process, while the resultant oxide residues are applicable for a variety of downstream applications such as cement additives [27]. Although the engineering design was not touched based in this study, a rotary kiln or fluidised bed is apparently suitable for the pyrohydrolysis of alkaline earth chloride wastes since it allows a longer residence time and sufficient mixing of chlorides and SiO_2. Future works will be conducted specifically to explore the overall reaction rate and the optimum conditions underpinning the design and operation of the specific equipment, in particular the pyrohydrolysis reaction rate of saturated droplet that is supposedly injected into a fluidised bed.

Reference

1. McKinley, C.; Ghahreman, A., Hydrochloric acid regeneration in hydrometallurgical processes: a review. *Mineral Processing and Extractive Metallurgy* **2017**, 1-12.
2. Rice, N. M., A hydrochloric acid process for nickeliferous laterites. *Minerals Engineering* **2016**, *88*, 28-52.
3. Cheng, Y.; Sato, A.; Ninomiya, Y.; Dong, Z., Kinetic study of chlorine behavior in the waste incineration process. *Proceedings of the Combustion Institute* **2009**, *32*, (1), 335-342.
4. Domazetis, G.; Barilla, P.; James, B., Lower emission plant using processed low-rank coals. *Fuel Processing Technology* **2010**, *91*, (3), 255-265.
5. Faverjon, F.; Durand, G.; Rakib, M., Regeneration of hydrochloric acid and sodium hydroxide from purified sodium chloride by membrane electrolysis using a hydrogen diffusion anode-membrane assembly. *Journal of Membrane Science* **2006**, *284*, (1), 323-330.
6. Janssen, L. J. J.; Hoogland, J. G., The electrolysis of an acidic NaCl solution with a graphite anode—III. Mechanism of chlorine evolution. *Electrochimica Acta* **1970**, *15*, (6), 941-951.
7. Yan, X. Y.; Fray, D. J., Molten Salt Electrolysis for Sustainable Metals Extraction and Materials Processing—A Review. *Electrolysis: Theory, Types and Applications, S. Kuai and J. Meng, eds., Nova Science, New York* **2010**.
8. Du, F.; Warsinger, D. M.; Urmi, T. I.; Thiel, G. P.; Kumar, A.; Lienhard V, J. H., Sodium Hydroxide Production from Seawater Desalination Brine: Process Design and Energy Efficiency. *Environmental Science & Technology* **2018**, *52*, (10), 5949-5958.
9. Hosseini, T.; Han, B.; Selomulya, C.; Haque, N.; Zhang, L., Chemical and morphological changes of weathered Victorian brown coal fly ash and its leaching characteristic upon the leaching in ammonia chloride and hydrochloric acid. *Hydrometallurgy* **2015**, *157*, 22-32.
10. Hosseini, T.; Selomulya, C.; Haque, N.; Zhang, L., Indirect carbonation of victorian brown coal fly ash for CO2 sequestration: multiple-cycle leaching-carbonation and magnesium leaching kinetic modeling. *Energy & Fuels* **2014**, *28*, (10), 6481-6493.
11. Zhou, S.; Hosseini, T.; Zhang, X.; Haque, N.; Zhang, L., Selective removal of sodium and calcium from low-rank coal–Process integration, simulation and techno-economic evaluation. *Fuel Processing Technology* **2018**, *172*, 13-28.

12. Akarsu, H.; Yildirim, M., Leaching rates of Icel-Yavca dolomite in hydrochloric acid solution. *Mineral Processing and Extractive Metallurgy Review* **2007**, *29*, (1), 42-56.
13. Royani, A.; Sulistiyono, E.; Prasetiyo, A. B.; Subagja, R. In *Extraction of magnesium from calcined dolomite ore using hydrochloric acid leaching*, AIP Conference Proceedings, 2018; AIP Publishing: 2018; p 020017.
14. Yan, Y.; Xuchen, L. U.; Wang, T.; Zhang, Z., A review on the technologies of high-purity magnesia production from brine. *Chemical Industry & Engineering Progress* **2016**.
15. Huang, Q.; Lu, G.; Wang, J.; Yu, J., Thermal decomposition mechanisms of MgCl2·6H2O and MgCl2·H2O. *Journal of Analytical and Applied Pyrolysis* **2011**, *91*, (1), 159-164.
16. Kerr, J. A.; Stocker, D., Strengths of chemical bonds. *CRC Handbook of Chemistry and Physics* **1993**, *9*, (144), 9-145.
17. Otake, T., Involvement of Solid Acids in the Thermal Decomposition of Calcium Chloride. *Kagaku Kogaku Ronbunshu* **1983**, *9*, 523-529.
18. Website of CrytalMaker Software. http://crystalmaker.com/
19. Jiao, F.; Iwata, N.; Kinoshita, N.; Kawaguchi, M.; Asada, M.; Honda, M.; Sueki, K.; Ninomiya, Y., Vaporization mechanisms of water-insoluble Cs in ash during thermal treatment with calcium chloride addition. *Environmental science & technology* **2016**, *50*, (24), 13328-13334.
20. Patnaik, P., *Handbook of inorganic chemicals*. McGraw-Hill New York: 2003; Vol. 529.
21. Ruilun, Y.; Bolin, W.; Ke, Z.; Zeying, Z., The properties and the crystal structure of the compound $Ca_{10}Si_6O_{21}Cl_2$ in the three component system CaO-SiO2-$CaCl_2$. *Journal of the Chinese Ceramic Society* **1986**, (02), 57-64.
22. Środek, D.; Juroszek, R.; Krüger, H.; Krüger, B.; Galuskina, I.; Gazeev, V., New Occurrence of Rusinovite, Ca10 (Si2O7) 3Cl2: Composition, Structure and Raman Data of Rusinovite from Shadil-Khokh Volcano, South Ossetia and Bellerberg Volcano, Germany. *Minerals* **2018**, *8*, (9), 399.
23. Qitu, Z., *Inorganic materials*. East China University of Science and Technology: 2010.
24. Gilbert, M., Site selectivity of dopant cations in Ca3 (SiO4) Cl2. *Journal of Physics and Chemistry of Solids* **2014**, *75*, (8), 1004-1009.

25. Lei, B.; Sha, L.; Zhang, H.; Liu, Y.; Man, S.-q.; Yue, S., Preparation and luminescence properties of green-light-emitting afterglow phosphor Ca8Mg (SiO4) 4Cl2: Eu2+. *Solid State Sciences* **2010**, *12*, (12), 2177-2181.

26. Cotton, A. F.; Wilkinson, G.; Bochmann, M.; Murillo, C. A., *Advanced inorganic chemistry*. Wiley: 1999.

27. Qian, B.; Li, X.; Shen, X., Preparation and accelerated carbonation of low temperature sintered clinker with low Ca/Si ratio. *Journal of Cleaner Production* **2016**, *120*, 249-259.

Chapter 6
Atomic Structures of Cl and Ca Derived from the Co-Pyrohydrolysis of Alkaline Earth Metal Chloride Wastes

It has been approved that 99% Cl can be released from the mixture of $CaCl_2$ and $MgCl_2$ at 1000 °C in chapter 5. However, the interaction between Ca^{2+} and Mg^{2+} in terms of their affinity with Cl^- at the co-pyrohydrolysis which is crucial for the exploration of Cl release cannot be unveiled from atomic structural level via XRD analysis. Consequently, a substantial interpretation of the mechanism upon the effect of $MgCl_2$ additions is absent. This chapter has studied the local atomic structure of chlorine (Cl) and its transformation upon the interaction between different cations during the co-pyrohydrolysis of $CaCl_2$ and $MgCl_2$ for the regeneration of HCl. An advanced analysis technique, synchrotron X-ray absorption spectroscopy (XAS) was used to fingerprint the Cl K-edge XANES spectra and Ca K-edge EXAFS spectra. In particular, the change on the local atomic environment of Ca^{2+} upon the intrusion of Mg^{2+} atom was interpreted. Consequently, an intermediate structure of Ca-O-Mg_y-Cl_x was revealed to address the synergism between these two cations in the atomic coordination environment level. This chapter has been reformatted from a manuscript which has been submitted to ***Journal of Hazardous Materials***: **Zhou, S.**; Qian, B.; Liu, C.; Hosseini, T.; Zhang, L., *Synchrotron X-Ray Absorption Spectroscopy (XAS) study on the atomic structures of chlorine and calcium derived from the co-pyrohydrolysis of alkaline earth metal chloride wastes*. ***Journal of Hazardous Materials*** 2019 (**Under review**).

Abstract

Chlorine (Cl) speciation and its atomic structures in high-temperature pyrohydrolysis-derived silicate crystals affect both its recovery as HCl gas and environmental impacts upon landfilling. However, they are poorly understood. This study for the first time investigated the local atomic environments of Cl and calcium (Ca) in various silicate crystals obtained from the co-pyrohydrolysis of Ca/$MgCl_2$ under 700-1000 °C, and at the co-existence of steam and silica. Synchrotron X-ray absorption spectroscopy (XAS) was employed for the detailed coordination environments of both elements. As have been found, the silicate crystals derived from pyrohydrolysis are highly ordered in the crystal structures, and bear less resemblance to $CaCl_2$ than those reported in the glassy melts. Unambiguous evidence for a mixed cation Ca-Mg_y-Cl_x intermediate (proposed elsewhere) was not found, since Ca^{2+} is always preferentially bound with O^{2-} at its first atomic shell. Instead, it is very likely that an intermediate form of Ca-O-Mg_y-Cl_x is formed from the co-pyrohydrolysis of the two chlorides, based on the co-existence of Mg^{2+} and Cl^- on the second shell centred on the Ca^{2+}. Consequently, the intrusion of Mg^{2+} compels the third shell which comprises of Ca^{2+} to go far away, causing a less-crystalline structure and thus promoting the Cl release.

Keywords: Pyrohydrolysis; Alkaline earth metal chlorides; Silicate crystals; XANES; EXAFS

6.1 Introduction

Chlorine (Cl), whose compounds are toxic industrial chemicals in most cases, is involved in a broad variety of natural phenomena and industrial processes. In the Earth's crust, it occurs in silica melts and its transport in subduction settings is a fundamental part of the global Cl cycle [1, 2]. Additionally, Cl is being used intensively in hydrometallurgical leaching and extraction of brine and various ores [3]. However, one big hurdle to these processes is to dispose of the numerous waste chlorides, which have been widely proven to pose deleterious impacts to the environment, human health and the lifespan of industrial equipment [4-7]. As the majority of chlorides are extremely soluble and very mobile, and there is no natural process by which chlorides can be broken down, metabolized or removed [8]. Thus, studies have been carried out to immobile or reuse the chloride waste, such as vitrification of Cl-rich radioactive wastes into borosilicates, and pyrohydrolysis of chlorides for the regeneration of HCl [3, 9]. However, understanding the local chemical and structural environment for Cl in the high-temperature solids/melts is still far from completion, though it is essential for the effective release and/or recovery of Cl at high-temperature processes. This is mostly due to the relatively low concentrations of Cl and the extreme complexity of its affinity with other elements in the high-temperature solids and/or melts.

Synchrotron based X-ray absorption spectroscopy (XAS) is an advanced analysis for the concentrations of an element on the parts per million (ppm) level, referring to the modulation of an atom's X-ray absorption possibility due to its chemical and physical states [10, 11]. It typically consists of two regimes, X-ray absorption near-edge spectroscopy (XANES) for the coordination geometry and oxidation state of the absorbing atom, and extended X-ray absorption fine structure spectroscopy (EXAFS) for the detailed atomic coordination

environment, including bond length (*R*), coordination number (*n*) and disorder (Debye-Waller factor or σ^2) of atomic shells around the absorbing element. To date, this technique has been employed to determine the speciation of Cl in high-temperature synthetic glasses and natural ones [2]. However, the information achieved is sparse. In the silicate melts achieved under the typical crust subduction environment (*i.e.* 1250 °C and 0.5 GPa), emphasis was given to prove the existence of mixed Ca-Mg_y-Cl_x species in the melts. However, unambiguous evidence was not found yet [2]. Similarly, in the borosilicate melts derived from Cl-bearing radioactive wastes, efforts were made to reveal the atomic structure of Cl upon its affinity with Ca in both Ca-rich and Ca-lean glasses, upon the co-existence of alkali metals (sodium and potassium). However, attention was not paid to magnesium although it is also present in most of the borosilicate samples [9]. In addition, as far as the authors are aware, no study has yet been conducted on the speciation of Cl derived from high-temperature pyrohydrolysis reaction which is a critical step for the regeneration of HCl in the mineral processing industry [12]. Compared to the melting conditions detailed elsewhere [2, 9], the pyrohydrolysis usually employs a temperature up to 1000 °C and hence, the resultant solid products/residues are still present in a solid or semi-solid state.

This study aims to clarify the Cl speciation, in particular its local coordination with both Ca^{2+} and Mg^{2+} in the solid residues derived from the co-pyrohydrolysis of $CaCl_2$ and $MgCl_2$ under different conditions. Silica was added into the chloride mixture to assist the cleavage of the strong Ca-Cl ionic bond, facilitating the formation of unstable Ca-Cl-Si intermediates that is in favour of the HCl release. Moreover, depending on the reaction temperature, the co-existence of $MgCl_2$ can either weaken the Ca-Cl affinity in the silica matrix, or compete against $CaCl_2$ for the reaction with silica (thus inhibits the Ca-Cl breakage) [12]. Upon a bench-scale X-ray diffraction (XRD) analysis, it was inferred that the promotive effect of Mg^{2+} might be attributed

to the substitution of a portion of Ca^{2+} by Mg^{2+} in the Cl-bearing silicate matrix, thus distorting and breaking the Ca-Cl bond. However, the mixed Ca-Mg_y-Cl_x intermediate cannot be confirmed from the XRD analysis, and a solid evidence for the explanation of the promotion effect of Mg^{2+} was also absent. Bearing these in mind, we have further conducted synchrotron XAS (XANES and/or EXAFS) for the fingerprints of both Ca^{2+} and Cl^- in the pyrohydrolysis residues, aiming to explore the existence of the above-mentioned mixed chloride and any other intermediates using this highly sensitive instrument with a strong focus on the atomic structure. Such an effort is expected to promote the understanding of the interaction between the two cations, Ca^{2+} and Mg^{2+} in terms of their affinity with Cl^- in non-molten silicates, which is an arguably interesting question for the knowledge related to chlorine in silicate matrix, and also helps us confirm the promotion mechanism of Mg^{2+} on the Cl release from the atomic perspective.

6.2 Experimental methodology

6.2.1 Pyrohydrolysis experiment

The detailed pyrohydrolysis experimental condition was provided in our previous study [12]. In brief, the mixture of $CaCl_2{\cdot}4H_2O$ and SiO_2 at an equi-molar ratio was completely blended with $MgCl_2{\cdot}6H_2O$, at varying Mg/Ca molar ratios from nil ($CaCl_2$ alone) to 4. All the reagents are chemical grade and mixed thoroughly prior to the test. The pyrohydrolysis was conducted in an electrical lab-scale horizontal furnace. For each test, the sample was loaded inside the furnace and then heated to the target temperature ranging from 700 to 1000 °C with an interval of 100 °C. The sample then remained at the target temperature for varying retention time from 0 to 6 h. A mixed gas of 70 v/v% steam in argon was continuously fed into the reactor to facilitate the pyrohydrolysis reaction. All the experimental conditions and the respective Cl

content in the pyrohydrolysis residues measured by X-ray fluorescence (XRF) is summarised in **Table 6.1**.

Table 6.1 Pyrohydrolysis conditions and the respective Cl (*wt%*) contents in the solid silicates.

Sample	Molar ratio of $CaCl_2$:$MgCl_2$	Reaction T (°C)	Reaction time at target T (h)	Cl content
$CaCl_2$	-	700	0	17.3
$CaCl_2$	-	800	0	14.8
$CaCl_2$	-	900	0	9.8
$CaCl_2$	-	1000	0	3.1
$CaCl_2$	-	1000	2	2.8
$CaCl_2$ & $MgCl_2$	1:4	700	0	10.7
$CaCl_2$ & $MgCl_2$	1:4	800	0	8.8
$CaCl_2$ & $MgCl_2$	1:4	900	0	6.7
$CaCl_2$ & $MgCl_2$	1:4	1000	0	2.1
$CaCl_2$ & $MgCl_2$	1:4	1000	2	0.8
$CaCl_2$ & $MgCl_2$	1:0	1000	2	2.8
$CaCl_2$ & $MgCl_2$	1:0.25	1000	2	2.6
$CaCl_2$ & $MgCl_2$	1:0.5	1000	2	1.8
$CaCl_2$ & $MgCl_2$	1:1	1000	2	1.5
$CaCl_2$ & $MgCl_2$	1:4	1000	2	0.8

6.2.2 XAS measurement

The XAS spectra were collected at the National Synchrotron Radiation Research Centre (NSRRC) in Taiwan on beamline BL16A1, which has a fixed exit double crystal Si (111) monochromator with a nominal beam size of 0.25 x 0.25 mm^2. This beamline can deliver monochromatic photons from 2 to 8 keV with an energy resolution of 0.5 eV. For the analysis of both standards and pyrohydrolysis residues, all the samples except $CaCl_2$ were further crushed in a nitrogen protection chamber and transferred onto a Cl-free kapton tape with a paintbrush. The $CaCl_2$ is highly hygroscopic and hence, the removal of its hydrate via a prior drying is implausible. However, this is not a problem since the nearest atom for Cl is Ca, rather than the hydrate oxygen (O) [2]. All the other samples including $MgCl_2$ were fully dried before the analysis. In particular, the dried $MgCl_2$ was immediately transferred to the sample chamber to avoid its secondary hydration. Hydrogen (H) has been reported to be the nearest atom next to Cl in the $MgCl_2$ hydrate [2]. Eight pieces of sample-ladden kapton type at a time were loaded on the sample holder and introduced into the sample chamber. For the Cl analysis, the sample chamber was purged with helium for minimum one hour to remove air prior to the analysis. This is however unnecessary for the Ca analysis. Both elements were analysed on the fluorescence mode, and the analysis of blank type did not detect any Cl and Ca signal.

Cl K-edge XANES spectra from 2622 eV to 2852 eV were only collected in this study, due to the interference of argon at an absorption edge of 3207 eV. The element Ru at 2838 eV was used for the energy calibration. In terms of the Ca K-edge, its full energy span for EXAFS analysis from -190 eV below to 250 eV above 4038 eV was recorded, and the element Sb at 4132 eV was employed for the energy calibration. Apart from the two pure chlorides ($CaCl_2 \cdot 2H_2O$ and dehydrated $MgCl_2$, crystalline reagents with a purity of >99% from Merck Ltd), three extra chloride references were synthesised and analysed, including $Ca_3SiO_4Cl_2$, $Ca_{10}(Si_2O_7)_3Cl_2$ and $Ca_8Mg(SiO_4)_4Cl_2$ that have been detected from the XRD analyses of the

pyrohydrolysis residues. These three standards were synthesised from analytical reagent grade chemicals including $CaCl_2$, CaO, SiO_2 and/or $MgCl_2{\cdot}6H_2O$, at 800 °C, 1000 °C and 1050 °C, respectively as per the procedure reported elsewhere [13-15]. The respective XRD patterns collected from Rigaku, Miniflex 600 with a scanning step of 0.02° are shown in **Figure 6.1**. As can be seen, no impurities were detected in the synthesised $Ca_8Mg(SiO_4)_4Cl_2$ and $Ca_3SiO_4Cl_2$. However, $Ca_{10}(Si_2O_7)_3Cl_2$ contains impurities including SiO_2, Ca_2SiO_4, and $CaSiO_3$. Since these inclusions do not contain Cl, their presence exerts no negative effect on the Cl XANES spectra at all [16].

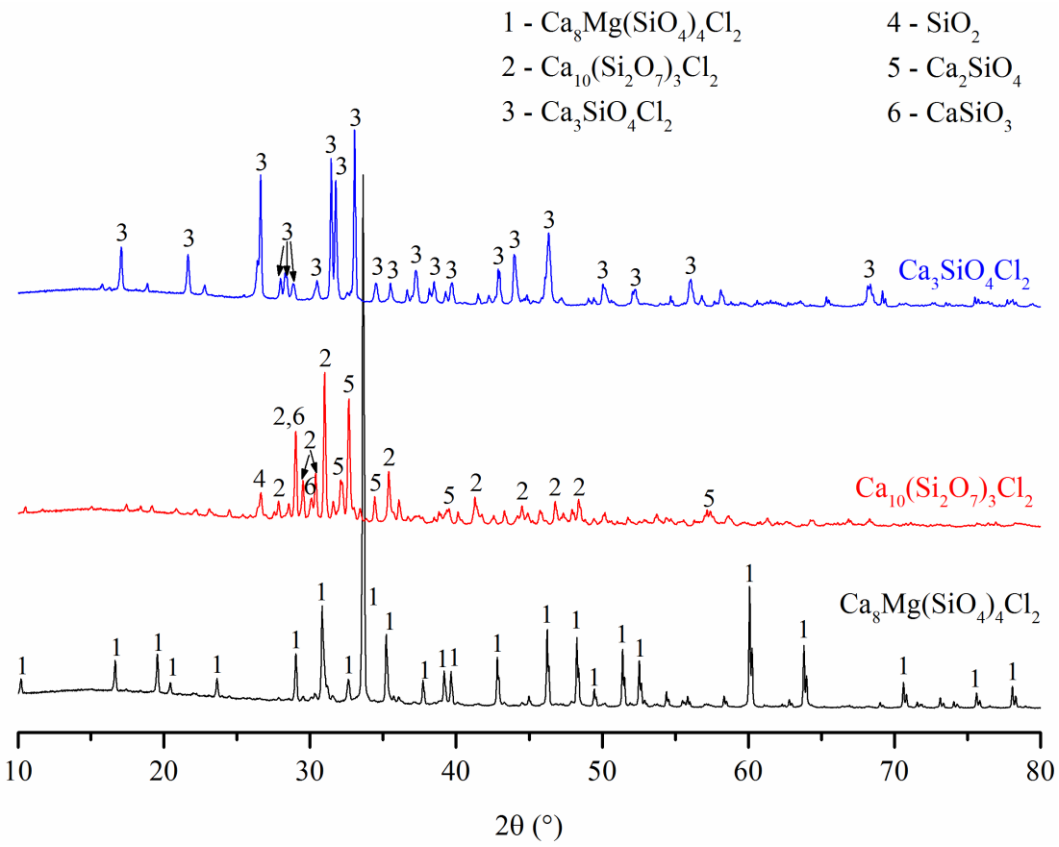

Figure 6.1 XRD patterns of reference calcium/magnesium silicate chlorides.

6.3 XAS data analysis

6.3.1 Cl XANES

All the Cl K-edge XANES spectra were processed using ATHENA software (a part of DEMETER package [17]) by conducting standard pre-edge linear background subtraction and normalisation [11]. Afterwards, the values of two parameters, E_{max} and E_0 were determined from the first derivative of the spectra. The former parameter refers to the position of the maximum first derivative for the main absorption edge, while the latter one represents the position of the energy where the first derivative passes through zero immediately after the main absorption edge, denoting the position of the first peak in the post-edge range [2]. In addition, linear combination fitting (LCF) was applied for the quantitative speciation of Cl. To evaluate the reliability of the LCF results, pure $CaCl_2{\cdot}2H_2O$ and $Ca_8Mg(SiO_4)_4Cl_2$ were mixed at five given mass ratios. Afterwards, the Cl K-edge XANES spectra were recorded for the mixtures, and the resultant XANES spectra were processed via LCF. **Figure 6.2** compares the LCF results and actual given percentages of $CaCl_2{\cdot}2H_2O$ in the mixture. It is clear that, the XANES measurement is reliable, offering a Cl signal in a linear proportion to the mass ratios of individual species. **Equation (1)** was thus derived for the calibration of the following LCF analysis in this study.

$$Y = 0.9823X + 0.0182 \qquad (1)$$

where X and Y refer to the $CaCl_2{\cdot}2H_2O$ percentage obtained by LCF analyses and its respective actual value in a standard $CaCl_2{\cdot}2H_2O$-$Ca_8Mg(SiO_4)_4Cl_2$ mixture, respectively.

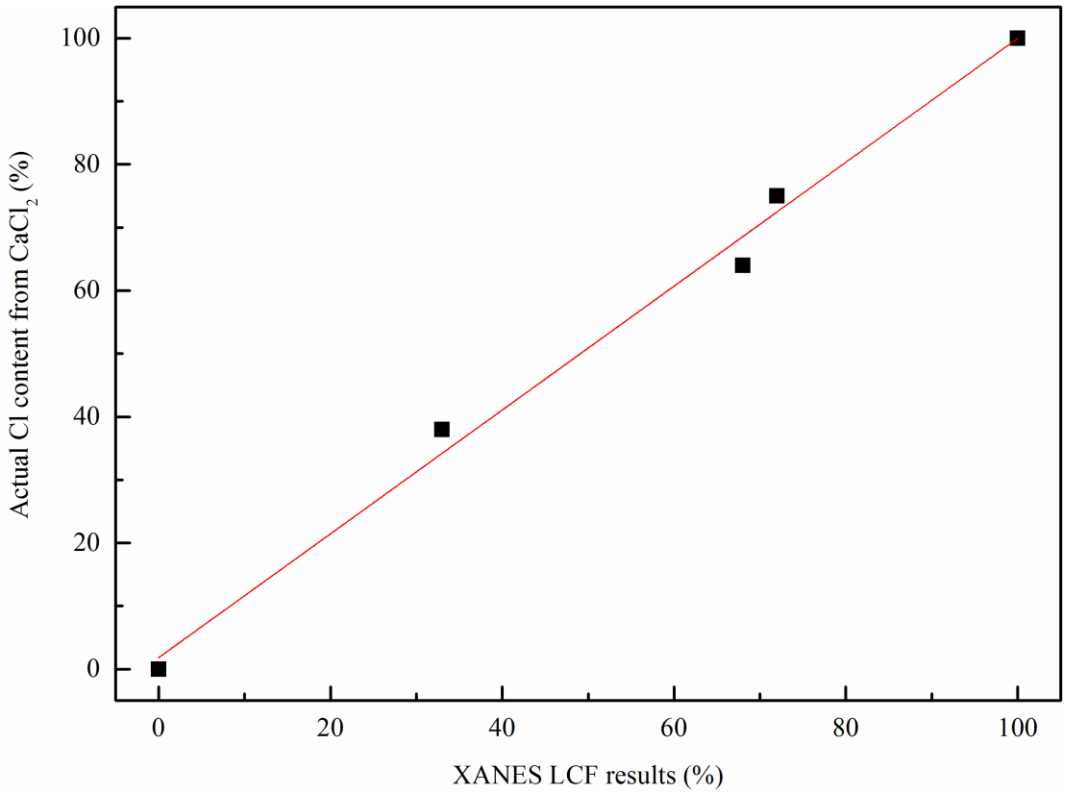

Figure 6.2 LCF analysis calibration of Cl K-edge XANES spectra.

6.3.2 Ca EXAFS

Ca EXAFS data were fitted using Artemis (part of Demeter) with FEFF version 8 [16]. The value s_0^2 (the scattering amplitude of photo-electron) was first determined to be 1.0 by fitting the pure reference $CaCl_2 \cdot 2H_2O$. This value was then used for the analyses of Ca K-edge EXAFS spectra across all the samples. The fitting result for pure $CaCl_2 \cdot 2H_2O$ based on the *R*-space is shown in **Figure 6.3**. The peaks correspond to different coordination spheres around the absorbing Ca atom, where *R* (bond length), *n* (coordination number) and σ^2 (Debye-Waller factor) for each atomic shell can be quantified. Due to the scattering phase shift, the peak position for atomic bond distance was found to be around 0.5 Å less than the actual bond distance [11]. For all the samples in this study, the fitting range was fixed at $1.0 \leq R \leq 3.5$ Å covering as many nearest-neighbour peaks as possible. The peaks beyond this range cannot be fitted due to the narrow *k*-

space EXAFS range ($2 \leq k \leq 7.9$ Å^{-1}). As can be observed in **Figure 6.3**, the predominant contribution to the Ca K-edge in $CaCl_2 \cdot 2H_2O$ consists of the Ca-O single scattering path at 2.32 Å and Ca-Cl path at 2.73 Å, which are very close to the reported bond length of Ca-O and Ca-Cl at 2.31 Å and 2.74 Å in $CaCl_2 \cdot 2H_2O$, respectively.

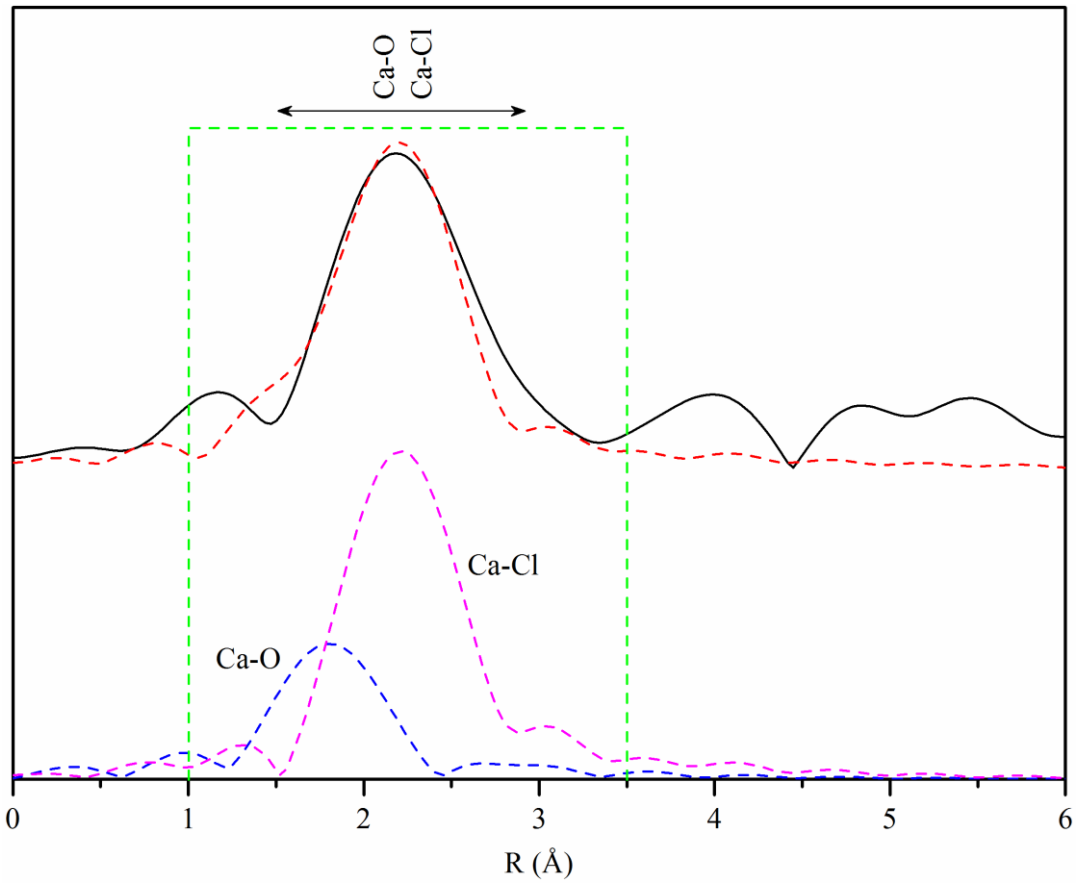

Figure 6.3 The fitting result of the Fourier transform of Ca K-edge EXAFS spectrum for the reference $CaCl_2 \cdot 2H_2O$. The solid (in black) and dashed (in red) curves refer to the measured and fitted EXAFS spectrum, respectively. The fitting range is shown by the green dashed line. The scattering paths of Ca-O and Ca-Cl are indicated as blue dash and pink dash, respectively.

6.4 Results and discussion

6.4.1 Cl XANES

6.4.1.1 Cl-bearing standards

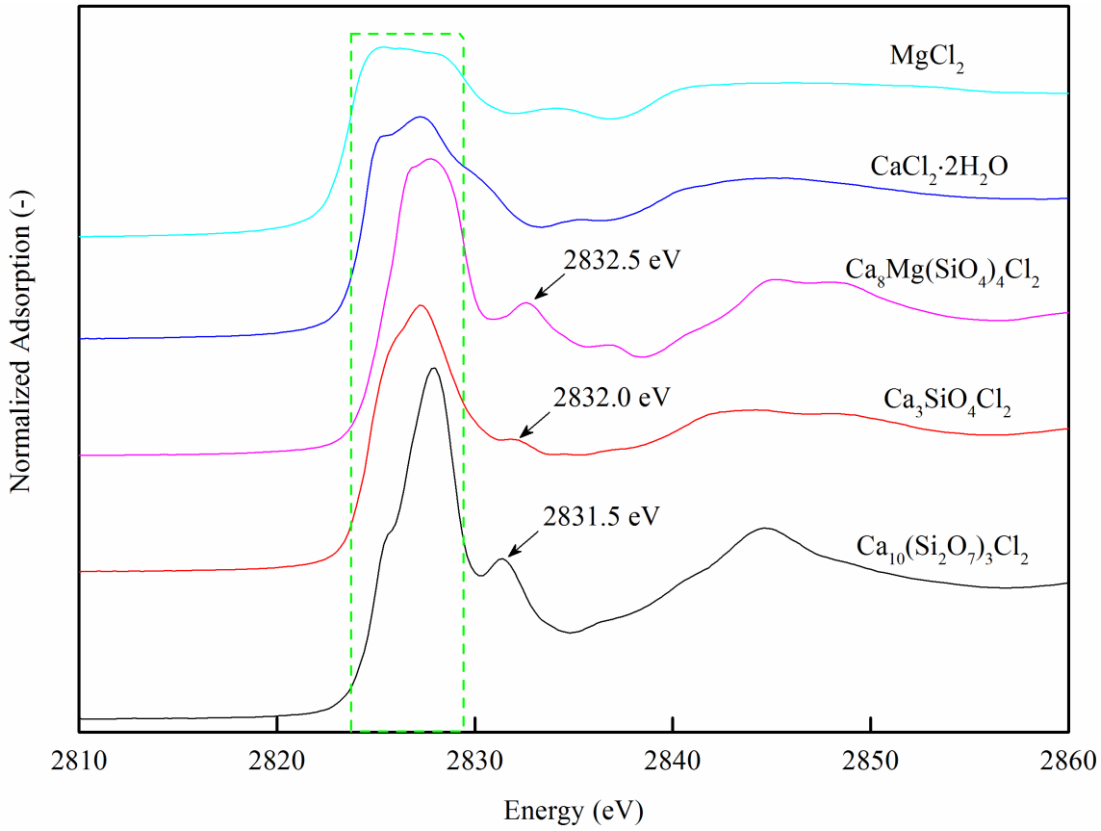

Figure 6.4 Cl K-edge XANES spectra of chloride references.

The Cl K-edge XANES spectra for the chloride references are shown in **Figure 6.4**. They can be readily distinguished by the variation in edge features. All XANES spectra exhibit a doublet first peak (inside the dashed rectangle), with varying ratios of the intensities for the two peaks. The doublet peak has roughly equal intensity for dehydrated $MgCl_2$. This is slightly different from the hydrated $MgCl_2 \cdot 6H_2O$ showing a much larger intensity for the first peak [2]. The distinctive asymmetries are observed for the remaining standards. The hydrated $CaCl_2$ produces a relatively large second peak, same as that has been observed elsewhere [2]. The remaining three silicate references each produce a much sharper spectra with a post-edge peak

located at 2831.5-2832.5 eV, which should be due to the distortion effect from the silicate crystal and/or Mg^{2+}. The references $Ca_8Mg(SiO_4)_4Cl_2$ and $Ca_3SiO_4Cl_2$ are most featureless with the first peak nearly disappearing. The largest intensity ratio of the second to first peak is witnessed for $Ca_{10}(Si_2O_7)_3Cl_2$. Additionally, it is evident that none of these silicate standards bear a close resemblance to $CaCl_2$. Such a finding is opposite the phenomena observed for the synthesised glasses/melts containing alumina (Al_2O_3) [2, 9].

The variation in the Cl K-edge XANES spectra reflects the different coordination environments of Cl^- in these chloride references. As shown in **Figure 6.5** obtained by the software CrystalMaker [12], Cl^- in dehydrated $MgCl_2$ is associated with 3 Mg^{2+}. In $CaCl_2{\cdot}2H_2O$, each Cl^- is entirely bonded with 2 Ca^{2+} as the nearest neighbour via a strong ionic bond [2]. Regarding $Ca_{10}(Si_2O_7)_3Cl_2$ and $Ca_3SiO_4Cl_2$, the Cl^- in both species is surrounded by 4 Ca^{2+}. However, their tetrahedral geometries is disordered to different extents, thereby bearing distinctively different XANES spectra in **Figure 6.4**. It has been confirmed that the Cl K-edge XANES is highly sensitive to the local chemical environment [2]. Regarding the last reference $Ca_8Mg(SiO_4)_4Cl_2$, it features Cl^- in a disordered octahedral configuration with the apexes being Ca^{2+} only.

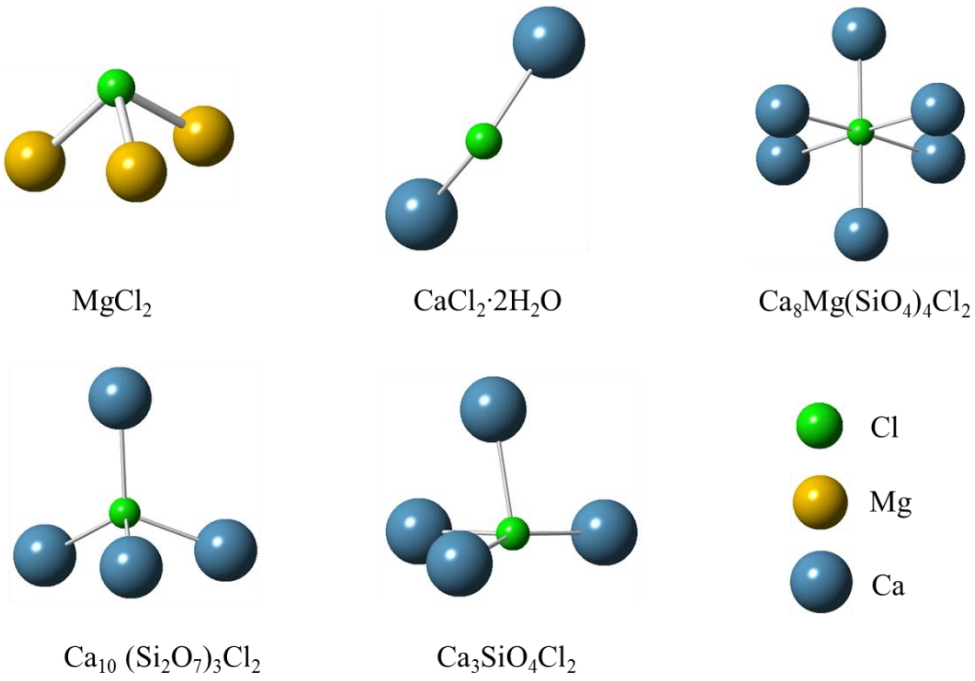

Figure 6.5 Local atomic environments of Cl in reference chlorides obtained by the software CrystalMaker.

6.4.1.2 Cl XANES LCF fitting results

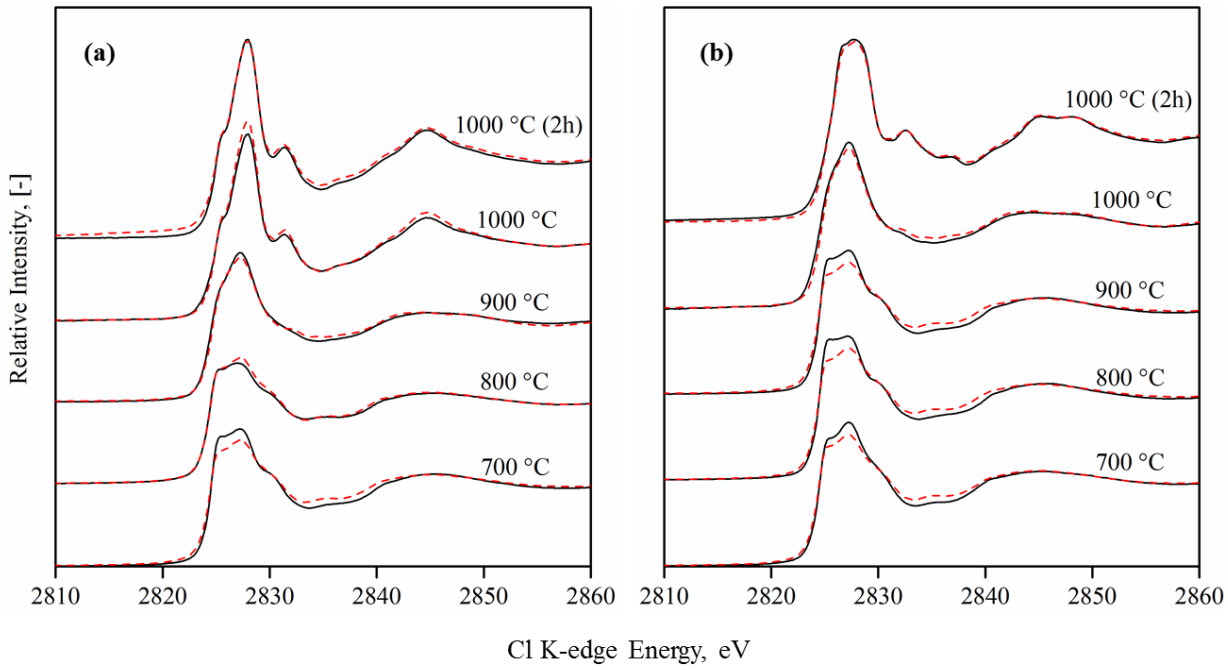

Figure 6.6 Cl K-edge XANES spectra and the LCF fitting results for the CaO-SiO_2-Cl silicates obtained without *(a)* and with *(b)* the addition of $MgCl_2$ to the reaction system. In both panel, the solid (in black) and dashed (in red) curves refer to the measured XANES spectra, and the fitting results from ATHENA, respectively.

Table 6.2 Comparison of Cl K-edge XANES LCF results and XRD analyses with respect to the Cl-species distribution in the residue obtained at different temperatures. The numbers in parenthesis refer to XRD results.

T, °C	$CaCl_2$ only			$CaCl_2$:$MgCl_2$=1:4		
	$CaCl_2$	$Ca_3SiO_4Cl_2$	$Ca_{10}(Si_2O_7)_3Cl_2$	$CaCl_2$	$Ca_3SiO_4Cl_2$	$Ca_8Mg(SiO_4)_4Cl_2$
700	100 (100)	0 (0)	0 (0)	100 (100)	0 (0)	0 (0)
800	100 (100)	0 (0)	0 (0)	100 (100)	0 (0)	0 (0)

900	10.4 (0)	89.6 (100)	0 (0)	100 (100)	0 (0)	0 (0)
1000	0 (0)	0 (0)	100 (100)	0 (0)	97.8 (100)	3.2 (0)
1000 (2h)	0 (0)	0 (0)	100 (100)	0 (0)	0 (0)	100 (100)

Figure 6.6 illustrates the Cl K-edge XANES spectra for the CaO-SiO_2-Cl silicates obtained upon the pyrohydrolysis of $CaCl_2$ at the presence of silica from 700 °C up to 1000 °C, with and without the addition of $MgCl_2$. Note that, once the target temperature was reached, the solid residues were quickly quenched. The spectra for the pyrohydrolysis residues obtained at 1000 °C with a retention time of 2 h is also included. The LCF fitting results are summarised in **Table 6.2** and the respective XRD data are included for comparison (The detailed XRD analysis can be found in our previous study [12]). For the case of $CaCl_2$ with silica only in *panel (a)*, the spectra of the residues produced up to 800 °C bear a close resemblance to that of $CaCl_2$ standard in **Figure 6.4**. The LCF fitting results in **Table 6.2** confirm an intact $CaCl_2$ due to its strong ionic bond. From 900 °C onwards, it is obvious that the doublet first peak becomes more featureless. The 1000 °C residue possesses a notable post-edge peak that is the unique feature for the silicate standards in **Figure 6.4**. The LCF results in **Table 6.2** quantifies 10.4% unreacted $CaCl_2$ in the 900 °C residue, which is accompanied by $Ca_3SiO_4Cl_2$. The XRD analysis failed to detect the unreacted $CaCl_2$, which might occur in amorphous structure that should be caused by melting. A further increase in the reaction temperature led to the release of nearly the entire Cl, as well as the agglomeration of $[SiO_4]^{4-}$ into the large cluster, $[Si_2O_7]^{6-}$. A longer retention time of 2 h at 1000 °C resulted in a small increase in the Cl release from 3.1 *wt%* down to 2.8 *wt%* in the residue. The Cl K-edge spectrum shape is also unchanged, suggestive of the stability of the structure for $Ca_{10}(Si_2O_7)_3Cl_2$. Regarding the addition of $MgCl_2$

at a molar ratio of 4 to $CaCl_2$ shown in *panel (b)*, the spectra of pyrohydrolysis residues still bear a close resemblance to that of $CaCl_2$ for the appearance of an asymmetric doublet first peak up to 900 °C. The LCF results in **Table 6.2** confirms that $CaCl_2$ is the sole Cl-bearing species in these products. Compared to the absence of $MgCl_2$, such a delay on the disappearance temperature of $CaCl_2$ can be attributed to the competition from $MgCl_2$ for which the resultant MgO scavenged all the silica [12]. With the temperature up to 1000 °C, the doublet first peak disappears, and is replaced by a featureless sharp peak that is in resemblance to the standard $Ca_3SiO_4Cl_2$. When the reaction time at 1000 °C is further extended to 2 h, the edge peak broadens and resembles the edge feature of $Ca_8Mg(SiO_4)_4Cl_2$. The LCF fitting result in **Table 6.2** further confirms this. Clearly, the intrusion of Mg^{2+} into the silica matrix took place, promoting a structural change from $Ca_3SiO_4Cl_2$ to $Ca_8Mg(SiO_4)_4Cl_2$, both of which possess a same skeleton of $[SiO_4]^{4-}$.

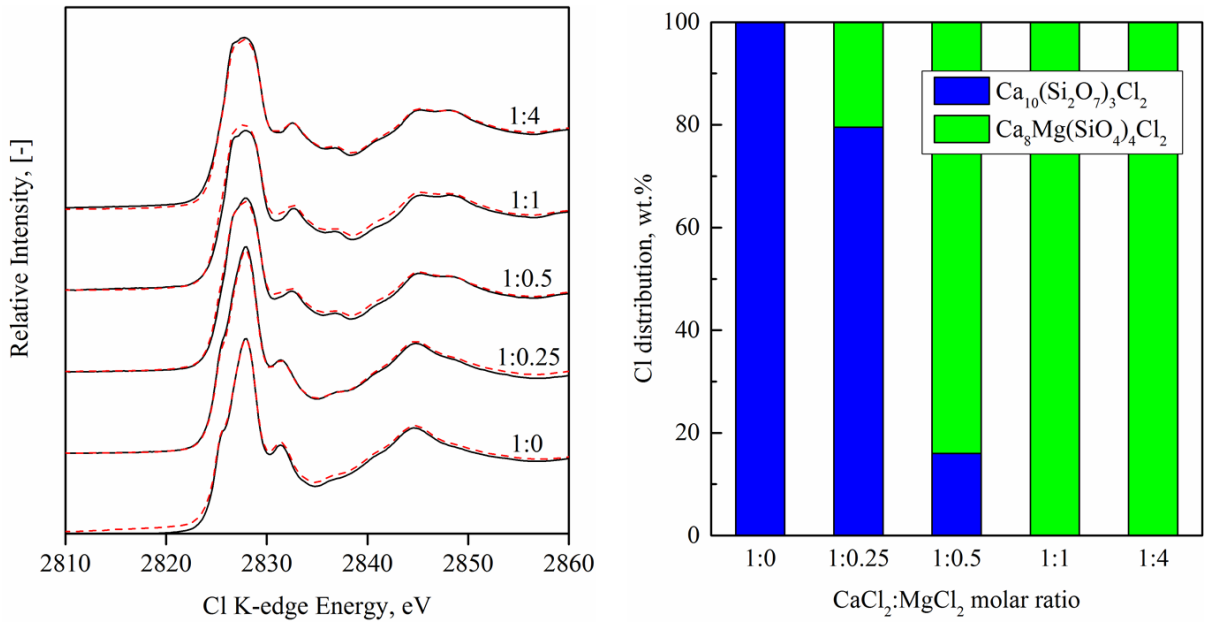

Figure 6.7 Cl K-edge XANES spectra for the residues produced from co-pyrohydrolysis of $CaCl_2$ and $MgCl_2$ at different molar ratios, and the respective LCF analysis results. The molar ratio of $CaCl_2$ to $MgCl_2$ is indicated. Conventions in **Figure 6.6** apply.

To further explore the effect of $MgCl_2$ addition on the change of the Cl coordination environment, co-pyrohydrolysis of $CaCl_2$ and $MgCl_2$ were conducted at different Mg^{2+}/Ca^{2+} molar ratios at 1000 °C. Note that, silica was still added at an equi-molar ratio into $CaCl_2$ for all the runs here, and a fixed retention time of 2 h at 1000 °C was also applied. **Figure 6.7** demonstrates the resultant Cl K-edge XANES spectra and the respective LCF fitting results. As the $MgCl_2$ addition increases, the Cl XANES edge peak broadens gradually. This is due to the formation of $Ca_8Mg(SiO_4)_4Cl_2$ and its substitution to $Ca_{10}(Si_2O_7)_3Cl_2$. Such a substitution commences once $MgCl_2$ is present in the system, as evident by the LCF results for the case of $CaCl_2/MgCl_2$ = 1:0.25. Upon the increase in the $MgCl_2$ amount, the content of $Ca_{10}(Si_2O_7)_3Cl_2$ decreases further, disappearing entirely when the two chlorides have an equi-molar ratio. Such a phase transformation facilitated the release of Cl, as evident by its mass percentage reduction from 2.8 *wt%* in the absence of $MgCl_2$ to 0.8 *wt%* in the presence of $MgCl_2$ at a molar ratio of 4 to $CaCl_2$. This hints that the enhanced HCl release observed here should be initiated by the free Mg^{2+} derived from the earlier decomposition of $MgCl_2$ at 600 °C in steam [12]. If that is the case, the intermediate Mg-Cl bond or a mixed Ca-Mg_y-Cl_x bond could be formed to facilitate the HCl release. However, based on the Cl spectra in **Figures 6.6** and **6.7**, none of these spectra bear a resemblance to the pure $MgCl_2$ shown in **Figure 6.4**. There is also not any unfitted peaks which could be an indicator for the presence of a mixed chloride. Bearing this in mind, efforts were made to analyse the Ca K-edge EXAFS spectroscopy.

6.4.2 Ca EXAFS

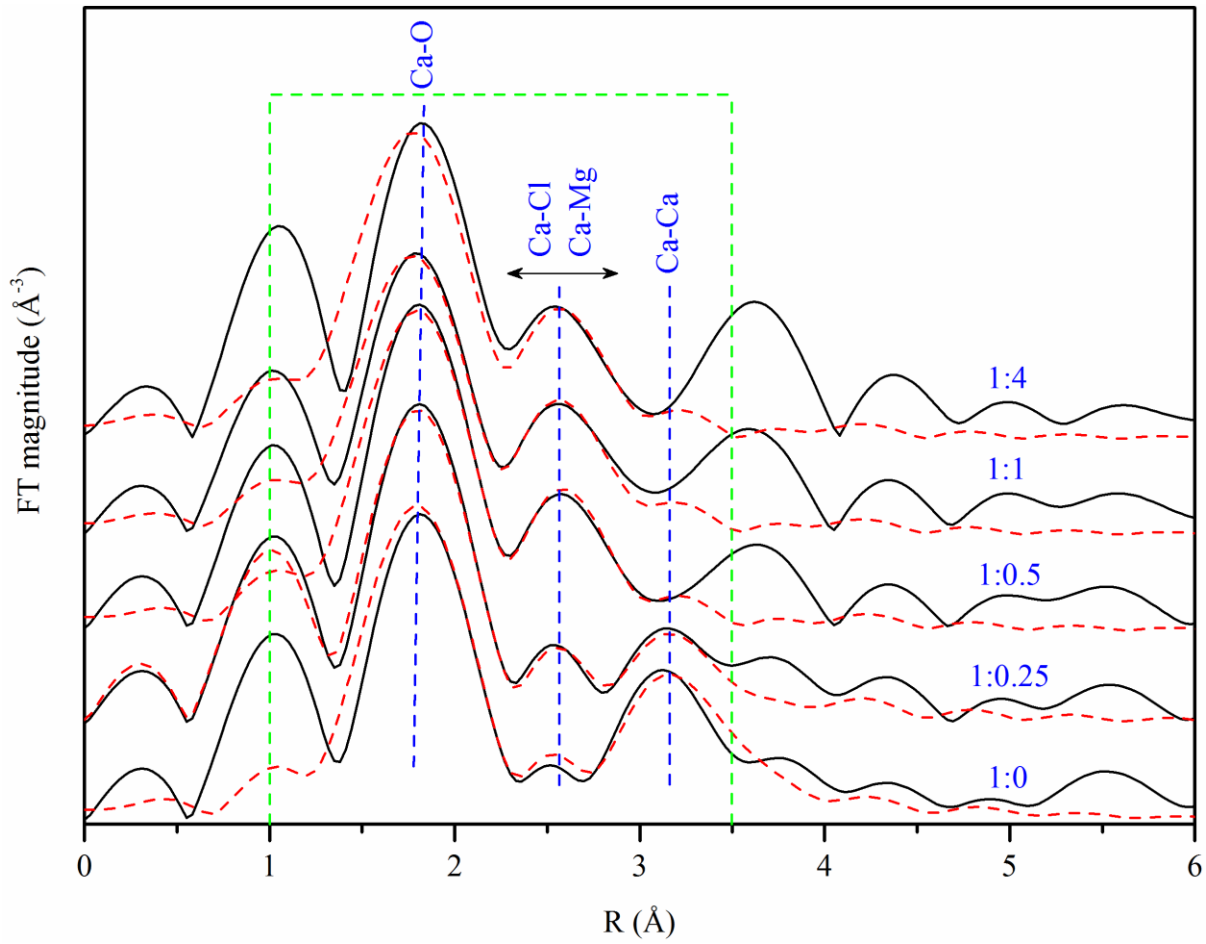

Figure 6.8 Fourier transform of Ca K-edge EXAFS spectra for the residues derived from co-pyrohydrolysis at different molar ratios at 1000 °C in 2 h. The molar ratio of $CaCl_2$ to $MgCl_2$ is indicated next to each spectrum. Conventions in **Figure 6.3** apply.

Due to the short k-edge range, it is essential to fix σ^2 (Debye-Waller factor for disorder) at the value of 0.005 for all the paths, allowing the refinement of the other parameters, including ΔE_0 (energy shift) which is shared by all paths, and n and ΔR (change in half-path length) which are path-dependent [16]. As shown in **Figure 6.8** for the Ca R-space EXAFS spectra, the model that best fits the spectra demonstrates a Ca-O scattering path for the peak near 1.8 Å, a Ca-Cl path and Ca-Mg path near 2.6 Å, and a Ca-Ca path near 3.1 Å. Additionally, the peaks near 1.0 Å are presumably the noise that are too close to the absorbing Ca^{2+} centre to be fitted by any paths.

Regarding the structural change of Ca upon the increase on the addition of $MgCl_2$, it is obvious that the peak intensity for the Ca-Ca path decreases gradually and even disappears from the molar ratio of 0.5 for $MgCl_2$ to $CaCl_2$. Simultaneously, the peak intensity for the second path, Ca-Cl/Ca-Mg increases monotonously.

Table 6.3 Ca^{2+} nearest-neighbour fitting results for the residues obtained at various molar ratios of $CaCl_2$ to $MgCl_2$. σ^2 ($Å^2$) was set as 0.005 for all fits. The numbers in parenthesis refer to the fitting error.

Molar ratio of $CaCl_2$:$MgCl_2$	R-factor	*R* (Å)	*n* (atoms)
Ca-O			
1:0	0.08	2.36 (0.04)	2.9 (0.6)
1:0.25	0.01	2.34 (0.09)	2.7 (0.9)
1:0.5	0.08	2.34 (0.03)	2.8 (0.6)
1:1	0.10	2.34 (0.04)	2.9 (0.6)
1:4	0.14	2.34 (0.07)	2.8 (0.9)
Ca-Cl			
1:0		2.99 (0.11)	0.9 (0.7)
1:0.25		2.98 (0.35)	0.9 (0.4)
1:0.5		3.02 (0.06)	1.2 (1.1)
1:1		3.01 (0.03)	1.2 (1.0)
1:4		3.02 (0.30)	1.1 (1.0)
Ca-Mg			
1:0		-	-
1:0.25		2.99 (0.37)	1.1 (1.3)

1:0.5	3.01 (0.03)	2.2 (1.8)
1:1	3.03 (0.07)	2.4 (1.7)
1:4	3.03 (0.40)	2.5 (1.9)
Ca-Ca		
1:0	3.65 (0.06)	2.2 (1.1)
1:0.25	3.63 (0.20)	1.2 (1.1)

The fitting results for Ca K-edge EXAFS spectra are tabulated in **Table 6.3**. The most accurate parameter obtained from EXAFS fitting is the bond length, while the coordination number is highly correlated with other parameters and the narrow *k*-range of EXAFS oscillations [9]. For the Ca-O bond, its bond length and coordination number are almost constant regardless of the $MgCl_2$ addition amount. The atom O^{2-} always stays in the first shell that is nearest to Ca^{2+}. The second atomic shell can be contributed to two scattering paths, Ca-Cl and Ca-Mg. Assigning this peak solely to Ca-Cl is implausible, since the Cl content in the residue decreases upon the increase in the $MgCl_2$ addition, as evident in **Table 6.1**. Its trend is opposite the enhancement in the intensity of the second peak upon the increasing $MgCl_2$ addition. Alternately, ignoring the Ca-Cl path completely is not reasonable either, because Cl is still present in the residue and the Ca-Cl length in the residue is quietly close to the position of this peak, according to the crystal structure refinement. In this sense, the increase in the peak intensity should be mainly attributed to Mg^{2+} which has an increased opportunity to intrude into the second atomic shell of Ca^{2+} and share with Cl with an increase in the addition amount of $MgCl_2$. Deconvolution of the second peak was thus conducted carefully to include both paths into the fitting of the second peak. The modelled Ca-Mg distance (shown in **Table 6.3**) is slightly smaller than the theoretical value from the crystal structure refinement of $Ca_8Mg(SiO_4)_4Cl_2$, ~3.0 Å vs ~3.2 Å. This might be a result of high-temperature reactions which slightly modulates the crystalline

structure of residues. For the Ca-Cl bond, its bond length increases slightly upon the increase of $MgCl_2$ amount. This shall be attributed to the distortion effect from Mg^{2+}. In terms of the Ca-Mg path, despite a marginal growth of the distance between the two cations, the increase in the atomic number of Mg^{2+} surrounding Ca^{2+} is most pronounced. In particular, upon an increase of the $MgCl_2$ fraction up to 0.5, the atomic number of Mg^{2+} around Ca^{2+} is doubled. These Mg^{2+} atoms should be derived from the decomposition of $MgCl_2$ at the earlier stage. The resultant Mg^{2+} atoms should be highly mobile and have opportunities to enter the crystal structure via the interatomic gaps. Once getting close to Ca^{2+}, a portion of the mobile Mg^{2+} might affiliate with Cl^-, creating an intermediate Mg-Cl bond that immediately decomposes into oxide and HCl. Vacancy are thus left on the second shell and occupied by the free Mg^{2+}. The intrusion of Mg^{2+} atoms even comples the Ca^{2+} in the third shell to go far away, as evident by a reduction on the atomic number of Ca^{2+} on the Ca-Ca shell from 2.2 for $CaCl_2$ alone to 1.2 for 0.25 $MgCl_2$ mixed with $CaCl_2$, and nil onwards. Note that, this model may not be the sole explanation of the Ca EXAFS features observed for the co-pyrohydrolysis residues. However, it is the best deconvolution we can achieve so far, considering the nature of the data and the complexity of silicate crystal structures.

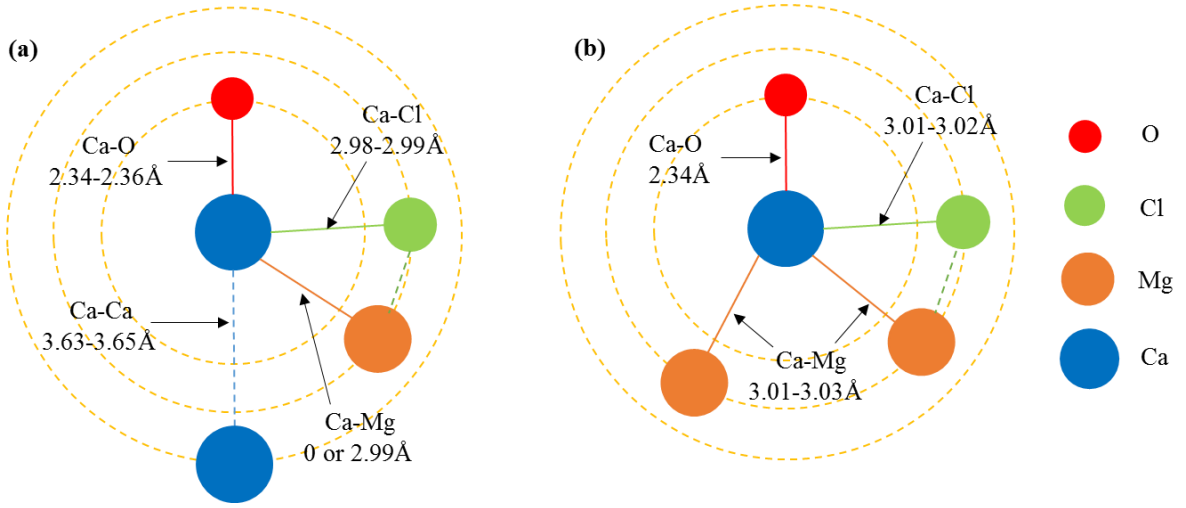

Figure 6.9 Hypothetical atomic structures of the co-pyrohydrolysis residues depicting plausible Ca^{2+} sites determined from EXAFS. ***(a)***: $CaCl_2$:$MgCl_2$=1:0-0.25; ***(b)***: $CaCl_2$:$MgCl_2$=1:0.5-4.

As per these observations, effort was finally made to plot the hypothetical atomic structures centred on Ca^{2+} in the two typical pyrohydrolysis residues, one having low $MgCl_2/CaCl_2$ molar ratios of 0.25-1, and another one with higher $MgCl_2/CaCl_2$ ratios. As illustrated in **Figure 6.9**, the first shell for Ca-O is barely changed upon the variation of the $MgCl_2$ amount. This is reasonable since O is always the first atom affiliating with Ca. The average bond length of Ca-Cl increases marginally by only 0.03 Å from the low end group to the high end one. Again, the most substantial difference is the third shell ranging from 3.63-3.65 Å which comprises of Ca^{2+} in **Figure 6.9** (a), but not in *panel (b)*. The presence of the third shell demonstrates a highly crystallised structure for the silica matrix, in which Cl^- is bound intensively and solely with Ca^{2+}. In contrast, for the Mg^{2+}-rich residue visualised in *panel (b)*, the occupation of Mg^{2+} on the same shell with Cl^- is established, which is also on the second shell surrounding the Ca^{2+} centre. However, a direct link with this into the formation of a mixed Ca-Mg_y-Cl_x intermediate (proposed in [2]) seems implausible, considering that Ca^{2+} atom is preferentially surround by

O atom at its first shell. In this sense, an intermediate form of Ca-O-Mg_y-Cl_x could be more reasonable for the description of the near-edge structure of Ca when it co-exists with the free Mg^{2+} in its second atomic shell. This is to certain extent similar with the pyrolysis of $MgCl_2$ alone via the formation of an intermediate of MgOHCl that immediately converts to MgO and HCl [12]. However, further investigation using alternative technique or forward modelling approaches based on XAS results are required to confirm this possibility.

6.5 Conclusions

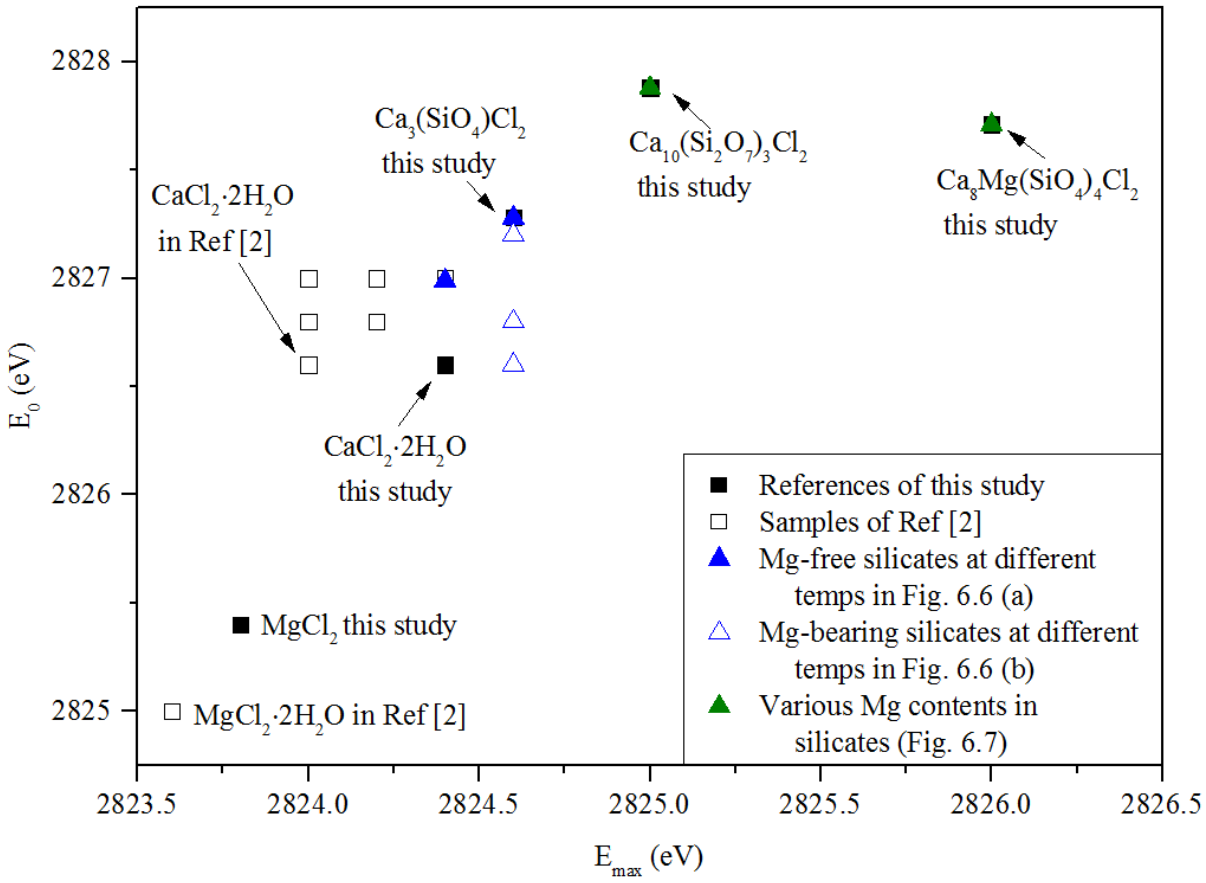

Figure 6.10 Correlation of E_{max} and E_0 for the reference standards and samples of this study and those reported in the reference [2].

It is for the first time that we have reported the XAS data and the respective atomic structures in the Cl-bearing pyrohydrolysis products/residues formed in the temperature range of 700-1000 °C, which is below the melting points of these products. As demonstrated in **Figure 6.10**, there is a tiny energy shift (approximately 0.2-0.4 eV) for the E_{max} of the two pure chlorides ($CaCl_2$ and $MgCl_2$) between this study and the reference [2], although the same beamline and conditions were employed in both studies. This is attributed to the high sensitivity of the synchrotron XAS analysis and the sample difference/purity. Nevertheless, the discrepancy for the silicates is much more obvious and far larger than the energy shift observed between this study and the glassy melts synthesised at 1250 °C and 0.5 GPa [2]. In comparison to the glasses that are closer to $CaCl_2$ representing an intimate affinity of the ionic Ca-Cl bond, the silicate crystals bear a relatively larger E_{max} and E_0, both of which also increase further upon the inclusion of Mg^{2+} into the silica matrix. These two values feature the multiple scattering phenomena in crystals and are enhanced by the highly ordered structure relative to the less ordered structure expected for glasses. The inclusion of Mg^{2+} is beneficial in distracting Cl^- out of the Ca-Cl bond, leading to the restructuring of the crystal matrix and the enhancement of the HCl release. The mechanism for the role of Mg^{2+} is dictated based on the Ca EXAFS analysis, in which a formula of Ca-O-Mg_y-Cl_x is more reasonable for the intermediates formed upon the interaction between these two cations.

Reference

1. Magenheim, A. J.; Spivack, A. J.; Michael, P. J.; Gieskes, J. M., Chlorine stable isotope composition of the oceanic crust: Implications for Earth's distribution of chlorine. *Earth and Planetary Science Letters* **1995**, *131*, (3), 427-432.
2. Evans, K.; Mavrogenes, J.; O'Neill, H.; Keller, N.; Jang, L. Y., A preliminary investigation of chlorine XANES in silicate glasses. *Geochemistry, Geophysics, Geosystems* **2008**, *9*, (10).
3. McKinley, C.; Ghahreman, A., Hydrochloric acid regeneration in hydrometallurgical processes: a review. *Mineral Processing and Extractive Metallurgy* **2018**, *127*, (3), 157-168.
4. Hearn, J.; Eichler, J.; Hare, C.; Henley, M., Effect of soil moisture on chlorine deposition. *Journal of Hazardous Materials* **2014**, *267*, 81-87.
5. Trubetskaya, A.; Kling, J.; Ershag, O.; Attard, T. M.; Schröder, E., Removal of phenol and chlorine from wastewater using steam activated biomass soot and tire carbon black. *Journal of Hazardous Materials* **2019**, *365*, 846-856.
6. Hanna, S.; Britter, R.; Argenta, E.; Chang, J., The Jack Rabbit chlorine release experiments: Implications of dense gas removal from a depression and downwind concentrations. *Journal of Hazardous Materials* **2012**, *213-214*, 406-412.
7. Trowbridge, P. R.; Kahl, J. S.; Sassan, D. A.; Heath, D. L.; Walsh, E. M., Relating Road Salt to Exceedances of the Water Quality Standard for Chloride in New Hampshire Streams. *Environmental Science & Technology* **2010**, *44*, (13), 4903-4909.
8. Bastviken, D.; Sandén, P.; Svensson, T.; Ståhlberg, C.; Magounakis, M.; Öberg, G., Chloride Retention and Release in a Boreal Forest Soil: Effects of Soil Water Residence Time and Nitrogen and Chloride Loads. *Environmental Science & Technology* **2006**, *40*, (9), 2977-2982.
9. McKeown, D. A.; Gan, H.; Pegg, I. L.; Stolte, W. C.; Demchenko, I., X-ray absorption studies of chlorine valence and local environments in borosilicate waste glasses. *Journal of Nuclear Materials* **2011**, *408*, (3), 236-245.
10. Hajji, S.; Montes-Hernandez, G.; Sarret, G.; Tordo, A.; Morin, G.; Ona-Nguema, G.; Bureau, S.; Turki, T.; Mzoughi, N., Arsenite and chromate sequestration onto ferrihydrite, siderite and goethite nanostructured minerals: Isotherms from flow-through reactor experiments and XAS measurements. *Journal of Hazardous Materials* **2019**, *362*, 358-367.

11. Newville, M., Fundamentals of XAFS. *Reviews in Mineralogy and Geochemistry* **2014**, *78*, (1), 33-74.
12. Zhou, S.; Qian, B.; Hosseini, T.; De Girolamo, A.; Zhang, L., Pyrohydrolysis of CaCl2 Waste for the Recovery of HCl Acid upon the Synergistic Effects from MgCl2 and Silica. *ACS Sustainable Chemistry & Engineering* **2019**, *7*, (3), 3349-3355.
13. Kurdowski, W.; Miskiewicz, K., Hydration of calcium chlorosilicate Ca3SiO4Cl2. *Cement and Concrete Research* **1985**, *15*, (5), 785-792.
14. Ding, W.; Wang, J.; Zhang, M.; Zhang, Q.; Su, Q., Luminescence properties of new Ca10 (Si2O7) 3Cl2: Eu2+ phosphor. *Chemical physics letters* **2007**, *435*, (4-6), 301-305.
15. Li, B.; Shi, J.; Zhang, W.; Wang, J.; Tang, Q.; Su, Q., The effects of rare-earth co-dopants on green long-lasting phosphorescence and thermoluminescence properties of Ca8Mg (SiO4) 4Cl2: Eu2+, RE3+. *Journal of The Electrochemical Society* **2010**, *157*, (5), J139-J142.
16. Kelly, S.; Hesterberg, D.; Ravel, B., Analysis of soils and minerals using X-ray absorption spectroscopy. *Methods of soil analysis. Part* **2008**, *5*, 387-463.
17. Low, F.; De Girolamo, A.; Wu, X.; Dai, B.; Zhang, L., Inhibition of lignite ash slagging and fouling upon the use of a silica-based additive in an industrial pulverised coal-fired boiler: Part 3–Partitioning of trace elements. *Fuel* **2015**, *139*, 746-756.

Chapter 7
Conclusions and Recommendations for Future Work

7.1 Conclusions

This thesis presented a comprehensive low-rank Xinjiang coal leaching process for selective removal of AAEMs in an environmentally-friendly manner for the first time. Through the Aspen Plus simulation, an integrated coal leaching and waste leachate treatment process has been established. The leaching mechanism for using recycled leachates and the recyclability of leaching reagents are elucidated. Additionally, an efficient HCl acid regeneration method from chloride wastes is explored and the corresponding mechanism is unveil from atomic level. The results provide a database for the design and scale-up of industrial low-rank coal leaching process.

Chapter 2 specified the research gaps for low-rank coal leaching after a thorough literature review. Chapter 3 established a framework for the overall map, where two core steps, coal leaching and waste leachate treatment are integrated effectively. The recyclability of two leaching reagents (water and HCl acid) was addressed in chapter 4. Chapter 5 presented an efficient HCl regeneration method from alkaline earth metal chlorides. The interaction between Ca^{2+} and Mg^{2+} regarding the affinity to Cl^{-} was elucidated in chapter 6.

7.1.1 Integrated coal leaching and waste leachate treatment process

The optimal configuration of coal leaching and waste leachate treatment units has been determined by using Aspen Plus. For the coal leaching step, both three-stage counter-current water leaching process and single-stage HCl acid leaching process can improve the ash fusion temperature of leached coal above the operating temperature of boilers, at 1200 °C. For the leachate treatment unit, evaporator which utilises the waste heat from power plants obtains extra water, attributing to the high moisture content of low-rank coal, at 25 *wt%* and its high

water recovery rate. Instead, the using of RO leads to a water loss of 251 kg/t coal, although its capital cost is around half of that of evaporator. However, through recycling the leachate before being sent to RO, the water consumption is proven to decrease significantly to 40-50 kg/t coal which is lower than 85 kg/t coal for black coal beneficiation process.

7.1.2 Multi-cycle leaching by water and HCl acid

The water-soluble (mainly Na) and HCl acid-soluble AAEMs witnesses different leaching performance upon the recycling of leaching reagents. The removal extent of water-soluble Na decreases gradually upon the recycling of water, as a result of the increase in the Na^+ content in recycled water and/or the decrease in the water-soluble Na content in coal. By contrast, the removal of HCl-soluble AAEMs keeps stable in each cycle for which the initial HCl acid concentration remains constant, at 0.7 M. The leachate is not able to remove elements any more after recycling for 15 times when it is saturated to NaCl, $CaCl_2$ and $MgCl_2$, at 15900, 67400 and 10600 ppm, respectively.

7.1.3 Recyclability prediction by leaching kinetics modelling

A modified SCM integrated with iterative calculation was developed and validated for the three-stage counter-current water leaching process. It indicates that the water-soluble Na removal is predominated by the intra-particle outward diffusion of Na^+. Upon the recycling of water, the water-soluble Na removal decreases exponentially from around 90% in the first cycle to negligible in 15^{th} cycle. On the contrary, the HCl-soluble element removal shows a good fit to a H^+ intra-particle diffusion model which considers a reducing proton concentration in bulk acid. This interprets the constant HCl-soluble element removal extent in each cycle with a constant initial proton concentration.

7.1.4 Efficient HCl acid regeneration from alkaline earth metal chlorides waste

With the assistance of silica and steam, 99% Cl can be released and recovered as HCl acid from the mixture of $CaCl_2$ and $MgCl_2$ via co-pyrohydrolysis. It is discovered that the addition of $MgCl_2$ poses a double-side effect on the pyrohydrolysis of $CaCl_2$: *1)* delaying the HCl release from $CaCl_2$ in the temperature-rise period from 700 to 1000 °C due to its competition with $CaCl_2$ to react with silica; *2)* promoting HCl release in the retention period at 1000 °C arising from the formation of $Ca_8Mg(SiO_4)_4Cl_2$, in which Cl- is bonded loosely and can be released more easily. Additionally, the optimum $MgCl_2$ addition is 0.5 mole/mole of $CaCl_2$, which can be contributed to the formation of $Ca_8Mg(SiO_4)_4Cl_2$, although a deeper mechanism elucidation is necessary.

7.1.5 Atomic structure analysis of Cl and Ca derived from the co-pyrohydrolysis of alkaline earth metal chloride wastes

The fundamental science underpinning the co-pyrohydrolysis is explored via using synchrotron X-ray absorption spectroscopy (XAS). Particularly, the variation on the local atomic environment of Ca^{2+} upon the intrusion of Mg^{2+} atom is interpreted. It is found that Ca^{2+} is always preferentially bonded with O^{2-} as its first atomic shell. A mixed cation intermediate, Ca-O-Mg_y-Cl_x is thus very likely to exist at the co-pyrohydrolysis of the two chlorides, instead of Ca-Mg_y-Cl_x proposed elsewhere, since of the co-existence of Mg^{2+} and Cl^- on the second shell centred on the Ca^{2+}. In addition, the intrusion of Mg^{2+} compels the third shell which comprises of Ca^{2+} to go far away, causing a less-crystalline structure and thus promoting the Cl release.

7.2 Recommendations for future work

The research results demonstrated in this thesis have proven the techno-economic feasibility of low-rank Xinjiang coal leaching for the selective removal of AAEMs. A comprehensive leaching process which integrates leaching and waste leachate treatment and recycling has been proposed and the optimised operation conditions for both steps have been clarified. The recommendations for future work is shown as follows.

7.2.1 Applicability study of the proposed leaching process for other low-rank coal

Research on the other types of low-rank coal, such as Victorian brown coal is recommended to examine the applicability of the leaching part in this thesis, especially the developed kinetics model. This applicability study will enhance the robustness of the research findings and promote the scale-up of low-rank coal leaching process in worldwide.

7.2.2 Pilot scale research

The next meaningful step is a pilot-scale process which uses contiguous feeding of low-rank coal, recycles the leachate to examine its recyclability, and regenerates HCl acid at a larger scale. The pilot-scale study can offer an insight into the technically feasible range of this process. Meanwhile, the environmental impact can be evaluated.

7.2.3 Effects of atmosphere on pyrohydrolysis

Since the atmosphere in the pyrohydrolysis conducted in this thesis was fixed, it is recommended to test the effect of atmosphere on the HCl release from chlorides. For example,

through using various partial pressure of steam, the reaction order for the pyrohydrolysis can be obtained. It is beneficial for the subsequent reactor design.

7.2.4 Research on energy requirement reduction of pyrohydrolysis

The intensive energy requirement will hinder the promotion of pyrohydrolysis, unless it can be conducted in lower temperatures and/or shorter reaction time. Therefore it is recommended to test the possibility to reduce the reaction temperature by adding other 'catalysts', such as clay which a combination of silica and alumina. Probably due to the participation of alumina, the reaction route will be modified and the activation energy could be reduced, achieving 'fast and/or low-temperature pyrohydrolysis'.

7.2.5 Application of the pyrohydrolysis method on other chlorides

Given the fact that the pyrohydrolysis can be used to generate high-purity oxides or silicates and HCl acid, it is worthwhile to apply this approach on other chloride wastes, such as rare earth metals, to obtain their oxides and even further reduce to pure metals. This might provide a new way to produce the precious rare earth metals.

Appendix A

Chapter 3 in publication form

Fuel Processing Technology 172 (2018) 13–28

Contents lists available at ScienceDirect

Fuel Processing Technology

journal homepage: www.elsevier.com/locate/fuproc

Research article

Selective removal of sodium and calcium from low-rank coal – Process integration, simulation and techno-economic evaluation

Song Zhou[a], Tahereh Hosseini[a], Xiwang Zhang[a], Nawshad Haque[b], Lian Zhang[a,*]

[a] Department of Chemical Engineering, Monash University, Clayton, Victoria 3800, Australia
[b] CSIRO Mineral Resources, Private Bag 10, Clayton South, Victoria 3169, Australia

ARTICLE INFO

Keywords:
Low-rank coal
Sodium and calcium removal
Process simulation
Techno-economic evaluation

ABSTRACT

This paper has addressed the techno-economic feasibility regarding the selective removal of sodium (Na) and calcium (Ca) from low-rank sub-bituminous coal, aiming to reduce the ash slagging and fouling propensity in the pulverized coal-fired boilers. Four novel process integrations were proposed and simulated in Aspen Plus. Both the novel counter-current three-stage water washing process and an acid-water two-stage washing process have proven to improve the ash fusion temperature satisfactorily, reducing the mass fraction of Na_2O in ash from 4.32 wt% to 0.85 and 0.19 wt%, respectively. In addition, the use of acid-water washing removed 12.5% CaO and 19.5 wt% total ash. For the recycle and treatment of wastewater, the water gain is desirable for the use of an evaporator, owing to the dewatering of the initially high-moisture coal (25 wt%) in the centrifugal and the high water recovery rate from the evaporator. However, the good performance of evaporator was counteracted by the considerable capital cost caused by the huge heat transfer area requirement. Instead, the use of reverse osmosis (RO) resulted in a water loss up to 228.4 kg/t coal. Additionally, prior to the RO treatment unit, the recycle and reuse of the unsaturated water for maximum six times and four times for three-stage water washing and acid-water two-stage washing, respectively, was critical in reducing both the water and power consumption. The water consumption dropped to 38.1 kg/t coal and 48.1 kg/t coal for the three-stage water washing and acid-water two-stage washing process, respectively. Both are remarkably lower than 85.0 kg-water/t black coal. In terms of the power consumption, it decreased to −9.4 kWh/t coal for the three-stage water washing process and further down to 5.8 kWh/t for the acid-water washing case, which was even slightly lower than 6.3 kWh/t for the black coal. Furthermore, the integration of acid-water washing and RO was also demonstrated to be economically viable by its high NPV, IRR and short payback period. Sensitivity analysis indicate that, the original Na content in raw coal is the most influential variable on the water and power consumption of the overall process, followed by the initial moisture content in the raw coal. For a low-rank coal containing > 2150–2520 ppm Na and/or < 19 wt% moisture, the washing process proposed would turn economically unviable compared to the existing black coal washing process. A minimum selling price of 136 RMB/t (−32% deviation) was also necessary to keep both NPV and IRR positive as well as the payback period shorter than the project lifetime.

1. Introduction

Low-rank coal, commonly referred to as brown coal and sub-bituminous coal, contributes to > 50% of the world's coal reserves [1]. It is abundant in regions such as Australia and China [2–3] and provides an economically attractive alternative to high-rank black coal (i.e. bituminous coal and anthracite) for electricity generation. The use of low-rank coal is becoming increasingly important with the ongoing depletion of high-rank bituminous coal. However, low-rank coal boilers are afflicted by severe slagging and fouling inside the boiler caused by its higher content of alkali and alkaline earth metal (Na, Ca, K and Mg) [3–5].

Conventional coal cleaning techniques are exclusively targeted at high-rank coal with a large portion of its inorganic metals present as discrete grains and separate from the coal matrix [6]. As the mineral matter has a larger density than the carbonaceous matrix, it can be removed physically [7]. Variations in surface properties can also allow for separation [8]. However, unlike black coal, sodium (Na) and calcium (Ca) in low-rank coal are deeply and chemically embedded within the coal matrix. Therefore, they cannot be removed using any physical

* Corresponding author.
E-mail address: lian.zhang@monash.edu (L. Zhang).

https://doi.org/10.1016/j.fuproc.2017.11.028
Received 29 August 2017; Received in revised form 28 November 2017; Accepted 28 November 2017

approaches based on either density or surface property discrepancy between mineral matter and coal matrix [9]. Instead, chemical leaching or solvent extraction has been examined to remove these two elements from low-rank coal. In particular, research has been focused on the removal of all ash-forming metals to produce ultra-clean coals (UCC) or ash-free hyper-coal (HPC), from both high-rank and low-rank coals [10–13]. However, the corrosive acid/alkali reagents and/or high pressure and temperature employed in existing chemical leaching processes [10,14–16] raise severe environmental concerns, the harsh requirement for equipment, and high capital/operating cost, limiting their advance in practical applications. Solvent extraction is also inappropriate for low-rank coal because of the low carbon yield (< 30 wt %) resulting from its cross-linked carbonaceous structure [10]. For conventional coal-fired boilers, the removal of all ash-forming metals is also unnecessary.

In this study, instead of removing all of the ash-forming metals, only Na and Ca were selectively targeted, considering that these two metals are the most critical triggers for ash slagging and fouling in a pulverized coal-fired boiler [3–5,17]. Moreover, based on the high-water solubility of Na in low-rank coals, the existing water-washing process for black coal was adapted for the low-rank coal. That is, multiple-stage water washing, either with or without acid dosing was employed to wash the low-rank coal, whereas the resultant used water was repeatedly used before it is saturated and then sent to the wastewater treatment unit to remove the inorganic impurities [18]. The innovative characteristics of the new water-washing process are hypothesized from the following three perspectives, 1) the use of water can significantly be reduced by reusing it before it is fully saturated with sodium; 2) the mature existing waste water treatment and recovery techniques, once integrated efficiently with the coal washing process, can further help recover the water cost-effectively; and 3) the integration of acid and water on coal water-washing can significantly increase the extraction yields of both Na and Ca out of coal matrix, according to the following two equations [19–20] where R stands for organic moieties in coal. Additionally, since the original acid is neutralized by Na and Ca, its disposal causes little environmental issues.

$$R - COONa + H^+ \leftrightarrow R - COOH + Na^+ \quad (1)$$

$$Ca(R - COO)_2 + 2H^+ \leftrightarrow 2R\text{–}COOH + Ca^{2+} \quad (2)$$

In this paper, we have conducted process simulations to assess four different scenarios so as to optimize the integration of individual units to produce a washed low-rank coal that has a comparable content of Na and Ca with that in black coal. Furthermore, the ash in the resultant washed low-rank coal is expected to have an ash fusion temperature above the boiler operating temperature, at 1200 °C. Aspen Plus has been employed for the process flow-sheeting. Aspen Process Economic Analyzer (APEA) was further used to perform the economic evaluation based in the context of China. Finally, sensitivity analysis was undertaken to examine the robustness of the overall process including the water and power consumption, and economic feasibility. As far as the authors are aware, such a study has yet to be examined in the literature. The results achieved are expected to promote the deployment of low-rank coal washing in a large industrial and commercial scale in the future.

2. Methodology

2.1. Coal properties

A low-rank sub-bituminous coal, termed Xinjiang Zhundong coal was used for this study. The low-rank coal washing plant was assumed to be located beside a coal mine in Xinjiang, China, which is rich in low-rank coal [2]. Additionally, a reference black coal was tested for comparison. Their properties are tabulated in Table 1. The volatile content (30.2 wt%) in Xinjiang coal indicates that it belongs to sub-bituminous coal [21]. It is much higher than the value of black coal, at 7.8%. The sub-bituminous coal is also characterized by the high moisture of 24.5% and low ash content of 7.8%, compared with black coal reference. The gross heat value of 24.9 MJ/kg shows that this sub-bituminous belongs to the intermediate-heating-value coal [21]. With respect to the particle size distribution of the as-mined Xinjiang coal shown in Table 2, one can see that this coal is very fine with a mass percentage of 49% < 4 mm. One major reason is due to its low-ash content.

Table 1
Compositions of as-received Xinjiang low-rank coal and black coal.

Components	Low-rank coal (wt%)	Black coal (wt%)
Moisture[a]	24.5	9.68
Ash[b]	7.78	22.49
Volatile[b]	30.2	7.78
FC[b]	62.02	69.73
Chlorine[b]	0.09	–
Gross heat value[c]	24.89 MJ/kg	26.93 MJ/kg

[a] Air-dried.
[b] Dried basis.
[c] Dry ash free basis.

Table 2
PSD of as-received Xinjiang low-rank coal and black coal.

Low-rank coal		Black coal	
PSD/mm	wt%	PSD/mm	wt%
< 0.2	8	0–5	30
0.2–0.6	12	5–40	60
0.6–1.0	8	> 40	10
1.0–4.0	21		
4.0–8.0	15		
> 8.0	36		

Table 3 compares the ash compositions of the two coals, which are expressed as the most stable oxide of each element. It is observed that the contents of both Na_2O and CaO in low-rank coal are significantly higher than in black coal, which is in agreement with the past studies [3–5]. In terms of the mode of occurrence of Na and Ca in Xinjiang coal, it has been widely reported that more than half of Na was water-soluble, with the rest being organically bound with carboxylic acid that can be entirely washed away by ammonium acetate [2,10,16,22]. Conversely, the major forms of Ca in low-rank coal vary from one study to another, indicative of its dependence on the coal-forming environment. For instance, Wijaya et al. (2011) found that Ca was equally soluble in water, ammonium acetate and hydrochloric acid, yet no < 35% of Ca was water-soluble due to the presence of their chlorides. However, Ma et al. (2014) claimed that calcite and gypsum were the two dominated forms found in low-rank coal.

2.2. Low-rank coal washing process

The whole process consists of two major components, coal washing, and waste water treatment and recycling. The raw coal first undergoes sieving and crushing to obtain the particles < 4 mm in diameter, before being sent to the washing reactor by a belt conveyer. With respect to the coal washing unit, three options were proposed hereafter: the use of a single stage washing tank shown in Fig. 1(a), the use of three-stage counter-current flow of water against the coal stream in Fig. 1(b), and the combination of acid and water in Fig. 1(c) and (d). With respect to the waste water treatment and recycling, the mixture of washed coal and water from the washing step is firstly separated by a dewatering screen. Subsequently, the wet washed coal is transferred to a centrifuge to squeeze out the remaining water and make the final product that contains around 11% moisture. The resultant water from the centrifuge is mixed with coal fine-water slurry received from the dewatering

Table 3
Typical ash compositions of Xinjiang low-rank coal and black coal.

Sample	Ash[a]	Na_2O	MgO	Al_2O_3	SiO_2	P_2O_5	SO_3	K_2O	CaO	Fe_2O_3
Low-rank coal	7.8	4.32	22.65	3.27	5.67	0.52	15.06	0.21	46.96	1.34
Black coal	22.5	1.48	1.05	28.14	52.14	0.21	2.97	1.91	1.48	10.62

[a] On the dried coal basis (wt%).

screen, and then passes through a thickener and pressure filter to yield the final by-products, wet tailings containing 22% moisture and wastewater with a low solid content. All the water streams are finally mixed together. It is either reused and sent back to the washing unit, or treated downstream by an evaporator or reverse osmosis (RO). Note that, except the coal washing tank, all the other units proposed are the same as that are being used in the existing black coal washing process which will be detailed later.

Back to Fig. 1, the four scenarios were designed and compared hereafter to address the discrepancy, between single-stage and multi-stage washing unit via Scenarios 1 versus 2; between evaporator and RO on water recovery via Scenarios 2 and 3; and between water-washing and acid-doped washing via Scenarios 3 and 4.

Scenario 1 is the simplest process to mimic the black coal washing process, using a single-stage water washing in combination with an evaporator for water recovery. Based on the optimum condition from experimental examination, a liquid-solid ratio of 1.25 was applied, resulting in 34% Na and 0.55% Ca removed in 30 min, under ambient conditions. After a bundle of solid-liquid separation units, the dirty water containing fine coal particles, Na and Ca was transported into an evaporator. Free flue gas at 150 °C [22] produced by the adjacent power generation plant was used as the heating source of the evaporator. Evaporated water coming from the top of the evaporator was condensed inside a cooler, which will use cooling water as the coolant. The bundle of evaporator-condenser allowed unwanted salts to be separated and exit the process as waste.

Scenario 2 adopts a counter-current three-stage water washing process, thereby removing more than twice the amount of Na than Scenario 1. However, due to the low water-solubility of organic Ca and $CaO/CaCO_3/CaSO_4$, Ca removal extent was

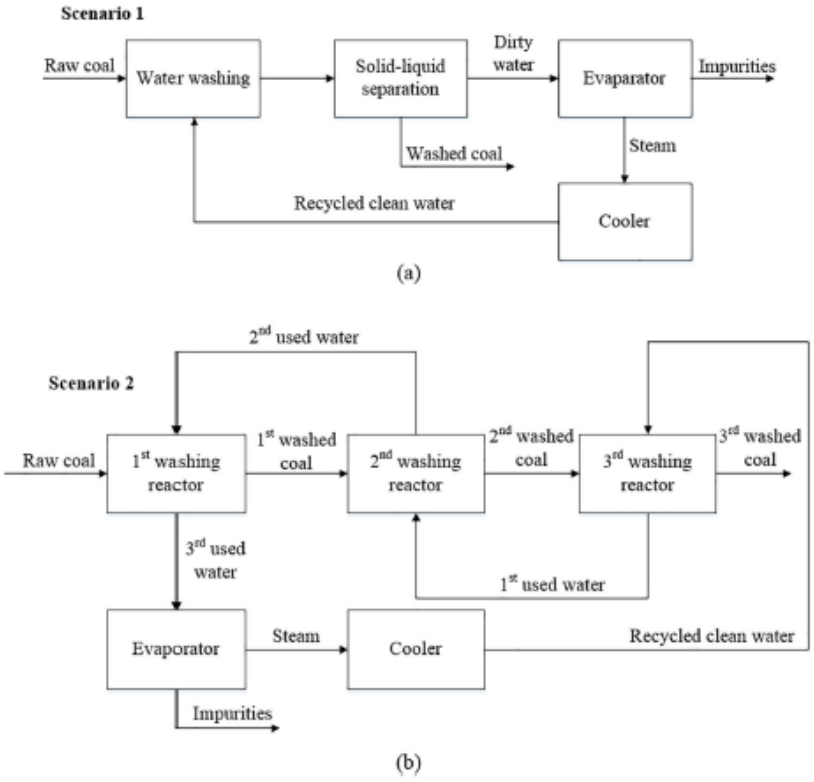

Fig. 1. Simplified low-rank coal washing diagram for Scenario 1 (one stage water washing with evaporator), Scenario 2 (counter-current water washing with evaporator), Scenario 3 (counter-current water washing with RO) and Scenario 4 (acid-water washing with RO).

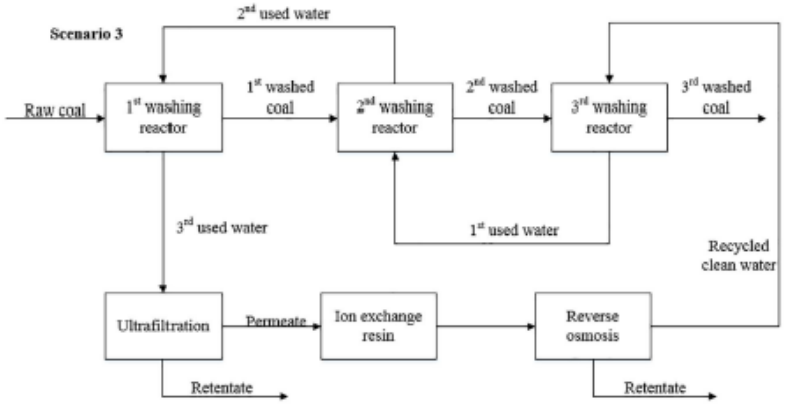

(c)

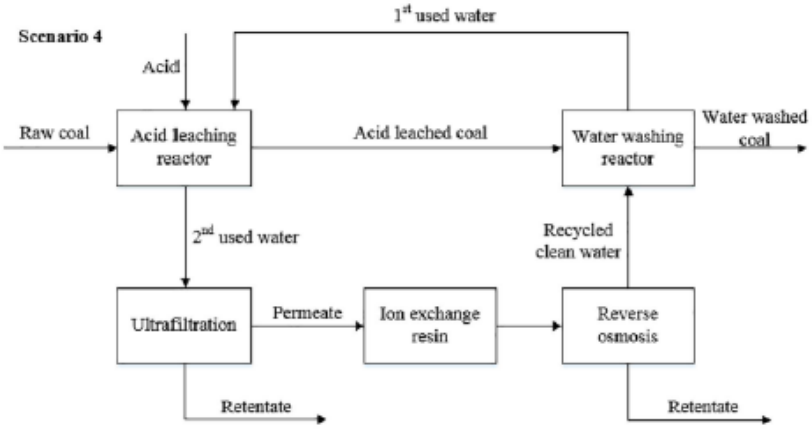

(d)

Fig. 1. (continued)

only slightly increased, at 0.7% totally. The washing conditions in each reactor remained the same as in Scenario 1. The counter-current washing process was introduced to rinse off any possible ions and the other unwanted species deposited on the coal particle surface in the last reactor.

Scenario 3 was further proposed to evaluate the use of RO for the wastewater recovery. Upstream of the RO, an ultrafiltration system (UF) to remove the suspended particles [24] and a strong-acid cation ion exchange resin (IER) to trap calcium ions [25–26] were installed.

Scenario 4 provides the integration of acid-water washing units and the use of RO for water recovery, aiming to reduce the residence time and to improve the process efficiency. In such a scenario, the coal washing process only comprises two stages with the first one for acid leaching and the latter one using pure water to rinse the washed coal. The wastewater recycle process remains the same as that in Scenario 3.

2.3. Model development and validation

Aspen Plus is claimed as a commercially reliable field-tested software for > 30 years and widely used by engineering design companies [23]. Aspen Plus V8.4 was employed to simulate the above-mentioned four low-rank coal washing scenarios, for a plant capacity of 400,000 t coal per annum. In addition, the lab-scale coal washing experiments were conducted to produce the extraction yields that are essential for the Aspen Plus simulation. Furthermore, to validate the accuracy of the Aspen plus model, an existing black coal washing process was also simulated and compared with the plant data. A jig machine which can reduce the ash content of black coal by ~ 50% (reported value from a black coal washing plant from the industry partner) was employed and simulated in the black coal washing process.

2.3.1. Aspen plus simulation

Based on the composition of Xinjiang low-rank coal as in Tables 1 and 3, it was assumed that Na exists as a mixture of NaCl and Na_2O which represents the water-soluble and organic sodium that bound with

Table 4
The simplified composition of Xinjiang low-rank coal for simulation.

Components	wt%
Moisture[a]	24.5
NaCl	0.15
NaOH	0.19
$Ca(OH)_2$	3.57
$CaSO_4$	0.87
C	70.72

[a] Air-dried.

the carboxylic acid, respectively. Similarly, Ca was postulated to be made up of $CaSO_4$ and CaO. Carbon was assumed to make up the remainder of the coal, on the dried and ash-free basis. Furthermore, to accommodate the default electrolyte module in Aspen Plus, the oxides (Na_2O and CaO) were further converted into the respective hydroxides (NaOH and $Ca(OH)_2$). Table 4 outlines the simplified composition of the two target elements in the raw low-rank coal tested here.

The washing reactor for low-rank coal was modelled by a stoichiometric reactor block (RStoic) [23]. For each reaction in RStoic, the reaction stoichiometry, fractional conversion of each reactant and the reaction condition were specified, based on the experimental results that are summarised in Tables 5 and 6. The experimental procedure will be outlined in the next section. Except the washing reactor and waste water treatment units, the same type equipment as in an existing black coal washing plant has been used, as summarised in Table 7. The pressure increase in each pump was assumed to be approximately 1 bar, which was deemed to be sufficient in overcoming the pressure drop within the equipment (e.g. 0.5 atm in a vertical flash separator [23]), and the pressure drop caused by piping in the plant. The outlet temperature of the cold side of the evaporator was set to be 101 °C because the saline water had a bubble point higher than 100 °C but lower than 101 °C in this study (Based on Aspen Plus simulation result between the bubble point of saline water and the concentration of salt).

In terms of RO simulation, the component separators were employed to simulate both the RO membrane and the ultrafiltration membrane installed upstream of the RO to pre-treat the water feed. In addition, the anion ion exchange resin (IER), a pre-treatment unit to RO to remove Ca^{2+}, was simulated by a combination of RStoic and component separator, with the former one in which a reaction between SO_4^{2-} and Ca^{2+} occurs to precipitate Ca^{2+} and the latter to remove the $CaSO_4$ precipitate. In this study, TFC 2832 HF-560 magnum RO membrane was chosen, due to its high maximum allowable salinity of feeding stream, at 32800 mg/L, when the feeding stream pressure is 5520 kPa, at 25 °C [27]. To achieve a high water recovery rate, a three-stage RO system was employed hereafter, ending up with a 75.3% water recovery rate shown in Table 7, where each stage of the RO was simulated as a pressure vessel containing four membranes in series (11% water recovery rate for single membrane). In addition, the feeding stream pressure and water recovery rate were set to be constant

Table 5
Na and Ca removal yields.

Process	Na or Ca	Reactor	Removal yield/wt%
Three-stage water washing	Na	First	34.0
	Na	Second	14.4
	Na	Third	10.0
One stage acid plus one stage water	Ca	First	0.55
	Ca	Second	0.20
	Ca	Third	0.00
	Na	Acid	67.1
	Na	Water	10.0
	Ca	Acid	12.5
	Ca	Water	0.0

Table 6
Optimum operational conditions.

Process	Variable	Value
Water washing	Residence time	30 min
	Liquid-solid mass ratio	1.25
	Particle size	1–4 mm
HCl leaching	Residence time	5 min
	Liquid-solid mass ratio	1.25
	Particle size	1–4 mm
	HCl concentration	0.4 M

Table 7
Summary of assumed input data in Aspen Plus.

Equipment item	Variable	Value
Pump	Efficiency	0.75 [22]
	Pressure increase	1 bar
Reactor	Operating condition	1 bar, 25 °C
Dewatering screen	Cut-off size	0.5 mm
Centrifuge	Water in solid outlet	0.08 [29]
	Solid in solid outlet	0.97 [29]
Pressure filter	Water in solid outlet	0.22 [29]
Evaporator ultrafiltration	Solid in solid outlet	0.98 [29]
	Outlet temperature of cold side	101 °C
	Water recovery rate	96% [23]
	Suspended fine solid removal yield	100%
	Feeding pressure	310 kPa
IER RO (three-stage)	Ca^{2+} removal yield	100%
	Water recovery rate	75.3% [26]
	Na^+ removal yield	100%
	Type of RO membrane	TFC 2832 HF-560 magnum
	Feeding pressure	5520 kPa [26]
	Maximum allowable salinity	32,800 mg/L [26]

at 5520 kPa and 75.3% respectively, although a lower salinity of feeding stream can increase the water recovery rate slightly and requires a lower feeding pressure. This assumption can simplify the simulation and cause a lowest water recovery rate and a highest power consumption, enhancing the credibility of simulation. The UF system was assumed to recover 96% of water and remove all the suspended fine solids [24].

2.3.2. Lab-scale experimental procedure

Lab-scale experiments were conducted to clarify the extraction yields of the two target ions, Na and Ca as a function of residence time, coal particle size, liquid-to-solid ratio, the use of fresh and used water, as well as acid, to yield the necessary data as the input in Aspen Plus. For the lab-scale experimental investigation, the single-stage washing was firstly conducted in a 2 L stirred tank reactor to examine its optimum operating condition. To conduct the three-stage counter-current water washing experiment in the laboratory, the pure water was first used to wash raw coal for 30 min rather than the 2nd washed coal shown in the washing part of Fig. 1(b), yielding a washed coal, termed as Coal A and used water. This is because the 2nd washed coal is unavailable at the start-up. Subsequently, the used water was applied to wash Coal A for another 30 min to attain a two-times-washed coal, as Coal B, which was finally washed with pure water to obtain the 3rd washed coal and 1st used water as shown in Fig. 1(b). Afterwards, 1st used water was employed to wash Coal A for 30 min, obtaining 2nd used water and 2nd washed coal. Finally, raw coal will be washed by the 2nd used water to get 1st washed coal and 3rd used water. All the washing experiments were conducted at a batch-scale. The acid-washing experimental procedure was the same as the single-water washing process, except the utilization of acid.

Inductively coupled plasma optical emission spectrometry (ICP-OES) was employed to quantify the contents of Na and Ca in both leachate and each solid sample, either raw coal or washed coal. The ICP-OES analysis followed a previously established standard procedure [28]. Additionally, the ash fusion temperature of raw coal and washed coal was calculated by a commercial thermodynamic equilibrium software, FactSage$^{6.1}$. The ash compositions in a coal sample, such as the results for raw coal ash listed in Table 3 were used as input for the calculation, plus a weak gas environment (1 vol% CO, 5% O_2, 10% H_2O and N_2 in balance) at 1 atm as an input too [29]. This is to mimic the local gas environment near a coal-fired burner in the boiler. A temperature span of 800 °C to 1600 °C was simulated, and the built-in FToxide_?Slag database in FactSage was selected to quantify the ash melting percentage versus temperature [4].

2.3.3. Black coal washing validation

An existing black coal washing plant with a coal feeding rate of 50 t/h of raw coal for a plant capacity of 400,000 t coal per annum was simulated. The black coal washing process mainly consists of a jig machine to remove the coarse minerals by the difference in the specific density of coal and coarse minerals in the pulsating water, and a variety of downstream liquid-solid separation units that are the same as that for the proposed low-rank coal washing process. As shown in Fig. 2, the coal was firstly screened by a vibrating screen with a cut-off size of 40 mm. The resultant oversize was sent to a crusher to reduce its size down to 40 mm. Subsequently, coal was washed in a jig machine which employed an air stream of 64.5 m^3/min and a water to a solid mass ratio of 2.8 to remove the ash content by ~ 50%, same as that reported by the plant operation. A component separator was chosen to simulate the jig machine. Subsequently, the outlet stream from the jig machine was transferred to a dual deck vibrating dewatering screen with two cut-off sizes of 25 mm and 0.7 mm, separating out the lump coal larger than 25 mm and a moisture content of 8%, and those between 0.7 and 25 mm with a moisture content of 28%, respectively. Afterwards, the slurry of coal fine - water was sent to a peat screen with a 0.5 mm cut-off size to remove the fine coal particles. Simultaneously, the overflow of the peat screen and the coal with a size of 0.7–25 mm were transferred to a centrifuge to reduce the moisture down to 11%, as well as to recover the water for reuse. The water coming from both centrifuge and peat screen was then mixed and sent to a thickener where the coal fines were agglomerated by using a coagulant namely polyacrylamide (PAM), with a mass concentration of 1 g/m^3-slurry [30]. The agglomerates passed through a pressure filter to squeeze out the water. The thickener, which is not a built-in block in Aspen Plus was simulated by a component separator. Finally, the water was recycled back into the jig machine to reuse and the by-product wet tailings of 22 wt% moisture is obtained.

2.4. Cost estimation methodology

Aspen Process Economic Analyzer (APEA) [31] was finally integrated with Aspen Plus to estimate the cost for each scenario proposed above.

Since the plant is located in Xinjiang, China, all the cost figures were expressed as Renminbi (RMB) by a USD/RMB currency conversion rate of 6.60, based on 2017 data. Subsequently, necessary parameters were specified, including the project type, project starting date, annual operating time, project fluids, utilities, labor cost, raw materials and product streams, as outlined in Table 8. For the flue gas used as a hot stream in Scenarios 1 and 2, it was assumed as free of charge since the

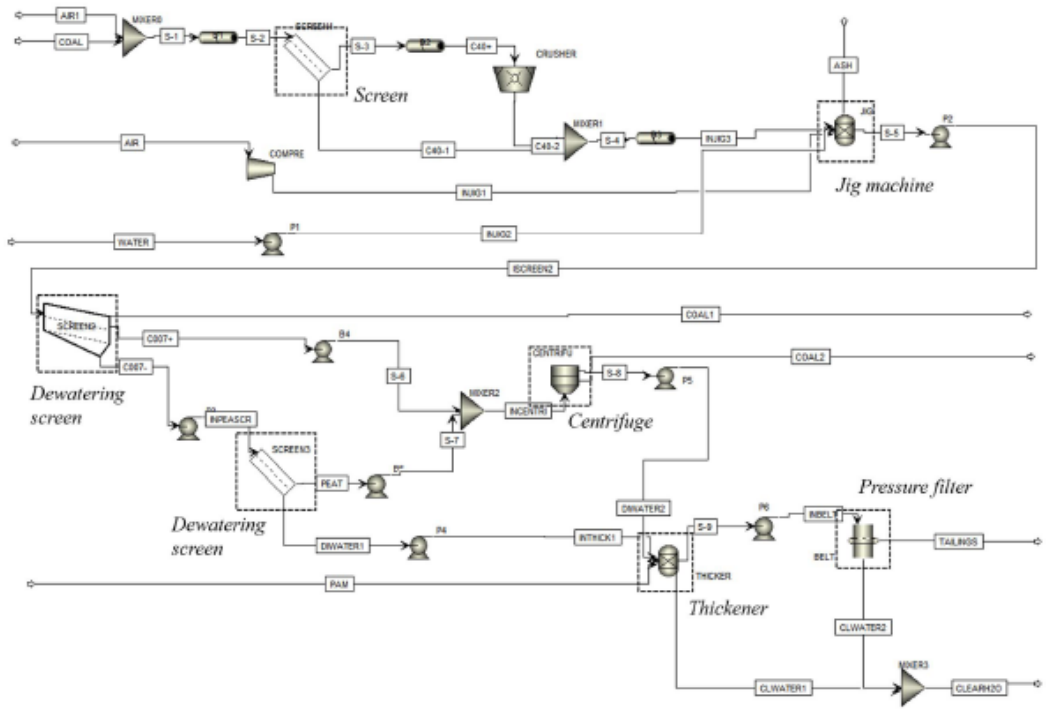

Fig. 2. Aspen Plus flowsheet for the black coal beneficiation process.

Table 8
Input economic parameters to Aspen process economic analyzer (APEA).

General economic parameters		Cash flow analysis parameters	
Plant location	Xinjiang, China	Depreciation	5% per year
Currency conversion rate	RMB/USD 6.60	Tax rate	30%
Project type	Clear field	Interest rate	10%
Source of utilities	Across the fence	Project lifecycle	20 years
Project fluids	Liquids and solids	Discount rate	10%
Operating hours per year	8000	Depreciation method	Straight line
Start date for engineering	1-Jan-17	Working capital	6.7% of the fixed capital cost

Raw material process		Utilities	
Raw Xinjiang coal	46 RMB/t[a]	Electricity	0.255 RMB/kWh[a]
Polyacrylamide	6500 RMB/t[a]	Flue gas	Free
Hydrochloric acid (31%)	Free[b]		
Water	3.7 RMB/m^3 [a]		

Products		labor	
Washed low-rank coal	200 RMB/t[a]	Operator	9.17 RMB/Operator/H[a]
Wet tailings	10 RMB/t[a]		

[a] Reported values from a black coal washing plant in China.

adjacent power plant is able to provide it. So was the hydrochloric acid that can be provided by an adjacent electrolyzer for the production of sodium hydroxide, according to the report of the industrial partner, Hubei Yihua Chemical Co Ltd. However, effort was still made to vary the price of HCl acid to assess its influence on the process feasibility. The prices of raw coal, electricity, water, coagulant polyacrylamide and labor were obtained based on the existing black coal-washing plant. The net present value (NPV), internal rate of return (IRR) and payback period were calculated by cash flow analysis [32] and the corresponding parameters were also outlined in Table 8.

Based on the equipment cost library in APEA, each unit in Aspen Plus needs to be mapped to size and further estimate the cost referring to the vendor quotes in the specified plant location. Centrifugal pumps and rotary lobe pumps were applied for pumping pure water and water-coal slurry, respectively [33]. Due to the volatility and corrosion of 31 wt% HCl, an enclosed agitated tank reactor of carbon steel shell lined by PVDF (polyvinylidene fluoride) was employed [34]. Additionally, the pump in contact with HCl was mapped by the plastic centrifugal pump. Carbon steel was used for all other agitated open-up water washing reactors as the shell material. In light of the residence time, 5 min and 30 min respectively for the acid leaching and water washing, reactors were sized as an internal diameter of 1.52 m and height of 5.64 m for the acid tank, and 2.59 m in diameter and 9.14 m in height for water tanks. Rotary crusher was used for sizing of the coal crusher [30]. The conveyor length and belt width of all belt conveyors were assumed to be 10 m and 500 mm, respectively, which was capable of conveying coal of any flow rates in the process [35]. Long tube vertical evaporator and field assembly cooling tower were selected for evaporator and cooling tower, respectively [36]. However, due to the lack of built-in model for RO in APEA, the cost of RO units were calculated based on an existing water treatment plant using RO in USA [37], which was further corrected by taking into account the plant capacity, location factor, inflation index, and currency exchange rate [38]. The assumptions for RO cost estimation are summarised in Table 9.

3. Results and discussion

3.1. Simulation validation using the existing black coal washing process

Table 10 illustrates the simulation results including the water and power consumption per tonne raw black coal, and the total equipment cost, with the actual plan operating data for comparison.

Table 9
The assumption for RO cost estimation.

Variable	Value
Plant capacity (Million gallon per day) [37]	150
Currency conversion rate	RMB/USD 6.38
Location factor for China [45]	0.95
Cost index 2001 [46]	406
Cost index 2017 [46]	1125

Table 10
Comparison of the actual and simulation values for black coal beneficiation process.

Variable	Simulation result	Actual value[a]	Unit
Water consumption	71	51–85	kg/t of raw coal
Power consumption	3.9	3.5–6.3	kWh/t of raw coal
Total equipment cost	5.1	4.2 (5.5)	million RMB

[a] Reported values from a black coal washing plant in China which was built in 2013. The number in the bracket is the net present value by converting 4.2 in 2013 to 2017 when this simulation is being conducted.

It is clear that the Aspen Plus simulation results are credible, particularly for the high accuracy for the total equipment cost by comparing the simulation result (5.1 million RMB) with the present value of actual data (5.5 million RMB). Note that, the actual value (4.2) in the year 2013 was converted to its present value (5.5) based on 2017 by taking into account the cost inflation indexes of 852 and 1125 for the years 2013 and 2017 respectively [46]. For the other two variables, the simulation results are also reasonable and fall in the range of the plant data. It should also be noted that the plant operation generally has a fairly large fluctuations on coal compositions and operational conditions, leading to a large variation on the water and power consumptions. Even so, given the fact that the major liquid-solid separation units including dewatering screen, thickeners, pressure filter and centrifuges in the black coal washing process have been considered and included in the modelling and the same units will be used for low-rank coal washing, the results in Table 10 provide a reasonable credibility to the simulation results obtained for the low-rank coal washing results to be discussed later. In addition, it is noteworthy that, the water loss for the black coal washing mainly takes place in the centrifugal stage where the final product reaches an equilibrated moisture content of 11 wt%.

Table 11
Ash composition changes after different washing processes.

Sample	Ash/%	Na_2O	MgO	Al_2O_3	SiO_2	P_2O_5	SO_3	K_2O	CaO	Fe_2O_3
Raw coal	7.8	4.32	22.65	3.27	5.67	0.52	15.06	0.21	46.96	1.34
Scenario 1	7.6	1.01	24.32	3.04	4.03	0.52	16.94	0.25	47.77	2.12
Scenario 2	6.4	0.85	21.23	4.38	6.59	0.45	19.86	0.21	45.95	0.48
Scenario 4	6.3	0.19	19.46	4.97	7.86	0.38	37.36	0.17	29.06	0.55

With respect to the power consumption, it is mainly due to the use of the jig machine that consumes a power of 2.3 kWh/t coal.

3.2. Comparison of low-rank coal washing stages in Scenarios 1 and 2

3.2.1. Lab-scale coal washing results

Table 11 compares the ash composition change of washed coal produced by the Scenarios 1 and 2, where coal was washed by a single-stage and three-stages, respectively. The total ash was rarely reduced in Scenario 1, although the mass fraction of Na_2O in ash was reduced noticeably from original 4.32 wt% down to 1.01 wt%. The Scenario 2 is clearly more pronounced, achieving a reduction of 1.4 wt% for the total ash, and a lower value of 0.85 wt% for Na_2O in the ash. Fig. 3 demonstrates that the majority of the ash produced for Scenario 2 does not melt until the temperature reaches 1200 °C, which is the design temperature for the combustion chamber in a pulverized coal-fired boiler.

3.2.2. Aspen plus simulation results

Fig. 4 shows the Aspen Plus flow-sheets for Scenario 1 and 2, where all the process units remain identical between the two scenarios, except the washing stages. The water recovery rate, water and power consumption of both scenarios are presented in Table 12. Interestingly, both new processes can produce, rather than lose about 140 kg water per tonne raw coal. This is a result of the 24.5 wt% moisture content in the original coal that was down to 11 wt% after centrifugal dewatering, resulting in more water recovered than what was lost in the tailing and other units. In terms of the external fresh water added into the process, the proposed two scenarios could recycle almost same fraction that is close to 93%, which is also close to the black coal. However, the total power consumption per tonne of raw coal for Scenario 2 is more than twice that for Scenario 1, 9.4 versus 4.6 kWh/t raw coal. This is mainly due to the use of extra pumps and agitation tanks for the three-stage washing that consumed 6.7 kWh/t coal in Scenario 2, triple of the power caused by only one tank in Scenario 1. The remaining process equipment in both scenarios consumed nearly equal power, at around 2.5 kWh/t coal.

3.3. Comparison of waste water treatment methods via Scenarios 2 and 3

Since the waste water treatment unit is crucial for the feasibility of the overall process, efforts were made to assess Scenario 3 where the three-stage washing unit plus a downstream RO-based wastewater treatment unit were adopted. Table 13 demonstrates the simulation results for its water and power consumption as well as water recovery rate, with the results of Scenario 2 included for comparison. Unsurprisingly, Scenario 3 consumed much more water, due to the low water recovery rate of the RO system, 75.3% (see Table 7). Accordingly, the application of RO system caused a lower water recovery rate (68.3%) for Scenario 3. A total of 228 kg/t coal water was thus lost in Scenario 3, compared with 137 kg/t coal water gain for Scenario 2. The water loss ratio in Scenario 3 is also far more than the 85 kg-water/t coal consumed for the black coal washing process. In this regard, the RO system seems to be overshadowed by the evaporator. However, the better performance of Scenario 2 about water recycling rate might be counteracted by the considerable capital cost was caused by the huge heat transfer area of the evaporator and cooling tower (further discussed later).

With respect to the large discrepancy in the power consumption between these two scenarios, the feeding stream pump in the RO system is crucial. The part of RO for Scenario 3 is further extended in Fig. 5. Two feeding pumps had to be added in to satisfy the specific feeding stream pressure into ultrafiltration system and reverse osmosis system, at 310 kPa and 5520 kPa, respectively. As a result, the total power consumption of Scenario 3 is 12.2 kWh/t of raw coal, which is larger than 9.4 kWh/t raw coal of Scenario 2, as evaporator consumes hot flue gas rather than electricity. In addition, compared to black coal which requires approximately 6.3 kWh/t coal for washing, the energy consumption for low-rank coal washing, as predicted here, is much higher especially for Scenario 3, indicating that a further optimization is necessary.

The discrepancy in the capital and operating costs between Scenarios 2 and 3 is also noteworthy. Although both scenarios require further optimization, clarifying the costs of different waste water treatments and their percentages in the total capital cost is critical. Fig. 6 presents the breakdown of capital costs for these two scenarios.

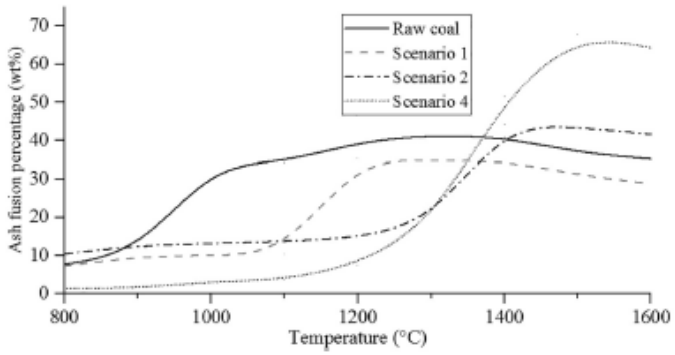

Fig. 3. Ash melting point comparison for Scenarios 1, 2 and 4.

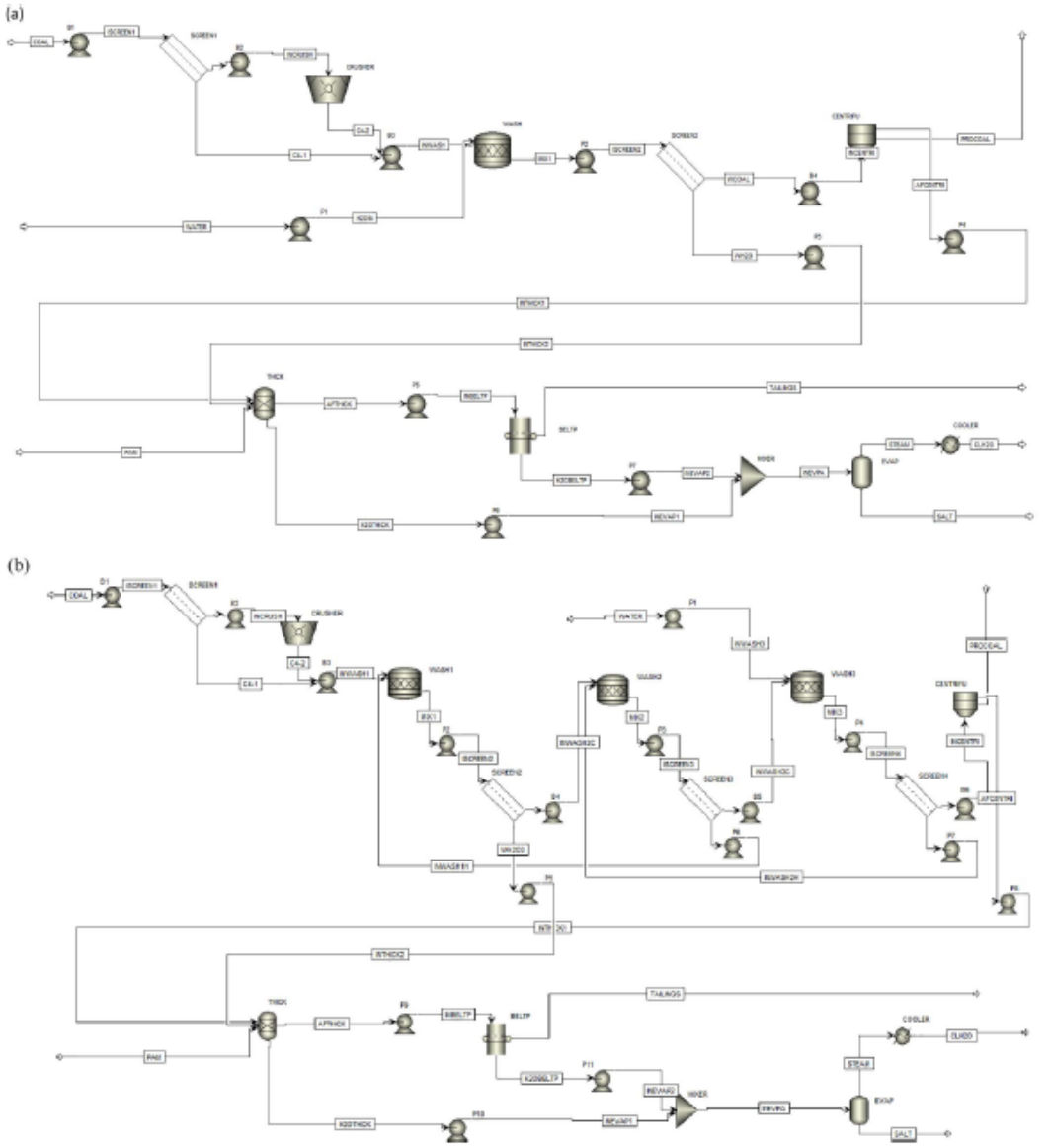

Fig. 4. Aspen Plus flowsheet for Scenarios 1 (a) and 2 (b).

The total capital cost of Scenario 3 using RO was estimated to be around half of the figure of Scenario 2 incorporating evaporator and cooling tower, due to the smaller equipment and piping costs for Scenario 3. By breaking down the equipment cost, it is found that for Scenario 2, the cost of evaporator and cooling tower is the largest contributor to the purchased equipment cost, might due to the requirement of large heat transfer area. It is made up of 69.5% and is more than four times the cost of RO system in Scenario 3. Additionally, the annual operating costs for the two scenarios are demonstrated in Fig. 7. Two scenarios have similar operating costs, of which the total raw material cost makes up the largest proportion. Due to the higher power consumption for Scenario 3, it is reasonable that the expenditure of utilities is higher than that of Scenario 2. Similarly, the marginal higher total raw material cost is also observed for Scenario 3 due to a slightly larger water consumption. However, Scenario 3 required much lower maintenance cost than Scenario 2, based on an assumption of allocating around 2% of the fixed capital cost to the maintenance fee [39–41], causing its even smaller total operating cost (24.4 compared with

Table 12
Comparison of water and power consumption for single and three-stage water washing.

Variable	Single stage	Three stages	Unit
Water consumption	144.1 (gain)	137.0 (gain)	kg/t of raw coal
Water recovery rate	93.3	92.8	%
Total power consumption	4.6	9.4	kWh/t of raw coal
Agitated tank power consumption	2.2	6.7	kWh/t of raw coal
Power consumption by left equipment	2.3	2.7	kWh/t of raw coal

Table 13
Comparison of water and power consumption for three-stage washing using evaporator and RO.

Variable	Using evaporator	Using RO	Unit
Water consumption	137.0 (gain)	228.4 (loss)	kg/t of raw coal
Water recovery rate	92.8	68.3	%
Power consumption	9.4	12.2	kWh/t of raw coal

25.2 Million RMB per year).

3.4. Optimization of Scenarios 3 for the integration of multi-stage washing unit and RO technique

3.4.1. Increasing the cycle numbers of waste water

The first optimization option chosen is the reuse of the semi-clean water obtained after the bundle of the solid-liquid separation units. Such a waste water, if unsaturated with salts, could be still sent back to and used in the 3rd washing tank. The hypothesis is that the unsaturated used water still has the capability to extract sodium out of the coal matrix, since the water solubility of Na-bearing species is usually large, e.g. 359 g/L for NaCl and 418 g/L for NaOH under the ambient conditions.

To find the maximum allowable cycle number of the semi-clean water, experiments were first conducted to wash the raw coal with the pure NaCl solutions of 0.2 wt% and 1 wt%, under the optimum condition as mentioned in the Subsection 2.3.1. These two NaCl solutions were made to mimic the water that has been reused once and six times, respectively. Due to the reuse of the water, the concentration of Na^+ should increase steadily upon a continuous dissolution of NaCl out of coal. Fig. 8 shows time-resolved concentration profile of Na^+ in the two NaCl solutions. Clearly, the use of 0.2 wt% is still able to extract Na out of coal. However, the content of Na^+ in the 1 wt% NaCl solution remains rather constant, indicating that the Na^+ concentration in the outer liquid film of coal particle should be equal or close to 1 wt% NaCl and thus has no momentum to diffuse out. In other words, the 1 wt% Na^+ referring to the reusing of water six times is the maximum allowable concentration of Na^+ in the used water. In addition, such a maximum allowable concentration of Na^+ is also far lower than the highest salinity of the feed stream, 32,800 mg/L with an equivalence of approximately 3 wt% NaCl that can be tolerated by the TFC 2832 HF-560 magnum RO membrane chosen here [27]. However, the concentrate of a RO membrane is the feed to the next RO membrane. Therefore, the salinity of the feeding stream to the third RO membrane is the highest, which was calculated to be 4307 mg/L based on the simulation result after the first cycle of washing. The maximum possible cycle number by RO membrane is thus seven times (4307 divided by 32,800), which is close to the six cycles determined by experiments.

Table 14 compares the change in the water and power consumption upon implementing the maximum six cycles for the reusing of the wastewater prior to it being treated by the RO system. Interestingly, the water loss rate declined significantly from 228.4 kg/t coal to 38.1 kg/t coal, which is even less than the half for black coal washing process. The power consumption also decreased due to the reuse of waste water, resulting from less use of the feeding pump prior to the RO system. However, it is still larger than that of black coal washing process. This is because the three agitation tanks are still the major component consuming huge energy.

3.4.2. Acid leaching

Efforts were made to reduce the coal washing steps, and to reduce the washing time (thus the size of a single washing tank) by using the acid-controlled leaching method. The hypothesis is that the use of a weak acid would increase the concentration of proton $[H^+]$ in the leachate, which in turn promotes both the diffusion and reaction Eqs. (1) and (2) to the right hand side. This thus reduces the washing time and the size of the washing tank consequently. In light of this, the coal washing process was further optimized as Scenario 4 in which are only two coal washing tanks, with the former tank for the acid-controlled leaching and the latter one for the rinsing by water only.

Back to Tables 5 and 6, it is obvious that the removal of both sodium and calcium has been improved remarkably, so was the leaching time that was reduced to only 5 min to maximize the removal of these two target elements. Back to Table 11, the percentages of Na_2O and CaO in ash declined significantly to 0.19 and 29.06 wt%, respectively, resulting in a decrease of 19.2% in total ash content. Consequently, the ash fusion temperature of washed coal by Scenario 4 exceeded 1200 °C

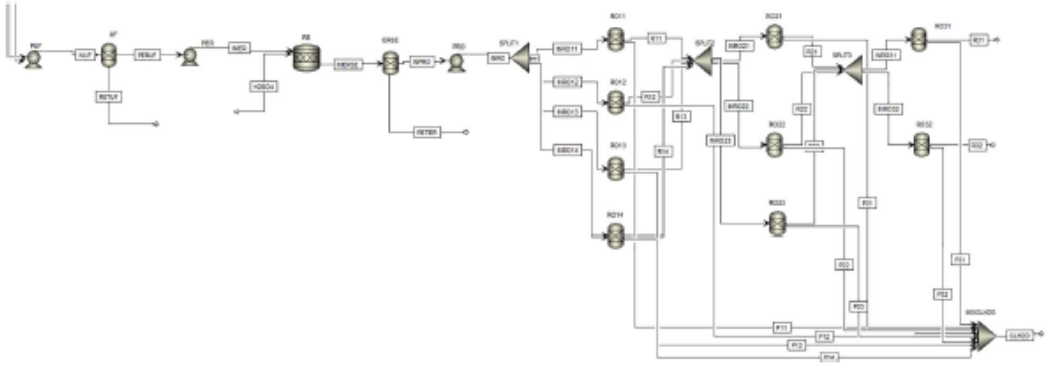

Fig. 5. RO part in the Aspen Plus flowsheet for Scenario 3.

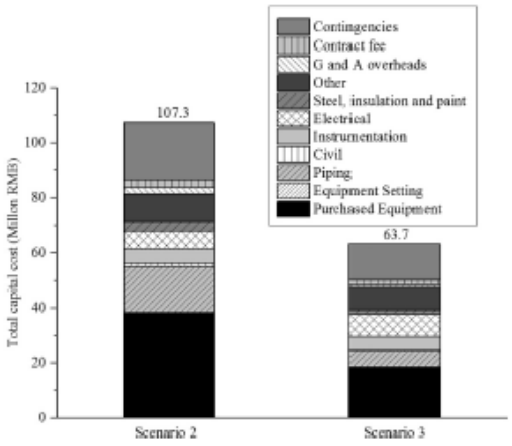

Fig. 6. Total capital cost and its break-down for Scenarios 2 and 3.

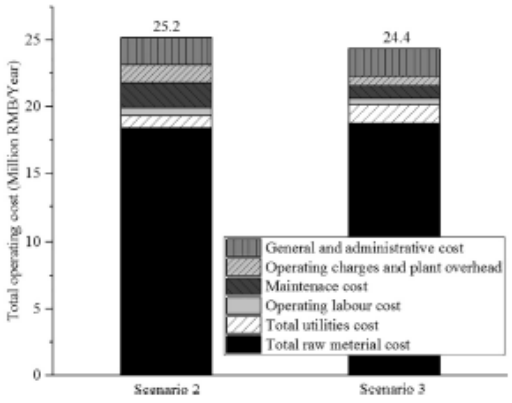

Fig. 7. Break-down of operating cost per year for Scenarios 2 and 3.

(the coal-fired boiler's operational temperature), as presented in Fig. 3.

Fig. 9 shows the Aspen Plus flowsheet of Scenario 4 without the inclusion of the RO part which is the same as in Fig. 8. Table 15 compares all the simulation results for the Scenarios 3 and 4. With regard to the maximum allowable cycle times, the number for Scenario 4 was smaller than Scenario 3 (4 versus 6), due to the higher Na and Ca removal extent in a single cycle. Therefore, the Scenario 4 consumed more water, at 48.1 kg/t coal, which is however still far lower than 85 kg/t coal required for the black coal washing process. In addition, the power consumption declined greatly, by nearly 50% from 9.4 kWh/t coal for Scenario 3 to 5.8 kWh/t coal that is also below the black coal case, 6.3 kWh/t coal. Clearly, the use of less agitation energy is much more influential than the increased energy consumption for the RO system. The use of less tank also slightly reduced the capital cost. Additionally, owing to the lower power consumption, Scenario 4 possesses a lower annual operating cost. This will be discussed in the next section.

Table 14
Comparison of water and power consumption before and after increasing the cycle.

8	Before	After	Black coal process	Unit
Water consumption	228.4(loss)	38.1(loss)	85	kg/t of raw coal
Power consumption	12.2	9.4	6.3	kWh/t of raw coal

3.5. Sensitivity analysis for Scenario 4

3.5.1. Effects of the principal variables on the number of water recycle, water and power consumptions

Considering the heterogeneity of raw coal, and uncertainty related to the dewatering performance of centrifuge caused by the hydrophilicity difference between the differently ranked coals, sensitivity analyses were further carried out to assess the changes of water and power consumption in Scenario 4, upon the variation of raw coal properties outlined in Table 16. In brief, the moisture content in raw coal varied from 10 wt% for the equilibrated content to the maximum possible value of 30 wt% as that has been reported for Xinjiang coal [5], with an interval of 5 wt%. The mass percentage of coal size < 0.5 mm (cut-off size of the screen after the coal washing unit) varied from nil to 90 wt% at an interval of 20 wt%, considering that the low-rank coal is generally soft and fine compared to high-rank coal. In addition, the contents of chlorine (Cl) and Na in the raw coal are crucial, affecting the recycle number of waste water. The contents of Cl and Na varied from 200 to 2000 ppm and 700 to 5200 ppm in raw coal, respectively, which was considered to include all possible contents [42]. Finally, the moisture of coal out of centrifuge was also varied. This is based on the concern that the commercial plant for low-rank coal washing and dewatering does not exist yet. Lab-scale experiments have been conducted in a batch-scale centrifuge (Allegra X-22 Centrifuge). It confirmed that the lowest moisture in the dewatered Xinjiang coal was around 22 wt%.

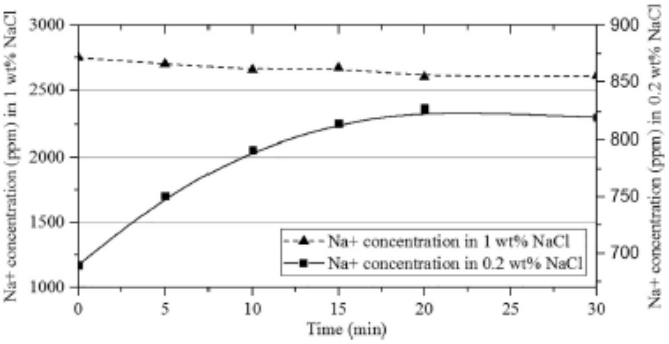

Fig. 8. Na ion concentration change in 0.2 wt% and 1 wt% NaCl versus time.

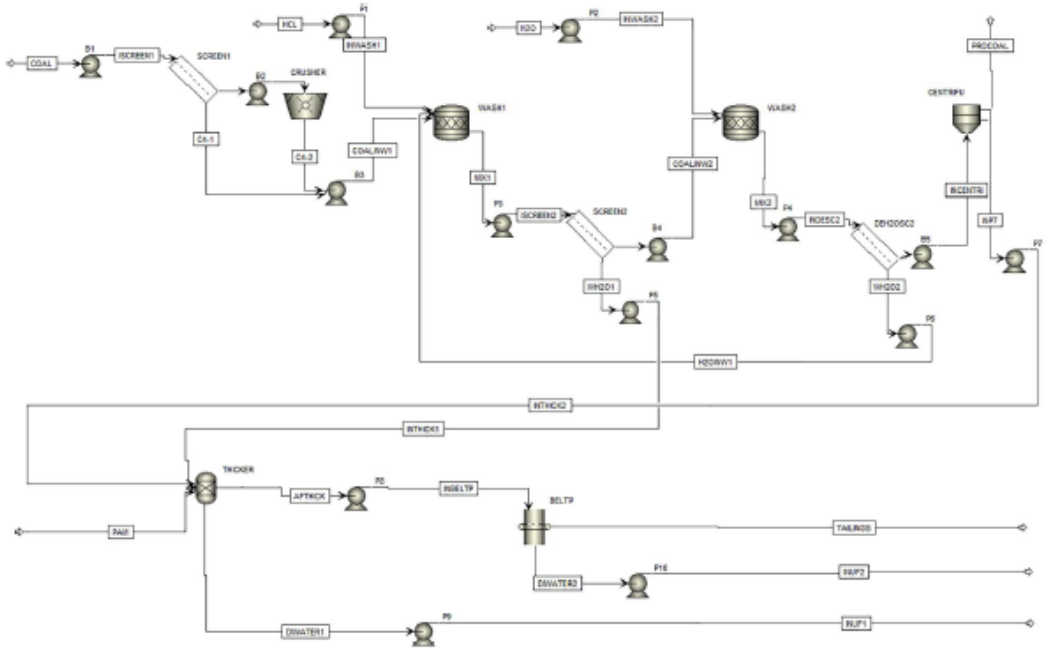

Fig. 9. Aspen Plus flowsheet for Scenario 4.

Table 15
Result summary of Scenarios 3 and 4.

Variable	Three-stage with RO	Acid with RO	Unit
Na removal yield	60.0	77.1	%
Ca removal yield	0.7	12.5	%
Cycle times	6	4	times
Water consumption	38.1(loss)	48.1(loss)	kg/t of raw coal
Power consumption	9.4	5.8	kWh/t of raw coal
Capital cost	63.7	56.3	million RMB
Operating cost	23.8	23.2	million RMB/Year

Table 16
Sensitivity variables and variation ranges.

Variable	Variation range	Variation pace
Initial moisture of raw coal	10–30 wt%	5 wt%
Mass fraction of coal fines < 0.5 mm	0–90 wt%	20 wt%
Total Cl content in raw coal	200–2000 ppm	200 wt%
Total Na content in raw coal	700–5200 ppm	500 wt%
Moisture wt% in dewatered coal	8–22 wt%	2 wt%

The discrepancy between the industry-reported value (8 wt%) and lab-based value (22 wt%) might be because of the different configuration of centrifuges as well as the strong hydrophilicity of low-rank coal. Therefore, the moisture of centrifuge-dewatered coal was set as a sensitivity variable with a variation range of 8 to 22 wt%.

As shown in Fig. 10 (a), the Na content in raw coal is the most sensitive variable, varying the wastewater recycle number from fourteen times to only once upon the rise of its original content in coal from 700 to 5200 ppm. Accordingly, the water and power consumptions are also highly sensitive to the variation of the original Na content, as evident in the panels (b) and (c). The highest cycle number for a minimum Na content of 700 ppm leads to the lowest water and power consumption, 14 kg/t coal and 5.14 kWh/t coal, respectively. However, once the Na content in raw coal reaches around 2150–2520 ppm (the base case is 1670 ppm), the water consumption and power consumption of Scenario 4 will reach the same values, 85 kg/t coal and 3.64 kWh/t coal for the black coal, respectively. With respect to another element of interest, Cl in the raw coal, its influence is marginal on the three dependent variables.

The initial moisture in the raw coal is the second most influential variable, which directly determines the amount of total water entering the process. The cycle number is therefore proportional to the initial moisture in the raw coal, ranging from three times to five times upon the change in the initial moisture from 10 wt% to 30 wt%. Consequently, the water consumption declines from 103 to 30 kg/t coal, reaching the same water consumption figure for black coal in the case that initial moisture is around 19 wt% in the raw Xinjiang coal. Compared to the black coal with 10 wt% moisture, such a threshold value in the Xinjiang coal is clearly high. This is because the Xinjiang coal is fine in size, resulting in a percentage of 13 wt% for the waste tailing. More interestingly, although the entry of high-moisture coal into the system results in the rise on the amount of the waste water to be processed in the RO unit, such a side effect is counteracted by the increase in maximum cycle number. Therefore, the rise of coal moisture content from 10 wt% to 30 wt% indeed results in a slight decline in the power consumption from 5.9 to 5.6 kWh/t coal, as evident in panel (c).

With respect to the mass fraction of coal fines and moisture content after the centrifugal dewatering, the increase on the former variable results in more coal to be sent to the centrifuge that produces a much lower moisture content (11 wt%) in the resultant dewatered coal, compared with the moisture of the wet tailings that is generally 22 wt %. As a result, the water consumption increases slightly from 46 to 58 kg/t coal when the particles smaller than 0.5 mm increases from 0 to 90 wt%. Nonetheless, such a rise is quite marginal and affects little on

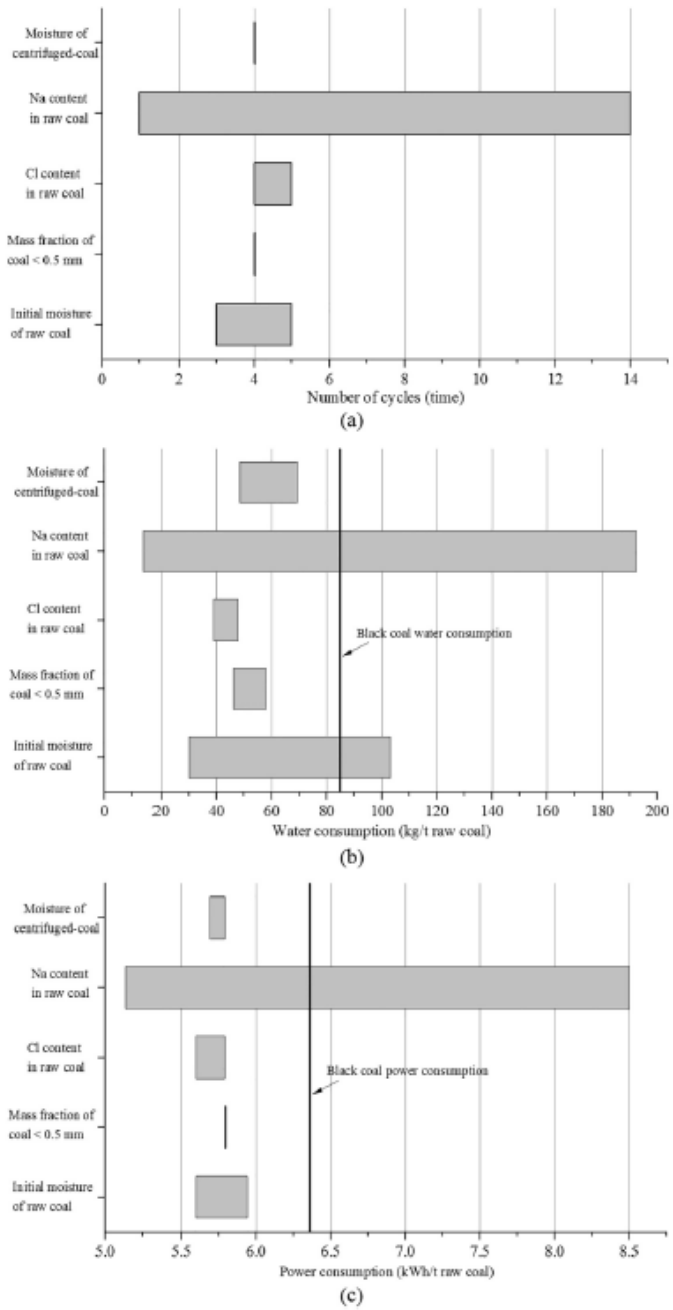

Fig. 10. Sensitivity analysis of the variables on (a) number of cycles, (b) water consumption and (c) power consumption per tonne of raw coal for Scenario 4.

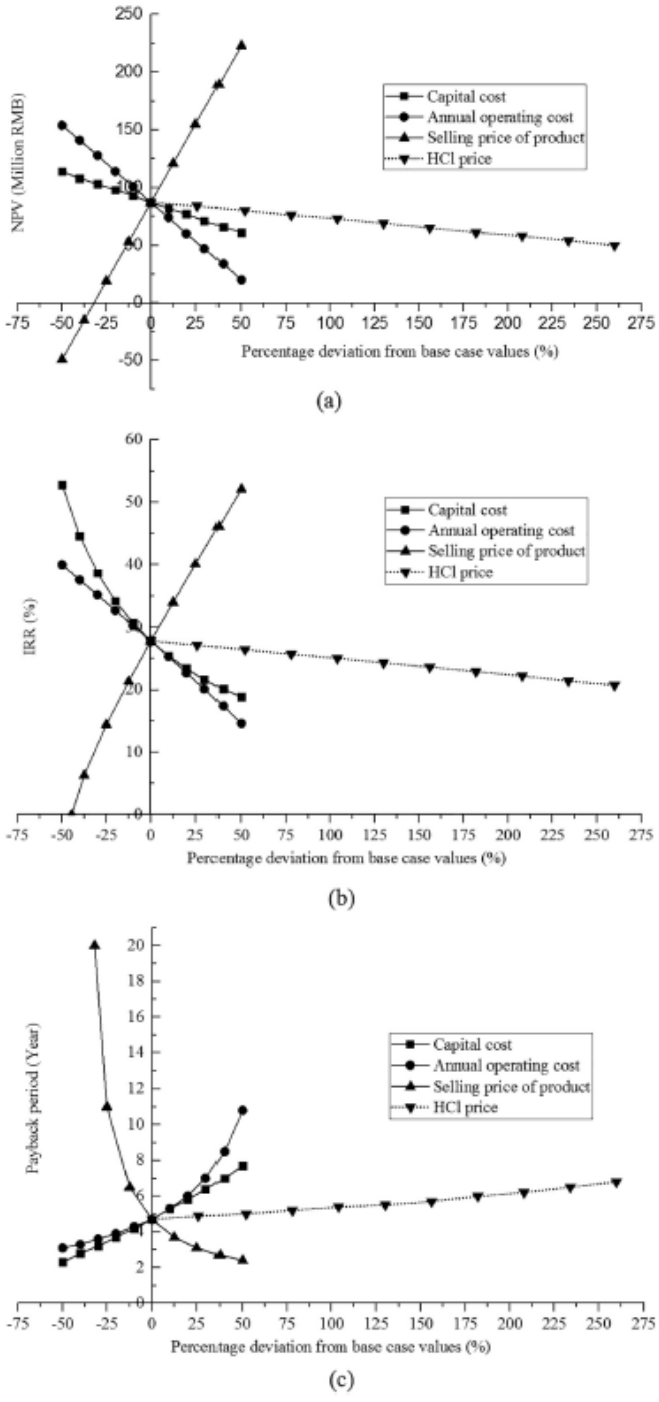

Fig. 11. Sensitivity analysis of effects of capital cost, annual operating cost, the selling price of product and HCl price on (a) NPV, (b) IRR and (c) Payback Period for Scenario 4.

the water cycle number and power consumption, as evident in panels (a) and (c). Finally, the increase in the moisture of coal out of centrifuge causes larger water consumption and smaller power consumption due to the decline in the water transferred to RO feeding pump, the main power consumption unit. However, similar to the PSD change, it affects little on the cycle number.

3.5.2. Effects of the principal variables on NPV, IRR and payback period

Cash flow analysis was implemented to determine the variation of NPV, IRR and payback period for the best Scenario 4. To reiterate, the income of this project is from the sale of the main product, washed coal with a price of 200 RMB/t in the local market, and by-product tailings at 10 RMB/t. With an economic lifecycle of 20 years for the base case Scenario 4, NPV, IRR and payback period are 87 million RMB, 27.8% and 4.7 years, respectively, indicative of a strong investment temptation. IRR is almost fivefold larger than the highest inflation rate in China in recent ten years, at 5.9% [43], showing a strong risk tolerance. In particular, considering the high NPV of 87 Million RMB and a short payback period of 4.7 years, a satisfactory profitability is envisaged.

Fig. 11 demonstrates the sensitivity of the economic analysis results upon a ± 50% variation of the principal variables except the HCl price changing from 0 to 260 RMB/t that is the market price in China [44]. Based on the panel (a), it is obvious that the NPV is mostly susceptible to the variation of the selling price of the final product, washed coal. A 50% increase in the selling price can make NPV soar to 223 million RMB. By contrast, NPV turns negative when the selling price decreases by 32% (136 RMB/t). With respect to the annual operating cost, its 50% increase causes NPV to drop to 20 million RMB, compared to the 154 million RMB when the operating cost decreases by 50% from the base case. The capital cost is a relatively insensitive parameter for NPV, as suggested by a much less steep slope. The HCl price also exerts a marginal effect on the NPV. Its 260% increase only results in NPV to decline from 87 to 50 million RMB.

In regard to the IRR in panel (b), the selling price of the final product is still the most influential parameter. A decrease to 44.5% for the final product price results in the IRR plummeting from 52.1% to nil, and then negative upon a further decline in the selling price of the main product. The variation of capital cost can also change the IRR greatly from 52.8% to 18.8% upon its change by −50% and +50% respectively. A similar trend is observed for the impact of the annual operating cost on IRR. A 50% increase in the operating cost makes IRR decline to 14.4% from 27.8% (the base case value). HCl price is the least sensitive variable to IRR, indicated by its rather flat slope. The IRR still remains above 20% even with a 260% increase in the HCl price.

With respect to the payback period, the selling price of the product also presents the highest sensitivity. Here again, a minimum selling price of 136 RMB/t (−32% deviation from base-case value) is essential to ensure that the payback period smaller than the lifespan of the project (20 years). A 50% rise in the selling prices, however, will shorten the payback period from 4.7 to 2.4 years. The sensitivities of payback period towards the annual operating cost and capital cost are close, increasing from approximately 2.5 years at −50% deviations of each of the variables to 10.8 and 7.7 years upon +50% deviations of the operating cost and capital cost respectively. With the increase in HCl price from 0 to 260 RMB/t, the payback period increases gradually from 4.7 to 6.8 years, indicating the least sensitivity of the variation of HCl price to payback period.

Finally, it is noteworthy that, the simulation and cost estimation results here are merely for a preliminary estimation and comparison with black coal purpose. The cost calculation results of this stage could have ± 30% error [23]. Detailed and more accurate pilot plant testing is underway to further adjust the results predicted here. Even so, one still can envisage that the proposed low-rank coal washing process is a promising technology solving the alkali element – related problems during the combustion of low-rank coals.

4. Conclusion

This paper has performed the techno-economic analysis of four different scenarios for the selective removal of Na and Ca from a low-rank sub-bituminous coal, targeting to improve the ash fusion temperature of the washed coal to reduce its slagging and fouling propensity in the pulverized coal-fired boilers. The major conclusions achieved are as follows:

1) From the technical perspective, the use of a three-stage counter-current water washing or a two-stage acid-controlled washing is essential for the improvement of the ash fusion temperature above the operating temperature of the boilers. These two scenarios can reduce the mass fraction of Na_2O in ash from original 4.32 wt% down to 0.85 and 0.19 wt%, respectively. The acid-controlled two-stage washing is also able to remove 12.5% calcium and 19.2% total ash.
2) For the recycle and treatment of wastewater, the water gain is desirable for the use of evaporator for a base case low-rank coal containing 25 wt% water. This is because the water in coal can be mostly squeezed out in the centrifuge. Instead, the use of RO results in a water loss accounting for maximum 228.4 kg/t coal. However, prior to the RO treatment unit, the reuse of the unsaturated water for a maximum six cycles is beneficial in reducing both the water and power consumption. The water consumption drops to 38.1 kg/t coal and 48.1 kg/t coal for the three-stage water washing and acid-washing process, respectively. Both are remarkably < 85 kg-water/t coal for the black coal. The power consumption drops to around 9.4 kWh/t coal for the three-stage water washing process and further down to 5.8 kWh/t in the case that acid-control washing is adopted, which is lower than 6.3 kWh/t for the black coal.
3) For the best scenario integrating acid washing and RO unit, its base case is economically viable. Based on a local selling price of 200 RMB for the washed coal, an NPV of 87 million RMB and IRR of 27.8% as well as short payback period of 4.7 years have been confirmed.
4) Sensitivity analysis indicates that the original Na content in raw coal is the most influential variable on the water and power consumption of the overall process, followed by the initial moisture content in the raw coal. For a low-rank coal containing > 2150–2520 ppm Na and/or < 19 wt% moisture, the washing process proposed would turn economically unviable compared to the existing black coal washing process. The influence of other three variables is rather marginal.
5) The selling price of washed coal influences the economic indexes mostly. Its 50% increase can improve the NPV and IRR from 87 million RMB and 27.8% (base case values) to 223 million RMB and 52.1%, respectively. A minimum selling price of 136 RMB/t (−32% deviation) is essential to keep both NPV and IRR positive as well as the payback period shorter than the project lifespan.

Acknowledgments

This project is supported by Hubei Yihua Chemical Co Ltd. The first author is also grateful to the China Scholarship Council – Monash University scholarship for a PhD scholarship. Professor Huanting Wang in the Department of Chemical Engineering Monash University is also thanks for the use of the centrifuge in his laboratory.

References

[1] Agritrade Resources Limited, All about coal (viewed 5th March 2016), http://www.agritraderesources.com/images/stories/pdf/Coal_Fact_Sheet_4th_July_2012.pdf.
[2] J. Li, X. Zhuang, X. Querol, Comparative study of coal qualities from three large coal basins in Xinjiang, Northwest China, Font O.31 Meeting of the Spanish Mineralogical Society (SEM 20122), Barcelona, 2011, pp. 121–122.
[3] X.J. Wu, X. Zhang, K. Yan, N. Chen, J. Zhang, X. Xu, L. Zhang, Ash deposition and

slagging behavior of Chinese Xinjiang high-alkali coal in 3 MW pilot-scale combustion test, Fuel 181 (2016) 1191–1202.
[4] B.Q. Dai, F. Low, D.G. Anthony, Z. Wu, L. Zhang, Characteristics of ash deposits in a pulverized lignite coal-fired boiler and the mass flow of major ash-forming inorganic elements, Energy Fuel 27 (2010) 6198–6211.
[5] X. Wu, X. Zhang, B.Q. Dai, X. Xu, J. Zhang, L. Zhang, Ash deposition behaviours upon the combustion of low-rank coal blends in a 3 MW pilot-scale pulverised coal-fired furnace, Fuel Process. Technol. 152 (2016) 176–182.
[6] M. Grabner, Industrial Coal Gasification Technologies Covering Baseline and High-Ash Coal, Wiley-VC (2015).
[7] U.S. Environment Protection Agency, AP 42: Compilation of Air Pollutant Emission Factors, Fifth ed., (2016) http://www6.epa.gov/ttnchie1/ap42/ch11/final/c11s10.pdf.
[8] J.G. Speight, The Chemistry and Technology of Coal, Third ed., CRC Press, 2012.
[9] M.G. Dong, The effect of coal with high sodium on slagging, and corrosion in boilers (In Chinese), Therm. Pow. Generation 09 (2008) 35–39.
[10] N. Wijaya, L. Zhang, A critical review of coal demineralization and its implication on understanding the speciation of organically bound metals and submicrometer mineral grains in coal, Energy Fuel 25 (2011) 1–16.
[11] K.M. Steel, J.W. Patrick, The production of ultra clean coal by chemical demineralisation, Fuel 80 (14) (2016) 2019–2023.
[12] E. Jorjani, G.H. Chapi, T.M. Khorami, Ultra clean coal production by microwave irradiation pretreatment and sequential leaching with HF followed by HNO_3, Fuel Process. Technol. 92 (10) (2016) 1898–1904.
[13] N. Okuyama, N. Komatsu, T. Shigehisa, T. Kaneko, S. Tsuruya, Hyper-coal process to produce the ash-free coal, Fuel Process. Technol. 85 (8–10) (2004) 947–967.
[14] R.B. Finkelman, C.A. Palmer, M.R. Krasnow, P.J. Aruscavage, G.A. Sellers, F.T. Dulong, Combustion and leaching behavior of elements in the Argonne premium coal samples, Energy Fuel 4 (1990) 755–766.
[15] D.Z. Shi, A Cyclical System of Removing Sodium From Coal: China (201210416906 [P]), (Feb 2 2012).
[16] W. Pantiono, J. Zhang, H.A.A. Abbas, X. Wu, X. Chen, L. Zhang, Influence of external clay and inherent minerals on lignite optical ignition and volatile flame propagation in air-firing and Oxy-Firing, Ind. Eng. Chem. Res. 53 (7) (2014) 2594–2604.
[17] E. Raask, Mineral Impurities in Coal Combustion: Behaviour, Problems, and Remedial Measures, 484 Hemisphere Publication Corporation, New York, 1985.
[18] Hubei Yihua Chemical Co Ltd, A High-efficient, Multistage and Recyclable Technique of Removing Sodium From Xinjiang Coal: China (201510095698.4[P]), (July 2015).
[19] Wuhuan Engineering Co.Ltd, A Technique of Removing Sodium From Coals With High Sodium Contents: China, 201210139478 3[P] (Sept 11 2013).
[20] J. Hayashi, K. Takeuchi, K. Kusakabe, S. Morooka, Removal of calcium from low rank coals by treatment with CO_2 dissolved in water, Fuel 70 (10) (1991) 1181–1186.
[21] Standardization Administration of the People's Republic of China, Division of Variety and Grading for Coal Products (GB/T 17608-2006), First ed., Standards Press of China, 2007.
[22] Y. Ma, Z.Y. Huang, H.R. Tang, The mineral evolution during the combustion of Zhundong coal and the effect of mineral additives on the ash fusion properties, J. Fuel Chem. Technol. 42 (1) (2014) 20–25.
[23] T. Hosseini, N. Haque, C. Selomulya, L. Zhang, Mineral carbonation of Victorian brown coal fly ash using regenerative ammonium chloride - process simulation and techno-economic analysis, Appl. Energy 175 (2016) 54–68.
[24] Z.Q. Jia, Membrane Technology And Science, First ed., Chemical Engineering Press, 2011.
[25] M. Wilf, M.K. Schierach, Improved performance and cost reduction of RO seawater systems using UF pretreatment, Desalination 135 (1–3) (2001) 61–68.
[26] G.K. Pearce, UF/MF pre-treatment to RO in seawater and wastewater reuse applications: a comparison of energy costs, Desalination 222 (1–3) (2008) 66–73.
[27] https://reverseosmosispk.wordpress.com/koch/.
[28] F. Low, L. Zhang, Microwave digestion for the quantification of inorganic elements in coal and coal ash using ICP-OES, Talanta 101 (2012) 346–352.
[29] J. Zhang, Q. Wang, Y. Wei, L. Zhang, Numerical modelling and experimental investigation on the use of brown coal and its beneficiated semicoke for coal blending combustion in a 600 MW_e utility furnace, Energy Fuel 29 (2) (2015) 1196–1209.
[30] S.Y. Wu, S.Y. Yue, Coal Preparation Design, Fourth ed., Coal Industrial Press, 2012.
[31] W.D. Seider, D. Seader, D.R. Lewin, Product and Process Design Principles: Synthesis, Analysis, and Evaluation, Wiley, New Jersey, 2004.
[32] N. Haque, W. Bruckard, J. Chevas, A techno-economic comparison of pyrometallurgical and hydrometallurgical options for treating high-arsenic copper concentrates, IMPC 17 (2012) 1908–1923.
[33] H.V. Maschinenbau, Injection housing - optimizing rotary lobe pumps for liquids with high solids content, World Pumps 489 (2007) 36–38.
[34] http://www.zeusinc.com/materials/pvdf-polyvinylidene-fluoride/chemical-resistance-chart-pvdf.
[35] http://www.hnzkjq.cn/products/shusong/237.html (In Chinese).
[36] J.K. Wang, Chemical Process Design, Second ed., Chemical Industry Press, 2006.
[37] C.J. Gabelich, Nonthermal Technologies for Salinity Removal, AWWA Research Foundation And American Water Works Association, 2001.
[38] M.S. Peters, K.D. Timmerhaus, Plant Design and Economics for Chemical Engineers, McGraw – Hill, New York, 1991.
[39] Technology, A., & Inc., Aspen Process Economic Analyzer V7.3.1 User Guide, (2011).
[40] S.N. Talati, Evaluation of reverse osmosis and evaporative desalination systems under feedwater supply constraints typical in arid countries, Desalination 97 (1–3) (1994) 353–361.
[41] U.K. Kesieme, N. Milne, H. Aral, C.Y. Cheng, M. Duke, Economic analysis of desalination technologies in the context of carbon pricing, and opportunities for membrane distillation, Desalination 323 (2013) 66–74.
[42] X. Zhang, X. Wu, X. Xu, J. Zhang, K. Yan, B.Q. Dai, L. Zhang, Experimental study on ash melting behavior of Xinjiang high-alkali coal blended with low-alkali coal during coal combustion, Clean Coal Technol. Sustain. Dev. (2016) 53–58.
[43] http://mini.eastday.com/a/160709100113671.html?btype=index&subtype=caijing&idx=6&ishot=0.
[44] http://www.china.cn/yansuan/3682451832.html.
[45] B. Bragan, Richardson products The Richardson name that you have trusted for your cost data needs for over 40 years + cost data on line, INC, Retrieved from, 2008. http://www.iceste.org/Book Reviews/CFM-Info.pdf, .
[46] http://www.bemoneyaware.com/blog/useful-info/cost-inflation-index-table/ or http://www.chartered club.com/cost-inflation-index/.

Appendix B

Chapter 4 in publication form

energy&fuels

Article

Cite This: Energy Fuels 2019, 33, 2142−2152

pubs.acs.org/EF

Selective Removal of Sodium from Low-Rank Xinjiang Coal upon Multistage Countercurrent Water Washing: Experimental Investigation and Kinetics Modeling

Song Zhou,[†] Tahereh Hosseini,[†] Jie Zhao,[†] Xiwang Zhang,[†] Hongwei Wu,[‡] and Lian Zhang*[,†]

[†]Department of Chemical Engineering, Monash University, Clayton, Victoria 3800, Australia

[‡]Discipline of Chemical Engineering, Western Australian School of Mines: Minerals, Energy and Chemical Engineering, Curtin University, GPO Box U1987, Perth, WA 6845, Australia

ABSTRACT: Prior washing of coal is an essential step for the minimization of ash-related slagging and fouling inside a coal-fired boiler. With regard to the coal washing process, the recyclability of the washing reagent, usually water, is critical from both cost-effective and efficiency perspectives. This paper addresses the washing kinetics of water-soluble Na^+ from two different low-rank Xinjiang coals using both fresh and used/recycled water to alleviate the ash-related fouling in low-rank coal-fired boilers. Apart from once-through fresh water washing, washing using recycled water via both multicycle single-stage and three-stage countercurrent processes was studied in detail to investigate the recyclability of water. Additionally, a modified shrinking core model (SCM) was developed to reveal the Na^+ removal mechanism under all washing conditions. Our experimental results showed that the Na^+ removal extent decreased with the recycling of used water due to an increase in the Na^+ concentration in the recycled water and/or a decrease in the Na^+ content in the washed coal. The saturation point of Na^+ in the used water, beyond which the water can no longer remove Na^+, is far below the solubility of NaCl in water. The modeling approach further confirmed that the overall rate for the removal of water-soluble Na^+ is dominated by the intraparticle diffusion within the coal matrix. The effective diffusion coefficient of Na^+ was within the range of 0.28×10^{-6} to 3.75×10^{-6} cm^2/s, which agrees with reported values in the literature. Additionally, a novel iterative calculation method integrating the modified SCM into the three-stage countercurrent washing process has been proposed to predict the Na^+ removal at each stage for each cycle. The results show that the water can be recycled a maximum of 15 times in the three-stage countercurrent process.

1. INTRODUCTION

Electricity generation from coal-fired power stations is projected to continue to increase to ~1 trillion kWh by 2040 although its share is foreseen to decline from the current 38% in the global energy matrix.[1] Use of low-rank coals for power generation becomes more attractive because of their abundant reserves and much lower price compared with black coals. For instance, 90% of the power in Victoria, Australia is generated in power stations firing huge reserves of local brown coal.[2] The situation is similar in Xinjiang Uyghur Autonomous Region, China.[3] However, boilers firing low-rank coals are known to suffer from severe fouling, among which the abundance of sodium (Na) is one of the main reasons.[4,5] It is estimated that billions of dollars has to be spent annually on abating the fouling-related issues.[6]

Prior washing to remove Na out of coal is a simpler approach to increase the fusion temperature of ash and hence reduce its fouling propensity.[3] To date, nearly all the coal washing technologies were developed and/or tested for high-rank coals that are rich in discrete mineral grains. None of these technologies are suitable for low-rank coal that is rich in organically bound species coal.[3] With regard to the studies on low-rank coal washing, most of them were conducted based on the use of different fresh washing reagents without considering their recyclability at all. This is critical for a cost-effective operation of the process and in particular important for the plant location where water is scarce, such as the Xinjiang region in China.[3,7]

For washing kinetics modeling, Neavel et al.[8] claimed that the water-soluble Na^+ removal from Illinois coal by fresh water could be fitted by a graphical solution of a diffusion model proposed by Crank.[9] The diffusion coefficient of Na^+ was found sensible to the washing time even for a fixed particle size range. However, no explanation has yet been given. This model was later applied by Readett et al.[10] to the removal of water-soluble Na^+ from a different lignite. It was found that the model for smaller particle size ranges failed to correlate satisfactorily with the experimental observations. Therefore, a semiempirical model was proposed and claimed to match the washing results. The empirical nature of this model caused a failure of calculation on the diffusion coefficients. Moreover, these existing models always assumed that the amount of water was significantly in excess of that of coal, which is, however, instinctively different from the reality where the liquid-to-solid ratio usually remains as small as possible to minimize the water usage and loss.[3] In addition, the leaching mechanism underpinning multicycle leaching processes where the spent reagent is reused has yet to be explored.

This study for the first time aims to investigate the washing kinetics of the water-soluble Na^+ from low-rank Xinjiang coals in a multicycle three-stage countercurrent washing process. A low liquid-to-solid ratio close to industrial application is employed,

Received: January 6, 2019
Revised: February 26, 2019
Published: February 27, 2019

DOI: 10.1021/acs.energyfuels.9b00055
Energy Fuels 2019, 33, 2142−2152

and a kinetics model is established to quantitatively describe the removal of Na^+ upon the recycling of water. Results are firstly reported from intensive experiments to assess the effect of various process parameters including coal particle size, liquid-to-solid ratio, and in particular the number of cycles for reusing the used water. Specific efforts are made to explore the saturation point and hence the maximum number of cycles for reusing the used water via the use of NaCl solutions mimicking the recycled water with a high Na^+ concentration. Subsequently, effort was made by us to derive a modified shrinking core model (SCM) to accommodate the use of both fresh and used water in which the dissolved Na^+ pre-exists. The validated model is expected to be applicable to the other low-rank coals, as well as to assist in the future scale-up.

2. METHODOLOGY

2.1. Coal Properties. Two Xinjiang sub-bituminous coal samples (namely, Coals A and B hereafter) were used. Tables 1 and 2 list the properties of the two coal samples with a variety of particle sizes. Note that these sizes are abundant and make up the majority of the two coals here. The moisture contents of these coal samples range from 16 to 22 wt % (as-received). The ash contents of these coal samples exhibit a similar dependence on particle size; broadly the ash content decreases with increasing coal size. However, the ash content of Coal B is twice higher than that of Coal A, approximately 12 wt % in Coal B versus 6 wt % on average for Coal A.

The contents of total Na in coal samples (on the as-received coal mass basis) were quantified by inductively coupled plasma optical emission spectrometry (ICP-OES), following a previously established standard procedure.[11] Since the water washing process was only able to remove the Na^+ that is water soluble, effort was thus first made to determine the content of water-soluble Na^+, that is, maximum water washable Na^+ in each coal. The raw coal was firstly crushed to a sample less than 100 mesh,[12] which was then washed using fresh water (deionized water) at a liquid-to-solid ratio (on a mass basis) of 2.5 for 90 min. After the solid and liquid separation, the residue was rinsed with fresh water to remove any possibly remaining water-soluble Na^+. Finally, the content of water-soluble Na^+ in the raw coal was determined via analyzing the leachate by ICP-OES. The contents of total Na^+ and water-soluble Na^+ in Coal A are around 3000 and 1500 ppm, respectively, in comparison to 1200 and 700 ppm in Coal B. Overall, for both coals, around 50−60% of the total Na is water-soluble. For both samples, a distinct correlation between Na content and particle size seems to be absent.

2.2. Experimental Procedure. Three sets of water washing experiments are conducted at room temperature and atmospheric pressure, as illustrated in Figure 1. These three sets are named fresh water − raw coal, used water − raw coal, and used

Table 1. Properties of Raw Xinjiang Coal A[a]

property	particle size (mm) 0.2−0.6	0.6−1	1−4	4−8
proximate analysis (wt %)				
moisture (ar)	20.24	21.05	21.35	21.94
volatile (db)	35.33	34.56	37.12	35.07
fixed carbon (db)	58.41	59.48	56.65	60.71
ash (db)	6.26	5.96	6.23	4.22
ultimate analysis (wt %, db)				
carbon	70.24	71.87	71.40	73.07
hydrogen	3.77	3.92	4.02	4.04
oxygen	24.73	22.94	22.71	21.72
nitrogen	0.69	0.67	0.66	0.77
sulfur	0.57	0.60	1.21	0.40
element content (ppm, as-received raw coal)				
total Na	2930	2753	3036	2919
maximum water-soluble Na	1604	1905	1400	1562

[a] ar: air-dried; db: dry basis.

Table 2. Properties of Raw Xinjiang Coal B

property	particle size (mm) 0.2−0.6	0.6−1	1−4	4−8
proximate analysis (wt %)				
moisture (ar)	16.1	16.1	16.7	16.7
volatile (db)	27.5	29.2	28.3	29.0
fixed carbon (db)	61.9	62.3	63.2	65.4
ash (db)	12.5	12	10.2	8.6
ultimate analysis (wt %, db)				
carbon	70.3	70.9	71.1	73.6
hydrogen	3.3	3.3	3.4	3.2
oxygen	25.54	24.58	24.56	22.04
nitrogen	0.61	0.72	0.69	0.76
sulfur	0.35	0.4	0.35	0.3
element content (ppm, as-received raw coal)				
total Na	1138	1324	1234	1365
maximum water-soluble Na	602	720	727	751

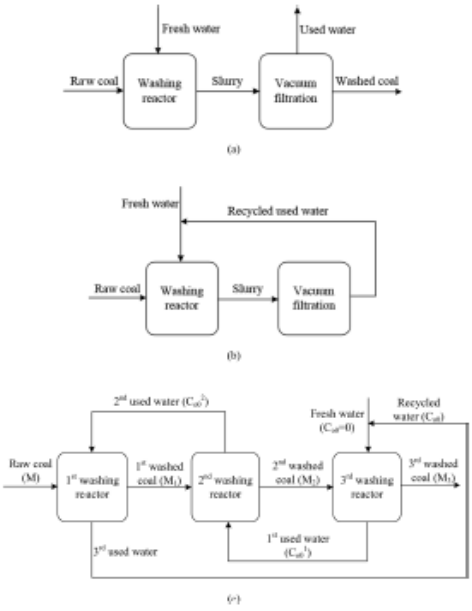

Figure 1. Experimental diagrams: (a) fresh water washing raw coal, (b) single-stage multicycle water washing, and (c) three-stage counter-current water washing.

DOI: 10.1021/acs.energyfuels.9b00055
Energy Fuels 2019, 33, 2142−2152

water − washed coal. The first set refers to the simplest once-through single-stage fresh water washing experiment in Figure 1a. Briefly, 30 g of raw coal and 45 g of fresh water were mixed and magnetically stirred in a glass beaker at a liquid-to-solid ratio of 1.5 (close to the practical value used in industry[13]). For different liquid-to-solid ratios, the mass of water was adjusted proportionally while the coal mass remained unchanged. During the washing, the leachate was sampled at intervals of 1−15 min. The leachate samples were then analyzed using ICP-OES for quantifying the concentration of Na^+ in leachates according to a standard procedure.[3] After washing, the resultant leachate and solid residue were separated via vacuum filtration using filter paper with a cutoff size of 2 μm. This set of experiments was conducted to determine the optimal washing conditions. The second set for the used water − raw coal is shown in Figure 1b, aiming to determine the maximum allowable Na^+ concentration in the used water. It is expected that, upon recycling the used water, the Na^+ is accumulated in the solution and Na^+ may also possibly redeposit on the coal surface. Therefore, the Na^+ saturation point has to be determined to guarantee the washing effectiveness of the used water. To start the single-stage multicycle water washing experiment, fresh water was used in the first cycle. After filtration, the used water was employed instead of fresh water for washing in the next cycle until the used water was inactive to remove Na^+. The last used water − washed coal set was designed on a batch scale to mimic the practical three-stage countercurrent water washing process shown in Figure 1c. In this case, fresh water is firstly used to wash the raw coal for 30 min, yielding a washed coal termed Coal 1 and used water. Subsequently, the used water was applied to wash Coal 1 for another 30 min to attain a two-time-washed coal, as Coal 2, which was finally washed by fresh water to obtain the 3rd washed coal and 1st used water as shown in Figure 1c. Afterward, the 1st used water was used to wash Coal 1 for 30 min, obtaining 2nd used water and 2nd washed coal. Finally, the raw coal was washed by the 2nd used water to get 1st washed coal and 3rd used water.

2.3. Modified Shrinking Core Model. Considering that the proposed coal washing process is a dissolution of water-soluble Na^+ of coal, the overall rate for Na^+ removal is very likely intraparticle diffusion controlled. In light of this, a widely applied leaching model, the shrinking unreacted-core model (SCM)[14] is considered here. However, there are two primary theoretical differences between the classic SCM and the required model in this study. First, in the classic SCM, the ash-diffusion-controlled formula is derived based on the liquid reactant diffusing inward to the unreacted shrinking core. However, the water-soluble Na removal is an opposite process that might be governed and driven by the concentration gradient of Na^+ between the internal pore and the bulk water outside the coal particles. Therefore, the intraparticle resistance against the outward diffusion of Na^+ out of coal particles might be rate-limiting. Second, the classical SCM assumes a sharp reaction interface and an unreacted shrinking core with a constant molar density of solid reactant, so as to achieve a relationship between solid reactant conversion and the decreasing radius of the shrinking, unreacted core. However, in this study, the water-soluble Na^+ concentration remaining in the shrinking core keeps decreasing because the water-soluble Na^+ dispersed in a whole coal particle gradually diffuses outward during the process. This does not agree with the fundamental assumption of a constant element concentration inside the shrinking core in the classical SCM model.

In this study, the following assumptions are made to modify the classic SCM depicted in Figure 2.

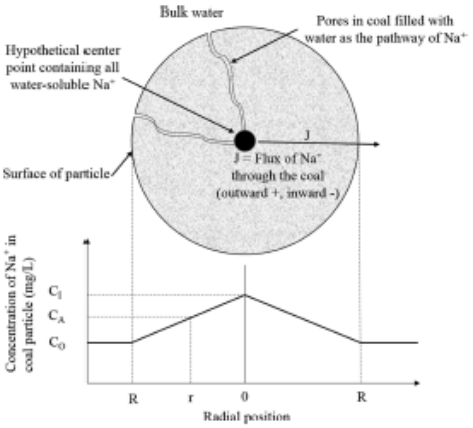

Figure 2. Diagram of a reacting particle when intraparticle diffusion of Na^+ is the controlling resistance.

(1) In the original coal particle, the water-soluble Na^+ is present in the capillary water entrapped inside the pores.[10,15,16]
(2) The overall removal of Na^+ is controlled by its outward diffusion toward the bulk water, whereas the diffusion resistance in bulk water and liquid film out of the particle can be eliminated at a certain stirring speed.[14]
(3) All coal particles are spherical and homogeneous.[14]
(4) The radius of the particle remains constant during the washing process. It is valid because of the absence of mechanical crushing in the washing process. The coal particle size distribution remains unchanged.
(5) All the water-soluble Na^+ is assumed to exist in a hypothetical center point of a single particle, and hence, its distribution is irrelevant to the particle radius.
(6) The flux of Na^+ is constant throughout particle radius.[14]

The modified SCM derivation block diagram is shown in Figure 3. In brief, based on the above assumptions and specific to one single coal particle, the Na^+ mass change in bulk water can be expressed by the classic formula of flux and Fick's first diffusion law. Upon unit conversion and integration in terms of time, a virgin model formula including an unknown parameter C_I can be derived. Afterward, C_I is expressed via Na^+ mass conservation, so as to obtain the final model equation. Aside from the single-stage fresh water washing, this model is further combined with the Na^+ mass balance in each stage and overall process and applied into the three-stage countercurrent process in order to predict the Na^+ removal in each cycle and the recyclability of water. Figure 4 illustrates the derivation diagram for the three-stage process. According to Figures 1c and 4, two Na^+ mass balance equations including only two unknown variables, the Na^+ removal extents in 2nd and 3rd stages, can be finally derived and solved. Furthermore, by plugging these two values into the model, the Na^+ removal in the 1st stage can be acquired easily. Finally, the Na^+ removal in each cycle can be

DOI: 10.1021/acs.energyfuels.9b00055
Energy Fuels 2019, 33, 2140−2152

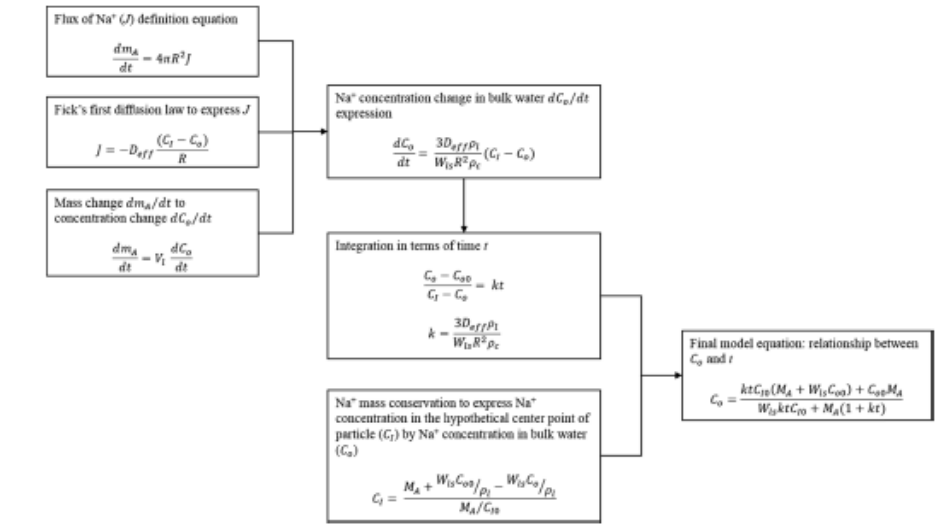

Figure 3. Modified SCM derivation block diagram.

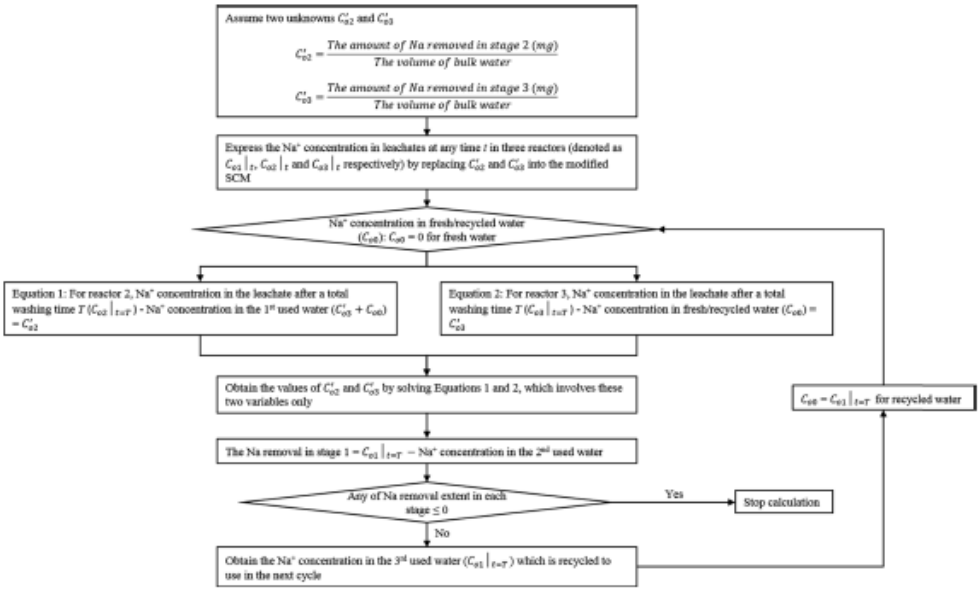

Figure 4. Three-stage countercurrent process model derivation block diagram.

calculated via an iterative calculation. The detailed derivation is shown below.

Assume that m_A is the mass of Na^+ in bulk water; the mass change of Na^+ in bulk water can be expressed by eq 1 based on a single coal particle, where J is the flux of Na^+ through the exterior surface of each particle $(mg/(s\cdot cm^2))$[14]

$$\frac{dm_A}{dt} = 4\pi R^2 J \quad (1)$$

DOI: 10.1021/acs.energyfuels.9b00055
Energy Fuels 2019, 33, 2142−2152

where t is the washing time (s) and R is the radius of coal particle (cm).

As per assumptions 5 and 6, J can be expressed by eq 2 according to Fick's first diffusion law[14]

$$J = -D_{\text{eff}}\frac{(C_1 - C_o)}{R} \times 1000 \tag{2}$$

where D_{eff} is the effective diffusion coefficient of Na^+ in coal particles (cm^2/s) and C_1 and C_o are the Na^+ concentrations in the hypothetical center point (mg/L) and in bulk water (mg/L) at any time t, respectively. Same as the derivation of the original SCM, the diffusion distance is simplified as R without the consideration of the tortuosity of coal particles. Combining eqs 1 and 2, eq 3 is obtained.

$$\frac{dm_A}{dt} = -4\pi R^2 D_{\text{eff}}\frac{(C_1 - C_o)}{R} \times 1000 \tag{3}$$

The mass change dm_A/dt is converted to the concentration change of Na^+ in bulk water as shown by eqs 4 and 5

$$\frac{dm_A}{dt} = V_1\frac{dC_o}{dt} \tag{4}$$

$$V_1 = W_{ls}\frac{\frac{4}{3}\pi R^3\rho_c}{\rho_1} \times 1000 \tag{5}$$

where V_1 is the volume of bulk water corresponding to a single coal particle (L), W_{ls} is the liquid-to-solid mass ratio, and ρ_c and ρ_1 are the densities of coal particle and water (kg/L), respectively. Substituting eqs 4 and 5 into eq 3, we have

$$\frac{dC_o}{dt} = \frac{3D_{\text{eff}}\rho_1}{W_{ls}R^2\rho_c}(C_1 - C_o) \tag{6}$$

Through the integration of eq 6 with respect to t and based on the boundary conditions of $C_o = C_{o0}$ at $t = 0$ and $C_o = C_o$ at t, we can yield

$$\frac{C_o - C_{o0}}{C_1 - C_o} = \frac{3D_{\text{eff}}\rho_1}{W_{ls}R^2\rho_c}t \tag{7}$$

where C_{o0} is the initial Na^+ concentration in bulk water (mg/L), which is zero for fresh water while not zero for recycled/used water. Upon the combination of all the constants in the right-hand side of eq 7 as a rate constant k (eq 8), eq 9 is further established.

$$k = \frac{3D_{\text{eff}}\rho_1}{W_{ls}R^2\rho_c} \tag{8}$$

$$\frac{C_o - C_{o0}}{C_1 - C_o} = kt \tag{9}$$

According to the conservation of Na^+ mass, C_1 can be expressed as eq 10

$$C_1 = \frac{M + {}^{W_{ls}C_{o0}}|_{\rho_1} - {}^{W_{ls}C_o}|_{\rho_1}}{V_1} \tag{10}$$

$$V_1 = \frac{M}{C_{10}} \tag{11}$$

where M is the maximum water-soluble Na^+ content in the raw coal (mg/kg-coal), V_1 is the volume of accessible pores of coal particles filled by water (L/kg-coal), which is assumed constant during water washing, and C_{10} is the maximum Na^+ concentration in the water contained in a coal particle (mg/L).

Substituting eqs 10 and 11 and $\rho_1 = 1$ kg/L for water into eq 9,

$$\frac{C_o - C_{o0}}{\frac{M + W_{ls}C_{o0} - W_{ls}C_o}{M/C_{10}} - C_o} = kt \tag{12}$$

Finally, the Na^+ concentration in bulk water (C_o) can be expressed as eq 13 by rearranging eq 12.

$$C_o = \frac{ktC_{10}(M + W_{ls}C_{o0}) + C_{o0}M}{W_{ls}ktC_{10} + M(1 + kt)} \tag{13}$$

The Na^+ removal extent X is defined as

$$X = \frac{\text{Na}^+\text{ concentration in leachate} \times W_{ls}}{\text{maximum water} - \text{soluble Na content of coal}} \times 100$$

$$X = \frac{(C_o - C_{o0})W_{ls}}{M} \times 100 \tag{14}$$

For the three-stage countercurrent water washing process shown in Figure 1c, the values of M and C_{o0} in eq 13 vary from one stage to another. The value of M for maximum water-soluble Na^+ decreases gradually from the initial value of Na^+ content for raw coal at stage 1 to the lowest value for the 2nd washed coal at stage 3. In contrast, the value of C_{o0} for the concentration of Na^+ in water increases gradually from zero in fresh water (1st cycle) at stage 3 to the highest value in the 2nd used water at stage 1. It is impossible to use eq 13 directly to predict the Na^+ concentration in the leachate of stage 1 due to the lack of Na^+ conversion in the other two stages and thus an unknown C_{o0} in this equation. Similarly, if eq 13 is used for back calculation from stage 3 first, an unknown M exists and it does not allow for the completion of the calculation either.

To address these concerns, the following derivations are further conducted in regard to the three-stage countercurrent water washing, as illustrated in Figure 4.

According to Figure 1c, at stage 1 (1st washing reactor), the Na^+ concentration in the 2nd used water, denoted as $C_{o0}{}^2$, can be expressed by eq 15

$$C_{o0}{}^2 = C'_{o2} + C'_{o3} + C_{o0} \tag{15}$$

where C'_{o2} and C'_{o3} are the amounts of Na^+ removed in stages 2 and 3 divided by the volume of bulk water, respectively (mg/L) and C_{o0} is the original Na^+ concentration in recycled water ($C_{o0} = 0$ for fresh water).

Replacing C_{o0} in eq 13 with $C_{o0}{}^2$, eq 16 is obtained, which involves two variables, C'_{o2} and C'_{o3} ($C_{o0} = 0$ for the first cycle using fresh water)

$$C_{o1}|_t = \frac{ktC_{10}(M + W_{ls}C_{o0}{}^2) + C_{o0}{}^2M}{W_{ls}ktC_{10} + M(1 + kt)} \tag{16}$$

where $C_{o1}|_t$ is the Na^+ concentration in leachate at time t in reactor 1 (mg/L) and k can be determined in the single stage. Assigning symbol T for the total washing time in one reactor, the Na content of 1st washed coal, denoted as M_1 (mg/kg-coal), is then equal to the difference between the Na^+ content in raw coal (M) and removed Na^+ in reactor 1 after washing time T, shown in eq 17.

$$M_1 = M - W_{ls}(C_{o1}|_{t=T} - C_{o0}{}^2) \tag{17}$$

DOI: 10.1021/acs.energyfuels.9b00055
Energy Fuels 2019, 33, 2142−2152

For stage 2, the Na^+ concentration in the 1st used water is defined as C_{o0}^{1}.

$$C_{o0}^{1} = C'_{o3} + C_{o0} \tag{18}$$

Similar to stage 1, after substituting C_{o0} in eq 13 by C_{o0}^{1}, we obtain eq 19

$$C_{o2}|_t = \frac{ktC_{10}(M_1 + W_{ls}C_{o0}^{1}) + C_{o0}^{1}M}{W_{ls}ktC_{10} + M(1 + kt)} \tag{19}$$

where $C_{o2}|_t$ is the Na^+ concentration in leachate at time t in reactor 2 (mg/L). Meanwhile, the Na^+ content in the 2nd washed coal, M_2 (mg/kg-coal), can be expressed by eq 20.

$$M_2 = M - W_{ls}(C_{o1}|_{t=T} - C_{o0}^{2}) - W_{ls}(C_{o2}|_{t=T} - C_{o0}^{1}) \tag{20}$$

After washing for a total time of T in reactor 2, the value of C'_{o2} in eq 15 is equal to the difference between the Na^+ concentration in the leachate ($C_{o2}|_{t=T}$) and the value in the 1st used water (C_{o0}^{1}), shown in eq 21.

$$C_{o2}|_{t=T} - C_{o0}^{1} = C'_{o2} \tag{21}$$

Similar to stages 1 and 2, we obtain the equations for stage 3 as follows

$$C_{o3}|_t = \frac{ktC_{10}(M_2 + W_{ls}C_{o0}) + C_{o0}M}{W_{ls}ktC_{10} + M(1 + kt)} \tag{22}$$

where $C_{o3}|_t$ is the Na^+ concentration in leachate at time t in reactor 3 (mg/L).

Similar to eq 21, eq 23 can be obtained.

$$C_{o3}|_{t=T} - C_{o0} = C'_{o3} \tag{23}$$

At the first cycle when the fresh water is used in stage 3, the value of C_{o0} is zero. There are thus only two variables C'_{o2} and C'_{o3} involved in eqs 21 and 23. After obtaining the values of C'_{o2} and C'_{o3} by solving eqs 21 and 23, the Na^+ removed in stage 1 C'_{o1} can be calculated by eq 24.

$$C'_{o1} = C_{o1}|_{t=T} - C_{o0}^{2} \tag{24}$$

Based on eq 13, the Na^+ removal percentage at each stage at any time can be finally attained.

The Na^+ removal extent in the following cycles can be obtained by an iterative calculation. As shown in Figure 1c, in the second cycle, the Na^+ concentration of the recycled water back to stage 3 (C_{o0}) is exactly the same as the value of the 3rd used water after a total washing time T ($C_{o1}|_{t=T}$) in the first cycle. Thus, the Na^+ removal extent in the second cycle can be obtained by repeating the above calculation and substituting the value of C_{o0} ($C_{o0} = 0$ in the first cycle) with $C_{o1}|_{t=T}$. Finally, the relationship between the Na^+ removal extent and cycle number can be obtained by an iterative calculation.

3. EXPERIMENTAL RESULTS AND DISCUSSION

Experiments were repeated at least three times per run. A satisfactory accuracy has been confirmed, as evident in Figure 5, which bears a standard deviation of around 0.5% only.

3.1. First Set of Experiments for Fresh Water versus Raw Coal. *3.1.1. Effect of Stirring Speed.* Figure 5 demonstrates the effect of stirring speed on the Na^+ removal extent after a washing duration of 90 min for the coarsest coal particle size of 4−8 mm and a liquid-to-solid ratio of 2.5. Note that Coal A was used in the whole Section 3.1. Clearly, the Na removal extent increases marginally with the initial increase in the stirring speed and reaches a plateau in excess of 300 rpm.

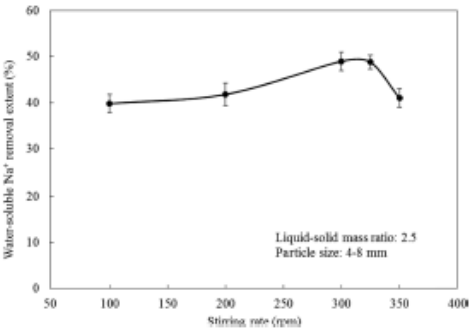

Figure 5. Effect of stirring rate on the water-soluble Na^+ removal extent.

This can be attributed to the elimination of the liquid film layer outside of particles and external diffusion resistance.[17,18] However, a further rise in the stirring rate to 350 rpm results in a decrease in the Na removal down to the same level as that achieved at 100 rpm. It is believed that the coal particles may rotate with the liquid water synchronously, which in turn leads to the regeneration of the negative influence of external diffusion and liquid film outside the coal particles.[19] Therefore, a stirring speed of 300 rpm was employed for the remaining experiments in this study.

3.1.2. Effect of Liquid-to-Solid Ratio. Figure 6 illustrates the effect of the liquid-to-solid ratio on the removal extent of Na^+ from two extreme particle size ranges, the smallest size bin of 0.2−0.6 mm and the coarsest one of 4−8 mm in Figure 6a,b, respectively. For the smallest size of 0.2−0.6 mm (Figure 6a), the Na^+ removal extent remains constant across the three different ratios and levels off rapidly in around 5 min. It suggests that there is a negligible external diffusion resistance while the intraparticle diffusion resistance may exist.[17,20] In contrast, the Na^+ removal extent for the coarsest size of 4−8 mm experiences a remarkable rise when the liquid-to-solid ratio increases from 1.25 to 1.5. Upon a further increase in the liquid-to-solid ratio to 2.5, there is however no change in the removal of Na^+. This is a clear indicator of the existence of an external diffusion at the lowest liquid-to-solid ratio in the case of the coarsest coal size, which cannot be eliminated unless the liquid-to-solid ratio reaches 1.5 or above. This is different from the smallest coal size and shall be attributed to the smaller contact area from the coarse coal particles. Since the washed coal in reality is a mixture of various sizes, a liquid-to-solid ratio of 1.5 has been chosen hereafter, which is noted to be considerably lower than that (reported to be 2.8[3]) for black coal washing.

3.1.3. Effect of Coal Particle Size. Figure 7 shows the removal extent of Na^+ as a function of coal particle size at optimized conditions (liquid-to-solid ratio: 1.5; stirring speed: 300 rpm). Clearly, the Na^+ removal extent decreases quickly with increasing coal particle size. For the smallest coal particles (0.2−0.6 mm), the Na^+ removal soars up to 60% in the first 5 min and then only increases slowly to 70% within the subsequent 25 min. For the two medium-sized coal samples, the Na^+ removal extent increases much slower, approaching the final Na removal extent of 70% in a considerably longer duration of ~90 min. For the largest coal particles, washing is the slowest and time-consuming, resulting in a Na^+ removal extent of only 45% after 90 min of washing. Clearly, intraparticle diffusion plays an increasingly important role in Na^+ removal from coal particles as coal particle size increases.

3.2. Second Set of Experiments for Used/Recycled Water versus Raw Coal. Following the experiments on the washing of raw coal by fresh water, Coal B was selected for experiments in the second scenario shown in Figure 1b to assess the Na^+ removal extent from raw coal upon the reuse of spent water.

The change of Na^+ removal efficiency upon using the repeatedly recycled water is presented in Figure 8. It is clear that the Na^+ removal

DOI: 10.1021/acs.energyfuels.9b00055
Energy Fuels 2019, 33, 2142−2152

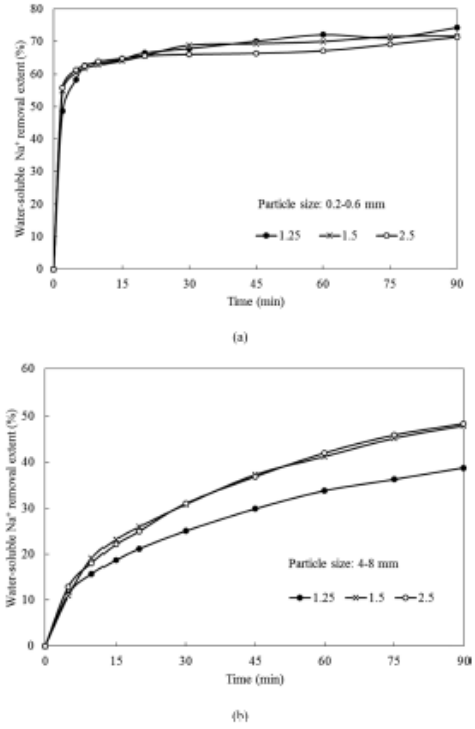

Figure 6. Effect of liquid-to-solid mass ratio on water-soluble Na^+ removal extent for coal particles of 0.2−0.6 (a) and 4−8 mm (b).

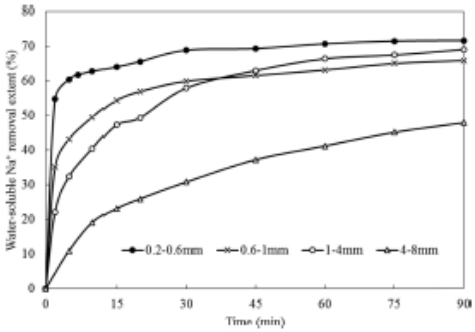

Figure 7. Effect of coal particle size on water-soluble Na^+ removal.

extent declines steadily with the increasing cycle number of water. This shall be due to a continuous increase in the Na^+ concentration dissolved in the recycled water, as evident for the concentrations of the major ions for the 4th recycled water in Table 3. It results in a gradual decrease in the diffusion driving force. More interestingly, for the second to fourth cycles where recycled water was used, the first 5 min always witnesses a rapid rise in the Na^+ removal extent, which then slows down and levels off gradually from 5 min onward. This indicates that the dissolved Na^+ in the leachate can quickly reach equilibrium with those remaining in the coal particles, thereby hindering the further outward diffusion of Na^+.

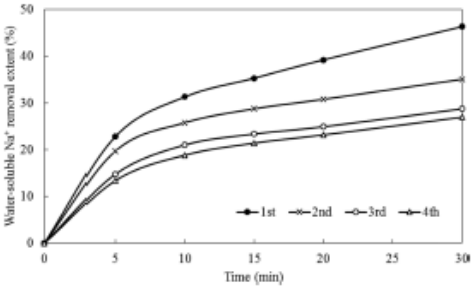

Figure 8. Water-soluble Na^+ removal extent change upon the recycling of used water washing of raw coal.

Based on Table 3, it is obvious that the content of Na^+ is almost equivalent to that of Cl^- (the most abundant anion) on a molar basis. It is thus inferable that almost all of the dissolved Na^+ shall be associated with Cl^-, which is in line with previous reports.[8,10] In light of this, the pure NaCl solutions with different concentrations were used to reveal the saturation or the turning point by which the recycled water loses its washing capability of Na^+. The use of pure NaCl solution rather than the recycled water is due to the fact that the concentration of Na^+ within it increases very slowly. As shown in Table 3, the Na^+ content only increases to 0.045 mol/L after four times of recycle, which is far below the theoretical solubility of NaCl in water (6.14 mol/L).[21] It was also assumed that the other elements including Ca^{2+} and SO_4^{2-} found in the recycled water in Table 3 played little role in the removal of Na^+. These ions were speculated to dissolve in parallel with Na^+ into water. The raw coal size of 1−4 mm was used for the test here, and the results achieved are depicted in Figure 9.

As shown in Figure 9, the Na^+ in the leachate keeps increasing over time when the coal is washed by the 0.5 wt % NaCl solution, suggestive of an unsaturation state for this solution. Instead, the concentration of Na^+ in the leachate remains unchanged when the coal is washed by 0.77 wt % NaCl. However, when the coal is washed by the two higher concentrations, the original Na^+ in the leachate is quickly absorbed on the coal surface in less than 10 min. After it, Na^+ concentration equilibrium inside and outside coal particles is achieved, leading to an unchanged concentration of Na^+ in the leachate. Clearly, the maximum allowable Na^+ concentration in the recycled water shall be around the value of 0.77 wt % NaCl solution (~3000 ppm), beyond which the washing capability of the leachate will be lost due to the reverse deposition of Na^+ on the coal surface. Such a saturation point is far below the solubility of NaCl in water (359 g/L (~36 wt %)) at room temperature.[21]

3.3. Three-Stage Countercurrent Washing. Last effort was made to explore the ultimate three-stage, countercurrent water washing process in which the used water encounters the washed coal. The results are plotted in Figure 10. In agreement with the results shown in the above section, the used water still has the capability to remove Na^+ even from the washed coal. In terms of the Na^+ removal extent, it reaches around 51% in stage 1 where the raw coal encountered the "dirtiest" used water, 22% in stage 2 where the less washed coal encountered the "dirtier" used water, and finally 15% in stage 3 where the intensively washed coal further encountered fresh water. Such a decrease reflects a continuously reducing driving force, that is, the Na^+ concentration difference between the inside and outside of coal particles.

4. KINETICS MODELING

The modified SCM was first validated by fitting the result of the first set of experiments, fresh water versus raw coal. This aims to

DOI: 10.1021/acs.energyfuels.9b00055
Energy Fuels 2019, 33, 2142−2152

Table 3. Concentration of Main Ions in the Used Water after Four Cycles

ions (mol/L)	Cl^-	Na^+	SO_4^{2-}	Ca^{2+}	Mg^{2+}	K^+
value	0.0448	0.0450	0.0126	0.0073	0.0044	0.0002

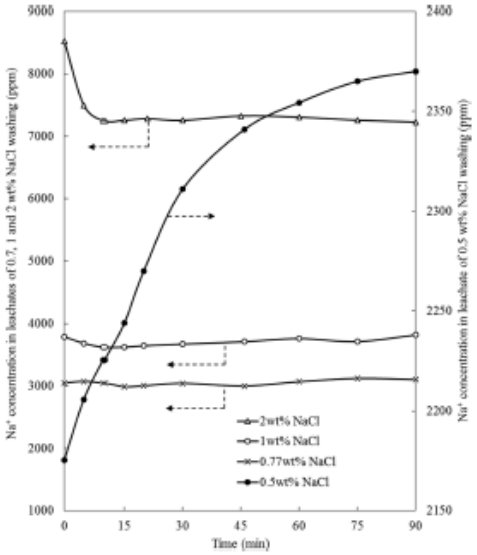

Figure 9. Na^+ concentration in leachates change upon washing time in different NaCl solutions.

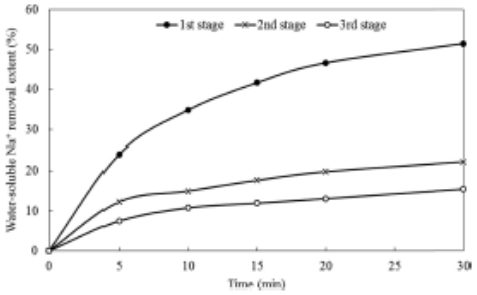

Figure 10. Experimental water-soluble Na^+ removal extent in each stage.

verify that the Na^+ removal is mainly controlled by its intraparticle diffusion. Afterward, the second set of experiments, used water versus raw coal, was modeled to validate the application of the modified SCM to used water washing and to predict the recyclability of water. Finally, the ultimate three-stage countercurrent water washing experiment was simulated to quantify the Na^+ removal extent of each stage at each cycle and the maximum possible recycle number of the used water.

4.1. Modeling of Fresh Water Washing Raw Coal with Various Particle Sizes. For comparison, the removal of Na^+ from raw coal by fresh water was firstly modeled against both the chemical reaction control and intraparticle water diffusion control defined by the original SCM.[14] The respective correlation coefficients (R^2) for the modeling accuracy are listed in Table 4. Clearly, the original SCM failed to fit the experimental data accurately, with the exception of the coarsest particle of 4−8 mm with an R^2 of 0.9959 for the diffusion control.

Table 4. R^2 Using the Reaction Controlled Model and Diffusion Controlled Model Defined by the Original SCM

particle size (mm)	reaction controlled model $1-(1-X)^{1/3}$	diffusion controlled model $1-3(1-X)^{2/3}+2(1-X)$
0.2−0.6	0.4435	0.6195
0.6−1	0.6252	0.7963
1−4	0.8060	0.9461
4−8	0.9091	0.9959

Instead, the Na^+ intraparticle diffusion control defined by the modified SCM presented in eq 12 was proven to fit all the experimental results satisfactorily. As evident in Figure 11, the

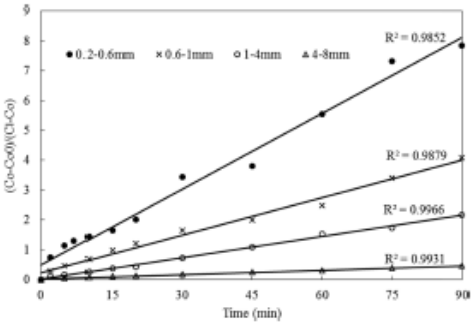

Figure 11. Plots for Na^+ diffusion out of coal particle defined by the modified SCM.

correlation coefficients achieved are beyond 0.98 for all the four sizes. Additionally, based on eq 8, the effective diffusion coefficient D_{ef} of Na^+ through the water phase contained in coal particles can be calculated, as listed in Table 5. These values fall in the reported range of the order of 10^{-7} to 10^{-5} cm^2/s.[8,22] On the other hand, D_{ef} increases with increasing coal particle size, which is consistent with previous studies.[8,23,24] It can be

Table 5. Effective Diffusion Coefficient (D_{ef}) of Each Particle Size Range

particle diameter (mm)	average particle diameter (mm)	D_{ef} ($\times 10^{-6}$ cm^2/s)
0.2−0.6	0.4	0.28
0.6−1	0.8	0.56
1−4	2.5	3.13
4−8	6.0	3.75

DOI: 10.1021/acs.energyfuels.9b00055
Energy Fuels 2019, 33, 2142−2152

explained as follows. As shown in eq 25,[24] in which D is the molecular bulk diffusion coefficient of Na^+ that is an invariant at fixed pressure and temperature, D_{eff} is only proportional to the porosity φ of coal particles if the tortuosity τ is assumed to be the same for all particle size ranges. Therefore, the larger coal particles tend to possess a larger D_{eff} since they have higher porosity values.[25] Both the reasonable value of D_{eff} and the right relationship between D_{eff} and coal particle size verified the physical meaning of this modified SCM. This further confirmed that the water-soluble Na^+ removal out of raw coal by fresh water is dominated by its intraparticle diffusion.

$$\frac{D_{eff}}{D} = \frac{\varphi}{\tau} \tag{25}$$

4.2. Modeling of Single-Stage Multicycle Used Water Washing of Raw Coal. For the single-stage multicycle used water washing fitting result, Table 6 summarizes the R^2, overall rate constant k (the slope of eq 12), and the initial Na^+ concentration in water for the first three cycles. The value of k is only a function of D_{eff} (eq 8) for a fixed particle size, which should be independent of Na^+ concentration. Therefore, aside from the high R^2, the relatively constant value of k for each cycle verifies the good fitting of the modified SCM. In addition, the applicability of this modified SCM has also been proven by the satisfactory fitting to Coal B to some extent.

Table 6. R^2 and k Using the Intraparticle Na^+ Diffusion Controlled Model Defined by the Modified SCM

recycle number	R^2	k (min^{-1})	initial Na^+ concentration in water (ppm)
1st	0.9892	0.0197	0
2nd	0.9810	0.0208	262
3rd	0.9833	0.0196	565
0.5 wt % NaCl	0.9814	0.0232	2175

To examine if the modified SCM can be extended to the washing by used water whose Na^+ concentration is accumulated to a very high value, the experimental result of 0.5 wt % NaCl washing raw coal shown in Figure 9 was further simulated. It can be observed from Table 6 that R^2 is above 0.98 for such a high initial Na^+ concentration. This satisfactory fitting allows us to use this model to predict the Na^+ removal change upon the recycling of the used water. Based on the results in Table 6, the average of k values of the first three cycles and the Na^+ concentration in the leachate after three cycles were calculated and substituted into eqs 13 and 14. Subsequently, the Na^+ removal in the fourth cycle was predicted and compared with the experimental result. As demonstrated in Figure 12, one can see a close match between the model prediction and the experimental observation. By an iterative calculation, the relationship between Na^+ removal extent and the cycle number of water can be further predicted, which is illustrated in Figure 13. This indicates that the Na^+ removal extent decreases exponentially upon the increase in the water recycling number. Once the recycling number approaches 20, the water nearly loses its washing capability for the raw coal and hence has to be desalinated.

4.3. Modeling of Three-Stage Countercurrent Water Washing Process. The fitting result of three-stage countercurrent water washing is tabulated in Table 7. The high R^2 of each stage indicates that all washing conditions included in the countercurrent washing can be modeled very well by the modified SCM, irrespective of fresh or used water and raw or washed coal. In addition, the validation of the modified SCM is substantiated by the close value of k for each stage, which is independent of the Na^+ concentration in bulk water and Na^+ content in coal.

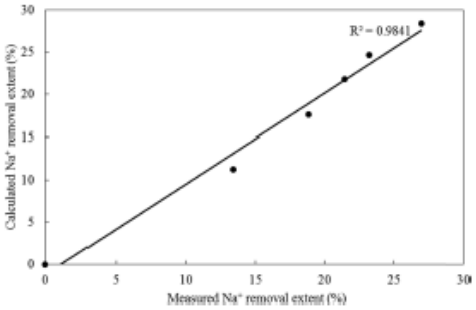

Figure 12. Comparison between calculated and measured Na^+ removal extent at the fourth cycle.

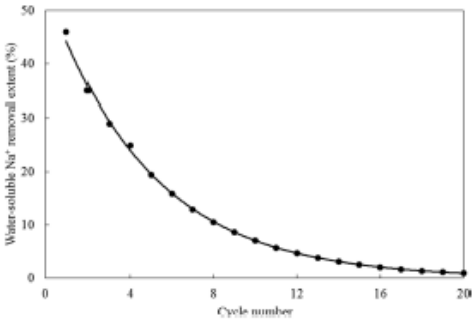

Figure 13. Na^+ removal extent change upon the recycling of used water.

Table 7. R^2 and k for Three-Stage Countercurrent Washing Fitted by the Modified SCM

stage number	R^2	k (min^{-1})
1st	0.9984	0.0239
2nd	0.9942	0.0235
3rd	0.9842	0.0238

Plugging the value of k into eqs 15−24, the water-soluble Na^+ removal at each stage was further predicted to examine the proposed calculation approach specific to the countercurrent washing process. Figure 14 compares the calculated and experimental Na removal extent of each stage. The excellent linear relationship with high R^2 proves that this calculation method can accurately predict the Na^+ removal extent at every stage at any time.

Similar to Figure 13, the relationship between the total Na^+ removal of three-stage countercurrent water washing and the recycling of water was predicted and is presented in Figure 15. Again, the total Na^+ removal extent (sum of Na removal extents of three stages) decreases exponentially upon the increase in the recycling number. However, the water loses its Na removal ability after 15 times of recycle, which is less than 20 times confirmed for the single-stage multicycle washing in Figure 13.

DOI: 10.1021/acs.energyfuels.9b00055
Energy Fuels 2019, 33, 2142−2152

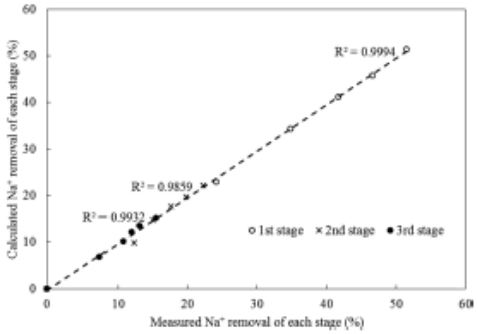

Figure 14. Comparison between calculated and experimental Na^+ removal extent of each stage.

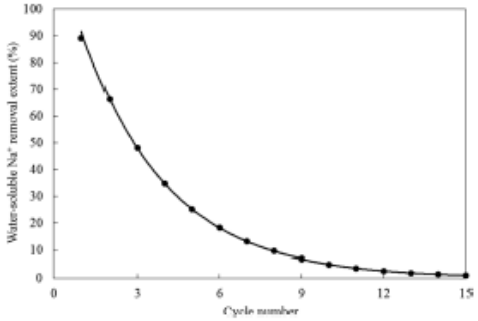

Figure 15. Total water-soluble Na^+ removal extent of three-stage countercurrent washing upon the recycling of used water.

This is mainly a result of the higher Na removal extent in each cycle that can be achieved by the three-stage washing process. Moreover, the relationship between Na^+ removal and the initial Na^+ concentration in water can also be obtained, as shown in Figure 16. This confirms a linear decrease in the Na^+ removal extent upon the rise of Na^+ concentration in the leachate, that is,

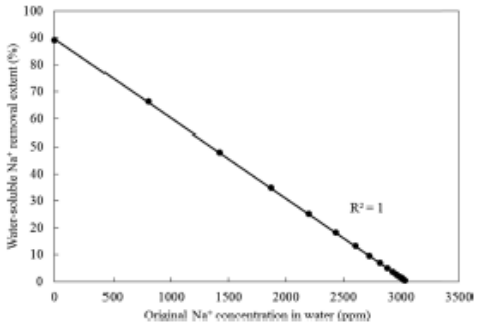

Figure 16. Total Na^+ removal extent in three-stage countercurrent washing upon the increase of Na^+ concentration in used water.

the recycling of the water. It can be expected from eqs 13 and 14 that, once the original Na^+ reaches around 3000 ppm, the recycled water loses its washability.

5. CONCLUSIONS

A comprehensive investigation on the washing propensity of Na^+ from two types of low-rank Xinjiang coals using both fresh and used water has been performed from both experimental and modeling perspectives. Apart from the parametric study on the once-through fresh water washing raw coal, other two scenarios including single-stage multicycle used water washing and three-stage countercurrent water washing have also been conducted. This aims to reveal the Na^+ removal extent upon the recycling of water and the recyclability of water. The major conclusions achieved are as follows:

(1) The Na^+ removal extent decreased upon the recycling of water in both the single-stage multicycle process and three-stage countercurrent process. It is a result of the increase in the Na^+ concentration in recycled water and/or the decrease in the remaining Na^+ content in the washed coal. The saturation point of Na^+ concentration for the used water was found to be far less than the solubility of NaCl in water.

(2) A modified SCM integrated with iterative calculation was developed for the multistage washing processes, which was also successfully validated by high correlation coefficients between experimental and model results and reasonable $D_{e\text{ff}}$ ranging from 0.28×10^{-6} to 3.75×10^{-6} cm^2/s, which is in line with the reported values. The model indicated that the overall Na^+ removal rate is controlled by the intraparticle diffusion of Na^+.

(3) Specific to the three-stage countercurrent process, it was found that the water loses its capability to remove Na^+ after recycling 15 times when the Na^+ concentration within it reaches the saturation point. Upon the increase in the cycle number, the overall Na^+ removal extent drops from around 90% in the first cycle quickly down to negligible in the 15th cycle. The overall Na^+ removal extent was also found bearing a reverse proportion to the concentration of Na^+ accumulated in the used water.

AUTHOR INFORMATION

Corresponding Author

*E-mail: lian.zhang@monash.edu. Tel: +61-3-9905-2592. Fax: +61-3-9905-5686.

ORCID

Song Zhou: 0000-0001-6422-0940
Xiwang Zhang: 0000-0002-4319-527X
Hongwei Wu: 0000-0002-2816-749X
Lian Zhang: 0000-0002-2761-880X

Notes

The authors declare no competing financial interest.

ACKNOWLEDGMENTS

This work was supported by the Australian Research Council Industry Research Training Hub (IH150100006) and the industry partner Hubei Yihua Chemical Co. Ltd. The first author also appreciates the China Scholarship Council – Monash University scholarship for a Ph.D. scholarship.

DOI: 10.1021/acs.energyfuels.9b00055
Energy Fuels 2019, 33, 2142−2152

NOMENCLATURE

C_i = Na^+ concentration in hypothetical center point at any time t (mg/L)
C_{i0} = Maximum Na^+ concentration in the water contained in a coal particle (mg/L)
C_o = Na^+ concentration in bulk water at any time t (mg/L)
C_{o0} = Na^+ concentration in fresh/recycled water (mg/L)
C_{o0}^1 = Na^+ concentration in the 1st used water (mg/L)
C_{o0}^2 = Na^+ concentration in the 2nd used water (mg/L)
$C_{o1}|_t$ = Na^+ concentration in leachate at time t in reactor 1 (mg/L)
$C_{o2}|_t$ = Na^+ concentration in leachate at time t in reactor 2 (mg/L)
$C_{o3}|_t$ = Na^+ concentration in leachate at time t in reactor 3 (mg/L)
C'_{o1} = Amount of Na removed in stage 1 divided by the volume of bulk water (mg/L)
C'_{o2} = Amount of Na removed in stage 2 divided by the volume of bulk water (mg/L)
C'_{o3} = Amount of Na removed in stage 3 divided by the volume of bulk water (mg/L)
D_{eff} = Effective diffusion coefficient of Na^+ in coal particles (cm^2/s)
J = Flux of Na^+ through the exterior surface of the particle ($mg/(s \cdot cm^2)$)
k = Rate constant
m_A = Mass of Na^+ in bulk water (mg)
M = Maximum water-soluble Na content of raw coal (mg/kg-coal)
M_1 = Na content of 1st washed coal (mg/kg-coal)
M_2 = Na content of 2nd washed coal (mg/kg-coal)
R = Radius of coal particle (cm)
t = Washing time (s)
T = Total washing time in one reactor (s)
V_1 = Volume of bulk water corresponding to a single coal particle (L)
V_1 = Volume of accessible pores of coal particles filled by water (L/kg-coal)
W_{ls} = Liquid-to-solid mass ratio
X = Na removal extent (%)
ρ_c = Density of coal particle (kg/L)
ρ_l = Density of water (kg/L)

REFERENCES

(1) *Electricity*. https://www.bp.com/en/global/corporate/energy-economics/statistical-review-of-world-energy/electricity.html.
(2) Li, C.-Z. *Advances in the science of Victorian brown coal*. Elsevier Science: Oxford. 2004.
(3) Zhou, S.; Hosseini, T.; Zhang, X.; Haque, N.; Zhang, L. *Fuel Process. Technol.* **2018**, *172*, 13−28.
(4) Wu, X.; Zhang, X.; Yan, K.; Chen, N.; Zhang, J.; Xu, X.; Dai, B.; Zhang, J.; Zhang, L. *Fuel* **2016**, *181*, 1191−1202.
(5) Dai, B.-Q.; Low, F.; De Girolamo, A.; Wu, X.; Zhang, L. *Energy Fuels* **2013**, *27*, 6198−6211.
(6) Barnes, I. IEA Coal Research, Clean Coal Centre. *Slagging and fouling in coal-fired boilers*. International Energy Agency Coal Research. 2009.
(7) Gao, Y.; Ding, L.; Li, X.; Wang, W.; Xue, Y.; Zhu, X.; Hu, H.; Luo, G.; Naruse, I.; Bai, Z.; Yao, H. *Fuel* **2017**, *210*, 8−14.
(8) Neavel, R. C.; Nahas, N. C.; Koh, K. K. *Trans. Soc. Min. Eng. AIME* **1977**, *262*, 263−267.
(9) Crank, J. *The mathematics of diffusion*. Oxford university press. 1979.
(10) Readett, D. J.; Quast, K. B.; Mulcahy, D. E.; Ketteridge, I. B. *Symposium on Extractive Metallurgy*, Aus, IMM Melbourne Branch. 1984, 103-109.
(11) Low, F.; Zhang, L. *Talanta* **2012**, *101*, 346−352.
(12) Finkelman, R. B.; Palmer, C. A.; Krasnow, M. R.; Aruscavage, P. J.; Sellers, G. A.; Dulong, F. T. *Energy Fuels* **1990**, *4*, 755−766.
(13) Hubei Yihua Chemical Co Ltd. A high-efficient, multistage and recyclable technique of removing sodium from Xinjiang coal: Chinese Patent CN2,015,100,956,984. 2015.
(14) Levenspiel, O. Chemical reaction engineering. *Ind. Eng. Chem. Res.* **1999**, *38*, 4140−4143.
(15) Zhang, J.; Han, C.-L.; Yan, Z.; Liu, K.; Xu, Y.; Sheng, C.-D.; Pan, W.-P. *Energy Fuels* **2001**, *15*, 786−793.
(16) Matsuoka, K.; Yamashita, T.; Kuramoto, K.; Suzuki, Y.; Takaya, A.; Tomita, A. *Fuel* **2008**, *87*, 885−893.
(17) Wijaya, N.; Choo, T. K.; Zhang, L. *Energy Fuels* **2012**, *26*, 5028−5035.
(18) Lee, L.-H.; Wang, Y.-J.; Chern, J.-M. *J. Hazard. Mater.* **2005**, *123*, 112−119.
(19) Fan, X.; Xing, W.; Dong, H.; Zhao, J.; Wu, Y.; Li, B.; Tong, W.; Wu, X. *Int. J. Nonferrous Metall.* **2013**, *02*, 63−67.
(20) Prasassarakich, P.; Thaweesri, T. *Fuel* **1996**, *75*, 816−820.
(21) *Sodium chloride*. https://en.wikipedia.org/wiki/Sodium_chloride.
(22) Piret, E. L.; Ebel, R. A.; Kiang, C. T.; Armstrong, W. P. *Chem. Eng. Prog.* **1951**, *47*, 405−414.
(23) Grathwohl, P. *Diffusion in natural porous media: contaminant transport, sorption/desorption and dissolution kinetics*. Springer Science & Business Media. 2012.
(24) Ingham, D. B.; Pop, I. *Transport phenomena in porous media*. Elsevier. 1998.
(25) Xin, W.; Changwu, L. *Procedia Eng.* **2011**, *26*, 1058−1064.

DOI: 10.1021/acs.energyfuels.9b00055
Energy Fuels 2019, 33, 2142−2152

Appendix C

Chapter 5 in publication form

ACS Sustainable Chemistry & Engineering

Research Article

Cite This: ACS Sustainable Chem. Eng. 2019, 7, 3349−3355

pubs.acs.org/journal/ascecg

Pyrohydrolysis of $CaCl_2$ Waste for the Recovery of HCl Acid upon the Synergistic Effects from $MgCl_2$ and Silica

Song Zhou, Binbin Qian, Tahereh Hosseini, Anthony De Girolamo, and Lian Zhang*

Department of Chemical Engineering, Monash University, Clayton, Victoria 3800, Australia

Supporting Information

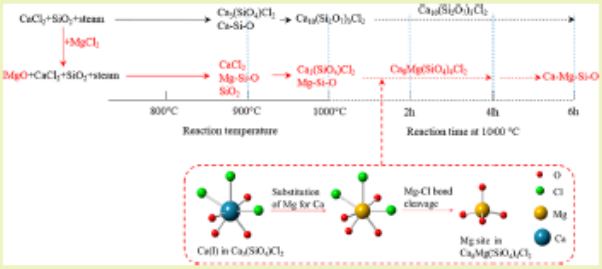

ABSTRACT: In this paper, an efficient HCl acid recovery method from the mixture of alkaline-earth-metal chlorides waste was demonstrated via co-pyrohydrolysis in a laboratory-scale horizontal furnace in a temperature range of 700−1000 °C, and fixed additions of SiO_2 and steam. The synergistic effect of $MgCl_2$ on the HCl recovery from $CaCl_2$ was explored intensively. A double-sided effect was revealed. For the reaction temperatures below 1000 °C, the $MgCl_2$ addition delayed the HCl release through competing with $CaCl_2$ for the inclusion into silica matrix. In contrast, once the chloride mixtures were subjected to 1000 °C with a noticeable residence time (e.g., 2 h) and at a minimum molar ratio of 0.5 of $MgCl_2$ to $CaCl_2$, the $MgCl_2$ addition promoted the HCl release remarkably, via promoting the conversion of $Ca_3(SiO_4)Cl_2$ into $Ca_8Mg(SiO_4)_4Cl_2$. A portion of Mg^{2+} derived from the early decomposition of $MgCl_2$ substituted the Ca(I) site in $Ca_3(SiO_4)Cl_2$, thereby resulting in the formation of weak Mg−Cl bond that is in favor of the HCl release. Additionally, the remaining Mg^{2+} consumed the excessive SiO_2 so as to cause the skeleton of $[SiO_4]^{4-}$ to be fully affiliated and balanced by cations to form $Ca_8Mg(SiO_4)_4Cl_2$ in which the weaker ionic polarization between Ca^{2+} and adjacent anions further enhanced the breakage of the Ca−Cl bonds.

KEYWORDS: *Pyrohydrolysis, Alkaline-earth-metal chlorides, HCl regeneration, Cl release, Silica*

INTRODUCTION

In the hydrometallurgical processing industry, hydrochloric acid possesses notable merits compared to other acids for the extractive leaching of metals, offering higher extraction kinetics, simpler leaching conditions, larger solubilities of metal complexes, and simplicity of the pretreatment requirement.[1,2] However, one major barrier to hydrochloric acid leaching is the difficulty in disposing of the waste lixiviant that is rich in chlorides. The chlorine-bearing lixiviant is prohibited from direct landfilling because it is corrosive and detrimental to the aquatic environment.[3,4] On the other hand, as an important chemical in most chemical industries,[1] hydrochloric acid is primarily produced by the electrolysis of NaCl solution that is energy-intensive, cost-ineffective, and prone to electrode corrosion and fouling.[5−8] Because of these considerations, a successful regeneration of HCl acid from chloride-based lixiviant is crucial for the sustainability of HCl-based industries across the world.

To date, extensive research has been conducted to regenerate HCl gas from chloride solutions, including electrowinning, sulfation precipitation, and pyrohydrolysis.[1] Compared to the other two methods, pyrohydrolysis has only been proven and commercialized for three metal chlorides, $MgCl_2$, $FeCl_2$, and $NiCl_2$.[1] To further advance the pyrohydrolysis technology on a large scale, it is critical to investigate the other metal chlorides such as $CaCl_2$, which is an abundant byproduct produced from a broad variety of hydrometallurgy processes.[9−14] Moreover, because they have similar properties and coexist in a large number of natural minerals and man-made wastes, $CaCl_2$ and $MgCl_2$ are often produced simultaneously, such as from the leaching of low-rank coal and its ash by HCl acid,[9−11] the production of magnesia from dolomite by HCl acid leaching,[12,13] and the production of high-purity magnesia from brine via the addition of slaked lime that generates 1.38−2.75 tonne of $CaCl_2$/tonne of MgO.[14]

Received: October 25, 2018
Revised: December 22, 2018
Published: January 3, 2019

DOI: 10.1021/acssuschemeng.8b05513
ACS Sustainable Chem. Eng. 2019, 7, 3349−3355

Table 1. Summary of HCl Release Extents Obtained at Each Experimental Condition

sample	molar ratio of $CaCl_2$:$MgCl_2$	steam?	SiO_2?	reaction T (°C)	holding time at target T (h)	overall HCl release from mixture (%)	HCl release extent from $CaCl_2$ (%)
$MgCl_2$		no	no	600	2	46	
$MgCl_2$		yes	no	600	2	99	
$CaCl_2$		yes	no	1000	2		0
$CaCl_2$		yes	yes	1000	2		90
$CaCl_2$		yes	yes	700	0		0
$CaCl_2$		yes	yes	800	0		25
$CaCl_2$		yes	yes	900	0		60
$CaCl_2$		yes	yes	1000	0		89
$CaCl_2$		yes	yes	1000	2		90
$CaCl_2$		yes	yes	1000	4		91
$CaCl_2$		yes	yes	1000	6		92
$CaCl_2$ and $MgCl_2$	1:4	yes	yes	700	0	80	0
$CaCl_2$ and $MgCl_2$	1:4	yes	yes	800	0	90	20
$CaCl_2$ and $MgCl_2$	1:4	yes	yes	900	0	93	43
$CaCl_2$ and $MgCl_2$	1:4	yes	yes	1000	0	98	84
$CaCl_2$ and $MgCl_2$	1:4	yes	yes	1000	2	99	94
$CaCl_2$ and $MgCl_2$	1:4	yes	yes	1000	4	99	98
$CaCl_2$ and $MgCl_2$	1:4	yes	yes	1000	6	99	99
$CaCl_2$ and $MgCl_2$	1:0	yes	yes	1000	2	90	90
$CaCl_2$ and $MgCl_2$	1:0.25	yes	yes	1000	2	93	90
$CaCl_2$ and $MgCl_2$	1:0.5	yes	yes	1000	2	96	93
$CaCl_2$ and $MgCl_2$	1:1	yes	yes	1000	2	98	94
$CaCl_2$ and $MgCl_2$	1:2	yes	yes	1000	2	98	94
$CaCl_2$ and $MgCl_2$	1:4	yes	yes	1000	2	99	94

The pyrohydrolysis of $MgCl_2$ involves dehydration, hydrolysis, and thermal decomposition in sequence.[15] An intermediate product, MgOHCl, is formed at 235 °C that subsequently converts to MgO and HCl gas at 415 °C via the reaction with steam. By contrast, the pyrohydrolysis of $CaCl_2$ is refractory because of the larger ionic bond energy of Ca−Cl compared to that of Mg−Cl, 409 vs 327 kJ mol^{-1}.[16] To resolve the breakage of Ca−Cl bond, the coaddition of silica and steam has been examined at 770−870 °C, for different molar ratios of silica to $CaCl_2$, various acidic solids, and partial pressure of steam.[17] The overall reaction route has been proposed as reaction 1 below. At the temperatures below its melting point (772 °C), $CaCl_2$ tends to dissolve into the cage of solid acid to form the $CaCl_2$·SiO_2 solid solution, from which HCl gas is then released. However, the detailed crystal structures of $CaCl_2$·SiO_2 and any of its intermediate compounds have yet to be clarified, and hence, the mechanisms underpinning this reaction still remain vague. More importantly, the effect of $MgCl_2$ on the pyrohydrolysis of $CaCl_2$ has not been explored at all. Upon the coexistence of these two alkaline-earth-metal chlorides, a quick decomposition of $MgCl_2$ at low temperatures presumably results in the formation of free MgO that may compete with $CaCl_2$ for the inclusion into silica matrix, thereby delaying the decomposition of $CaCl_2$. However, in the later stage when $CaCl_2$·SiO_2 solid solution is formed, the invasion of Mg^{2+} cation into the matrix and its substitution to Ca^{2+} could weaken the Ca−Cl affinity, and hence, promote the decomposition of $CaCl_2$.

$$CaCl_2{\cdot}SiO_2(s) + H_2O(g) \rightarrow CaO{\cdot}SiO_2(s) + 2HCl(g) \quad (1)$$

In this study, a series of experiments were designed to prove the above-mentioned hypothesis, and to explore the synergism between $MgCl_2$ and $CaCl_2$ during the co-pyrohydrolysis. The pyrohydrolysis experiment was conducted in a laboratory-scale fixed-bed reactor, under the conditions of 700−1000 °C, a fixed steam partial pressure of 0.7 bar, and varying retention time at the terminal temperature. A non-isothermal heating procedure was first employed so that the residues produced at intermediate temperatures were quenched and subjected to X-ray fluorescence (XRF) and X-ray diffraction (XRD) to quantify the remaining Cl content and its crystalline species, respectively. Scanning electron microscopy (SEM) analysis was also conducted to distinguish the phase of the residues. The changes in the atomic structure of the residues were further determined by CrystalMaker software.[18] In addition, thermodynamic calculations were conducted in FactSage 6.4.[19] All these efforts were made to attain the mechanistic insights governing the co-pyrohydrolysis of $CaCl_2$ and $MgCl_2$, and

DOI: 10.1021/acssuschemeng.8b05513
ACS Sustainable Chem. Eng. XXXX, XXX, XXX−XXX

hence, to promote the HCl regeneration rate from this abundant, mixed waste.

EXPERIMENTAL METHODOLOGY

Experimental Rig and Conditions. An electrically heated horizontal furnace was employed, the schematic of which is illustrated in Figure S1, in the Supporting Information (SI). The thermal decomposition took place inside a quartz tube with an inner diameter of 51 mm and a total length of 1200 mm. A sample-laden corundum plane (Al_2O_3 > 99.7%) was placed in the middle of the furnace. Argon was blended with steam and used to purge the reactor continuously, which also swept away the HCl gas once generated.

For each run, approximately 1 g of $CaCl_2{\cdot}4H_2O$ was blended thoroughly with $MgCl_2{\cdot}6H_2O$ by a roll mill, with varying molar ratios. The amount of $MgCl_2{\cdot}6H_2O$ varied from 0 to 4 mol/mol of $CaCl_2{\cdot}4H_2O$. Additionally, SiO_2 was further mixed with each chloride mixture in an equimolar ratio. All the reagents used are analytical reagent grade with a purity >99% and purchased from Merck. Ltd. (chlorides) and Sigma-Aldrich Co. (silica). The reaction temperature ranged from 700 to 1000 °C with an interval of 100 °C. The temperature was ramped from room temperature at a heating rate of 10 °C/min and then maintained at the target temperature for various durations, ranging from 0 to 6 h. Once the experiment was finished, the sample pan was quickly pulled out and moved to the cold end of the quartz tube, whereas the steam was stopped immediately while pure argon of around 10 L/min was turned on to quench the hot decomposition residue. The volumetric percentage of steam in the feeding gas was fixed at 70% v/v, to guarantee a complete conversion of Cl radicals released to HCl gas.

The overall Cl-bearing gas is simply HCl, and its release extent for the pyrohydrolysis of $CaCl_2$ or $MgCl_2$ alone or their mixtures was determined by the mass difference of Cl between the original chloride sample and its decomposition residue, as shown in eq 2 below.

$$\text{overall Cl release extent}\,(\%) = \frac{M_1 \times P_1 - M_2 \times P_2}{M_1 \times P_1} \times 100 \qquad (2)$$

where M_1 and M_2 are the mass of the original chloride and its residue, respectively, and P_1 and P_2 denote the Cl mass percentage of the original chloride and its residue tested by XRF (SPECTRO IQ II), respectively. The XRF was previously calibrated by the Cl-bearing mixtures ($MgCl_2$ and SiO_2) with different Cl contents.

XRD and Crystal Structure Analysis. Each reaction residue was ground to less than 45 μm to minimize the preferred orientation and improve the statistical distribution of the lattice planes in the reflection. The XRD patterns were recorded on a Rigaku, Miniflex 600 with Cu Kα radiation (λ = 0.15406 nm) under 40 kV and 15 mA. The powdered samples were scanned between 10° and 80° with a D/teX Ultra detector, with a scanning speed of 5°/min and a scanning step of 0.02°. The optical configuration was a fixed divergence slit (1.25°) and a fixed incident antiscatter slit (2.5°). The standards used for the XRD fitting are listed in Table S1. Note that a portion of these standards highly overlap with one another at their most intense peak of approximately 33°. However, their second and third most intense peaks are highly distinctive and sufficient for differentiation. All the Cl-bearing standards bear a very large discrepancy of peak positions and, hence, can be identified easily.

The crystal structure for each identified species was further extracted from the software CrystalMaker through simply importing the respective CIF files shown in Table S1. To extract the local atomic environment of individual atom, the function of "Define Cluster" was applied via defining the cluster range centering on the target atom.[18]

Thermodynamic Equilibrium Calculation. FactSage 6.4 was employed to conduct thermodynamic equilibrium calculations. The equilibrium mode was chosen as OPEN that is specifically designed to simulate a continuous flow system as used in this study. The total step number of injecting gases in the OPEN mode was set as the largest allowable number of 25 to be as close to the practical condition as possible. To reiterate, the inlet gas was defined as 70% v/v of steam and 30% v/v argon, which are exactly the same as the experimental condition mentioned above. The thermodynamic databases applied included FactPS and FToxid. The output products include ideal gas, liquid phases, and solids phases.[19]

RESULTS AND DISCUSSION

Table 1 provides a summary of all the HCl release extents from the experiments conducted throughout this study. Note that the reliability of these experimental data has been assessed by repeating some of the pyrohydrolysis experiments three times. A high accuracy has been confirmed. For instance, for the condition of $CaCl_2$ only at 1000 °C for 2 h, its HCl recovery extents were found to be 89%, 89%, and 90%, bearing a standard deviation of only 0.6%. Additionally, the gaseous Cl-bearing species has also been sampled by impinge trains containing sulfuric acid. The collected Cl^- ion was quantified by a chlorine ion selective electrode detector. The mass balance of Cl reached 95−98% in most of the cases.

Pyrohydrolysis of $MgCl_2$ and $CaCl_2$ Alone. Decomposition of $MgCl_2$ alone was first conducted as a reference. As shown in Table 1 and Figure S2, the addition of steam was essential, promoting the decomposition extent of $MgCl_2$ to 99% at 600 °C for 2 h, relative to 46% only in the absence of steam. In contrast, for the pyrohydrolysis of $CaCl_2$ alone, a higher temperature up to 1000 °C was essential, and so was the coaddition of steam and SiO_2, as evident in Table 1. Upon the addition of SiO_2 at an equimolar ratio to $CaCl_2$, the HCl release extent reached 90% at 1000 °C for 2 h, relative to a nondetectable extent in the presence of steam only. The XRD patterns for the respective residues in Figure 1 demonstrate

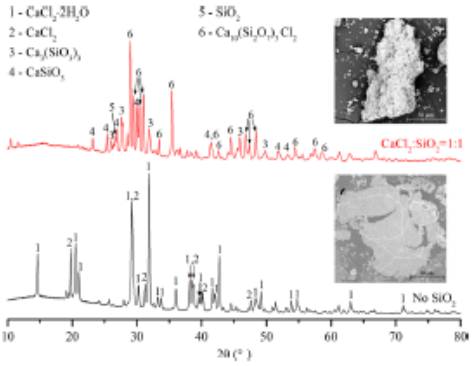

Figure 1. Effect of SiO_2 addition on the pyrohydrolysis of $CaCl_2$ at 1000 °C for 2 h. (The SEM of decomposition residue is included.)

that the $CaCl_2{\cdot}4H_2O$ feedstock was only partially dehydrated in the absence of silica. The inset SEM picture indicates a dense surface for the residue because of the melting of $CaCl_2$ which has a low melting point of 772 °C.[20] In this case, instead of gaseous HCl, the gaseous $CaCl_2$ should be formed because of its liquid−gas equilibrium partitioning. Moreover, the molten cluster could hinder the outward diffusion of Cl radicals and the inward diffusion of steam water molecules. By contrast, the addition of SiO_2 led to the conversion of $CaCl_2$ into the form of $Ca_{10}(Si_2O_7)_3Cl_2$ which has a melting point of 1065 °C. The residue thus remained as fine solid particles with large porosity evident by the inset SEM picture. Such a large surface area and the interatomic clearance in the solid crystal

DOI: 10.1021/acssuschemeng.8b05513
ACS Sustainable Chem. Eng. XXXX, XXX, XXX−XXX

clearly facilitated an easy dissociation of Cl, and an inward diffusion of steam to react with Cl radicals to form HCl. This finding is in line with the previous study.[17]

Co-pyrohydrolysis of $CaCl_2$ and $MgCl_2$ in the Presence of Silica. *HCl Release from $CaCl_2$ as a Function of Temperature.* Figure 2 shows both the experimental and

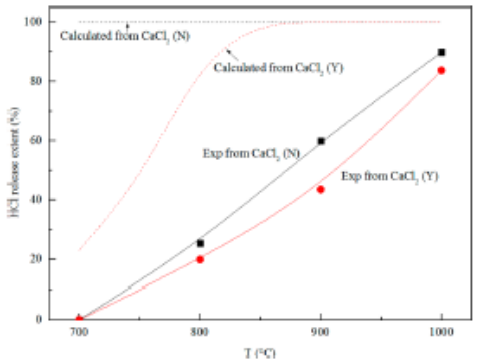

Figure 2. Experimental and Factsage calculated HCl release extent with and without $MgCl_2$ addition versus reaction temperature. (Y and N in parentheses refer to the cases with and without $MgCl_2$ addition, respectively; solid and dashed lines are for the experimental and calculated results, respectively; molar ratio of $CaCl_2$:$MgCl_2$ = 1:4.)

thermodynamic equilibrium prediction results for the co-pyrohydrolysis of $CaCl_2$ and $MgCl_2$ at a fixed molar ratio of 1:4 and different reaction temperatures. Note that, for the experimental works conducted at different temperatures, the *X*-axis refers to the terminal temperature to which the samples have reached upon nonisothermal heating. Once the terminal temperature was reached, the solid residues were quickly quenched. Moreover, considering the full decomposition of $MgCl_2$ before 700 °C, the *Y*-axis was calculated for the HCl release extent from $CaCl_2$ alone, by assigning the remaining Cl in the residue to $CaCl_2$. For all the conditions examined here, the molar ratio of silica was fixed as 1 mol/mol to $CaCl_2$.

In principle, upon the absence of $MgCl_2$, $CaCl_2$ alone can decompose entirely into HCl from 700 °C. The addition of $MgCl_2$ would however postpone the full decomposition of $CaCl_2$ until 900 °C because of their competition for the inclusion into silica matrix. However, the experimental investigation revealed a very slow release of HCl from $CaCl_2$, irrespective of the addition of $MgCl_2$. This is an indicator of the kinetic control for the overall reaction before 1000 °C. At 1000 °C, the HCl release extent was much closer to the thermodynamic prediction, demonstrating a diminutive effect of the kinetic control. Moreover, the inhibitory effect of $MgCl_2$ was experimentally confirmed, which commenced at 800 °C, maximized at 900 °C, but slightly reduced at 1000 °C. Apparently, this links with the change in the crystalline structures of the Cl-bearing residue and its intermediates.

The XRD patterns for all the respective residues are displayed in Figure S3. Considering that each residue contained only one Cl-bearing species which also consists of Ca (because of the strong affinity of these two elements), the molecular ratio of Cl/Ca of the Cl-bearing species in the resultant residue was plotted versus reaction temperature as solid lines in Figure 3. For comparison, the thermodynamic equilibrium calculation results are included as dashed lines.

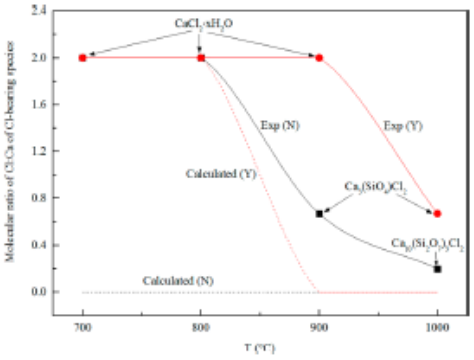

Figure 3. Molecular ratio of Cl/Ca of the Cl-bearing species in the decomposition residues obtained from experiments and Factsage calculations versus reaction temperature. (Y and N in parentheses refer to the cases with and without $MgCl_2$ addition, respectively; experimental results were determined by XRD in Figure S3.)

According to the thermodynamic equilibrium prediction, no Cl-bearing species is present (thus, Cl/Ca = 0) for the case of $CaCl_2$ alone across the whole temperature range. In contrast, $CaCl_2$ remains stable until 900 °C for the case of the addition of $MgCl_2$. This proves the thermodynamic preference for the inclusion of MgO (derived from $MgCl_2$) into the silica matrix before 900 °C. With regard to the experimental observation, $CaCl_2$ disappeared at 900 °C when no $MgCl_2$ was added, converting into $Ca_3(SiO_4)Cl_2$ as the sole Cl-bearing component with a molar Cl/Ca ratio of 0.67, relative to 2.0 for $CaCl_2$. Upon a further rise of the temperature to 1000 °C, the Cl-bearing species converted into $Ca_{10}(Si_2O_7)_3Cl_2$ with a Cl/Ca ratio of 0.2, demonstrating the continuous release of the remaining Cl out of the Ca−Cl affinity. The remaining Cl should be tightly embedded within the matrix, and hence, not able to be released easily. Regarding the case with $MgCl_2$ addition, $CaCl_2$ did not disappear until the temperature reached 1000 °C where $Ca_3(SiO_4)Cl_2$ with a Cl/Ca molar ratio of 0.67 was formed. Clearly, the addition of $MgCl_2$ delayed the formation of the above two intermediate products that are not predicted by the thermodynamic equilibrium model at all. The stronger ability of MgO to react with SiO_2 agreed with the calculation results.

HCl Release from $CaCl_2$ as a Function of Reaction Time at 1000 °C. To further narrow down and even eliminate the inhibitory effort of $MgCl_2$, different retention times at 1000 °C was experimentally explored. The resultant residues were characterized by XRD (Figure S4). Figure 4 compares the HCl release extent with and without the addition of $MgCl_2$ as a function of retention time, where the principal Cl-bearing species and other major compounds in the residues are also listed. As expected, the HCl release extent with the addition of $MgCl_2$ was slightly lower than that without $MgCl_2$ at the beginning, 84% versus 89%. Interestingly, the HCl release extent upon the addition of $MgCl_2$ increased quickly to 94% after a retention period of 2 h, overtaking the value achieved in the absence of $MgCl_2$ that was almost unchanged. It further

DOI: 10.1021/acssuschemeng.8b05513
ACS Sustainable Chem. Eng. XXXX, XXX, XXX−XXX

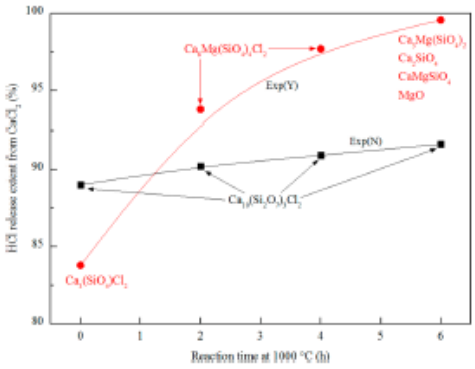

Figure 4. Experimental HCl release extents from $CaCl_2$ with and without $MgCl_2$ after different reaction times at 1000 °C. (The Cl-bearing species is included, determined by XRD in Figure S4.)

increased exponentially, reaching almost 100% in 6 h. Clearly, the effect of $MgCl_2$ addition turned positive upon the increase in the reaction time at 1000 °C.

For the absence of $MgCl_2$, $Ca_{10}(Si_2O_7)_3Cl_2$ was the only Cl-bearing species in the residue, regardless of the retention time. It was transformed from $Ca_3(SiO_4)Cl_2$, which was also the only Cl-bearing species at 900 °C (Figure 3). Upon the addition of $MgCl_2$, the Cl-bearing species changed its structure from $Ca_3(SiO_4)Cl_2$ (Cl/Ca = 0.67) to $Ca_8Mg(SiO_4)_4Cl_2$ (Cl/Ca = 0.25), and then to the mixture of $Ca_3Mg(SiO_4)_2$, Ca_2SiO_4, and $CaMgSiO_4$ with none of them containing Cl at all.

The crystal structure of $Ca_{10}(Si_2O_7)_3Cl_2$ is displayed in Figure 5. It holds a monoclinic structure with space group $P2_1/a$.[21−23] Its basic skeleton is made of isolated groups of $[Si_2O_7]^{6-}$, which are "face-sharing", as shown in Figure 5. Each $[Si_2O_7]^{6-}$ is transformed from two units of $[SiO_4]^{4-}$ (the basic skeleton of $Ca_3(SiO_4)Cl_2$) via sharing one oxygen apex. The isolated $[SiO_4]^{4-}$ exists only in the case of sufficient cations to reach a charge balance.[23] In other words, when the molar ratio of $CaCl_2/SiO_2$ was only one in this study, the molar amount of Ca^{2+} was far from enough to establish a $[SiO_4]^{4-}$-based structure requiring a molar ratio of Ca/Si ≥ 2. Consequently, $[SiO_4]^{4-}$ sites may have to combine on its own to transform into a $[Si_2O_7]^{6-}$-based structure, $Ca_{10}(Si_2O_7)_3Cl_2$ with a smaller Ca/Si of 1.67. This is accompanied by the combination of a portion of silica (SiO_2) with free Ca^{2+} to form another stable species, $CaSiO_3$, and unreacted SiO_2 because of the insufficiency of Ca^{2+} (as evident by the XRD pattern in Figure S4). Back to the sole Cl-bearing species $Ca_{10}(Si_2O_7)_3Cl_2$, $[Si_2O_7]^{6-}$ is "face-sharing" in its atomic structure, in which calcium ions of three types are coordinated with oxygens and/or chlorines. Ca(I) is coordinated with two chlorine and six oxygen, Ca(II) with one chlorine and nine oxygen, and Ca(III) with 13 oxygen.[23] The remarkable ionic polarization between Ca^{2+} and its adjacent anions (O^{2-} and Cl^-) might induce the deviation of their electron clouds to each other, thus leading to varying degrees of overlap of their outer orbitals. Consequently, the bond length and polarity of Ca−Cl decrease, resulting in a transformation of the Ca−Cl bond from purely ionic to "intermediate bond" with the properties of covalent bond.[23] This is beneficial for the release of Cl out of the solid matrix.

Regarding the addition of $MgCl_2$, $Ca_3(SiO_4)Cl_2$ formed at the reaction time of 0 h has a monoclinic structure, with space group $P2_1/c$ and $[SiO_4]^{4-}$ tetrahedrons as the basic skeleton.[24] It was studied that a portion of Ca^{2+} in this species is present as Ca(I) that stays between the lamellar layers of $[SiO_4]^{4-}$ tetrahedrons, being the most weakly bonded and thus the most favorably substituted by any other divalent cations such as Mg^{2+}. Instead, the remaining Ca^{2+} as Ca(II) and Ca(III) sitting in the plane of $[SiO_4]^{4-}$ tetrahedrons are too tough to be substituted.[24] A portion of Ca(I) in $Ca_3(SiO_4)Cl_2$ was gradually substituted by Mg^{2+} and transferred into $Ca_8Mg(SiO_4)_4Cl_2$, as shown in Figure 6a. The resultant Mg−Cl bonds easily broke down and released the Cl. Such a solid−solid substitution reaction is obviously slow, and hence, its effect was observed only when the reaction time was extended to 2 h at 1000 °C. In addition, a portion of the original silica was consumed by Mg^{2+} to form magnesium silicates, leading to sufficient cations to balance the negative charges of the $[SiO_4]^{4-}$ skeleton. In other words, the addition of Mg^{2+} inhibited the self-combination of $[SiO_4]^{4-}$. In terms of the Ca^{2+} coordination environment, Ca(II) as the only site bonded with chlorine is coordinated with six oxygen and two chlorines, as illustrated in Figure 6b. It is affiliated with less anions (O^{2-} and Cl^-) than in $Ca_{10}(Si_2O_7)_3Cl_2$. This may result in weaker ionic polarization between the Ca^{2+} and adjacent anions and the longer bonds of Ca−Cl in $Ca_8Mg(SiO_4)_4Cl_2$.[21,22,25,26] Consequently, the Cl release is easier from $Ca_8Mg(SiO_4)_4Cl_2$ than from $Ca_{10}(Si_2O_7)_3Cl_2$. Upon the release of Cl, the skeleton of $Ca_8Mg(SiO_4)_4Cl_2$ collapses gradually, leading to the formation of various nesosilicates including Ca_2SiO_4, $Ca_3Mg(SiO_4)$, and $CaMgSiO_4$.

Effect of $MgCl_2$ Amount on the HCl Release from $CaCl_2$. The last effort was made to further confirm and optimize the promotion effect of $MgCl_2$ addition at 1000 °C. The decomposition experiments were conducted by mixing various amounts of $MgCl_2$ into the mixture of $CaCl_2$ and SiO_2 at equimolar ratio at 1000 °C for 2 h. As demonstrated in Figure 7 for both HCl release extent from $CaCl_2$ and the major Cl-bearing species in the residues, the HCl release extent was almost stabilized at 90% at the $MgCl_2$ addition ratio less than 0.25, and then it experienced a notable increase to

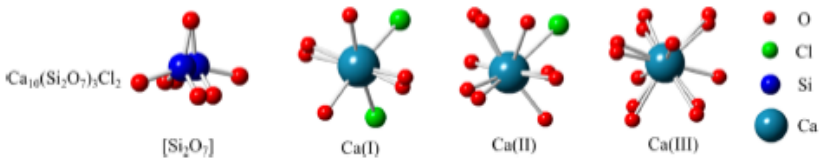

Figure 5. Crystal structure of $Ca_{10}(Si_2O_7)_3Cl_2$ obtained by CrystalMaker software (clusters size defined as 3 Å).

DOI: 10.1021/acssuschemeng.8b05513
ACS Sustainable Chem. Eng. XXXX, XXX, XXX−XXX

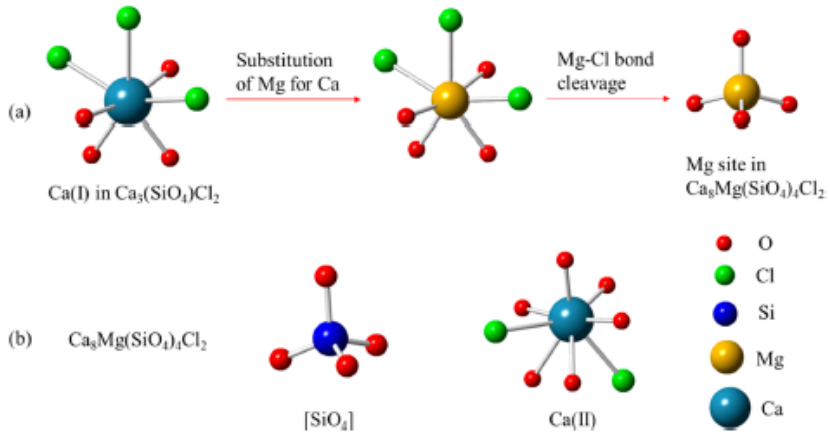

Figure 6. Role of Mg in the formation process of $Ca_8Mg(SiO_4)_4Cl_2$ from $Ca_3(SiO_4)Cl_2$ (a) and the local atomic environments of Si and Ca(II) in $Ca_8Mg(SiO_4)_4Cl_2$ (b).

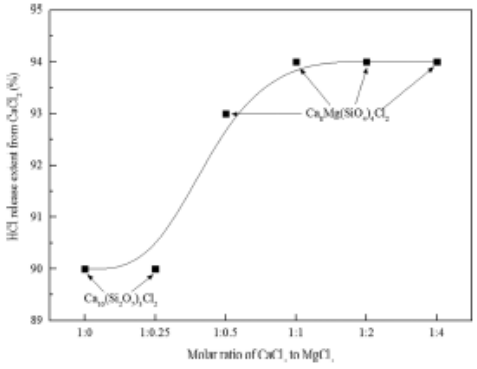

Figure 7. Effect of the $MgCl_2$ addition amount on the HCl release from $CaCl_2$ at 1000 °C for 2 h obtained by experiments. (The Cl-bearing species determined by XRD is also included here. The original XRD patterns are displayed in Figure S5.)

approximately 94% at the equimolar ratio between these two chlorides. Again, this is due to the transferring of Cl-bearing species from $Ca_{10}(Si_2O_7)_3Cl_2$ to $Ca_8Mg(SiO_4)_4Cl_2$ that was formed at the Mg/Ca molar ratio of 0.5 and above. Clearly, the $Ca_8Mg(SiO_4)_4Cl_2$ was fully saturated and stabilized at this ratio. The excessive $MgCl_2$ added simply converted into free MgO (XRD in Figure S5). The reason for optimum dosage of 0.5 mol of $MgCl_2$/mol of $CaCl_2$ should be attributed to the atomic coordination structure of $Ca_8Mg(SiO_4)_4Cl_2$. Again, to balance the negative charge of $[SiO_4]^{4-}$ and $2Cl^-$, two Ca^{2+} cations has to be accompanied by one Mg^{2+}. In this sense, a molar ratio 0.5 for Mg^{2+} to Ca^{2+} is sufficient for a complete release of HCl out of $CaCl_2$.

This study is primarily significant for the environmental management of the chloride wastes which has not yet found a viable manner for disposal. Additionally, this study and the results achieved are critical to a variety of hydrometallurgy processing industries in which the HCl acid recovery from the alkaline-earth-metal chloride is a critical step to improve both the environmental friendliness and cost-effectiveness. Upon a successful regeneration from the solid chlorides, the resultant HCl gas can be further reused in the process, while the resultant oxide residues are applicable for a variety of downstream applications such as cement additives.[27] Although the engineering design was not touched on in this study, a spraying roaster or fluidized bed is apparently suitable for the pyrohydrolysis of alkaline-earth chloride wastes since it allows much smaller size, a longer residence time and sufficient mixing of chlorides and SiO_2. Future works will be conducted specifically to explore the overall reaction rate and the optimum conditions underpinning the design and operation of the specific equipment, in particular, the pyrohydrolysis reaction rate of saturated droplet that is supposedly injected into a spraying roaster or fluidized bed.

CONCLUSIONS

Upon the assistance of silica and steam, HCl has been successfully recovered from the co-pyrohydrolysis of alkaline-earth-metal chlorides ($CaCl_2$ and $MgCl_2$). The influences of a variety of variables have been examined, including reaction temperature and time and molar ratio between two alkaline-earth chlorides. In particular, the synergistic effect of $MgCl_2$ on the pyrohydrolysis of $CaCl_2$ has been discussed extensively. As far as the authors are aware, a double-sided effect of the $MgCl_2$ addition has been revealed for the first time in this study: (1) impediment of HCl release in the temperature-rise period (700−1000 °C) via competition with $CaCl_2$ for inclusion into the solid silica matirx; (2) promotion of HCl release in the retention period at 1000 °C through the formation of an intermediate Cl-bearing compound, $Ca_8Mg(SiO_4)_4Cl_2$, in which the weaker ionic polarization between the Ca^{2+} and adjacent anions facilitated the release of Cl as HCl. Additionally, the addition of 0.5 mol of $MgCl_2$/mol of $CaCl_2$ was found as the optimal dosage, which increased the HCl release notably because of the formation of $Ca_8Mg(SiO_4)_4Cl_2$.

DOI: 10.1021/acssuschemeng.8b05513
ACS Sustainable Chem. Eng. XXXX, XXX, XXX−XXX

■ ASSOCIATED CONTENT

Supporting Information

The Supporting Information is available free of charge on the ACS Publications website at DOI: 10.1021/acssuschemeng.8b05513.

Tabular XRD data for the species used for peak fitting; horizontal thermal decomposition rig schematic and sample loading pan; effect of steam on the decomposition of $MgCl_2$ at 600 °C; XRD patterns of decomposition residues obtained at different temperatures without and with the addition of $MgCl_2$; XRD patterns of decomposition residues obtained after different reaction times at 1000 °C without and with the addition of $MgCl_2$; XRD patterns of decomposition residues of $CaCl_2$ mixed with different amounts of $MgCl_2$ (PDF)

■ AUTHOR INFORMATION

Corresponding Author

*E-mail: lian.zhang@monash.edu. Tel.: +61-3-9905-2592. Fax: +61-3-9905-5686.

ORCID

Song Zhou: 0000-0001-6422-0940
Binbin Qian: 0000-0001-7145-2926
Lian Zhang: 0000-0002-2761-880X

Notes

The authors declare no competing financial interest.

■ ACKNOWLEDGMENTS

This work was supported by the ARC ITRH (150100006). The first and second authors are also appreciative of the China Scholarship Council – Monash University scholarship for the Ph.D. living allowance scholarships.

■ REFERENCES

(1) McKinley, C.; Ghahreman, A. Hydrochloric acid regeneration in hydrometallurgical processes: a review. *Int. J. Miner. Process. Extr. Metall.* **2018**, *127* (3), 157–168.

(2) Rice, N. M. A hydrochloric acid process for nickeliferous laterites. *Miner. Eng.* **2016**, *88*, 28–52.

(3) Cheng, Y.; Sato, A.; Ninomiya, Y.; Dong, Z. Kinetic study of chlorine behavior in the waste incineration process. *Proc. Combust. Inst.* **2009**, *32* (1), 335–342.

(4) Domazetis, G.; Barilla, P.; James, B. D. Lower emission plant using processed low-rank coals. *Fuel Process. Technol.* **2010**, *91* (3), 255–265.

(5) Faverjon, F.; Durand, G.; Rakib, M. Regeneration of hydrochloric acid and sodium hydroxide from purified sodium chloride by membrane electrolysis using a hydrogen diffusion anode-membrane assembly. *J. Membr. Sci.* **2006**, *284* (1), 323–330.

(6) Janssen, L. J. J.; Hoogland, J. G. The electrolysis of an acidic NaCl solution with a graphite anode—III. Mechanism of chlorine evolution. *Electrochim. Acta* **1970**, *15* (6), 941–951.

(7) Yan, X. Y.; Fray, D. J. Molten salt electrolysis for sustainable metals extraction and materials processing—a review. *Electrolysis: Theory, Types and Applications*; Nova Science: New York, 2010.

(8) Du, F.; Warsinger, D. M.; Urmi, T. I.; Thiel, G. P.; Kumar, A.; Lienhard V, J. H. Sodium hydroxide production from seawater desalination brine: process design and energy efficiency. *Environ. Sci. Technol.* **2018**, *52* (10), 5949–5958.

(9) Hosseini, T.; Han, B.; Selomulya, C.; Haque, N.; Zhang, L. Chemical and morphological changes of weathered Victorian brown coal fly ash and its leaching characteristic upon the leaching in ammonia chloride and hydrochloric acid. *Hydrometallurgy* **2015**, *157*, 22–32.

(10) Hosseini, T.; Selomulya, C.; Haque, N.; Zhang, L. Indirect carbonation of victorian brown coal fly ash for CO_2 sequestration: multiple-cycle leaching-carbonation and magnesium leaching kinetic modeling. *Energy Fuels* **2014**, *28* (10), 6481–6493.

(11) Zhou, S.; Hosseini, T.; Zhang, X.; Haque, N.; Zhang, L. Selective removal of sodium and calcium from low-rank coal–Process integration, simulation and techno-economic evaluation. *Fuel Process. Technol.* **2018**, *172*, 13–28.

(12) Akarsu, H.; Yildirim, M. Leaching rates of Icel-Yavca dolomite in hydrochloric acid solution. *Miner. Process. Extr. Metall. Rev.* **2007**, *29* (1), 42–56.

(13) Royani, A.; Sulistiyono, E.; Prasetiyo, A. B.; Subagja, R. Extraction of magnesium from calcined dolomite ore using hydrochloric acid leaching. *AIP Conf. Proc.* **2017**, *1964*, 020017.

(14) Yan, Y.; Lu, X.; Wang, T.; Zhang, Z. A review on the technologies of high-purity magnesia production from brine. *Huagon Jinzhan.* **2016**, *35* (10), 3251–3257.

(15) Huang, Q.; Lu, G.; Wang, J.; Yu, J. Thermal decomposition mechanisms of $MgCl_2{\cdot}6H_2O$ and $MgCl_2{\cdot}H_2O$. *J. Anal. Appl. Pyrolysis* **2011**, *91* (1), 159–164.

(16) Kerr, J. A.; Stocker, D. Strengths of chemical bonds. *CRC Handbook of Chemistry and Physics*; CRC Press: Boca Raton, FL, 1993; Vol. 9 (144), pp 9–145.

(17) Otake, T.; Tone, S.; Komasawa, I.; Kawashima, M. Involvement of Solid Acids in the Thermal Decomposition of Calcium Chloride. *Kagaku Kogaku Ronbunshu* **1983**, *9*, 523–529.

(18) CrytalMaker Software. http://crystalmaker.com (2018).

(19) Jiao, F.; Iwata, N.; Kinoshita, N.; Kawaguchi, M.; Asada, M.; Honda, M.; Sueki, K.; Ninomiya, Y. Vaporization mechanisms of water-insoluble Cs in ash during thermal treatment with calcium chloride addition. *Environ. Sci. Technol.* **2016**, *50* (24), 13328–13334.

(20) Patnaik, P. *Handbook of inorganic chemicals*; McGraw-Hill: New York, 2003.

(21) Ye, R.; Wu, B.; Zeng, K.; Zhang, Z. The properties and the crystal structure of the compound $Ca_{10}Si_6O_{21}Cl_2$ in the three component system $CaO{\cdot}SiO_2{\cdot}CaCl_2$. *J. Chin. Ceram. Soc.* **1986**, *14* (2), 57–64.

(22) Srodek, D.; Juroszek, R.; Krüger, H.; Krüger, B.; Galuskina, I.; Gazeev, V. New Occurrence of rusinovite, $Ca_{10}(Si_2O_7)_3Cl_2$: composition, structure and Raman Data of rusinovite from Shadil-Khokh Volcano, South Ossetia and Bellerberg Volcano, Germany. *Minerals* **2018**, *8* (9), 399.

(23) Zhang, Q. *Inorganic materials* (In Chinese); East China University of Science and Technology: 2010.

(24) Gilbert, M. Site selectivity of dopant cations in $Ca_3(SiO_4)Cl_2$. *J. Phys. Chem. Solids* **2014**, *75* (8), 1004–1009.

(25) Lei, B.; Sha, L.; Zhang, H.; Liu, Y.; Man, S.; Yue, S. Preparation and luminescence properties of green-light-emitting afterglow phosphor $Ca_8Mg(SiO_4)_4Cl_2$: Eu^{2+}. *Solid State Sci.* **2010**, *12* (12), 2177–2181.

(26) Cotton, A. F.; Wilkinson, G.; Bochmann, M.; Murillo, C. A. *Advanced inorganic chemistry*; Wiley: 1999.

(27) Qian, B.; Li, X.; Shen, X. Preparation and accelerated carbonation of low temperature sintered clinker with low Ca/Si ratio. *J. Cleaner Prod.* **2016**, *120*, 249–259.

DOI: 10.1021/acssuschemeng.8b05513
ACS Sustainable Chem. Eng. XXXX, XXX, XXX–XXX